UNIVERSITÁ DEGLI STUDI DI MILANO-BICOCCA
SCUOLA DI SCIENZE
DIPARTIMENTO DI SCIENZA DEI MATERIALI

Doctorate in Materials Science
XXVIII cycle

Continuum modeling of vertical heterostructures: elastic properties and morphological evolution

Doctorate Thesis of
Marco Salvalaglio

Supervisor: Prof. Leonida Miglio
Coordinator: Prof. Gian Paolo Brivio

FEBRUARY 2016

Contents

Introduction

The development of cutting-edge opto- and micro-electronic devices requires increasingly high standards on material quality and novel fabrication techniques. In this context, epitaxial heterostructures represent noteworthy systems, as they allow for a high degree of customization exploiting the properties of different materials and their fine tuning. Therefore, they offer viable paths for the achievement of important technological improvements.

Since the fabrication of the first microelectronic devices, group-IV semiconductors have represented the most suitable materials to get full control of electric currents thanks to the peculiar electronic structure, easily tunable by doping. The first transistor (Shockley, Bardeen, and Brattain - Bell Laboratories - 1947 [1]) was made of Germanium, but Silicon immediately became the backbone of electronics. Indeed, Si devices account for more than 90% of all microelectronics despite other semiconductors have higher carrier mobility, ensuring better charge transport, or larger band gap, yielding to semiconductor properties in a larger range of working temperatures. In addition to its abundance, one important property favored the choice of Si, i.e. the possibility to form good interfaces with its native oxide, SiO_2, that allows for selective deposition and etching processes [2].

Ge/Si heterostructures revealed to be very effective in the integration of many applications in the Si-based technology, such as high-performance transistors [3], memories [4], thermoelectrics [5], solar cells [6, 7] and photodetectors [8]. Indeed, Ge has superior optoelectronic properties and it allows for a high hole mobility [9]. This holds true also for $Si_{1-c}Ge_c$ alloys, even mentioned in the original patent of the bipolar transistor [2]. The use of Ge/Si heterostructures is somehow consolidated in technology. However, some important integration issues concerning the control of the growth morphology, the lattice- and thermal-misfit strain, and the related extended defects are still to be fully solved in order to extend their use to more demanding devices [10, 11]. Moreover, the improvement of performances related to the miniaturization of electronic components, depicted by the Moore's law, is approaching the limit in size of the current technology (whose node is expected to be 10 nm in 2016, according to the International Technology Roadmap for Semiconductors [12]). Possible further lowering of sizes is then tentatively assigned to new pioneering devices [13–15], far from the consolidated technology used nowadays. In light of this, "More than Moore" approaches based on functionalization, diversification and optimization of the physical phenomena in standard systems, without strictly providing a lowering of dimensions, seems to be an alternative and feasible solution for the future developments of electronics.

It is worth mentioning here that the integration of "More than Moore" modules in Si tech-

nology, based in general on high-quality materials and novel device concepts, is a complex task. Indeed, it requires knowledge and expertise from many different research fields, with contributions ranging from theoretical studies up to the most advanced fabrication and characterization techniques. According to this, it appears clear that material science research plays a key role in understanding the present technology to optimize and design the future devices [16]. In particular, theoretical models and simulations with predictive character are highly needed to fully understand the growth at the micro- and nano-scale, and tailor semiconductor heterostructures for specific applications.

Recently, *vertical heterostructures* (VHEs) have been introduced. The adjective "vertical" is here meant to indicate the large height-to-base aspect ratios (AR) of the structures (AR$\geq$1), at variance with planar systems and typical three-dimensional structures obtained in the standard heteroepitaxy (e.g. 3D-islands [17]). These VHEs represent a convenient way to solve most of the issues usually affecting the crystalline quality in Ge on Si standard heteroepitaxy. Indeed, nanometer-wide VHEs, e.g. the so-called nanowires or large aspect-ratio Ge dots, have been proved to be dislocation-free under certain lateral sizes, thanks to the significant relaxation induced by the free surfaces [18]. At the micron scale, instead, VHEs allow for the full relaxation of the thermal stresses [19, 20] and for the removal of dislocation threading arms at crystal tops by controlling the faceted morphology with the growth temperature [21, 22]. In this thesis, a detailed investigation of the main features of these structures is carried out with the aid of a continuum modeling. The general aim is to provide a deep understanding of their properties and to face the investigation of unexplored configurations, in order to suggest new solutions for the achievement of heterostructures with unprecedented material quality.

The choice of a continuum modeling is driven by the strong need to describe systems in a wide range of sizes, roughly from $\sim$10 nm to 10 μm. These sizes are typical of the mesoscale science, where phenomena occurring at the atomic-scale influence global properties of the system [23, 24]. Coarse-grained models are adopted here to describe defects of the crystal structure or the diffusion of adatoms at the surface of solids. In particular, the plasticity onset in VHEs is deeply investigated with the aid of the linear elasticity theory [25] taking into account the explicit elastic fields yielded by the presence of extended defects, i.e. dislocations [26, 27]. Finite Element Method (FEM) simulations are performed to describe the exact strain field in the presence of free surfaces in VHEs, and a quasi-3D model is introduced in order to optimize the required calculations [28]. Moreover, we focus our attention on the morphological evolution of VHEs during high-temperature treatments by means of a Phase Field (PF) model [29, 30], whose equations are solved with the FEM toolbox AMDiS [31] (which allows three-dimensional PF simulations to be efficiently managed). Some dedicated developments of the method [32], which involved the collaboration with Prof. A. Voigt and his research group at the *Technische Universität Dresden*, are illustrated. The morphological evolution of micrometer-wide VHEs is discussed using the PF approach. In particular, the effect of annealing processes is investigated by means of PF simulations, providing an effective description of the diffusion of thermally-generated adatoms on surfaces [33]. The modeling required to account for a fine description of the growth kinetics is also introduced.

As it will be clear by reading the present manuscript, being aware of the physical properties through an accurate modeling allows one to explain and assess experimental evidences [34–38], and also to design new device concepts and processing. Indeed, the predictions provided with the modeling presented in this work have been eventually confirmed by targeted experiments [34, 39–41]. These comparisons provide striking evidences of the model capabilities, also offering interesting information from the technological point of view.

This thesis is organized as follows. In the first two chapters, we introduce the theoretical framework and the main system of interest of the work. In particular, in *Ch*. 1 we introduce the basis of elasticity/plasticity description using the linear elasticity theory, the morphological evolution, and the numerical approach used in this work. In *Ch*. 2 we recall the main aspects of Ge/Si heteroepitaxy and vertical heterostructures are introduced, pointing out their peculiar properties. Then, the models and their applications to real systems are discussed. For the sake of readability, the description of the original theoretical methods and the applications are separated in different chapters. In *Ch*. 3 we describe the modeling of elasticity and plasticity carried out in VHEs, discussing the formulation of a quasi-3D model and the theoretical results. The application of such a modeling to real systems is shown and discussed in *Ch*. 4, where even further developments of the method are introduced according to the specific applications. In *Ch*. 5 we introduce the modeling of the morphological evolution of crystals, describing the details of the PF method developed and implemented to investigate the evolution of VHEs. This modeling allowed us to predict the effect of the annealing process on isolated and closely-spaced VHEs as discussed in *Ch*. 6, where some results involving the growth kinetics are also reported. Finally, the outcomes resulting from this work are summarized in the Conclusions.

1

Theoretical framework

In the first chapter, we provide the theoretical basis for the investigations reported in this thesis. The main aspects of the Linear Elasticity Theory are introduced along with its application to the modeling of plastic relaxation. Then, the main mechanisms contributing to the morphological evolution of heteroepitaxial systems are discussed, focusing on surface diffusion and crystal growth. The Finite Element Method (FEM), adopted to numerically solve the partial differential equations present in this work, is also briefly introduced. This chapter is not meant to be exhaustive. Indeed, only the main concepts and tools explicitly used in the following chapters are reported. Further details about the topics covered here are left to specific textbooks and references within the text.

1.1 Basis of the linear elasticity theory

The elasticity theory deals with the study of elastic media, whose shape can be deformed by a generic load [25]. It describes elastic deformations, but it is also very useful to model inelastic behaviors such as plasticity.

1.1.1 Displacement and strain

Let us consider a continuous medium in an undeformed state (reference configuration), where $\mathbf{x}$ denotes the coordinates of a generic point. After a deformation, the point previously in $\mathbf{x}$ is in another position $\mathbf{X}$. The displacement of points within the solid is

$$\mathbf{u}(\mathbf{x}) = \mathbf{X} - \mathbf{x}. \tag{1.1}$$

Point coordinates in the deformed solid are then given by $\mathbf{X} = \mathbf{x} + \mathbf{u}(\mathbf{x})$, so that an elastic deformation is fully determined once $\mathbf{u}(\mathbf{x})$ is known for each position $\mathbf{x}$. For infinitesimal displacements, deformations can be described by the *Linear Elasticity Theory*, where superposition principle holds. Under such an approximation, transformation of the solid coordinates are described by means of the Jacobian matrix $\mathbf{J}$ of $\mathbf{u}$, where $J_{ij} = u_{i,j}$ with $u_{i,j} = \partial u_i / \partial x_j$. In particular, a convenient choice for this matrix is to make explicit its symmetric and antisymmetric part as

$$J_{ij} = \frac{1}{2}(u_{i,j} + u_{j,i}) + \frac{1}{2}(u_{i,j} - u_{j,i}) \equiv \epsilon_{ij} + \omega_{ij}, \tag{1.2}$$

where $2\varepsilon_{ij} = (u_{i,j} + u_{j,i})$ (symmetric as $\varepsilon_{ij} = \varepsilon_{ji}$) and $2\omega_{ij} = (u_{i,j} - u_{j,i})$ (antisymmetric as $\omega_{ij} = -\omega_{ji}$). Notice that a nonzero displacement field does not necessarily deform the

solid. Indeed, for $\mathbf{u}(\mathbf{x})$ equal to a constant vector, a rigid-body translation is obtained and $\varepsilon_{ij} = \omega_{ij} = 0$. Moreover, for a rigid-body rotation the relative position in the solid are conserved with $\omega_{ij} \neq 0$ and $\varepsilon_{ij} = 0$. Indeed, deformations in the system are described by $\boldsymbol{\varepsilon}$, namely the *strain* tensor, while $\boldsymbol{\omega}$ is defined as *rotation* tensor describing the eponymous transformation. Notice that the definition of $\boldsymbol{\omega}$ corresponds to the curl of $\mathbf{u}(\mathbf{x})$.

1.1.2 Stress and Hooke's law

Once displacement and/or the strain field are defined, also the forces acting on the solid due to the deformation can be considered. They are described by means of the so-called *stress* tensor $\boldsymbol{\sigma}$, defined as the force per unit area along the j-th direction, acting on the i-th face of an infinitesimal cubic volume in the solid. This quantity can be related to the strain tensor by means of a constant tensor $\boldsymbol{C}$. Since both the strain and the stress are second-order tensor, $\boldsymbol{C}$ is a fourth-order tensor[1] (C_{ijkl}, with 3^4 components):

$$\sigma_{ij} = C_{ijkl}\varepsilon_{kl}. \tag{1.3}$$

$\boldsymbol{C}$ is called *Stiffness* tensor, while Eq. (1.3) is often referred to as the Hooke's law. By exploiting the symmetries of stress and strain tensors it can be shown that the independent components in C_{ijkl} are only 21 [25]. Moreover, the convenient Voigt notation may be adopted

$$xx \to 1, yy \to 2, zz \to 3, xy \to 4, xz \to 5, yz \to 6 \implies \sigma_i = C_{ij}\varepsilon_j \quad i,j = 1,..,6$$

allowing to depict $\boldsymbol{C}$ as a symmetric 6×6 matrix. By considering the symmetries of a specific crystal lattice, other relations can be exploited producing a further lowering of the number of independent constants in the stiffness tensor. The materials investigated in this thesis have a cubic lattice. In this case, the independent constants are only 3, namely C_{11}, C_{12} and C_{44}, in the following form:

$$\boldsymbol{C} = \begin{bmatrix} C_{11} & C_{12} & C_{12} & 0 & 0 & 0 \\ C_{12} & C_{11} & C_{12} & 0 & 0 & 0 \\ C_{12} & C_{12} & C_{11} & 0 & 0 & 0 \\ 0 & 0 & 0 & C_{44} & 0 & 0 \\ 0 & 0 & 0 & 0 & C_{44} & 0 \\ 0 & 0 & 0 & 0 & 0 & C_{44} \end{bmatrix}. \tag{1.4}$$

The isotropic condition can also be considered, leading to the additional equation $C_{11} = C_{12} - 2C_{44}$, which lowers the number of the independent constant in $\boldsymbol{C}$ to 2. The components of the elastic constant tensor can then be expressed by C_{12} and C_{44}, also called Lamé constants λ and μ, as

$$C_{ijkl} = \lambda\delta_{ij}\delta_{kl} + \mu\left(\delta_{il}\delta_{jk} + \delta_{ik}\delta_{jl}\right). \tag{1.5}$$

Alternatively, quantities corresponding to some measurable values can be considered as the Young modulus E, which quantifies the ratio of the stress and the strain along the same direction, and the Poisson ratio ν, which quantifies the effect of a uniaxial deformation on perpen-

[1] The summation over repeated indices is adopted hereafter.

dicular directions [25]. They are related to μ and λ by the following equations:

$$E = \mu\frac{3\lambda + 2\mu}{\lambda + \mu} \qquad \nu = \frac{\lambda}{2\left(\mu + \lambda\right)}. \tag{1.6}$$

The energy stored in the system due to the deformations, namely the elastic energy G_ε [25], is

$$G_\varepsilon = \int_V \frac{1}{2} C_{ijkl}\varepsilon_{kl}\varepsilon_{ij}dV = \int_V \frac{1}{2}\sigma_{ij}\varepsilon_{ij} = \int_V \rho_\varepsilon dV, \tag{1.7}$$

where V is the solid volume and ρ_ε is the elastic energy density. For an isotropic media it is given by

$$\rho_\varepsilon = \mu\sum_i \varepsilon_{ii}^2 + 2\mu\sum_{i,j}^{i<j}\varepsilon_{ij}^2 + \frac{\lambda}{2}\left(\sum_i \varepsilon_{ii}\right)^2. \tag{1.8}$$

Notice that the elastic energy is related only to the strain tensor, i.e. only to the deformation of the solid, and not to $\boldsymbol{\omega}$. Indeed, rotations do not contribute to the elastic energy as relative position in the medium are not changed by such a transformation.

1.1.3 Mechanical equilibrium

At the equilibrium, the net force at each point in the elastic body must be zero. Let us consider a generic three-dimensional domain Ω as an elastic medium, bounded by a surface Γ. For a given i-th direction we can observe forces acting per unit volume f_i and tractions at the surface $T_i = \sigma_{ij}n_j$. At the equilibrium,

$$\int_\Omega f_i dV + \int_\Gamma \sigma_{ij}n_j dS = 0, \tag{1.9}$$

and applying the divergence theorem

$$\int_\Omega \left(f_i + \frac{\partial\sigma_{ij}}{\partial x_j}\right) dV = 0. \tag{1.10}$$

This equation must be valid for any arbitrary volume at the equilibrium, even in the limit of a vanishingly small volume, i.e. it must hold point-wise (for each component). Therefore, the equilibrium condition generally reads

$$\mathbf{f} + \nabla\cdot\boldsymbol{\sigma} = 0. \tag{1.11}$$

External forces, applied to the surface of the body, can be included as boundary conditions. At the equilibrium, where an external force $\mathbf{P}$ defined on the infinitesimal surface area dS is present, we must have a force balance described by $P_i\mathrm{d}S - \sigma_{ik}\mathrm{d}S_k = 0$ where $dS_k = dS\hat{n}_k$ is the surface element multiplied by the k-th component of $\hat{\mathbf{n}}$, i.e. the outer-pointing normal. So that, by explicitly writing the expression for dS_k in terms of dS, the condition at the boundary of the elastic medium is

$$\boldsymbol{\sigma}\cdot\hat{\mathbf{n}} = \mathbf{P}. \tag{1.12}$$

In the absence of forces per unit volume, the mechanical equilibrium equation reads

$$\nabla\cdot\boldsymbol{\sigma} = 0, \tag{1.13}$$

and the *free* surface boundary condition ($P_i = 0$) is

$$\boldsymbol{\sigma} \cdot \hat{\mathbf{n}} = 0. \tag{1.14}$$

Notice that all the equations where $\boldsymbol{\sigma}$ appears, also hold when considering $\boldsymbol{\varepsilon}$ by exploiting Eq. (1.3), provided that elastic constants are known. Other boundary conditions will be adopted in the following, concerning *fixed* surfaces (Dirichlet boundary condition for the displacement)

$$u_i = 0 \qquad \forall i, \tag{1.15}$$

and *gliding* boundary condition

$$u_i = 0 \qquad \forall i \neq j, \tag{1.16}$$

with j the index of the direction along which no displacement constraint is imposed, actually allowing for the gliding of points along the direction parallel to the j-th axis.

As widely used in the calculations of *Chs*. 3 and 4, we can take into account a reference state for the deformations by means of the *eigenstrain* formalism, defined in the Eshelby's theory of inclusion [42]. Let us consider a permanent deformation of an elastic medium. A given point has an eigenstrain ε^*_{ij} if the stress vanishes for $\varepsilon_{ij} = \varepsilon^*_{ij}$. So that the stress tensor can be rewritten as

$$\sigma_{ij} = C_{ijkl}(\varepsilon_{kl} - \varepsilon^*_{kl}). \tag{1.17}$$

Moreover, the *eigenstress* can be defined as

$$\sigma^*_{ij} = C_{ijkl}\varepsilon^*_{kl}. \tag{1.18}$$

Solving Eq. (1.13) by imposing an eigenstrain (or eigenstress) consists of determining the equilibrium stress/strain distribution when an initial deformation is imposed by ε^*_{ij} (or σ^*_{ij}), in agreement with the selected boundary conditions. In general, an elastic medium is not able to reach the state of zero stress in every point. So that both the initially deformed regions, and also nearby domains in the medium with a vanishing eigenstrain, will exhibit further deformations which lower the elastic energy. This formulation will be used to account for the heteroepitaxial elastic field, originating from the misfit between the epilayer and the substrate, and for the elastic field induced by the presence of dislocations.

1.2 Dislocations by linear elasticity theory

Dislocations are linear, extended defects of the crystals lattice [26, 27]. They can be formally defined by means of two vectors: the dislocation line $\boldsymbol{\ell}$ and the Burgers vector $\mathbf{b}$. The former is defined as the unit vector parallel to the line that identifies the linear defect. The latter represents the displacement induced by the dislocation in the crystal lattice, defined as the difference in the length of a closed circuit along crystal lattices with and without the dislocation. Such a quantity is illustrated in *Figs.* 1.1(a) and 1.1(b) (for the simple case of the so-called edge dislocation, defined in the following) where it corresponds to the difference in the length of the closed polygonal chains SF and S'F'. Notice that the dislocation, marked by the symbol $\perp$, must be inside the selected closed circuit.

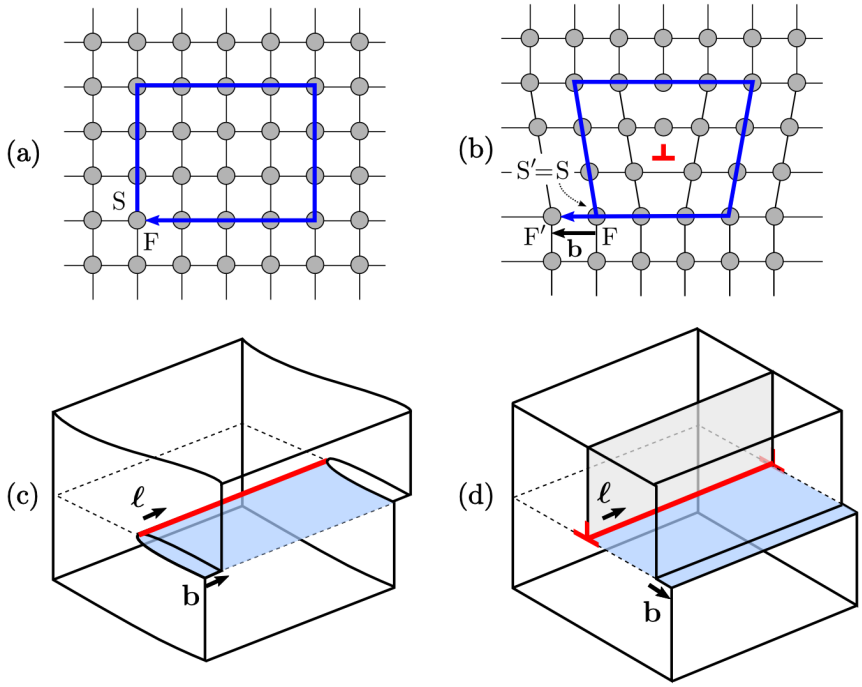

Figure 1.1: Illustration of the dislocation properties. (a) Closed circuit along crystal sites in an undeformed crystal. (b) Path of panel (a) in a lattice with an edge dislocation. The difference between SF and S'F' quantifies the Burgers vector $\mathbf{b}$. (c) Schematic representation of a screw dislocation. (d) Schematic representation of an edge dislocation.

In a continuous medium, the Burgers vector is given by the line integral (taken in a right-handed sense relative to $\boldsymbol{\ell}$) of the displacements $\mathbf{u}$ from the perfect lattice position, around the dislocation [26], i.e.

$$\mathbf{b} = \oint \frac{\partial \mathbf{u}}{\partial l} dl. \tag{1.19}$$

The main dislocation types are the *edge* dislocation, where $\mathbf{b} \perp \boldsymbol{\ell}$, and the *screw* dislocation, where $\mathbf{b} \parallel \boldsymbol{\ell}$. These types are illustrated in *Figs.* 1.1(c) and 1.1(d), respectively. Such characters are rarely observed in real crystals. Generic, *mixed* dislocation are usually present. However, the latter can be described by means of a combination of edges and screw dislocations. Sometimes, dislocations are also referred to by means of the *dislocation character* which is the angle between $\mathbf{b}$ and $\boldsymbol{\ell}$ ($90°$ for edges dislocations, $0°$ for screw dislocations, and between $0°$ and $90°$ for a mixed dislocation).

By means of the linear elasticity theory, introduced in *Sect*. 1.1, it is possible to describe the elastic field induced by the presence of a dislocation in a bulk material in terms of stress and/or strain tensor [26, 27]. Let us consider a dislocation line $\boldsymbol{\ell}$ parallel to the $\hat{\mathbf{z}}$ axis. In the case of a screw dislocation, the stress components have the following expressions:

$$\sigma_{xz} = -\sigma_0 b(1-\nu)\frac{y}{x^2+y^2}, \qquad \sigma_{yz} = \sigma_0 b(1-\nu)\frac{x}{x^2+y^2}, \tag{1.20}$$

while $\sigma_{xx} = \sigma_{yy} = \sigma_{zz} = \sigma_{xy} = 0$. σ_0 is a constant equal to $\mu/(2\pi(1-\nu))$. For an edge

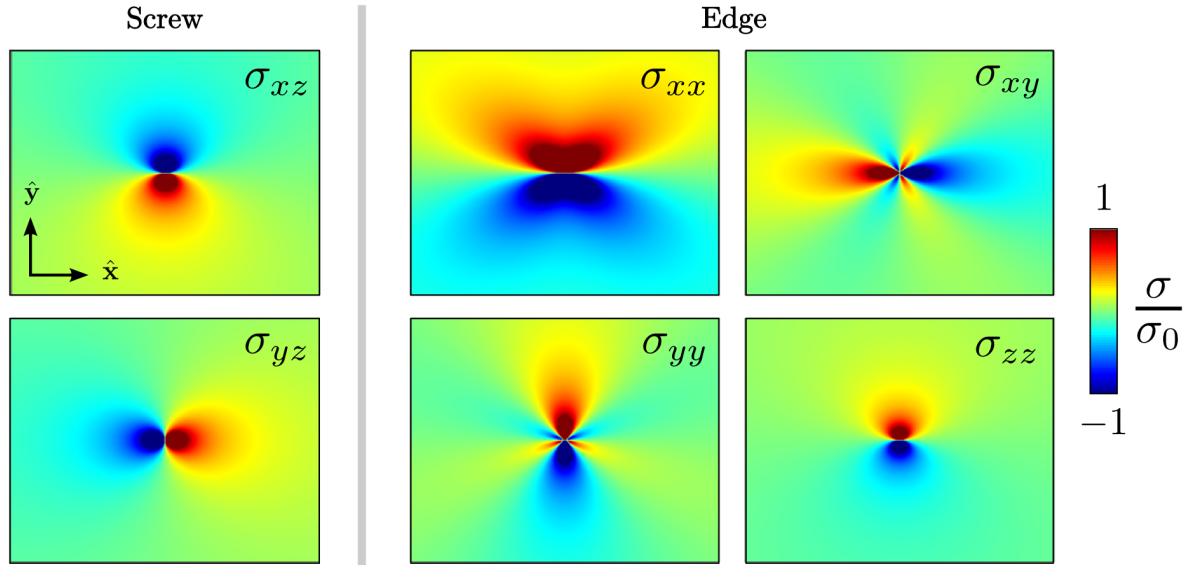

Figure 1.2: Stress components of a screw dislocation (left) and an edge dislocation (right), from Eqs. (1.20) and (1.21), respectively. Stress values are shown in σ_0 units with $|\mathbf{b}| = 1$.

dislocation with $\mathbf{b}$ parallel to $\hat{\mathbf{x}}$ axis they result

$$\begin{aligned} \sigma_{xx} &= -\sigma_0 b \frac{y(3x^2+y^2)}{(x^2+y^2)^2}, & \sigma_{yy} &= \sigma_0 b \frac{y(x^2-y^2)}{(x^2+y^2)^2}, \\ \sigma_{xy} &= \sigma_0 b \frac{x(x^2-y^2)}{(x^2+y^2)^2}, & \sigma_{zz} &= \nu(\sigma_{xx}+\sigma_{yy}), \end{aligned} \tag{1.21}$$

and $\sigma_{xz} = \sigma_{yz} = 0$. Notice that in both Eqs. (1.20) and (1.21) the stress tensor should be considered symmetric, i.e. $\sigma_{ij} = \sigma_{ji}$. The nonzero stress field components generated by Eqs. (1.20) and (1.21) in the xy-plane, i.e. the plane perpendicular to the dislocation, are shown[2] in *Fig.* 1.2, where the stress values are plotted in σ_0 units, with unitary Burgers vector for both edge and screw dislocations.

The elastic field of a mixed dislocation, with $\mathbf{b} = b_x\hat{\mathrm{i}} + b_y\hat{\mathrm{j}} + b_z\hat{\mathrm{k}}$ can be obtained by the superposition of the screw stress/strain components with $b = b_z$ (as $\ell \,||\, \hat{\mathbf{z}}$) and edges components with $b = b_x$ and $b = b_y$. Notice that a change of coordinates $y \to x$ and $x \to -y$ is required to account for the elastic field of the edge components related to b_y. It can be noticed that stresses cannot be evaluated at the dislocation line as a singularity is present at $(x, y) = (0, 0)$. A cut-off radius r_0 for the distance to the singular point is then introduced to avoid such a contribution, and it may be considered as the radius of the *dislocation core*. Indeed, under such a distance from the dislocation line, the continuum description fails, and elastic fields should not be evaluated. The elastic energy associated to dislocations can be computed directly from the integral of equation (1.8) by considering the deformation field described by Eqs. (1.20) and (1.21) and the r_0 parameter. It is often referred to as dislocation *self-energy*. Its expression, obtained by writing the elastic field in polar coordinates and integrating on a plane perpendicular to $\boldsymbol{\ell}$,

[2]The singularity at the dislocation core has been removed exploiting the non-singular formulation reported in *Sect.* 1.2.1

with r_0 as lower integration limit for r, reads

$$G_\varepsilon = \frac{\mu b^2(1-\nu\cos^2\alpha)}{4\pi(1-\nu)}\ln\left(\frac{R}{r_0}\right), \tag{1.22}$$

where α is the dislocation character, $b = |\mathbf{b}|$ and R the distance from $(0,0)$.

Equations reported so far are valid when a straight dislocation in a bulk system is considered. It should be noticed that energy computed as in Eq. (1.22) is infinite when evaluated for $R \to \infty$. This leads to the conclusion that a single straight dislocation cannot be present in a bulk system. Indeed, dislocation loops are usually present, which have a finite energy also in bulk [26]. Actually, the energy of a dislocation when (at least) one free surface is present results always finite, recalling the physical meaning of a straight dislocation. When considering a system with a single free surface, the equilibrium elastic field changes and analytic solutions still exist as discussed in Refs. [43–45]. They are obtained by the superposition of the elastic fields originating from a bulk dislocation, an image dislocation (i.e. mirrored with respect to the free surface with opposite Burgers vector) and a further correction [43] in order to recover the free surface boundary condition described by Eq. (1.14). It is worth mentioning that for screw dislocations, with a line parallel to the surface (i.e. perpendicular to $\hat{\mathbf{n}}$ with a constant distance from the surface), Eq. (1.14) is satisfied just by considering the image dislocation (without any correction), which is not enough if any edge component is present [26]. When more than one free surface is present, analytic solutions are not available and the solution of both Eqs. (1.13) and (1.14) should be computed numerically [28, 46, 47].

1.2.1 Non-singular continuum theory of dislocations

As discussed above, the singularity at the dislocation core is usually healed by evaluating all the elastic field components and the energy outside a cutoff radius r_0. An exact evaluation of the elastic field within the core radius is not possible for continuum approaches as a few atoms are present and a finer description should be adopted. However, a formulation has been developed by Wei Cai et al [48] in order to remove the singularity at the dislocation core. This approach provides finite stress values everywhere, recovering the standard bulk elastic field far from the dislocation core. An additional parameter ζ is introduced ($\sim$ 0.1-0.15 nm in our systems). It quantifies the region where the regularization is active and can be tuned in order to adapt energies to match independent atomistic calculations. Bulk expressions (1.20) and (1.21) are recovered for $\zeta = 0$ and they always coincide to the regularized one for $r \gg \zeta$. In this work, we always exploited such a non-singular formulation for the elastic field, particularly convenient when integrals over the whole volume are computed, such as for the evaluation of the total elastic energy.

In Ref. [48] the stress field components for dislocation segments are derived. Here we report the non-singular stress field in the 2D xy-plane for an infinite straight dislocation obtained by

computing the limit for dislocation-segment endpoints $z_{1,2}$ at $\pm\infty$:

$$\begin{aligned}
\sigma_{xx} &= \frac{\sigma_0\left[b_y x\left(\zeta^2+x^2-y^2\right)-b_x y\left(3\zeta^2+3x^2+y^2\right)\right]}{\left(\zeta^2+x^2+y^2\right)^2},\\
\sigma_{yy} &= \frac{\sigma_0\left[b_y x\left(3\zeta^2+x^2+3y^2\right)-b_x y\left(\zeta^2-x^2+y^2\right)\right]}{\left(\zeta^2+x^2+y^2\right)^2},\\
\sigma_{zz} &= \frac{2\nu\sigma_0\left(2\zeta^2+x^2+y^2\right)\left(b_y x-b_x y\right)}{\left(\zeta^2+x^2+y^2\right)^2},\\
\sigma_{xy} &= \frac{\sigma_0\left[b_x x\left(\zeta^2+x^2-y^2\right)-b_y y\left(\zeta^2-x^2+y^2\right)\right]}{\left(\zeta^2+x^2+y^2\right)^2},\\
\sigma_{xz} = \frac{b_z(\nu-1)\sigma_0 y\left(2\zeta^2+x^2+y^2\right)}{\left(\zeta^2+x^2+y^2\right)^2}, &\qquad \sigma_{yz} = -\frac{b_z(\nu-1)\sigma_0 x\left(2\zeta^2+x^2+y^2\right)}{\left(\zeta^2+x^2+y^2\right)^2}.
\end{aligned} \tag{1.23}$$

The expressions reported here correspond to the stress field components of dislocations used for 2D and quasi-3D (see *Sect*. 3.1) simulations. When full 3D systems are considered (see for instance the results of *Fig*. 3.4), the explicit regularized stresses for dislocation segments from Ref. [48] are used.

1.2.2 Fracture mechanics

The accumulation of a tensile strain in crystalline materials can lead to the mechanical failure with the formation of cracks, i.e. fractures that partially relieve the elastic load. They can be considered as planar defects and their occurrence in materials is described by means of the so-called Griffith theory [26, 49]. The basics of fracture mechanics deeply exploit the concepts of the elasticity theory introduced in *Sect*. 1.1 in terms of the stress field in an elastic medium and of the relaxation mechanism when extending free surfaces within the material.

Let us consider a generic system under a tensile stress σ_{p} in $\hat{\mathbf{x}}$ direction. Cracks may form along a perpendicular-to-$\hat{\mathbf{x}}$ direction $\hat{\mathbf{y}}$ to relieve the stress by introducing free surfaces with normal along $\hat{\mathbf{x}}$ (mode I crack). The energy of creating the free surfaces in the xy-plane, i.e. per unit depth, can be expressed as $2\gamma l$, where l is the length of the crack (along $\hat{\mathbf{y}}$ direction). The factor 2 is needed to account for the two free surfaces formed by the crack insertion and γ is the surface energy density corresponding to the exposed free surfaces. The elastic energy release induced by the elongation of the crack can be quantified as $G = \pi l\sigma_{\mathrm{p}}^2/E$ [26]. The quantity Gdl is the total change in the elastic energy, released by an increase in the length of dl. The amount of surface energy (per unit depth) related to this elongation is $2\gamma dl$ and a crack would propagate spontaneously if $Gdl \geq 2\gamma dl$ with the critical condition given by the equality of the right- and left-hand side. By considering the explicit expression of G, such a critical condition is

$$\frac{\pi l\sigma_{\mathrm{p}}^2}{E} = 2\gamma, \tag{1.24}$$

where the critical stress for the propagation of a crack with length l is

$$\bar{\sigma}_{\mathrm{p}} = \left(\frac{2\gamma E}{\pi l}\right)^{1/2}. \tag{1.25}$$

1.3 Surface energy

When considering a finite solid, an excess of energy is expected due to the presence of surfaces with respect to the bulk material. It derives from the presence of broken chemical bonds at the surfaces, and it can be quantified as the work required to create two infinitely extended surfaces by separating the bulk material. This energy cost per unit area is defined as the surface energy density γ [50, 51]. In solids, this quantity may also depend on the local strain values [52, 53]. The total surface free energy G_γ is

$$G_\gamma = \int_\Gamma \gamma dS, \tag{1.26}$$

where Γ is the surface of the solid and dS the infinitesimal surface element. The γ function may be affected by several factors such as the proximity of the surface to other interfaces/materials, polarity effects (i.e. with III-V compounds) and the specific orientation of the lattice [50]. The latter directly reflects crystal properties such as symmetries within the lattice or surface reconstruction by atom rearrangement. When such a dependance on the local surface orientation $\hat{\mathbf{n}}$ is present, the surface energy density $\gamma(\hat{\mathbf{n}})$ is *anisotropic*. Its determination is far from trivial and both theoretical, ab-initio calculation [54, 55] and experimental methods [56] have been proposed to provide reliable values.

In the absence of strain, the $\gamma(\hat{\mathbf{n}})$ function determines the equilibrium configuration, i.e. the *equilibrium crystal shape* (ECS). This shape can be derived by the so-called Wulff construction [51, 57, 58]. Let us consider a polar representation of the surface energy density, i.e $\gamma(\hat{\mathbf{n}})\hat{\mathbf{n}}$. The Wulff construction consists in taking the convex hull of all the planes tangential to $\gamma(\hat{\mathbf{n}})\hat{\mathbf{n}}$. Such a construction is equivalent to consider the polar representation of the so-called Cahn-Hoffman vector $\boldsymbol{\xi}$ [59–61] defined by

$$\boldsymbol{\xi} = \nabla \left[r\gamma(\theta, \phi) \right] = \gamma \hat{\mathbf{e}}_r + \frac{\partial \gamma}{\partial \theta} \hat{\mathbf{e}}_\theta + \frac{1}{\sin\theta} \frac{\partial \gamma}{\partial \phi} \hat{\mathbf{e}}_\phi, \tag{1.27}$$

with $\hat{\mathbf{e}}_r = \mathbf{r}/|\mathbf{r}|$ and $\mathbf{r} = r\hat{\mathbf{n}}$ a generic vector. $\hat{\mathbf{e}}_\theta$ and $\hat{\mathbf{e}}_\phi$ are unit vectors in the direction along which θ and ϕ increase, respectively. Notice that $\boldsymbol{\xi}$ is not affected by the magnitude of $\mathbf{r}$ but depends only on its orientation $\hat{\mathbf{e}}_r = \hat{\mathbf{n}}$. For isotropic surface energy, $\boldsymbol{\xi} = \gamma\hat{\mathbf{n}}$ and the ECS corresponds to a sphere (or a circle in 2D). Two different conditions can be identified for one anisotropic $\gamma(\hat{\mathbf{n}})$: *weak anisotropy* when the ECS contains all the possible orientations $\hat{\mathbf{n}}$, and *strong anisotropy* when sharp corners appear and some orientations are missing in the ECS. A general criterion to distinguish among these conditions is based on the convexity of $\boldsymbol{\xi}$ [62]. When the product of the two principal curvatures $K_1 K_2$ of the $1/\gamma$-plot (i.e. the gaussian curvature of $1/\gamma$) is always positive, the anisotropy is weak. If it is negative for certain orientations the anisotropy is strong. The critical condition between these two regimes is defined by

$$K_1 K_2 = 0. \tag{1.28}$$

$K_1 K_2$ can be determined as [62]

$$K_1 K_2 = \left(\frac{\gamma}{\xi} \right)^4 \left[v^2 + vu + n_z^2 \left(\frac{\partial^2 \gamma}{\partial n_x^2} \frac{\partial^2 \gamma}{\partial n_y^2} - \left(\frac{\partial^2 \gamma}{\partial n_x \partial n_y} \right)^2 \right) \right], \tag{1.29}$$

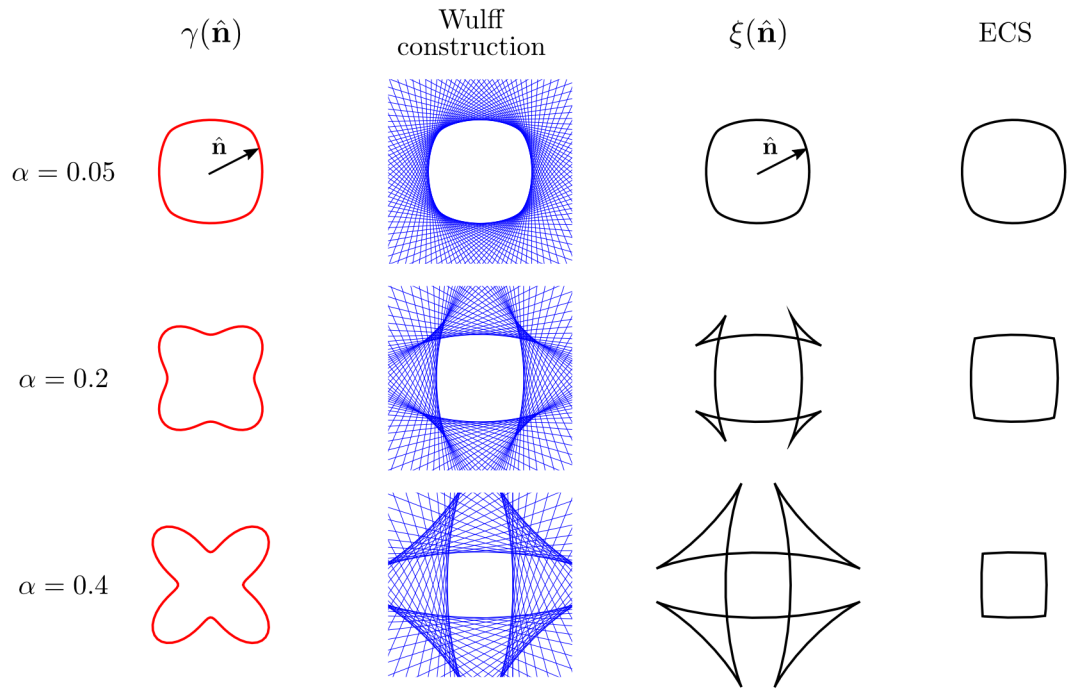

Figure 1.3: From the surface energy density to the ECS. Columns show $\gamma(\hat{\mathbf{n}})\hat{\mathbf{n}}$-plot, the construction obtained by tangent-to-$\gamma(\hat{\mathbf{n}})$ planes, the polar representation of $\boldsymbol{\xi}(\hat{\mathbf{n}})$ and the resulting ECS, respectively. Rows show the outcomes of different anisotropy strength.

with

$$
\begin{aligned}
v &= \gamma - n_x \frac{\partial \gamma}{\partial n_x} - n_y \frac{\partial \gamma}{\partial n_y}, \\
u &= \frac{\partial^2 \gamma}{\partial n_x^2}\left(1 - n_x^2\right) + \frac{\partial^2 \gamma}{\partial n_y^2}\left(1 - n_y^2\right) - 2 n_x n_y \frac{\partial^2 \gamma}{\partial n_x \partial n_y}, \\
\xi &= \sqrt{\left(v n_x + \frac{\partial \gamma}{\partial n_x}\right)^2 + \left(v n_y + \frac{\partial \gamma}{\partial n_y}\right)^2 + (v n_z)^2},
\end{aligned}
$$

and $\gamma \equiv \gamma(n_x, n_y)$. The third component n_z is implicitly defined from the normalization condition $n_z = \sqrt{1 - n_x^2 - n_y^2}$.

In order to inspect the ECS derivation by the aforementioned constructions and the anisotropy regimes, let us consider a simple 2D γ function, corresponding to

$$\gamma(\theta) = 1 - \alpha \cos(N\theta). \tag{1.30}$$

In particular, let us focus on $N = 4$. In *Fig.* 1.3, three different $\gamma(\hat{\mathbf{n}})$ polar plots are shown, obtained with different values for α, i.e. the *anisotropy strength*. Then, the Wulff construction obtained by tangent-to-$\gamma(\hat{\mathbf{n}})\hat{\mathbf{n}}$ planes and the polar representation of $\boldsymbol{\xi}(\hat{\mathbf{n}})$ are illustrated. The latter has been computed from Eq. (1.27) by neglecting dependence on ϕ with $\mathbf{r} = \hat{\mathbf{n}}$. The ECS associated to each $\gamma(\hat{\mathbf{n}})$ in *Fig.* 1.3 actually corresponds to the inner convex hull of tangential planes. According to the α values, different qualitative results are obtained. For $\alpha = 0.05$ the $\boldsymbol{\xi}$ vector is always convex and *weak* anisotropy is present. For $\alpha = 0.2$ and $\alpha = 0.4$, the anisotropy is *strong* and unphysical *ears* appears for the $\boldsymbol{\xi}$ plot. In this case the ECS is the shape bounded by

convex value of $\boldsymbol{\xi}$ excluding such ears, whose orientations are actually missing in the expected equilibrium configuration. The critical anisotropy strength $\bar{\alpha}$, representing the α value at which sharp corners appear, can be obtained by solving Eq. (1.28). In a two-dimensional system it is obtained by solving

$$\gamma(\theta) + \frac{\partial^2 \gamma(\theta)}{\partial \theta^2} = \tilde{\gamma}(\theta) = 0, \tag{1.31}$$

where $\tilde{\gamma}(\theta)$ is called surface stiffness. For the surface energy density used in Eq. (1.30) the critical value is $\bar{\alpha} = 1/(N^2 - 1)$.

1.4 Thermodynamic material transport at the surface

Let us consider a crystal with a shape far from the ECS, with no material deposition. In close-to-equilibrium conditions, e.g. at high temperatures, material transport is mainly driven by the tendency to recover the equilibrium condition. This means that the evolution leads to an increase of the entropy S or, similarly, to the minimization of the free energy[3] $G = U - TS + pV = \sum_i \mu_i N_i$, where U is the internal energy, V the total volume, T the temperature, N_i the number of the i-type particles with a chemical potential defined by $\mu_i = \partial G / \partial N_i|_{p,T,N_{j\neq i}}$ [63]. For N particles of the same type, at constant T and p the dynamics is then driven by the chemical potential only.

Let us consider the evolution of a generic surface profile Γ, where μ is defined pointwise, for a single-component system. By assuming a constant density $n = 1/V_\mathrm{a}$ with V_a the atomic volume and $N = nV$, the chemical potential can be written as $\mu = V_\mathrm{a} \delta G / \delta V$, i.e. it is the change in the free energy induced by a local variation of the volume of the solid phase (bounded by Γ). For the sake of simplicity, V_a will not appear explicitly in equations, but it will be incorporated in the constant coefficient multiplying the chemical potential. Changes of Γ morphology are described here by the local normal velocity $\mathbf{v}_{\hat{\mathbf{n}}}$, defined as $\hat{\mathbf{n}}[(d\mathbf{x}/dt) \cdot \hat{\mathbf{n}}]$ with $\mathbf{x}$ a generic point on Γ and $\hat{\mathbf{n}}$ the outer-pointing normal. Such a velocity describes the local increase/decrease of the solid volume (i.e. $dV/dt = v_{\hat{\mathbf{n}}} dS$ with dS the infinitesimal surface element and $v_{\hat{\mathbf{n}}} = |\mathbf{v}_{\hat{\mathbf{n}}}|$), and should obey a dynamics determined by μ inhomogeneities. The material transport along the surface can mainly occur by means of two different mechanisms: *evaporation-condensation* and *surface diffusion*. In principle, even bulk diffusion can contribute to the morphological evolution, but only to a minor extent with respect to surface mechanisms, and it is here neglected.

If the temperature is sufficiently high and the vapor phase surrounding the solid has an appreciable density, evaporation/condensation of adatoms at the surface is favored [50]. In particular, evaporation is expected in each point where $\mu > \mu_0$, with μ the chemical potential of the solid phase (at the surface) and μ_0 the chemical potential of the vapour phase, the latter assumed to be constant in the approximation of fast evaporation/condensation (or at least when chemical potential can be considered constant in a thin layer surrounding the solid). Vice versa, if $\mu < \mu_0$ condensation occurs. The evolution law describing such an evaporation-

[3] Notice that experimental condition usually consists of constant temperature T and pressure p, so that the Gibbs free energy G should be considered. However, under the assumption of very low pressure, no appreciable pressure-volume work is present and G coincides with the Helmholtz free energy F.

condensation mechanism in terms of $v_{\hat{\mathbf{n}}}$ is

$$v_{\hat{\mathbf{n}}} = -k(\mu - \mu_0), \tag{1.32}$$

with k a generic constant. Notice that equation (1.32) does not inherently conserve the volume of the solid phase. Indeed, if $\mu > \mu_0$ everywhere, a loss of material is expected. In order to describe a material redistribution at the surface, obeying an evolution law as in Eq. (1.32) with volume conservation, the μ_0 term is replaced by $\langle\mu\rangle = \int_\Gamma \mu d\mathbf{x} / \int_\Gamma d\mathbf{x}$.

If the vapour phase has a low density, or when the solid is considered under vacuum, the constant k in Eq. (1.32) is very small and the dominating transport mechanism consists of a material redistribution along the surface by means of *surface diffusion* [33]. In the absence of evaporation, changes in the surface profile are given by the conservation equation

$$v_{\hat{\mathbf{n}}} = -\nabla_\Gamma \cdot \mathbf{j}, \tag{1.33}$$

i.e. by the divergence at the surface of the material current $\mathbf{j}$, determined, in turn, by the Onsager Linear law [64, 65]

$$\mathbf{j} = -M\nabla_\Gamma \mu. \tag{1.34}$$

M is the mobility coefficient describing the motion of the adatoms at the surface and ∇_Γ is the gradient evaluated along the surface profile. Diffusion is a thermally activated mechanism, so that the mobility coefficient is expected to be defined by the Arrhenius law as $M \sim \exp(-A/k_\mathrm{b}T)$ with A an effective energy barrier and k_b the Boltzmann constant. From the Eqs. (1.33) and (1.34) the surface diffusion equation can then be derived as

$$v_{\hat{\mathbf{n}}} = \nabla_\Gamma \cdot [M\nabla_\Gamma \mu]\,. \tag{1.35}$$

An illustration of the material transport by surface diffusion, reporting the main quantities of Eqs. (1.33), (1.34) and (1.35), is shown in *Fig.* 1.4(a). The material transport by surface diffusion can occur only along a continuous profile. If separated crystals are present, their evolutions are totally independent. It is worth mentioning that surface diffusion strictly holds only for vicinal surfaces, where steps are present and the surface can be described by means of a continuous profile. On singular surfaces, i.e. surfaces corresponding to perfect planes for the lattice crystal (as (001) for Si and Ge), profiles with discrete thicknesses accounting for step dynamics should be considered. However, a continuum description is always well-posed in real systems due to deviation from ideal conditions. This is even enforced when external material fluxes (Φ in *Fig*. 1.4(a)) are present providing a constant perturbation of equilibrium configurations (see a dedicated discussion in Ref. [66]).

The equations reported so far hold for a generic form of the free energy that may include different contribution such as the surface energy G_γ from (1.26) and the elastic energy G_ε from (1.7). As it will be discussed in the following, the morphological evolution in our systems of interest is mainly driven by the surface energy minimization, so that we will take into account only the chemical potential related to G_γ. However, notice that a general continuum modeling of heteroepitaxial systems, in particular when considering thin films, must account for the elastic energy contribution to the evolution (mainly provided by lattice misfit).

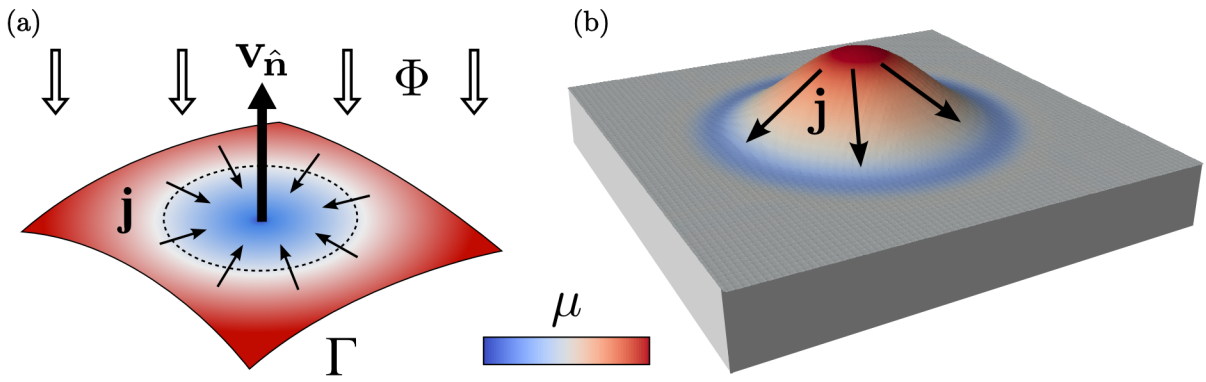

Figure 1.4: Surface diffusion mechanism. (a) Illustration of the main quantities involved in the transport along the surface described by Eqs. (1.33), (1.34) and (1.35). (b) Chemical potential at the surface of a generic profile with isotropic surface energy, i.e. proportional to the local curvature. The arrows illustrate the material flow from regions of high chemical potential toward regions of low chemical potential.

For a single crystal, in the absence of strain, the free energy corresponds to the surface energy of Eq. (1.26). Therefore, following the previous discussion, $\mu = \delta G_\gamma / \delta V$. The three-dimensional formulation for μ can be written using the $\boldsymbol{\xi}$ vector [59, 60], i.e.

$$\mu = \nabla_\Gamma \cdot \boldsymbol{\xi}. \tag{1.36}$$

Notice that for isotropic surface energy density (i.e. no differences in γ among different orientations), according to Eq. (1.27), $\mu = \nabla_\Gamma \cdot (\gamma \hat{\mathbf{n}}) = \gamma\kappa$ where κ is the sum of the two (local) principal curvatures as $\kappa = \nabla \cdot \hat{\mathbf{n}} = \kappa_1 + \kappa_2$. For a two-dimensional profile, the orientation can be represented by means of an angle θ and $\mu = \gamma\kappa$ where κ is here the curvature of the profile in 2D. This can be also demonstrated by considering a 2D perturbation $z(x)$ with isotropic surface energy γ. Indeed, the surface element in Eq. (1.26) can be written as $dS = dx/\cos(\theta) = dx/\sqrt{1+z'^2}$, $\delta G_\gamma / \delta V$ corresponds to $\delta G_\gamma / \delta z$, and

$$\mu = \frac{\delta G_\gamma}{\delta z} = \gamma \left[-\frac{z''}{(1+z'^2)^{3/2}} \right] = \gamma\kappa. \tag{1.37}$$

The chemical potential is then proportional to the surface energy density and to the local curvature κ. Notice that for a small variation in the $z(x)$ profile, we have $\kappa \sim z''(x)$. When considering an anisotropic surface energy density in 2D, the chemical potential reads

$$\mu = \left[\gamma(\theta) + \gamma''(\theta)\right] \kappa = \tilde{\gamma}(\theta)\kappa, \tag{1.38}$$

where $\tilde{\gamma}(\theta)$ is the *surface stiffness* introduced in Eq. (1.31).

In *Fig.* 1.4(b) the chemical potential, with isotropic surface energy (i.e. $\mu = \gamma\kappa$), is shown for a three-dimensional profile made of a generic island. High values of μ are present at the top, as high curvature values are obtained in such a convex region. The concave region around the island shows, in turn, smaller μ values. According to Eq. (1.34), material fluxes are expected as illustrated by the black arrows. When the surface energy density is isotropic, the evolution law describing the surface diffusion is well-posed and the same also applies for anisotropic $\gamma(\hat{\mathbf{n}})$

which lies in the weak anisotropy regime. For strong anisotropy regimes, the surface diffusion equation becomes backward-parabolic for any missing orientations and the evolution law is ill-posed. In order to describe the evolution of sharply faceted profiles, a method accounting for the evolution of shapes made of segments have been introduced by Carter et al in Ref. [67]. Despite it allows to well describe the dynamics of 2D completely faceted surfaces, it requires the definition of a large number of rules to face the production and disappearance of facets and its extension in 3D is far from trivial. In order to describe the evolution of a generic surface (not made of segments) also in the strong anisotropy regime, a proper regularization is, hence, required.

1.4.1 Surface energy regularization

Regularization procedures are usually adopted in order to investigate the evolution of systems also in the strong anisotropy regime. Indeed, they allow one to remove the instabilities in the evolution law, arising from the orientations which are missing in the ECS and from infinite curvatures at sharp corners. Some constructions can be adopted, forcing the orientation excluded from the ECS to be present in a small region close to corners [68, 69]. Similar procedures are often referred to as *Frank's convexification* and they generally require explicit modifications of the surface energy density. A different regularization approach, deeply exploited in *Ch*. 5, consists of adding an energy contribution to γ proportional to the local surface curvature κ [51, 70]

$$\gamma_{\mathrm{reg}}(\hat{\mathbf{n}}) = \gamma(\hat{\mathbf{n}}) + \beta\kappa^2, \tag{1.39}$$

where β is a positive constant, corresponding to a *corner energy* parameter. It can be considered as a higher order approximation of the surface energy density as function of $\hat{\mathbf{n}}$ [51, 71, 72], i.e.

$$\gamma(\hat{\mathbf{n}}, \nabla\cdot\hat{\mathbf{n}}, ...) = \gamma(\hat{\mathbf{n}}) + \beta\left(\nabla\cdot\hat{\mathbf{n}}\right)^2 + ... \tag{1.40}$$

When the dynamics is driven by the surface energy with such a regularized $\gamma_{\mathrm{reg}}(\hat{\mathbf{n}})$, the tendency toward the formation of sharp corners, driven by the $\gamma(\hat{\mathbf{n}})$ term, is balanced by the energy contribution proportional to $\beta\kappa^2$. As a result, rounded shapes are formed at the corners and edges of the ECS. Such a corner rounding is found to have an extension proportional to $\sim\sqrt{\beta}$. For $\beta\to 0$ the limit of the ECS as obtained by the Wulff construction (or by $\boldsymbol{\xi}$) is recovered [70].

1.5 Crystal growth

In *Sect*. 1.4, we described the material transport at the surface driven by the minimization of the surface energy. The growth of the solid phase can be described in such a framework as a condensation mechanism using Eq. (1.32). When the deposition of material is present, crystal growth can be also modeled by accounting for an external material source, describing a growth velocity proportional to the material flux Φ. This holds true, in particular, when the deposition in ballistic regimes is considered such as with Molecular Beam Epitaxy (see also *Sect*. 2.2.3), but can be also adopted for other growth techniques such as Chemical Vapor Deposition, provided that a proper flux distribution is considered. Such a contribution can be modeled by considering the accumulation and redistribution of adatoms at the surface delivered by the deposition flux. Let us consider the adatom density at the surface as $N_{\mathrm{tot}}(\mathbf{x}) = N(\mathbf{x}) + N_{\mathrm{eq}}(\mathbf{x})$. $N_{\mathrm{eq}}(\mathbf{x})$ is

the equilibrium density at a given temperature while $N(\mathbf{x})$ is the density of excess adatom due to the deposition. The growth velocity of the surface depends on $N(\mathbf{x})$ and on the average time before crystallization τ_{c}. At a given point $\mathbf{x}$ it reads

$$v_{\hat{\mathbf{n}}} = \frac{N}{\tau_c}. \tag{1.41}$$

The exceeding adatom density N at the surface can be obtained by the following rate-equation:

$$\frac{\partial N}{\partial t} = \Phi - \frac{N}{\tau} + \nabla_\Gamma \cdot [D \nabla_\Gamma N], \tag{1.42}$$

where τ^{-1}=τ_{c}^{-1}+τ_{d}^{-1} with τ_{d} the lifetime before desorption. The last term of Eq. (1.42) corresponds to the adatom diffusion along the surface according to the Fick's law with D the diffusion coefficient.

For high deposition rates (or low temperatures, leading to small D values), the adatom diffusion at the surface can be neglected leading to a kinetic regime where each facet grows independently. By considering an initial condition $N = 0$, a stationary adatom density $N_{\mathrm{st}} = \tau\Phi$ is obtained after a transient stage. By substituting N_{st} in Eq. (1.41) the velocity at the stationary state reads

$$v_{\hat{\mathbf{n}}} = \frac{1}{1 + \tau_c/\tau_d}\Phi = \chi\Phi, \tag{1.43}$$

where $\chi = 1/(1 + \tau_c/\tau_d)$ is defined as incorporation rate. This equation can actually be generalized as

$$v_{\hat{\mathbf{n}}}(\hat{\mathbf{n}}, \mathbf{x}) = \chi(\hat{\mathbf{n}})\Phi(\mathbf{x}), \tag{1.44}$$

where $\chi(\hat{\mathbf{n}})$ represents an anisotropic function accounting for orientation-dependent incorporation and/or desorption rate, and $\Phi(\mathbf{x})$ is the amount of material reaching the surface. The latter may be affected by the geometry of the growing profile itself, resulting in a function of the spatial coordinates.

With a generic anisotropic growth velocity (for which we omit the subscript $\hat{\mathbf{n}}$ hereafter), the shape in the steady state can be described by the Wulff construction by replacing $\gamma(\hat{\mathbf{n}})$ with $v(\hat{\mathbf{n}})$ as introduced in Refs. [73, 74]. The same also applies when negative, anisotropic velocities are considered for dissolution or etching processes [75]. Such a shape is often referred to as *kinetic Wulff shape*, and it is fully determined by the growth velocity along the unit vectors normal to the facets. However, in order to describe the growth of crystals with a continuum approach, a continuous $v(\hat{\mathbf{n}})$ function should be considered, with values for any orientation. A method to recover such a velocity distribution is illustrated in the next section.

1.5.1 Continuum description of faceted growth

A continuum approach for the evolution of faceted crystals is reported in Ref. [76]. It is based on the definition of a discrete set of velocities $\mathbf{w}_i$, oriented along the outer-pointing surface normal in the growing faceted profile. These vectors $\mathbf{w}_i$ are then used to construct a continuous $\mathbf{v}(\hat{\mathbf{n}})$ function which recover the corresponding kinetic Wulff shape during the growth. An illustration of the procedure is reported in *Fig.* 1.5. For a given point at the surface, let us

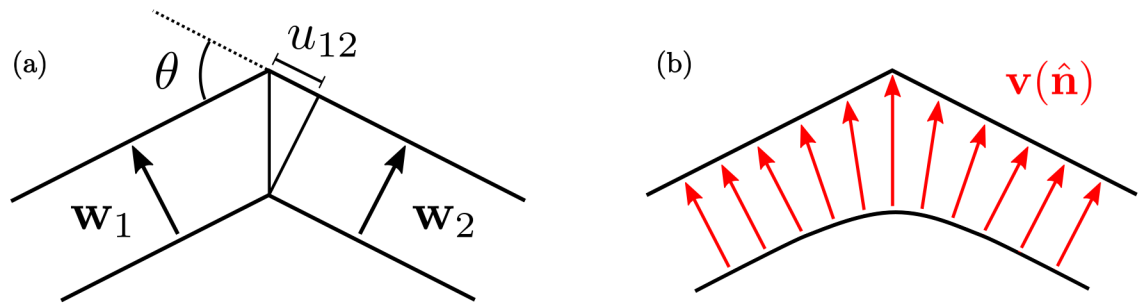

Figure 1.5: Definition of a continuous growth velocity [76]. (a) Schematic representation of the fully-faceted growth defined by discrete velocities $\mathbf{w}_1$ and $\mathbf{w}_2$. Parameters used to define the continuous $\mathbf{v}(\hat{\mathbf{n}})$ function by the procedure in *Sect.* 1.5.1 are shown. (b) Illustration of a growing continuous profile recovering the fully faceted profile by means of the continuous $\mathbf{v}(\hat{\mathbf{n}})$ function.

consider first the index k of the facet which is closest in direction to the local orientation $\hat{\mathbf{n}}$, given by

$$k = \arg\max_m (\hat{\mathbf{n}} \cdot \hat{\mathbf{w}}_m). \tag{1.45}$$

The velocity of such a point is then defined as

$$\mathbf{v}(\hat{\mathbf{n}}) = |\mathbf{w}_k|\hat{\mathbf{n}} + u\hat{\boldsymbol{\tau}}, \tag{1.46}$$

with $\hat{\boldsymbol{\tau}}$ the tangential direction

$$\hat{\boldsymbol{\tau}} = \frac{\hat{\mathbf{n}} - (\hat{\mathbf{n}} \cdot \hat{\mathbf{w}}_k)\hat{\mathbf{w}}_k}{[|\hat{\mathbf{n}} - (\hat{\mathbf{n}} \cdot \hat{\mathbf{w}}_k)\hat{\mathbf{w}}_k|^2 + \delta^2]^{1/2}}. \tag{1.47}$$

δ is a (small) numerical parameters which ensures that $\hat{\tau}$ smoothly vanishes when the numerator goes to zero. The scalar value u is the tangential velocity, which should be set in order to keep sharp corners in the growing profile. It can be derived from geometrical considerations about the angle formed by the two nearest $\mathbf{w}_i$ for a given orientation $\hat{\mathbf{n}}$. For the simple, 2D case of *Fig.* 1.5(a) it reads

$$u_{12} = \frac{|\mathbf{w}_2| - |\mathbf{w}_1|\cos\alpha}{\sin\alpha}. \tag{1.48}$$

By using this procedure, starting from an initial generic profile, the kinetic Wulff shape is recovered after a certain t_w. The evolution for $t < t_\mathrm{w}$ has not particular physical meaning as it results from the construction adopted to recover the desired shape [76]. Notice that this approach is expected to deliver, by means of a continuous $\mathbf{v}(\hat{\mathbf{n}})$ function, the feature of the fully-faceted profile evolution during growth described by the Borgstrom construction [77]. This $\mathbf{v}(\hat{\mathbf{n}})$ would produce, indeed, the enlargement of the facet with the lowest velocity for convex profile or with the highest velocity for concave profiles. The illustration in *Fig.* 1.5(b) shows this behavior, as the velocity at the round corner of the (convex) profile are higher than the others and the corresponding orientations disappear. As a result, the orientations with low velocity extend.

1.6 Numerical integration of PDEs

In order to find the solution for generic PDE systems, defined on a complex domain and with nontrivial boundary conditions, numerical techniques are usually adopted. Several different methods exist such as the Finite Difference Method (FDM), the Spectral Method (SM) and the Finite Element Method (FEM). In the FDM, the differential operators are approximated, and the solution is computed on a discrete set of points (or generally on a grid). The SM mainly consists of approximating the solution by using a set of basis function, often corresponding to Fourier series (with cosines or sines as basis functions). The FEM is based on the partitioning of the whole simulation domain in smaller, simpler parts, i.e. the Finite Elements, and allows the exact operators to be considered with an approximation of the solution using basis function on each element (and not on the whole domain such as with the SM). This latter approach allows differential equations to be solved with a high accuracy also with complex boundary conditions, unmanageable with other approaches. It is widely used in this thesis and an overview of its main concepts is provided in this section. Fine details and extended treatments can be found elsewhere in the literature [78].

1.6.1 Finite element method

In order to describe the basis of the FEM approach, let us begin with the definition of a PDE problem in a d-dimensional space Ω, with Dirichlet boundary condition on $\Gamma_{\mathrm{D}} \subset \partial\Omega$ and Neumann boundary condition on $\Gamma_{\mathrm{N}} = \partial\Omega \backslash \Gamma_{\mathrm{D}}$. It consists of a differential problem in the *strong form*

$$-\nabla \cdot (\mathbf{A}\nabla u) + \mathbf{b} \cdot \nabla u + cu = f \qquad \text{on } \Omega \tag{1.49}$$

$$u = g \qquad \text{on } \Gamma_D \tag{1.50}$$

$$\mathbf{A}\nabla u \cdot \hat{\mathbf{n}} = h \qquad \text{on } \Gamma_N \tag{1.51}$$

where c, f, g, h are generic function, $\mathbf{b}$ a d-dimensional vector, $\mathbf{A}$ a $d \times d$ matrix, and $\hat{\mathbf{n}}$ the normal of Γ_N. The problem should be now reformulated in the so-called *weak form*. It consists of the integration of equation (1.49) against a *test function* ϕ

$$-\int_\Omega \nabla \cdot (\mathbf{A}\nabla u)\phi d\mathbf{x} + \int_\Omega \mathbf{b} \cdot \nabla u \phi + \int_\Omega cu\phi = \int_\Omega f\phi d\mathbf{x}. \tag{1.52}$$

ϕ can be chosen arbitrarily and, in order to describe the current PDE problem, it is set to satisfies homogeneous boundary conditions, i.e the Dirichlet boundary conditions (given by $\phi = g$ on Γ_D). Therefore, the space where ϕ is defined is the Hilbert space $X := \left\{H^1(\Omega) \ : \ \phi = g \text{ on } \Gamma_D\right\}$. Exploiting the integration by part of the first term in Eq. (1.52) and applying the divergence theorem we obtain

$$-\int_\Omega \nabla \cdot (\mathbf{A}\nabla u)\phi d\mathbf{x} = \int_\Omega \mathbf{A}\nabla u \cdot \nabla\phi d\mathbf{x} - \int_{\partial\Omega} \mathbf{A}\nabla u \cdot \hat{\mathbf{n}}\phi d\mathbf{x}, \tag{1.53}$$

so that, as far as the last integral corresponds to the integral on the boundary of the left-hand side of Eq. (1.51), the Neumann boundary conditions are automatically satisfied in Eq. (1.52) $\forall \mathbf{x} \in \Gamma_N$ with $h(\mathbf{x}) = 0$. For a generic h function the boundary condition can be included by

adding its integral against ϕ on Γ_N at the right-hand side of Eq. (1.52). This equation corresponds to a weaker formulation of the problem (1.49)-(1.51) (a solution of the strong form is always solution of the weak form but not vice versa).

Once the problem is defined in the weak form the Finite Elements should then be defined, solving the whole problem in simpler domains. Let us consider first a discretization of the PDE in the weak form. A finite set of basis $\{\phi_i\}_{i=1}^N \in X$ is considered such as the test function can be written as $\phi(\mathbf{x}) = \sum_{i=1}^N v_i \phi_i(\mathbf{x})$, where v_i are arbitrarily chosen. Then, we consider an approximation $u^\star$ of the solution u, defined by $u^\star(\mathbf{x}) = \sum_{j=1}^N U_j \phi_j$, where U_j are the unknowns. By substituting the expressions for $u^\star$ in the weak form formulation (1.52) together with the discretization of the test function, and rearranging the equation to cancel v_i coefficients (for the sake of simplicity Neumann BC are not considered here)

$$\sum_{j=1}^{N} U_j \underbrace{\int_\Omega \mathbf{A}\nabla\phi_j \cdot \nabla\phi_i d\mathbf{x} + \int_\Omega \mathbf{b}\cdot\nabla\phi_j\phi_i d\mathbf{x} + \int_\Omega c\phi_j\phi_i d\mathbf{x}}_{M_{ij}} = \underbrace{\int_\Omega f\phi_i d\mathbf{x}}_{F_i}, \tag{1.54}$$

The same discretization introduced for u applies to all the functions in Eqs. (1.49)-(1.51) as g, which is discretized as $g^\star = \sum_{j=1}^N G_j\phi_j$ and the Dirichlet boundary condition is considered by imposing $U_k = G_k$ if k is the label of a basis function located on Γ_D. As directly illustrated in Eq. (1.54), the N equations resulting from the discretization can then be written as one matrix-vector equation

$$\mathbf{M}\cdot\mathbf{U} = \mathbf{F}, \tag{1.55}$$

where this is the linear system of equations that has to be assembled. The solution for the coefficient vector $\mathbf{U}$ can be computed with several approaches dealing with matrix equations.

In order to apply the FEM method, the domain and its discretization should be explicitly defined. In the FEM approach, it is usually performed by considering a simple space tessellation, obtained by exploiting a geometric object with flat sides, namely a *simplex*, which corresponds to intervals in 1D, triangles in 2D and tetrahedra in 3D. Local basis functions can be defined on the simplexes, defining the *Finite Elements*. A suitable choice for ϕ functions consists of the so-called Lagrangian basis. They consist in localized functions at points called *nodes* such as $\phi_i(x_j) = \delta_{ij}$, i.e. $\phi_i = 1$ on the i-th node and zero on the other nodes. Basis functions can be constructed by first or higher-degree polynomials degree, satisfying the condition mentioned above. In the case of a first-order polynomial, i.e. with *linear elements*, the nodes correspond to the $d+1$ vertexes of the simplex. Higher order elements are characterized by a larger number of nodes within the simplex.

In this work, we exploited two FEM codes. For static evaluation of elastic and plastic relaxation (see *Chs*. 3 and 4) we used the commercial FEM package Comsol Multiphysics as it was suited to perform standard calculations concerning the solution of mechanical equilibrium. For the solution of time-dependent PDEs related to Phase-Field Modeling (see *Chs*. 5 and 6), the open-source FEM toolbox AMDiS [31, 79] has been deeply exploited as this topic required an original implementation of the differential operators and custom numerical methods.

2

Overview on Ge/Si heteroepitaxy

Heteroepitaxy has been a topic of intense research for several decades. Indeed, its deep knowledge is key to fabricate engineered electronic components, realize heterojunctions for electronic applications, and integrate devices in the mainstream technology [11]. It consists in the growth of a crystalline material A on a substrate made of a different crystalline material B. The result of such a process is the formation of heterostructures, whose morphologies are related to the differences between the physical properties of the materials. In this chapter, an overview on the main features of Ge on Si heteroepitaxy is presented. It will introduce all the main features of Ge/Si heterostructures which represent the essential background for the investigations reported in the next chapters. The specific choice of Ge/Si systems is twofold. First, they form prototypical systems for the investigation of heteroepitaxial structures with lattice and thermal misfit, thanks to the complete miscibility of Ge and Si (offering the possibility to tune the lattice mismatch) along with the absence of bond-polarity effects (as, for instance, in III-V compounds). Second, the modeling reported in this thesis has been mainly applied to Ge/Si systems due to their relevance for technological applications. Ge/Si heterostructures with large aspect-ratios (i.e. VHEs), obtained by peculiar growth condition and substrate patterning, are then introduced at the end of the chapter, pointing out their differences with respect to the standard heteroepitaxial systems grown on planar substrates.

2.1 Heteroepitaxial growth modalities

The heteroepitaxial growth on planar substrates usually occurs with three different modalities: layer by layer 2D-growth (*Frank van der Merve*; FM), 3D islands formation on the substrate (*Volmer-Weber*; VB) or 3D island formation on a thin wetting layer, (*Stranski-Krastanov*; SK) [11]. These growth modalities are illustrated in *Fig.* 2.1. From the energetic point of view the main

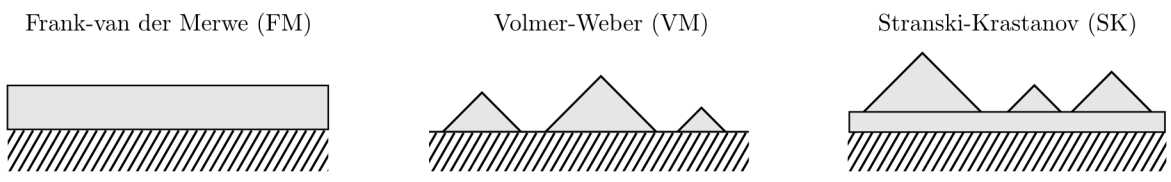

Figure 2.1: Schematic representation of heteroepitaxial growth modalities.

contributions playing a role in the heteroepitaxial growth are the surface energies per unit area of both the epilayer γ_{e} and the substrate γ_{s}, the energy per unit area of the epilayer-substrate interface γ_{i} and the elastic energy per unit volume ρ_{ε}. The latter results from the deformation of the lattice parameter in the epilayer to match the one of the substrate. The FM and VB growth modality can be easily described by considering only surface and interfacial energies. The energy balance corresponding to the covering of the substrate with the epilayer is

$$\Delta\gamma = \gamma_{\mathrm{e}} + \gamma_{\mathrm{i}} - \gamma_{\mathrm{s}}. \tag{2.1}$$

If $\Delta\gamma < 0$, the wetting of the substrate is favored and layer-by-layer growth (FM) occurs while, if $\Delta\gamma > 0$, 3D growth (VM) is expected. The SK growth can be understood by explicitly accounting for the volumetric contribution related to the misfit strain in the epilayer. In particular, such a modality is observed when the balance of Eq. (2.1) is negative with a non-zero elastic energy in the film. In the first stages of the growth, the epilayer tends to wet the substrate as the volume is small and surface contributions dominate. So that a wetting layer is formed. When increasing the volume of the epilayer, elastic energy increases and the growth of islands is favored, as the free surfaces in 3D structures allow the in-plane deformations in the epilayer to be partially relieved. In this regime, for relatively small strains, this elastic relaxation is effective after a few monolayers and the growth of islands occurs on a wetting layer (SK). For larger strain, the total energy can be lowered by the formation of 3D structures before the formation of the first mono-layer, and this would result again in the direct 3D-growth on the substrate (VM).

The energy balance which describes the aforementioned growth modalities can be quantified by means of the formation energy for a 3D-island with respect to the flat film configuration as

$$\Delta G(V) = G_{\mathrm{island}}(V) - G_{\mathrm{film}}(V) = k_1 V + k_2 V^{2/3}, \tag{2.2}$$

where V is the volume of the deposited material, $G_{\mathrm{island}}(V)$ the total energy when arranging the material in 3D islands while $G_{\mathrm{film}}(V)$ the total energy when considering a flat-film configuration. $k_1 = \rho_{\mathrm{island}} - \rho_{\mathrm{film}}$ is the difference between the averaged elastic energy density between an island and a film with the same volume. $k_1 < 0$ as ρ_{island} is typically lower than the one of the film. $k_2 = \gamma(s_{\mathrm{island}} - s_{\mathrm{film}})$, where s_{island} and s_{film} are the ratio between exposed surface S and $V^{2/3}$ of an island and a film, respectively. $k_2 > 0$ as a larger exposed surface is expected for islands. The behavior of Eq. (2.2) is illustrated in *Fig.* 2.2(a), where the formation energy for islands with two different height-to-base aspect ratio (AR) is shown. For small volumes ($V < V_1$), the $V^{2/3}$ term dominates the energy balance, so that $\Delta G > 0$ and the film configuration is favored. For larger volumes ($V_1 < V < V_2$), the contribution proportional to V (multiplied by the negative coefficient k_1) become more important and $\Delta G < 0$, i.e. the free energy is lowered when forming islands. The formation energy becomes negative for shallow islands first (i.e. the one with the lower AR). Steep islands generally expose larger area so that their surface energy is higher than the shallow islands. However, they show a better relaxation of the misfit strain and for large volumes ($V > V_2$) they become the favorite configuration. In general, by increasing the total volume, islands with higher and higher aspect ratio are expected (until

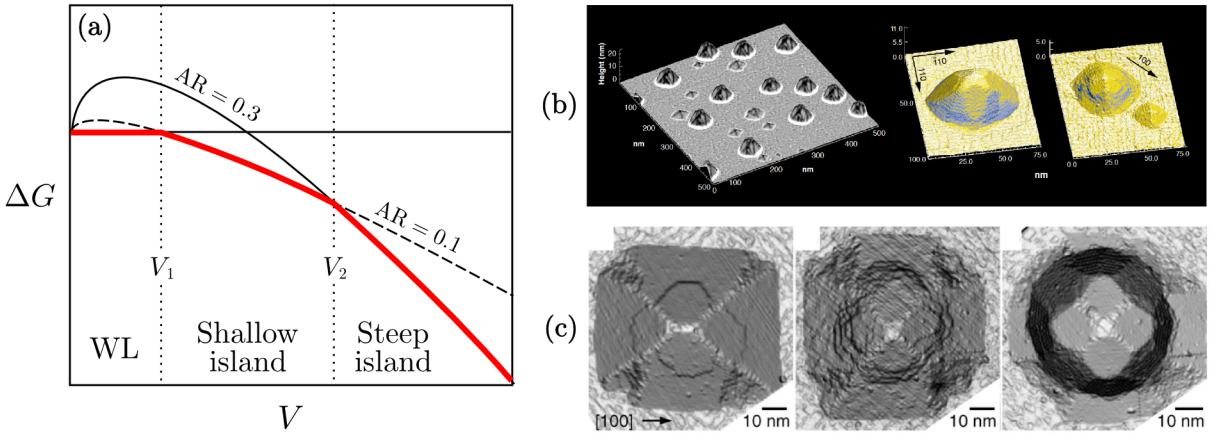

Figure 2.2: 3D heteroepitaxial growth. (a) Energy balances described by Eq. (2.2) as function of V, with parameters extracted from Ref. [84]. The dashed and solid (black) lines report $\Delta G(V)$ for $\mathrm{AR} = 0.1$ and $\mathrm{AR} = 0.3$, respectively. The solid, red-line marks the minimum energy configuration, corresponding to the WL for small volumes ($V < V_1$), to the shallow island for intermediate volumes ($V_1 < V < V_2$) and eventually to steep islands for large volumes ($V > V_2$). (b) Images of Ge on Si heteroepitaxial islands from Ref. [17]. (c) Increase of island aspect ratio with peculiar faceted morphologies during the growth from Ref. [85]: the transition from pyramid- (left) to dome-shaped (right) islands is reported.

reaching the plasticity onset as discussed in the following). This qualitative discussion is based only on a comparison between different equilibrium configurations. In fact, only the energy of different states is considered without taking into account the real kinetic pathway towards the formation of islands during the growth. This description of the SK growth is actually available in literature and its basis can be found in the so-called Asaro-Tiller-Grienfield (ATG) stability analysis [80–82], leading to the same conclusions reported above.

It is worth mentioning that, the close-to-equilibrium conditions which lead to the mechanism discussed so far, can be frustrated by growth kinetics. Despite mismatched semiconductors are expected to undergo SK or VM growth, by means of high external fluxes or low temperatures it is possible to obtain different growth morphologies [83]. For instance, a planar film can be obtained, also when 3D structures are expected according to the free-energy minimization.

2.2 SiGe/Si Stransky-Krastanov growth

Ge and Si have the same diamond crystal structure, i.e. a Face Centered Cubic (FCC) lattice. However, they have different lattice parameters, $a_{\mathrm{Ge}} = 5.658$ Å and $a_{\mathrm{Si}} = 5.432$ Å, so that the epitaxial growth of Ge or SiGe alloys on Si is characterized by the presence of a misfit strain and elastic energy is then accumulated in the system. The misfit strain in a pure Ge epilayer, whose lattice parameter is adapted to the one of the Si substrate, is

$$\varepsilon_{\mathrm{m}} = \frac{a_{\mathrm{Si}} - a_{\mathrm{Ge}}}{a_{\mathrm{Ge}}} = -0.0399. \tag{2.3}$$

For a SiGe alloy, the lattice parameter of the epilayer can be effectively described according to the Vegard's law

$$a_{\mathrm{SiGe}}(c) = a_{\mathrm{Ge}}c + a_{\mathrm{Si}}(1-c), \tag{2.4}$$

where c is the Ge content. In this work, we always use this assumption, adopting linear interpolation as in Eq. (2.4) also for elastic constants of alloys. A linear dependance of the misfit strain on the Ge content is also assumed, i.e. $\varepsilon_{\mathrm{m}}(c) \sim \varepsilon_{\mathrm{m}}c$.

By exploiting the linear elasticity theory equations introduced in *Sect*. (1.1), the volumetric contribution of the elastic energy in the $Si_{1-c}Ge_c$/Si films can be easily determined. In a bulk system, the deformation of the lattice parameter is given by an hydrostatic stress $\boldsymbol{\sigma}$, related to the strain s with respect to the undeformed lattice paramerer by $\sigma_{ij} = sC_{ijkl}\delta_{kl}$. In an infinite Ge layer on Si, with $\hat{\mathbf{z}}$ the outer-pointing normal of the free surface, the deformation corresponds to such a condition for in-plane directions $\hat{\mathbf{x}}$ and $\hat{\mathbf{y}}$, with $s = \varepsilon_{\mathrm{m}}$. In the out-of-plane direction, the free surface boundary conditions has to be considered. According to Eq. (1.14) it reads

$$\sigma \cdot \hat{\mathbf{z}} = \sigma_{xz} + \sigma_{yz} + \sigma_{zz} = \sigma_{zz} = 0. \tag{2.5}$$

where $\sigma_{xz} = \sigma_{yz} = 0$ due to the aforementioned definition of the stress. Being σ_{xx} and σ_{yy} uniform, the mechanical equilibrium condition reads $\partial\sigma_{zz}/\partial z = 0$. In agreement with condition (2.5) at the surface, it is satisifed by $\sigma_{zz} = 0$ within the whole film. Then, ε_{zz} is determined by exploiting the Hooke law (1.3) and it results

$$\varepsilon_{zz} = -\frac{C_{12}}{C_{11}}\left(\varepsilon_{xx} + \varepsilon_{yy}\right) = -\frac{2C_{12}}{C_{11}}\varepsilon_{\mathrm{m}}. \tag{2.6}$$

It can be noticed that the deformation along the $\hat{\mathbf{z}}$ axis has an opposite sign with respect to the misfit strain ε_{m}. Indeed, the relaxation of the film consists of a tetragonal distortion of the cubic cells. Since both $\boldsymbol{\sigma}$ and $\boldsymbol{\varepsilon}$ are known, the elastic energy in the film can be determined by Eq. (1.7). The elastic energy density results

$$\rho_{\mathrm{film}} = \left(C_{11} + C_{12} - \frac{2C_{12}^2}{C_{11}}\right)\varepsilon_{\mathrm{m}}^2 = Y\varepsilon_{\mathrm{m}}^2. \tag{2.7}$$

$Y = \left(C_{11} + C_{12} - 2C_{12}^2/C_{11}\right)$ is the Young modulus under biaxial stress [86]. The isotropic elastic constants adopted in this work, for Ge and Si, are: $E_{\mathrm{Ge}} = 103$ GPa, $\nu_{\mathrm{Ge}} = 0.26$, $E_{\mathrm{Si}} = 130$ GPa, $\nu_{\mathrm{Si}} = 0.27$. By exploiting such values for a pure Ge epilayer in Eq. (2.7), with the proper change in the constants following Eq. (1.6), we obtain $\rho_{\mathrm{film}} = 2.85 \times 10^8\,\mathrm{J/m^3} = 1.3849\,\mathrm{eV/nm^3}$.

The presence of the elastic energy per unit volume ρ_{film} is the main driving force for the SK growth modality in Ge/Si systems. It has been shown that γ_{Ge} is generally lower than γ_{Si} and the interfacial energy is negligible compared to the other terms [54, 55], so that the surface energy balance in Eq. (2.1) is negative and Ge tends to wet the Si substrate. In the early stages of the growth, this layer is actually energetically favored and it usually consists of a few monolayers (ML), 2-3 ML for pure Ge. Then, the epilayer undergoes the transition towards 3D structures [17, 87–91]. Examples of Ge/Si islands are shown in *Fig*. 2.2(b). The increase of the aspect ratio during the deposition with the changes in the morphology is shown in *Fig*. 2.2(c). Other details about the energy balance of Eq. (2.2), for the specific case of the Ge/Si SK growth, can be found in Ref. [84].

The argument mentioned above well describes the qualitative features of close-to-equilibrium Ge/Si SK growth and recall some important basis for the following investigations. However, further phenomena involved in heteroepitaxy have not been explicitly considered. The surface energy and the compression within the field actually depend on the distance from the Si substrate, and this is found to play a role in the stability of the early stages of the SK growth [92]. Moreover, the surface energy density for Ge and Si crystals depends on strain (if present) and it is usually anisotropic, leading to the faceting of islands. Intermixing effects between Ge and Si are also found to take place. Eventually, even if the growth of 3D islands leads to elastic relaxation, after certain volumes the onset of plasticity is expected.

2.2.1 Islands morphology

Faceted morphologies are usually observed for three-dimensional, epitaxial heterostructures [17]. Some examples are reported in *Figs*. 2.2(b) and 2.2(c). The presence of the facets is related to the lattice structure and, in thermodynamic regimes, the exposed surfaces are the ones with a minimum in the surface energy density γ, which can be also affected by local strain (see also *Sect*. 1.3 for a discussion on the theoretical basis of crystal morphologies). On Si(001) substrates, the first Ge islands formed on the WL are pyramids exposing $\{105\}$ facets, reported as first morphology in *Fig.* 2.2(c). They have been demonstrated to be a stable configuration when a compressive strain is present [93, 94]. Then, with further Ge deposition, the resulting increase of the aspect ratio produces a dome-like shape with the appearance of $\{113\}$ and $\{15\ 3\ 23\}$ facets, as shown by the last morphology in *Fig.* 2.2(c). A barn-like shape is eventually formed with the addition of $\{20\ 4\ 23\}$ and $\{23\ 4\ 20\}$ facets together with the $\{111\}$ facets, followed by the formation of a cupola-like shape with $\{715\}$, $\{12\ 1\ 5\}$ and $\{322\}$ facets. The addition of new facets occurs from the base of the islands while the top grows with the morphology recognized for lower aspect-ratio (except for $\{105\}$ facets as they are stabilized by compressive strain, which is relieved at later stages). An overview on the whole mechanism is shown in Ref. [95]. The same set of facets are found to be present also on other substrate orientations [96] and in other heteroepitaxial systems made of FCC crystals as InAs/GaAs [97], revealing the generality of the reported observations.

In order to provide an accurate evaluation of Eq. (2.2), or in general to evaluate properties related to the surface energy, an anisotropic $\gamma(\hat{\mathbf{n}})$ function should then be considered, including a reliable dependance on the surface orientation and including all the facets whose appearance is expected when the aspect ratio increases. Choosing the right values for the surface energy density is actually far from trivial and it generally requires some care. For Ge/Si systems, theoretical calculations are available [98], but they deal with infinite surfaces and, for nano- and micro-structures, finite sizes are present. Experiments can be also useful in order to determine surface energy density values. However, it is worth mentioning here that the extrapolation of such values from experiments, usually performed by exploiting the Wulff construction [51, 57] (see also *Sect*. 1.3), is well-posed only if the equilibrium is reached. More general approaches should then be used when out-of-equilibrium morphologies are observed [32], accounting for the explicit kinetic pathway towards the equilibrium. With the modeling provided in *Ch*. 5 we will also face this problem providing a general tool able to investigate morphologies of

out-of-equilibrium nano- and micro-structures.

2.2.2 Intermixing

Heteroepitaxy, by definition, involves more than one material which may show intermixing effects leading to their alloying. In Ge/Si systems this phenomenon is found to occur and it is mainly driven by entropic effects [99]. Moreover, the alloying of the epilayer with the substrate material, leads to the reduction of the misfit strain, resulting in an enthalpic contribution [100, 101]. The general mechanism consists mainly in atomic exchange, occurring in the first few monolayers (∼2-3 ML) from the surface. Bulk inter-diffusion is also possible, but it is kinetically limited at the usual time scale and temperatures of the growth processes [102]. Several experimental results report about intermixing effect. It is found to occur from the first few monolayers of the growth corresponding to the formation of the wetting layer [103]. Then it becomes stronger in islands, yielding to non-uniform Ge (or Si) distributions, as seen by selective etching experiments [104]. Low Ge contents in islands of $\sim 50\%$ can be observed even when pure Ge deposition is performed [105].

Several theoretical studies have been performed to investigate such a process, involving Atomistic [106] and Monte Carlo (MC) [107, 108] simulations, the latter also combined with FEM calculations of the elastic field [46]. Then, also the evolution in time of the growth by including in standard ATG simulation the contribution of intermixing has been proposed [109, 110], yielding to a complete description of the SK growth dynamics for Ge/Si systems, also when considering patterned substrates [111].

In this work, we mainly neglect the explicit Ge content distribution given by the intermixing effects, and when reported in experimental measurements, typically in nanostructures, we consider uniform $Si_{1-c}Ge_c$ alloys with the resulting average Ge content. The only exception is given in the modeling of the structures in *Sect*. 4.2, as the non-uniformity of the Ge content in the nanostructure is found to play a key role and its explicit modeling has been required. Conversely, at the micron scale, intermixing effects are not taken into account as they usually involve very small length scales compared to the size of the whole structures.

2.2.3 Growth techniques

The techniques adopted for the growth of heteroepitaxial systems generally determine the growth regime and, in turn, the morphology of the final structure. When a low deposition flux is considered, the growth is close to the thermodynamic equilibrium as atoms reaching the surface are free to explore a wide area, allowing for a dynamics driven by the total energy minimization. Moreover, diffusion at the surface is an activated process, which is then enhanced at high T. Low fluxes and high-temperature processes, indeed, lead to a close-to-equilibrium growth. Conversely, with high deposition rates, adatoms at the surface strongly interact each other leading to a short mean free path and surface diffusion is not effective. The result, in this case, is a growth process mainly related to out-of-equilibrium, kinetic effects. In the following, we briefly describe the common techniques used for Ge/Si systems, focusing on the ones used to grow the structures analyzed in the present work.

Two main techniques are used to grow $Si_{1-c}Ge_c$ on Si: the Molecular Beam Epitaxy (MBE)

and the Chemical Vapor Deposition (CVD). The latter is a more generic term, which applies also to non-crystalline films, and it is also referred to as Vapour Phase Epitaxy (VPE). Other names are used to specify the chemical nature of the vapor phase such as organometallic vapor phase epitaxy (OMVPE) or chemical vapor deposition (OMCVD - MOCVD), always referring to the same general process. A detailed overview on such growth techniques can be found in Ref. [11] and in the references therein.

MBE consists of the deposition under ultra-high-vacuum (UHV, $p < 10^7$ Pa) of atoms (or molecules) on a heated substrate generally made of a single-crystal phase. Atom beam is generated in the proper evaporation cells and interactions of the deposited atoms are not present until they reach the substrate. This technique allows for very low deposition rates, and the resulting mean free path of atoms is large. Due to these features, the growth by MBE is generally in the thermodynamic regime, where diffusion process can lead to material rearrangement up to the equilibrium condition during the deposition. According to this, the SK growth is achievable. SiGe alloys with any Ge (or Si) content may be obtained by MBE, usually in the temperature range of 500-900 °C. The growth at lower temperatures is also possible and, when $T < 600$ °C, a significant modification of the kinetics is achieved, even suppressing the tendency to 3D structures of the SK growth modality for high Ge contents.

The CVD technique is characterized by the presence of a gaseous phase, where chemicals containing the material to deposit, namely the precursors, are transported by a carrier gas. When the precursors reach the substrate, usually heated, they react. If the deposition involves more species, as for binary semiconductors, different chemicals are present. The most used precursors for Ge and Si are usually germane (GeH_4) and silane (SiH_4), respectively, but also compound with Cl can be used. In order to realize the deposition, chemicals should react and this happens at the surface of the substrate. Also with CVD, various Ge content alloys can be obtained, by using mixtures of the different precursors. With these techniques, deposition fluxes higher than MBE can be achieved and they are related to the partial pressure of the precursors in the growth chamber. Notice that, focusing on the growth by means of silane/germane, the effective flux is determined by the desorption rate of H at the surface. This is proportional to the temperature, but an upper limit exists in order to preserve the structural properties of the material. In order to enhance the growth rate, other hybrid techniques have been developed such as the Plasma Enhanced Chemical Vapor Deposition (PECVD). By means of a Plasma reactor, reactive species as radical and/or ions are directly formed in the gaseous phase and they are more reactive when reaching the surface. In order to avoid material damaging due to the high kinetic energy acquired in the plasma, Low-Energy PECVD may be exploited [112, 113]. The micrometer-wide VHEs discussed in this work have been first obtained thanks to this LEPECVD technique [19, 20] (see also *Sect*. 2.5.2).

2.3 Plastic relaxation

The first stages of the heteroepitaxial growth have been introduced in *Sects*. 2.1 and 2.2, with a focus on the growth of a few nanometer thick, coherent layers or islands. However, if later stages are considered another important relaxation mechanism is observed, consisting in the

plastic relaxation given by the nucleation of dislocations [26, 27]. Such extended defects are detrimental for the performances of electronic devices and they are found to occur always in standard heteroepitaxy. For close-to-equilibrium conditions and high Ge content they are found to nucleate after the formation of 3D structures [114], while at low Ge contents and/or under strong out-of-equilibrium growth conditions, dislocations directly nucleate in the flat-film configuration [86, 105]. Thanks to the elastic relaxation, the onset during the deposition is delayed for three-dimensional growth with respect to planar growth. A convenient quantity used to investigate the onset of plasticity during the deposition is the so-called *critical thickness* $\bar{h}$ [115], which consists of the thickness at which the insertion of a dislocation is favored. In this section, the main features of the dislocation present in SiGe systems are illustrated, also introducing the determination of the critical thickness for plasticity.

2.3.1 Dislocations in Ge/Si crystals

In the diamond crystal structure of Si and Ge, $\{111\}$ planes have the higher density of lattice sites while the shortest lattice vectors correspond to $a/2\langle 110\rangle$. Therefore, the latter is expected to be the most favored Burgers vectors, while the former represent the so-called glide planes, i.e. the planes on which dislocation may glide within the lattice structure [26, 27]. Pairs made of a Burgers vector and a glide plane are often referred to as *slip systems*. The glide planes may be formally defined as the vector product between the Burgers vector and the dislocation line ($\mathbf{b} \times \boldsymbol{\ell}$). Dislocation lines $\boldsymbol{\ell}$ are typically found to be oriented along $\langle 110\rangle$ directions in (001) film. They may be also oriented along $\langle 112\rangle$ directions, for instance when (111) substrates are used. In this work, we mainly deal with (001) substrates, so that dislocation lines along $\langle 110\rangle$ are taken into account (except for the system discussed in *Sect*. 4.3, where a dedicated discussion is reported). Due to the symmetry of the crystal structure, the possible combinations of $\mathbf{b}$ and glide planes are 12. They are illustrated in *Fig.* 2.3 where the so-called Thompson tetrahedron is shown in the actual FCC structure and in a two-dimensional representation, where the triangular facets of the tetrahedron are reported on a plane. The facets correspond to the $\{111\}$ glide-planes. The edges of the tetrahedron correspond to all the possible Burgers vectors and also the $\langle 110\rangle$ dislocation lines. $\langle 112\rangle$ possible directions for ℓ are also reported.

In SiGe thin films, also including three-dimensional structures, dislocations usually form at the surface as half loops. Then, they move along their glide plane in order to deposit the misfit segment, i.e. the part of the loop which relieves the strain in the epilayer, at the interface with Si. Indeed, this position generally corresponds to a minimum in energy as it maximizes the induced relaxation. A few dislocation types are observed in SiGe systems. The most favorite is the one having $\mathbf{b}$ and $\boldsymbol{\ell}$ along $\langle 110\rangle$ directions, forming a 60° angle in between. They can nucleate and propagate along the $\{111\}$ glide planes. This kind of dislocation will be explicitly considered when evaluating the plasticity onset in the following chapters. It will be referred to as *60° dislocation*. Pure screw dislocations are also observed, which show parallel $\mathbf{b}$ and $\boldsymbol{\ell}$, along $\langle 110\rangle$ directions. They are usually present in the threading arms of the half-loops connecting the segment at the Ge/Si interface to the free surfaces. Another dislocation is also found, showing perpendicular orientation for $\mathbf{b}$ and $\boldsymbol{\ell}$. It is a pure edge dislocation, which is actually not predicted by the Thompson tetrahedron. Indeed, the possible glide planes for such a dislocation

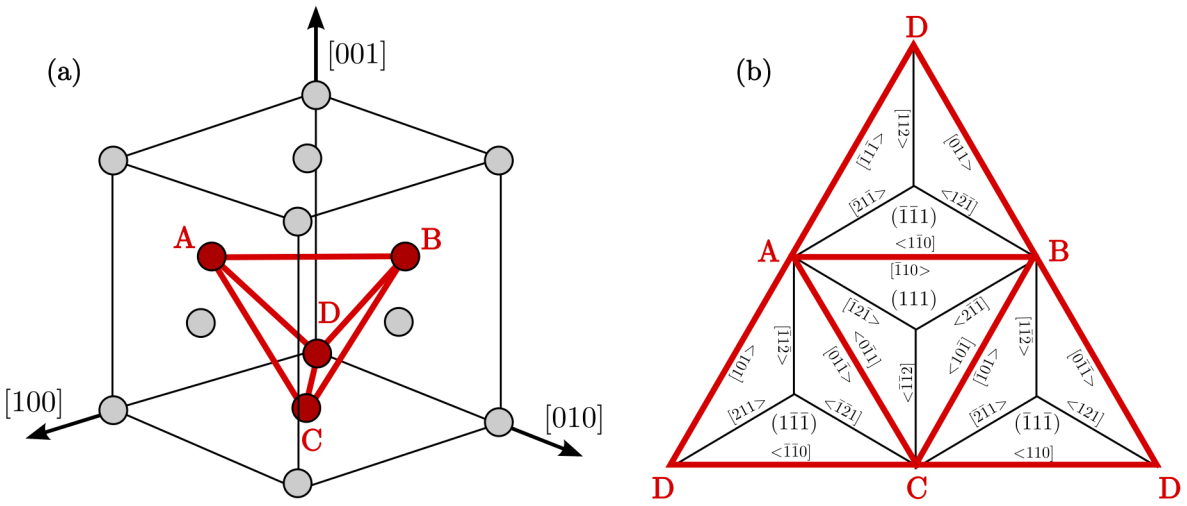

Figure 2.3: Thompson tetrahedron. (a) FCC lattice with the Thompson thetrahedron (red lines). (b) 2D representation of the red tetrahedron in panel (a). Thetraedron facets represents the slip systems formed by Burgers vectors along the red edges, and dislocation lines along all the reported solid lines (adapted from Refs. [116] and [117]).

are the $\{100\}$, which do not appear in *Fig*. 2.3. So that the motion of these dislocations within the FCC crystal structure is not favorite. However, they are found to offer a better relaxation than the 60° dislocations and are observed in experiments [105]. It has been demonstrated that they can be obtained by a reaction of two different 60° dislocations when an activation barrier, allowing for different motions with respect to gliding along planes (i.e. climbing mechanisms [26]), is overcome. A detailed investigation of their formation mechanism, reporting experiments, continuum modeling by means of the linear elasticity theory and molecular dynamics simulation is shown in Ref. [44].

All the investigations reported in this work will deal with the modeling of the misfit segment at the equilibrium, i.e. the dynamics of dislocation is not explicitly considered. In order to evaluate the dislocation elastic field as introduced in *Sect*. 1.2, a plane perpendicular to $\boldsymbol{\ell}$ should be considered. Therefore, a $\pi/4$ rotation around the $\hat{\mathbf{z}}$ axis is adopted. The following directions are then considered as coordinate system: $\hat{\mathbf{x}} = [110]$, $\hat{\mathbf{y}} = [1\bar{1}0]$, $\hat{\mathbf{z}} = [001]$.

2.3.2 Critical thickness

As mentioned before, an important quantity in Ge on Si heteroepitaxy, which allows the onset for plastic relaxation to be evaluated, is the critical thickness for dislocation insertion. This quantity was first investigated by elastic energy minimization leading to an estimation of the thermodynamic limit for plasticity onset. Both general approaches and direct applications to the materials with diamond crystal structure have been reported [118–121]. These works are mainly based on the balance between the elastic energy release by the dislocations and their self-energy. In particular, by focusing on the energetics of the misfit segment and neglecting threading arms, the following expression for the critical thickness has been introduced [122]

$$\bar{h} = \frac{b(1-\nu\cos^2\theta)}{8\pi|\varepsilon_m|(1+\nu)\cos\phi}\left[\ln\left(\frac{h_c}{b}\right)+1\right], \tag{2.8}$$

with θ the angle between the dislocation line $\boldsymbol{\ell}$ and its Burgers vector $\mathbf{b}$ (i.e. the dislocation character), and ϕ the angle between $\mathbf{b}$ and the line at the interface perpendicular to $\boldsymbol{\ell}$. For the heteroepitaxial film considered here, the 60° dislocation would lead to $\cos\theta = \cos\phi = 1/2$ and $b = a_{\mathrm{epi}}/\sqrt{2}$, i.e. the in-plane component of the Burgers vector. The derivation of $\bar{h}$ has been provided also by means of a force-based criterion [115]. In this approach, the force acting on the dislocation loop are considered and $\bar{h}$ is the thickness at which the misfit segment begins to elongate. Notice that, as will be also discussed in *Ch*. 3, the energy criterion evaluated in a plane perpendicular to the straight dislocation would lead to an estimation of the tendency to elongate the misfit segment analogously to a force criterion. Despite the assumption under the derivation of Eq. (2.8), it well describes $\bar{h}$ at high temperatures, where behaviors close to equilibrium (i.e. driven by thermodynamics) is expected. Conversely, the estimation of the thermodynamic critical thickness is generally found to underestimate the experimental critical thickness, at low temperatures. This is mainly due to the lack of kinetic contributions accounting for nucleation or motion barriers which may lead to far-from-equilibrium conditions. Alternative approaches have been also considered in order to account for additional energy contribution required for the nucleation of dislocations [123]. The thermodynamic estimation of $\bar{h}$ will be deeply exploited in *Ch*. 3 in order to evaluate the plasticity onset in our system of interest.

2.4 Thermal strain

At the growth temperature, Ge/Si heteroepitaxial systems are mainly relaxed, due to the elastic and plastic relaxation mechanisms discussed in the previous sections. However, these materials have different thermal expansion coefficients α and, when the system is cooled down to the room temperature, they show a different variation of their lattice parameter. Therefore, an additional mismatch is expected between the epilayer and the substrate, resulting in the so-called *thermal strain* $\varepsilon_{\mathrm{th}}$. In particular, $\alpha_{\mathrm{Si}} = 2.7 \cdot 10^{-6}\ \mathrm{K}^{-1}$ and $\alpha_{\mathrm{Ge}} = 5.9 \cdot 10^{-6}\ \mathrm{K}^{-1}$. Therefore, $\alpha_{\mathrm{Ge}} > \alpha_{\mathrm{Si}}$ and, with decreasing of temperature, Ge would shrink more than Si. A tensile strain of Ge is then expected. According to the usual temperature ranges, the theoretical thermal strain is $\sim 0.2\%$. Notice that it is more than one order of magnitude lower than the misfit strain, and it is usually neglected when strong misfit strains are present. However, when the system is relaxed (via elastic or plastic relaxation) at the growth temperature, the thermal strain may be an important contribution and in SiGe system it is responsible for crack propagation, leading to the mechanical failure of the materials [10, 124] (see also *Sect*. 1.2.2). In general, the rise of thermal stress, when cooling the sample in systems where dislocations are present, may involve their motion and a change in the residual misfit stress [105].

In order to better quantify the strain induced by differences in α and temperature variations, let us consider a generic Ge/Si planar system. For a given lattice parameter a_1 at high temperature T_1, one can write the correspondent low temperature T_2 values a_2 via the thermal expansion coefficient as

$$a_2 = a_1 \left(1 + \int_{\mathrm{T_1}}^{\mathrm{T_2}} \alpha(\mathrm{T}) \mathrm{dT} \right). \tag{2.9}$$

Notice that α generally depends on the temperatures [125, 126]. Following the definition of

Eq. (2.3), the heteroepitaxial strain at a generic temperature T can be defined by means of the effective lattice parameter provided by Eq. (2.9), both for Ge and Si. Moreover, by considering that the integral in Eq. (2.9) is $\ll 1$ (typically in the order of 10^{-3}) and $a_{\mathrm{Ge}}/a_{\mathrm{Si}} \approx 1$, it can be shown that the thermal strain corresponds to the difference between the lattice-misfit at high temperature (which is around zero if plastic relaxation occurs), and the one at the room temperature. Its well-known expression [10] is given by

$$\varepsilon_{\mathrm{th}} = \int_{T_1}^{T_2} [\alpha_{\mathrm{Ge}}(T) - \alpha_{\mathrm{Si}}(T)]\, dT. \tag{2.10}$$

2.5 Vertical heterostructures

The features described so far refer to the growth of $Si_{1-c}Ge_c$ structures on planar Si, where the formation of three-dimensional structures occurs as a self-assembled process and thermodynamic/kinetic driving forces determine the evolution. However, the outcomes of the growth process can be generally controlled by exploiting top-down techniques as, for instance, the substrate patterning. This would allow for a lot of important improvements of materials properties, required to close the gap between pioneering experiments and applications. Examples of the features achievable by patterning are selective deposition, ordering of three-dimensional structures and tuning of sizes [127, 128].

In this section, we focus our attention on specific systems, resulting by both peculiar growth condition and patterning. They consist of structures with large height-to-base aspect ratio compared to the usual systems obtained by the Stranski-Krastanov growth. As stated in the introduction, they will be generally named *Vertical Heterostructures* (VHEs). Such VHEs, can be realized at different length scales, and exhibit peculiar properties according to their size. In this section, a few specific examples are introduced, corresponding to the structures investigated in the following chapters.

2.5.1 Nanometer-wide VHEs

In Ref. [133], then recalled and expanded in Refs. [129], [134] and [135], the growth of nanometer-wide VHEs was proposed as a new way to lower the misfit between an epilayer and its substrate. In turn, by lowering the main driving force for the insertion of dislocations, a significant improvement of the material quality was expected. The main idea investigated in such works consisted in the growth of heterostructures on substrates with lateral free surfaces, in order to maximize the compliance effects in the elastic relaxation as illustrated in *Fig.* 2.4(a). This effect is peculiar of patterned, vertical substrates as nano-pillars, at variance with planar substrates. By increasing the thickness of the deposited material, the epilayer lattice parameter can be recovered, i.e. full relaxation is achieved. This opened the possibility to obtain relaxed crystals at the top of patterned substrates and it was also proposed as a way to form elastically relaxed suspended film by exploiting the merging of crystals at later stages [129, 133, 135], as illustrated in *Fig.* 2.4(b). Such a layer formation from separated Ge nano-crystals was firstly named *Nano-Heteroepitaxy* [129]. From the experimental point of view, the main challenge of this approach consists in the vertical growth of the deposited material. Despite a pillar-patterned substrate can be easily obtained by lithographic techniques, self-assembled growth is usually far from

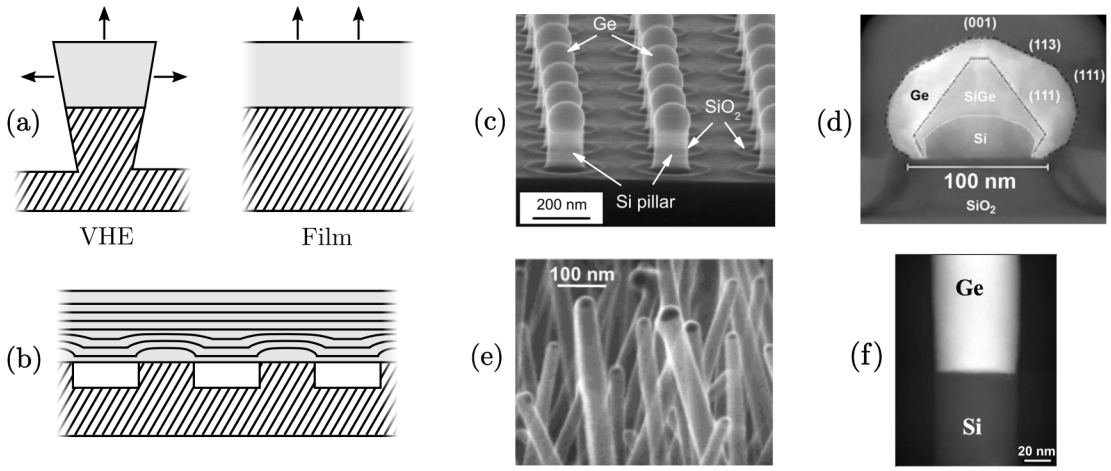

Figure 2.4: Nanometer-wide VHEs. (a) Schematic representation of the relaxation mechanism in vertical heterostructures (left) with respect to planar systems (right) [129]. (b) Coherent film formation by merging of ideally relaxed crystals [129]. (c) Nanometric Ge crystals grown on top of Si pillars from Ref. [130]. (d) Nanometric Ge on Si nanopillars with a SiGe buffer island in between from Ref. [34]. Examples of Ge/Si nanowires: (e) from Ref. [131] and (f) from Ref. [132].

vertical, especially at the nanoscale (where also short mean free path are generally enough to give close-to-equilibrium shapes). However, even before the formation of a suspended layer, the growth of dots which exploit an enhanced lateral relaxation of vertical systems would be an appealing system. Indeed, the presence of lateral free surfaces produces an enhancement of elastic relaxation which leads to a significant delay in plastic relaxation with respect to films. This has been observed for islands [46, 136, 137] and such an effect is expected to be even more effective if the substrate can contribute to the accommodation of the misfit strain. Coherent, i.e. not dislocated, systems can be very useful for optoelectronic devices, allowing for an almost perfect crystal structure where the usual non-radiative recombination at dislocations would be suppressed. The growth of isolated Ge crystals on $\sim$50 nm Si nano-pillars has been recently proposed in Ref. [130, 138]. In Ref. [139] similar systems were proven to have high material quality and a strong indication of coherency has been reported. Representative images of such structures are shown in *Figs*. 2.4(c) and 2.4(d). The assessment of the delay in plastic relaxation in such systems will be illustrated by exploiting the model discussed in *Ch*. 3 and will be reported in *Ch*. 4. It is worth mentioning that the investigations of these systems inspired the study of VHEs with grading in the Ge content which will be illustrated in *Sect*. 3.3.

The mechanism discussed so far is an important feature of another prominent example of vertical heterostructures, i.e. the so-called *nanowires*. They consist of very high aspect-ratio structures with a diameter of a few tens of nanometers. Examples of Ge nanowires [131, 132] are reported in *Figs*. 2.4(e) and 2.4(f). They are known in the scientific community for the excellent properties related to quantum confinement, transport, and optical properties [140]. A crucial role in these structures is played by the high-quality of their crystalline structures ensured by the small sizes. In the remarkable work by F. Glas [18], the lateral size of a coherent system is determined according to the misfit between the epilayer and the substrate. Such an

investigation demonstrates that for a given mismatch, under a certain basis value, dislocations are not favored for any epilayer thickness. Then, when increasing the size, a critical condition is always present, after which dislocations are inserted but with a critical thickness of the epilayer increased with respect to planar films. The main physical contributions behind this delay of plastic relaxation are the same as the ones introduced for nanoheteroepitaxy, investigated in Ref. [18] for nanowires (originally referred to as nanowhiskers). An analytic model leading to similar conclusions can be found in Ref. [141]. After these works, other approaches have been developed to better investigate the relaxation mechanism and provide more accurate predictions as in Ref. [142] where the critical thickness for nanowires is determined by FEM simulations, showing also a very good agreement with experimental data about nanowires coherency. The method introduced in *Ch*. 3 can be considered as an alternative approach with respect to the one in Ref. [142]. As discussed in *Ch*. 4, this method allows us to investigate and assess several experimental systems where nanoheteroepitaxy is directly exploited to obtain coherent structures.

2.5.2 Micrometer-wide VHEs

Micrometer-wide, self-aligned vertical heterostructures have been recently proposed as a solution for most of the issues typically affecting heteroepitaxial growth [19, 20]. This result was made possible by the out-of-equilibrium growth condition of the Low-Energy Plasma Enhanced Chemical Vapor Deposition (LEPECVD) technique (see *Sect*. 2.2.3) combined to peculiar deeply-patterned substrates made of Si pillars. Indeed, such a vertical growth was determined by both the orientation-dependent incorporation rate and the mutual shielding of the incoming material flux by the growing crystals. Typical growth conditions consisted in deposition fluxes of $\sim$4 nm/s and relatively low temperatures (400°C-600°C). The growth of crystalline materials at these conditions is possible thanks to the formation of radical within the plasma and no need to activate precursors at the crystal surface [112, 113]. A typical Si pillar-patterned substrate is shown in *Fig*. 2.5(a), where 8 μm tall, 2$\times$2 μm^2 wide Si pillars, spaced by 2 μm trenches, are reported [19]. This patterned substrate is shown in *Fig*. 2.5(a) and it is fabricated by deep reactive ion etching (DRIE) based on the Bosch process [143]. The crystals obtained by the technique mentioned above are shown in *Fig*. 2.5(b) and consists of 8 μm tall Ge crystals grown at 500 °C. The VHE obtained by such a method show a peculiar faceting [20] which is strongly affected by the deposition temperature. Scanning electron microscopy (SEM) images of the crystal top obtained by deposition at two different temperatures are shown in *Fig*. 2.5(c) [20].

Despite misfit dislocations are inherently present in these VHEs due to the large sizes [18], some important properties are achieved. They have been proved to allow for thermal strain relaxation thanks to lateral free surfaces avoiding, in turn, the crack insertion. This mechanism can be related to the one discussed in *Sect*. 2.5.1, acting on the thermal strain which is, at least, one order of magnitude lower than the misfit strain relieved by dislocations. Moreover, X-Rays measurements assessed the crystal quality which is comparable to the one of the bulk-like material [19] and they can be arranged in order to exploit peculiar photoluminescence features [144]. These systems also allow for defect managing in order to avoid the presence of the dislocation threading arms reaching the top surface [21, 22]. Indeed, according to the

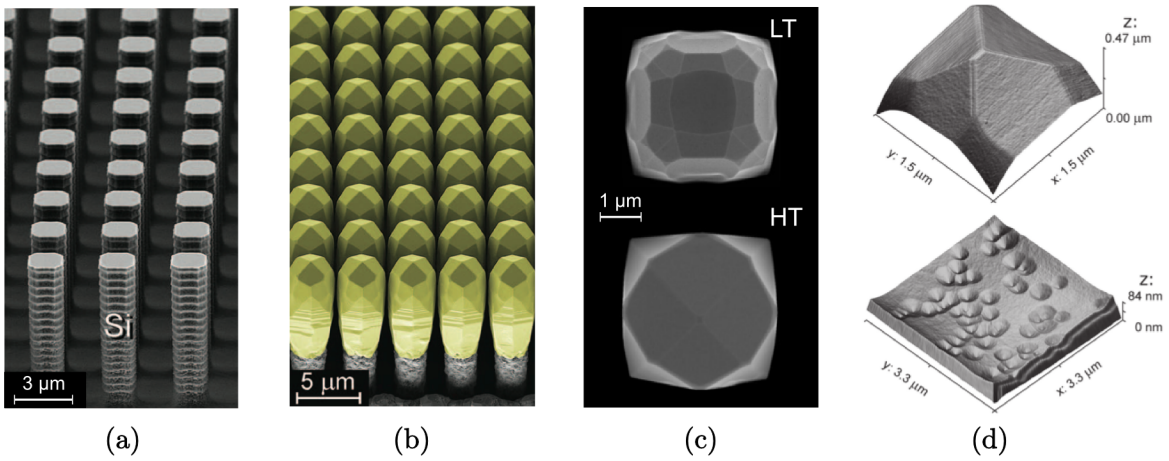

Figure 2.5: Micrometer-wide VHEs. (a) Perspective SEM image of Si pillars prior to deposition and (b) color-enhanced perpective SEM image of 8 μm tall Ge crystal grown on 8 μm tall, 2×2 μm^2 wide Si pillars (adapted from [19]). (c) Typical top-morphologies as resulting by the out-of-equilibrium growth process by LEPECVD at low temperature (LT), i.e. $T = 450$ °C, and at high temperature (HT), i.e. $T = 500$ °C (adapted from Ref. [20]). (d) AFM scan of the top of Ge crystals, after etching procedure to highlight the presence of defect at the surface. Pyramidal morphology (top) is found to have no surfacing dislocations while they are observed for crystals with a flat top surface (bottom) (adapted from Ref. [21]).

growth temperature, the faceting of the crystal top can be finely tuned [20], as also shown in *Fig.* 2.5(c), and dislocations may be forced to bend towards lateral surfaces. The proof of this concept is given in Ref. [21] and it is shown in *Fig.* 2.5(d) by atomic force microscopy (AFM) images. All the properties mentioned here, in particular for what concerns thermal strain relaxation, are proved to hold also for multilayer systems, allowing for the integration of other semiconductors such as GaAs [35, 38] (see also *Sect*. 4.5).

Despite the good properties of VHEs at the micron scale, the presence of misfit dislocations still represents an important limitation for applications. The investigation on how it is possible to remove such defects, mainly exploiting the concept of *Sect*. 2.5.1, is the main motivation of the modeling reported in *Ch*. 3 [28]. The experimental proof of the theoretical results is also discussed in *Sect*. 4.4 [40].

For many applications to electronic systems, the use of planar layers would be preferred with respect to isolated crystals arranged in VHEs. However, Ge/Si film grown with standard techniques have poor quality and VHEs offer a viable path towards a significant improvement of material quality. The realization of a suspended film with the peculiar properties of micrometer VHEs would then be the solution. This represents the main subject of the investigation reported in *Ch*. 6 [39, 41], provided thanks to the modeling reported in *Ch*. 5.

3

Modeling of elasticity and plasticity onset in VHEs

The micrometer-wide VHEs introduced in *Sect*. 2.5 show peculiar properties in terms of morphology and elastic relaxation. However, despite these structures have been widely investigated both theoretically and experimentally, some important questions are still open. An important challenge consists in the design of VHEs where, not only a vanishing threading dislocation density is obtained at the top [21, 22], but also misfit dislocations are missing at the interface with Si. In the work by F. Glas reported in Ref. [18], it has been demonstrated that, under certain lateral sizes dependent on the misfit between the epilayer and the substrate, it is possible to avoid the presence of misfit dislocations. However, such a condition is usually reached at the nanoscale and different concepts, exploiting the finite lateral sizes combined with other effects, should be inspected in order to further extend the sizes of fully-coherent structures.

In this chapter, we illustrate the detailed modeling of the competitive relaxation mechanisms in Ge/Si VHEs, presented in Ref. [28]. In particular, a quasi-3D method is introduced, allowing us to provide a wide investigation of the coherency limits for Ge on Si VHEs. The analysis of a single $Si_{1-c}Ge_c$ layer is discussed and then extended to multilayered configurations with increasing Ge content from the Si pillar towards the epilayer. The results are explicitly obtained for a few hundreds of nanometer-wide structures. However, they are also generalized in order to design coherent structures for larger sizes (see in particular *Sect*. 3.3.1). Finally, a model is also proposed for the investigation of thermal strain relaxation in planar systems, as it exploits the developed framework for the evaluation of plasticity onset and delivers general information on Ge/Si systems (also recalled in *Ch*. 6).

The application of the theoretical modeling to some real, nanometric VHEs will be reported in *Ch*. 4 along with the design of micrometer-wide VHEs and their assessment by means of dedicated experiments.

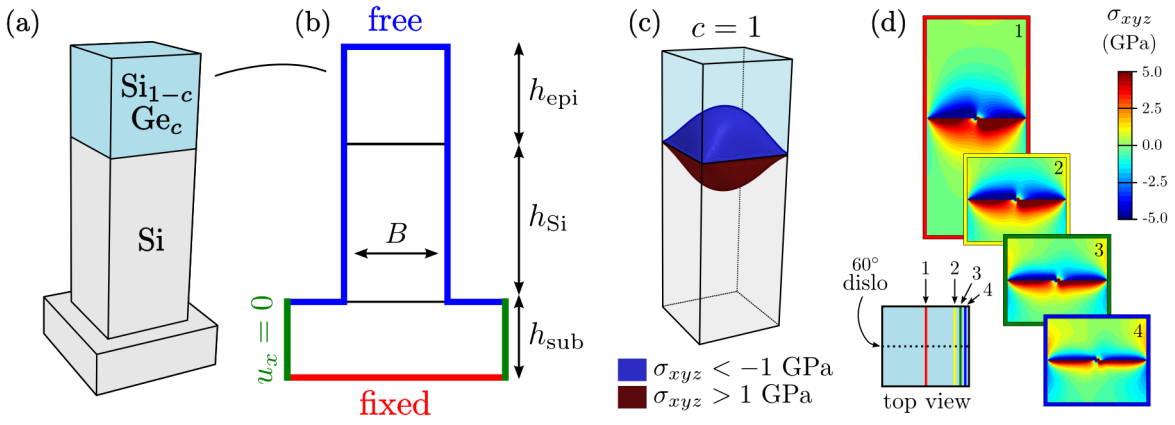

Figure 3.1: Modeling of single-layer VHEs for the investigation of elastic properties. (a) Schematic representation of the whole structure. (b) Cross-section reporting the main parameters and the boundary conditions for the mechanical equilibrium. (c) Illustrative map of the hydrostatic stress field, in the case of a coherent, Ge on Si VHE with $B = 25$ nm. The regions with $\sigma_{xyz} > 1$ GPa (red) and $\sigma_{xyz} < -1$ GPa (blue) are shown. (d) Elastic field obtained after inserting a straight 60° misfit segment in the VHE, at the Ge/Si interface. The total (misfit+dislocation) hydrostatic stress is shown in four representative transversal sections of the VHE.

3.1 Model description

The modeling of the elastic relaxation in three-dimensional structures has been considered by exploiting the linear elasticity theory introduced in *Sect*. 1.1. For the sake of simplicity we consider here a simplified VHE, with a parallelepipedal shape, made of a $Si_{1-c}Ge_c$ epilayer on a Si pillar, as depicted in *Fig*. 3.1(a). A "large" Si substrate underlying the Si pillar is then considered. This choice of a structure with a simplified shape allows the physics of the system to be investigated, focusing on main features such as the lateral size, the thickness of the epilayer and the Ge content of $Si_{1-c}Ge_c$ alloys. This is justified as details of the surface morphology are not found to play a significant role in the elastic strain relaxation of VHEs [145]. However, possible refinements of the model will be discussed with the investigation of specific real systems in *Ch*. 4.

The competition between pure elastic and plastic relaxation is investigated by following an energy criterion, similar to the one mentioned in *Sect*. 2.3.2 for the derivation of the critical thickness. It consists in the evaluation of the formation energy ΔG for the dislocation insertion

$$\Delta G = G_{\text{dislo}} - G_{\text{coh}}, \tag{3.1}$$

where G_{dislo} and G_{coh} are the total elastic energy of the VHE with (not coherent) and without (coherent) the dislocation, respectively. When $\Delta G < 0$, the presence of the dislocation is favored, so that plasticity sets in. On the contrary, if $\Delta G > 0$ the insertion of the dislocation would increase the total energy, i.e. the dislocation is not expected and the structure results coherent. $\Delta G = 0$ represents the critical condition for the insertion of dislocations. We define *critical parameter* each value $\bar{p}$ at which $\Delta G(\bar{p}) = 0$. If $\bar{p} = h$, the condition $\Delta G(h = \bar{h}) = 0$ defines the critical thickness $\bar{h}$. An explicit expression for a flat film can be found in Eq. (2.8).

In order to compute the formation energy in Eq. (3.1), the elastic field within the structures should be determined. The stress originating from the misfit between the epilayer and the Si pillar $\boldsymbol{\sigma}_{\mathrm{het}}$ can be computed from Eq. (1.13) by considering an initial eigenstress, defined by Eqs. (1.17) and (1.18), as:

$$[\sigma^*_{\mathrm{het}}]_{ij} = -c\varepsilon_{\mathrm{m}} C_{ijkl}\delta_{kl} \tag{3.2}$$

with ε_{m} the misfit strain from Eq. (2.3) and c is the Ge content. Notice that such an eigenstress vanishes in the Si pillar as $c = 0$, and corresponds to an eigenstrain $\varepsilon^*_{ij} = -c\varepsilon_{\mathrm{m}}\delta_{ij}$. The elastic constant tensor is assumed to be isotropic as defined in Eq. (1.5). The Vegard's law is adopted when considering $\mathrm{Si}_{1-c}\mathrm{Ge}_c$ alloys, with a linear interpolation for the elastic constants: $E(c) = cE_{\mathrm{Ge}} + (1-c)E_{\mathrm{Si}}$ and $\nu(c) = c\nu_{\mathrm{Ge}} + (1-c)\nu_{\mathrm{Si}}$. According to the presence of many free surfaces, the solution of the mechanical equilibrium is computed by FEM, imposing the boundary conditions (BCs) as illustrated in *Fig.* 3.1(b): Dirichlet BC with $u_i = 0$ from Eq. (1.15) at the bottom of the Si substrate (i.e. fixed BC), gliding BC from Eq. (1.16) for the lateral sidewalls of the silicon substrates, and free-surface BC from Eq. (1.14) for all the other boundaries of the geometry. An illustration of the stress field resulting from the FEM simulations is reported in *Fig.* 3.1(c). In this figure, the hydrostatic stress $\sigma_{xyz} = \sigma_{xx}+\sigma_{yy}+\sigma_{zz}$ is shown for $B = 25$ nm by means of the regions where $\sigma_{xyz} > 1$ GPa (red) and $\sigma_{xyz} < -1$ GPa (blue). Notice that the stress is localized at the interface between the epilayer and the Si substrate. Moreover, a symmetric redistribution of deformation with the substrate is achieved.

When a dislocation is present, the elastic energy can be evaluated as proposed in Ref. [146]. The mechanical equilibrium is considered by adding to $\boldsymbol{\sigma}^*_{\mathrm{het}}$ an additional eigenstress $\boldsymbol{\sigma}^*_{\mathrm{dislo}} = -\boldsymbol{\sigma}^\star$ with $\boldsymbol{\sigma}^\star$ the elastic field of a dislocation in bulk (as defined in *Sect*. 1.2.1), i.e.

$$\boldsymbol{\sigma}^*_{\mathrm{tot}} = \boldsymbol{\sigma}^*_{\mathrm{het}} + \boldsymbol{\sigma}^*_{\mathrm{dislo}}. \tag{3.3}$$

In particular, a 60° dislocation is considered as its nucleation is always favored in $\mathrm{Si}_{1-c}\mathrm{Ge}_c$/Si systems with respect to other dislocation types (as discussed in *Sect*. 2.3.1). A dislocation line along $\boldsymbol{\ell} = [110]$ direction is considered, with Burgers vector of the type $\mathbf{b} = a/\sqrt{2}\langle 101\rangle$ [146] as discussed in *Sect*. 2.3.1. In all the calculations, we selected a coordinates system with one axis parallel to the dislocation line and the vertical axis along the $[001]$ direction.

In order to carefully describe the presence of a dislocation in the full 3D geometry of the VHE, a complete, 3D description of the dislocation line should be, in principle, required. This is a complex task as the elastic field in the heterostructure varies a lot from the center of the structure towards the sidewalls, as shown in *Fig.* 3.1(c), and the proper dislocation geometry is not generally known. We consider first a prototypical full-3D straight dislocation at the interface, and the resulting elastic field is shown in *Fig.* 3.1(d) where the central cross-section perpendicular to the dislocation line is reported, together with other representative transversal sections. It can be noticed that the superposition of the heteroepitaxial and the dislocation elastic field varies a lot according to the distance to the lateral free surfaces. Moreover, the larger plastic relaxation is provided in the central cross-section. This results in a lower formation energy at the center with respect to the regions close to the sidewalls. Therefore, even if in the central section a negative formation energy is obtained, ΔG may be positive when consider-

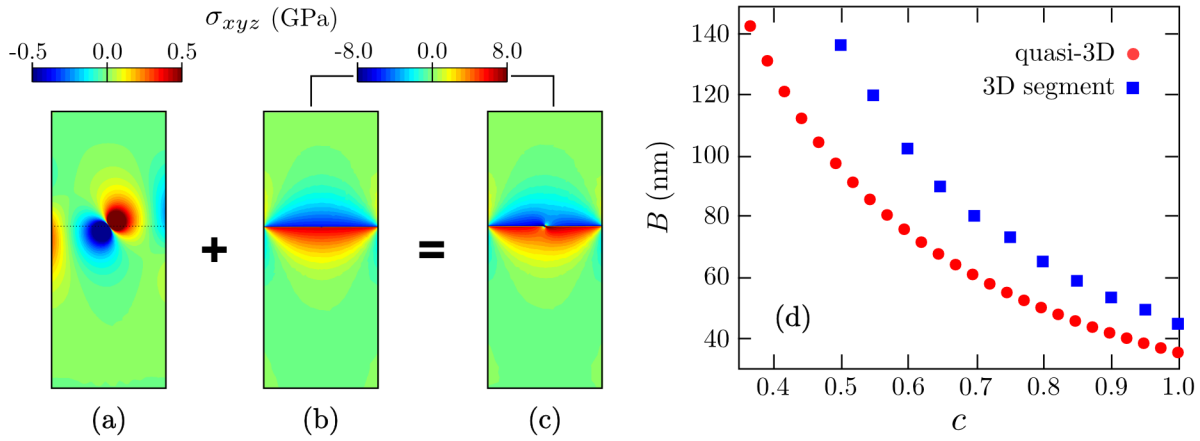

Figure 3.2: Investigation of the plasticity onset. Quasi-3D approach illustrated by means of hydrostatic stress maps shown in the central section of the 3D parallelepipedal shape: (a) σ_{dislo} computed in the 2D section, (b) σ_{het} extracted from the 3D calculation, (c) superimposition of elastic fields reported in panels (a) and (b). ΔG defined in Eq. (3.1) is the difference in energy between the deformation observed in panels (c) and (b). B is set here to 80 nm. (d) Curves of the critical base values with quasi-3D approach (red circles) and with a full 3D dislocation segment (blue squares), as function of c.

ing the entire volume. The energy for a full dislocation segment crossing the whole structure, hence, may be too high also when a small dislocation segment is favored within the structure. So that the full treatment of the dislocation may lead to an underestimation of the tendency towards plasticity. In addition, it is worth mentioning that the description of a full dislocation line within a three-dimensional structure is computationally demanding and this does not allow to perform a large number of calculations to determine the most probable configuration.

In order to overcome such a theoretical and numerical limitations, we focused our attention on the central cross-section perpendicular to the dislocation line. Indeed, evaluating the ΔG in this region corresponds to inspect the lower formation energy within the structure, thus providing information about the very first plasticity onset without considering the full geometry of the first dislocation. The main steps of the method, summarized in *Figs.* 3.2(a)-3.2(c), are:

1. Calculate the elastic field resulting from the misfit stress relaxation in the full-3D VHE, as in *Fig.* 3.1(c).

2. Extract the elastic field in the 2D central slice, as in *Fig.* 3.2(b), and compute the corresponding G_{coh} per unit length.

3. Calculate the exact elastic field in the 2D slice for an infinite dislocation perpendicular to the plane. Its line is set to be at the center position as shown in *Fig.* 3.2(a).

4. Compute the elastic energy G_{dislo} as resulting from the superposition of $\boldsymbol{\sigma}_{\text{het}}$ and $\boldsymbol{\sigma}_{\text{dislo}}$, as in *Fig.* 3.2(c).

5. Compute ΔG from Eq. (3.1).

The ΔG obtained by this *quasi-3D* procedure is defined in a 2D domain corresponding to the central cross-section and its values are expressed in terms of an energy per unit length, i.e. negative values for this ΔG actually corresponds to the tendency of an infinitesimal misfit segment to elongate. From this point of view, this method can be considered as a direct extension of the classical approaches to evaluate critical parameters for planar structures [86, 115].

3.1.1 Interpretation of simulation results

Dislocation segments, even if localized at the center of the structure, have always finite dimensions. Therefore, being limited to the central slice actually leads to an overestimation of the tendency towards plasticity. Indeed, if $\Delta G \lesssim 0$ in the central slice of the VHE, it may happen that a small elongation of the misfit segment toward the sidewalls would bring the dislocation in a region with lower stress value (see *Fig.* 3.1), where $\Delta G > 0$, and host a linear defect within the structure may result not convenient. However, as previously discussed, the full 3D problem, where a straight 60° dislocation segment is put at the interface with a total length equal to the VHE base value, is known to overestimate the critical size $\bar{B}(c)$. The latter approach likely represents the final configuration of a loop nucleated at the center of the structure, which deposited its misfit segment up to completely expel the threading arms.

Let us consider what should happen in real systems. Both the two approaches would represent two limiting cases, as dislocations are not formed by an infinitesimal misfit segment at the center of the structure and, at the same time, they can hardly be present as full straight segments, exactly placed at the center of the structure. According to this, the real plasticity onset should be expected within the two limiting cases. The curves in *Fig.* 3.2(d) report the critical B values obtained with the two approaches as function of c. Notice that their values differ by a factor $1.2 - 1.5$. Moreover, the quasi-3D approach leads to lower estimations for $\bar{B}(c)$ with respect to the calculation with the full 3D modeling of the dislocation. In the following, to provide estimations of the plasticity onset, we solely use the faster *quasi-3D* approach. Being an underestimation, it will allow to determine with a high degree of reliability the coherency of heterostructures. It is worth mentioning here that we are generally interested in systems with high misfit, i.e. high Ge content, where a good agreement between experimental data and thermodynamic predictions is usually obtained [115]. When misfits are low, the thermodynamic estimation is weaker, as nucleation mechanisms and kinetic barriers for dislocation insertion are expected to play an important role, further delaying the plasticity onset [86, 123]. However, quantitative lower values of $\bar{B}(c)$ are interesting also in this case, providing the indication of the worst scenario in order to achieve the growth of coherent structures.

3.1.2 Computational details

The domain adopted for FEM calculations consists of an ideal infinite substrate under the pillar structure made of the silicon support and the overlayers. The substrate, illustrated as a small parallelepiped under the VHE in *Fig.* 3.1(a), was chosen five times wider and higher than the pure Si pillar. The aspect-ratio of the latter is set in order to ensure the limit of infinitely-tall Si pillar, i.e. no significant deformation reaches the Si substrate. In particular, an aspect ratio equal to five is used (we directly verified that for $h_{\mathrm{Si}}/B \gtrsim 1.5$ the results are already independent of

the Si pillar height, in agreement with Ref. [18]).

A strongly non-uniform space discretization has been adopted. Finer mesh has been considered close to the dislocation line with respect to other regions, in order to better describe the strong inhomogeneity of the elastic field induced by the linear defect. For all the simulations, the mesh has been selected by checking the convergence of the numerical method. When considering an eigenstress $\boldsymbol{\sigma}^*_{\text{dislo}}$ corresponding to the bulk elastic field for a dislocation, a spurious contribution may appear due to the presence of fixed and gliding boundary conditions. Indeed, dislocations in bulk are found to have a long-range elastic field (see *Sect*. 1.2). To avoid such contributions, $\boldsymbol{\sigma}^*_{\text{dislo}}$ is set to be the elastic field of a dislocation dipole where an image dislocation is considered, mirrored with respect to the upper free surface [28].

In order to provide $\bar{h}$ values, the epilayer thickness has been sampled ensuring an height-to-base aspect-ratio range, $\text{AR} = h/B$, from $\text{AR} \sim 0$ up to $\text{AR} = 1.5$. Beyond such a value, indeed, any further material added on top is fully relaxed and does not contribute to the elastic energy (see also Ref. [18]). If $\Delta G > 0$ when $\text{AR} = 1.5$, we consider that the plastic relaxation is not favored by further increasing the epilayer thickness. $\bar{B}$ values are instead evaluated by varying the base from $B \sim 0$ up to the value which satisfies $\Delta G(B) = 0$ with an epilayer aspect ratio equal to 1.5 as well. This sampling of the parameter space is adopted also for the epilayer in multilayered VHEs (see *Sect*. 3.3). In all the calculations, isotropic elastic constants are used as in *Sect*. 2.2. Solutions of the equations defined by (1.13) and by boundary conditions (1.14), (1.15) and (1.16) were calculated by using the commercial FEM package Comsol Multiphysics.

3.2 Single-layer heterostructures

The first target for the evaluation of the coherency limits in VHEs is the investigation of the plasticity onset in single, $\text{Si}_{1-c}\text{Ge}_c$ epilayers on a $\text{Si}(001)$ pillar. In particular, the critical thickness of the epilayer is evaluated by varying B and c. Moreover, the critical base $\bar{B}$ at which $\Delta G(h)$ is always positive for any thickness of the epilayer is determined. *Fig.* 3.3 summarizes all the information obtained by such calculations and can be seen as a phase diagram for the VHE as a function of the lateral size and the Ge content in the epilayer. The solid red curve shows the critical base values as a function of c. Under such a curve, the VHE is predicted to be always coherent. Over the $\bar{B}(c)$ curve, the formation energy shows negative values provided that $h \geq \bar{h}$, i.e. once the critical thickness is reached. Isolines of $\bar{h}$ values are shown by dashed curves.

In order to appreciate all the information reported in *Fig.* 3.3, let us focus our attention on a fixed value of c. For small values of B, the system is always coherent. Then, by increasing the base value, the $\bar{B}(c)$ curve is reached. Over such a curve, the critical thickness has a larger value than the film configuration. Indeed, the relaxation provided by lateral free surfaces is not sufficient to prevent dislocation insertion but it still induces a delay of plastic relaxation. For large B values in the limit of $B \to \infty$, the critical thickness of the film is recovered.

The same discussion applies to the Ge content influence in a structure at a fixed B value. For small Ge content, the misfit is low and dislocation insertion is not favored. Then, the critical base curve is reached, here considered as $\bar{c}(B)$. For $c > \bar{c}$ a critical thickness is obtained and it

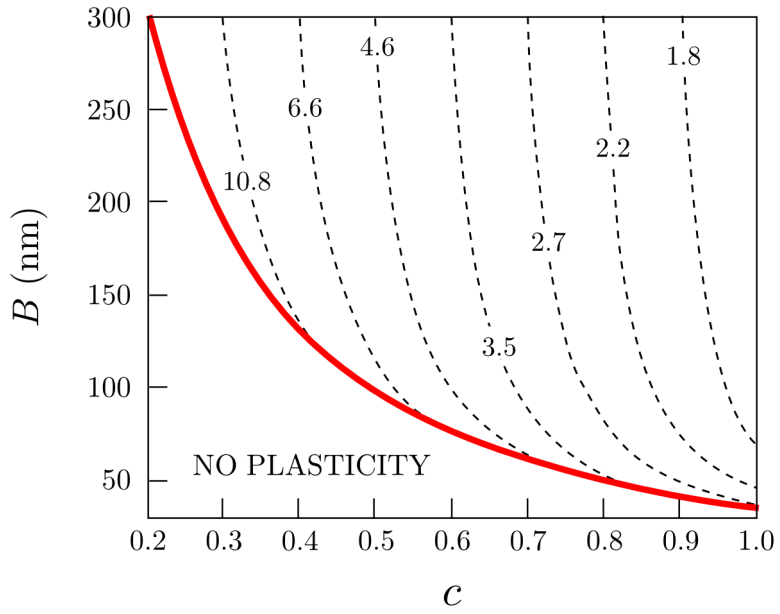

Figure 3.3: Critical parameters for dislocation insertion as function of the Ge content c and of the pillar base B. The solid red curve represents the critical base values $\bar{B}(c)$. A dislocation-free VHE is predicted for any point under such a curve. Critical thickness $\bar{h}(c, B)$ isolines are shown by means of dashed lines, their values are expressed in nm.

decreases for higher Ge content up to the $c = 1$ case.

The results discussed here, well reproduce the behavior discussed by Glas in Ref. [18] and by Ertekin *et al* in Ref. [141]. However, some differences can be noticed, especially for what concerns the quantitative estimations. For instance, the critical base predicted here for coherent pure-Ge VHEs is ∼40 nm, which is about a factor 2 smaller than the value reported in Ref. [18]. Actually, in such a work, a semi-analytical approach was developed and some differences can be easily recognized. First, the shape of the VHE is modeled with a different geometry (parallelepipedal here and cylindrical in Ref. [18]). Second, different elastic constants are used, but this difference is expected to play only a very marginal role. It is worth to recall that the quasi-3D method adopted here is known to provide underestimation of critical parameters. However, an important improvement of this method with respect to the literature is that we are treating free surfaces exactly and their influence on both heteroepitaxial and the dislocation elastic field is carefully accounted for. In Ref. [142], a similar approach exploiting FEM simulations is reported, yielding to a similar critical curve for a different system (InGaAs/GaAs nanowires). Dedicated simulations including material parameters similar to the one adopted in Ref. [142] led, indeed, to very similar results, assessing the reliability of our FEM approach.

In order to provide an easy way to extract results from *Fig.* 3.3, concerning in particular the $\bar{B}(c)$ values, we fitted the numerical results with interpolating curves. An almost perfect fit is obtained using the following expressions, yielding the dependence of the critical base $\bar{B}$ on the Ge content c:

$$\bar{B}(c) = \frac{k_1}{c} + \frac{k_2}{c^2} + (\bar{B}_{c=1} - k_1 - k_2), \tag{3.4}$$

with $k_1 = (55.2 \pm 0.3)$ nm and $k_2 = (2.52 \pm 0.06)$ nm as best-fit parameters. $\bar{B}_{c=1} = (35.6 \pm 1.0)$ nm is the critical base for a Ge-pure epilayer, as directly calculated by simulations. On the other hand, also the critical Ge content $\bar{c}$ (beyond which plasticity sets in for an assigned base value B) can be written by a similar semi-analytical expression as

$$\bar{c}(B) = \frac{\bar{B}_{c=1}k_1'}{B} + \frac{(\bar{B}_{c=1})^2 k_2'}{B^2} + (1 - k_1' - k_2'), \tag{3.5}$$

where $k_1' = 1.31 \pm 0.01$ and $k_2' = -0.38 \pm 0.01$.

3.3 Multilayered heterostructures

From the investigation reported in *Sect*. 3.2, it can be noticed that VHEs made of pure Ge on Si are likely to be plastically relaxed above a lateral size of $\bar{B} \sim 40$ nm. This is an intrinsic limit which can hardly be overcome in the single-layer configuration. Looking to the results shown in *Fig*. 3.3, however, it is clear that the key in order to increase the $\bar{h}$ or $\bar{B}$ values is to provide a lowering of the effective misfit across the interface. In single-layer VHEs, it can be obtained only by means of the lowering of the Ge content. However, the elastic fields provided in *Figs*. 3.1(c) and 3.2(b) shows that for an AR of the epilayer larger than 1-1.5, full relaxation is achieved at the top of the structure, as also stated in Ref. [18]. Therefore, for a given base values B, a Ge content $c < \bar{c}(B)$ can be grown providing a coherent first layer, which reaches full relaxation for large thicknesses. Then, another layer can be added, ensuring a coherent structure provided that each change in the Ge content between layers is lower than the critical value $\bar{c}(B)$. Notice that, in this discussion the differences in the elastic constants are neglected, as they are found to play only a minor role. In this section, exploiting the method and the main concepts discussed above, we investigate the plasticity onset in VHEs made of multilayers with increasing Ge content.

Let us start with the structure illustrated in *Fig*. 3.4(a), where all the parameters setting the geometry of the VHE with a single buffer layer are illustrated. c represents the Ge content in the buffer while $\mathrm{AR_{BL}}$ is its height-to-base aspect-ratio. Selecting an epilayer with pure Ge content allows us to focus on the structure where the highest misfit should be accommodated by the buffer insertion. In *Figs*. 3.4(b)-3.4(d), we show the hydrostatic stress field of a pure Ge epilayer on Si with a $Si_{0.5}Ge_{0.5}$ layer in between (no B values are specified here as the elastic field is self-similar). Different $\mathrm{AR_{BL}}$ are considered. The presence of a buffer layer modifies the stress field within the structure and, for thick enough buffers, two interfaces appear showing tensile and compressive lobes. Notice that such lobes are independent with $\mathrm{AR_{BL}} = 0.8$ while they interact for $\mathrm{AR_{BL}} = 0.4$.

In order to evaluate the plasticity onset, we compute the formation energy ΔG putting a dislocation at the center of the structure as made for the single-layer VHE. Now, two interfaces are present with also a non-trivial elastic field superposition in the buffer layer. Our aim is to provide the limit for coherency of such a two-layer structure so that the Ge content of the buffer layer is chosen in order to be coherent according to the results shown in *Sect*. 3.2 and described by Eq. 3.5. To obtain a coherent structure with $B = 75$ nm, for instance, c can be chosen lower than $\bar{c}(75) = 0.6$ while, if $B = 150$ nm, c should be lower than $\bar{c}(150) = 0.36$. Therefore, the

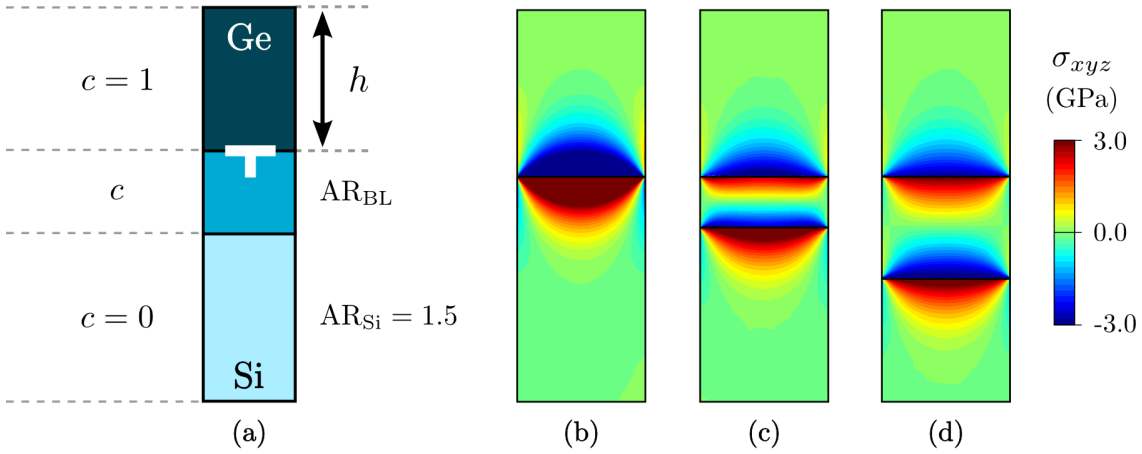

Figure 3.4: Single buffer-layer configuration. (a) Schematic representation and parameters. The hydrostatic stress field in Ge/$Si_{0.5}Ge_{0.5}$/Si structures is shown for (b) $\mathrm{AR_{BL}} = 0$, (c) $\mathrm{AR_{BL}} = 0.4$, (d) $\mathrm{AR_{BL}} = 0.8$. The color map shows σ_{xyz} in the central cross-sections of the full 3D structures.

plasticity onset will be investigated in the details at the interface between the epilayer and the buffer, as sketched in *Fig.* 3.4(a), exploring configurations with $c < \bar{c}(B)$.

In *Fig.* 3.5, the critical thickness $\bar{h}(c)$ for a pure Ge epilayer on a BL with Ge content c is shown, as a function of $\mathrm{AR_{BL}}$. It is worth mentioning here that with dislocations, the self-similarity is broken and the results in terms of critical parameters also depend on the base size, at variance with elastic field distribution in coherent structures as in *Figs.* 3.4(b)-3.4(d). In order to make clear the information in *Fig.* 3.5, let us focus first on *Fig.* 3.5(a). The base is set to $B = 75$ nm so that, as mentioned before, $c < 0.6$ to ensure coherency at the first interface. In the limit of $\mathrm{AR_{BL}} \to 0$ the critical thickness of the pure Ge epilayer is unaffected by the buffer Ge content and it corresponds to the value of $\bar{h}(B, 1)$ which can be read from *Fig.* 3.3. For $\mathrm{AR_{BL}} \to \infty$, well represented with $\mathrm{AR_{BL}} > 1$, the $\bar{h}$ corresponds to the one of an alloy $Si_{1-c'}Ge_{c'}$ where $c' = 1 - c$ (the values do not match exactly due to different the elastic constants with respect to the $Si_{1-c'}Ge_{c'}$ on Si case). So that the higher is c the lower is the misfit to relieve between the epilayer and the buffer. Moreover, for $c > 0.3$ the formation energy is always positive so that the structure is coherent. A more complex behavior is recognized for intermediate $\mathrm{AR_{BL}}$ values. $\bar{h}$ slightly increases for low values of c, while a strong increase is observed for higher c values also leading to coherent structure even for $c = 0.3$. This behavior can be explained by looking at the elastic field in *Fig.* 3.4(c). For $\mathrm{AR_{BL}} \sim 0.4$ the lobes with opposite sign tend to cancel within the BL. Therefore, the buffer layer is partially relaxed with a lowering of the elastic energy gain in the introduction of a misfit dislocation at the interface. For $c > 0.4$ the effect is also present but it is hidden as for large aspect ratio the structure is still found to be coherent as mentioned before. This behavior for intermediate $\mathrm{AR_{BL}}$ values can be very helpful as it ensures that the condition for high $\mathrm{AR_{BL}}$ is satisfied without growing a thick buffer layer, with an important save of material.

For larger basis, the behavior is qualitatively the same, with the features observed in *Fig.* 3.5(a) occurring at different values of c. In *Fig.* 3.5(b), $\bar{h}$ as a function of AR is shown for $B = 100$ nm.

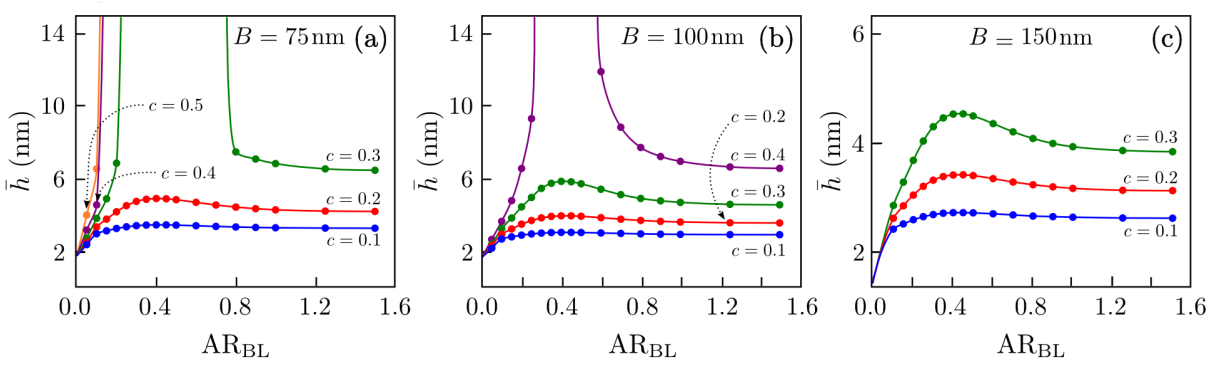

Figure 3.5: Critical thickness of Ge epilayer grown on Si with a buffer layer. $\bar{h}$ values are plotted as a function of AR_{BL}: (a) $B = 75$ nm, (b) $B = 100$ nm, (c) $B = 150$ nm. Different curves are obtained by varying the Ge content c in the BL, as illustrated in the panels.

The buffer layer Ge content is chosen lower than 0.5 according to the coherency limit $\bar{c}(100) \sim 0.49$. Notice that in this case a fully coherent Ge epilayer can be obtained only with $c = 0.4$ and $AR_{BL} \sim 0.4$. So that this base represents a limit in order to obtain coherent Ge epilayer in a two-layer structure. The same calculation performed for $B = 150$ nm (with $c < \bar{c}(150)$ and $\bar{c}(150) \sim 0.36$) are reported in *Fig.* 3.5(c). It is evident that the critical thickness of the pure Ge epilayer can be raised only up to ~ 5 nm. All the effects mentioned before are present, but the full coherency is never reached. Notice that the maximum in the critical thickness is always located at $AR_{BL} \sim 0.4$ in *Fig.* 3.5 and this value seems to be not affected by the size of the structure and by the Ge content of the buffer layer. This suggests that it consists of a geometrical effect at which the most efficient interaction between elastic lobes within the buffer layer is realized.

From the results reported so far we can conclude that with a single buffer layer we can extend the limit of coherency for pure Ge epilayer from $\lesssim$40 nm (see *Fig.* 3.3) to $\sim$100 nm (see *Fig.* 3.5).

3.3.1 Recipe for coherent, multilayered VHEs

The effect induced by the presence of a buffer with an intermediate SiGe alloy can be generalized by the insertion of further BLs. The aim here is to provide a recipe for the achievement of coherent structures at any arbitrary width of the VHEs. In particular, we focus our discussion on a constant increase of the Ge content moving from the Si pillar toward the pure Ge epilayer. So that, for a given Ge content c of the first buffer layer, the n-th layer should have a Ge content nc. A simple three-layer structure including two buffer layers and the pure Ge epilayer is sketched *Fig.* 3.6(a). Let us consider the last case discussed in *Fig.* 3.5 where $B = 150$ nm, i.e. a lateral size which does not allow the growth of coherent Ge to be achieved with only one buffer layer. For this size, $\bar{c}(150) \sim 0.36$ from Eq. (3.5). By setting two buffer layers with a Ge content equal to $c = 0.35$ and $2c = 0.7$ respectively, the final misfit between the pure Ge layer and the last buffer layer should be equivalent to the one of a $c = 0.3$ alloy on Si, ensuring, in turn, coherency.

In order to confirm such an argument, in *Fig.* 3.6(b) the formation energy ΔG for a dislo-

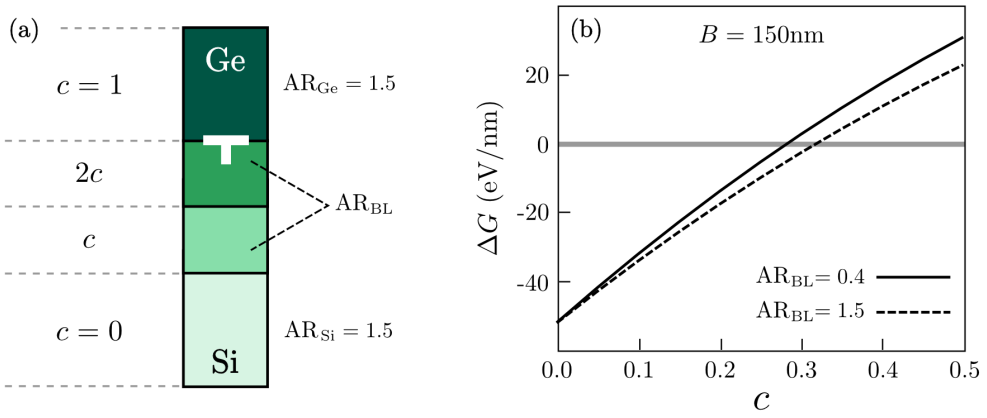

Figure 3.6: Multilayered configuration with two buffer layers. (a) Schematic representation and parameters. (b) Formation energy for a dislocation in the Ge epilayer is shown as function of the Ge content parameter c with $B = 150$ nm. Two different values of $\mathrm{AR_{BL}}$ are considered: 0.4 (solid line) and 1.5 (dashed line).

cation at the last interface (as sketched in *Fig.* 3.6(a)) is reported for different values of c. Two curves are considered corresponding to the limit of infinitely thick buffer layer, $\mathrm{AR_{BL}} = 1.5$, and to the aspect ratios which ensured an enhancement of critical thickness, i.e. $\mathrm{AR_{BL}} = 0.4$ as discussed for the results in *Fig.* 3.5. The thickness of the pure Ge epilayer is set to achieve the infinite thickness limit ($h_{\mathrm{epi}}/B \sim 1.5$), in order to investigate the critical condition in terms of $\Delta G(c) = 0$. Our prediction about coherency for the pure-Ge epilayer is confirmed as positive formation energy is obtained with $c = 0.35$, for both the $\mathrm{AR_{BL}}$ values. Moreover, the value of c at which $\Delta G = 0$, is approximately halved with respect to the single-buffer configuration. Selecting $\mathrm{AR_{BL}} = 0.4$ allows the critical Ge content to be still lowered, confirming that the enhancement mechanism, due to elastic lobes compensation, is still present in multilayered structures. However, its effect on the shift of c is weak.

It can be easily inferred that beyond a certain B value, two buffer layers are not enough to provide full coherency. However, a different number of buffer layers with arbitrary Ge contents can be selected. In order to design a coherent structure with an arbitrary base B, we should ensure that the increase of the Ge content between consecutive layers is lower than $\bar{c}(B)$. This is actually valid by assuming $\mathrm{AR_{BL}} > 1$ and it is a conservative criterion for $\mathrm{AR_{BL}} > 0.4$. The number of buffer layers n_{BL} required to reach a pure Ge epilayer ($c = 1$) is then

$$n_{\mathrm{BL}}(B) = \frac{1}{\bar{c}(B)} - 1, \tag{3.6}$$

The ceiling function $\lceil n_{\mathrm{BL}}(B) \rceil$ should actually be considered as we are dealing only with discrete values of n_{BL}. The previous results indicate that with $\mathrm{AR_{BL}} \sim 0.4$ the number of buffer layers can also be lowered. A similar effect should be present when considering the change in the elastic constants, softer when increasing the Ge content. Despite the main physics is already contained in the present discussion, such refinements of the results may be an interesting work of optimization, really helpful for the realization of such a structures.

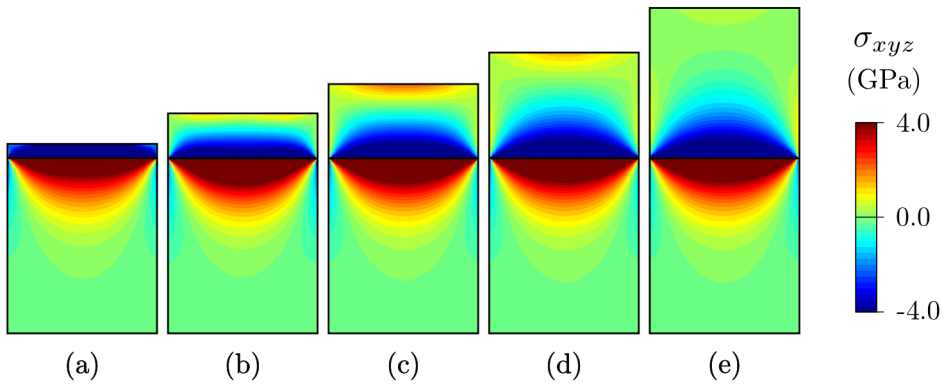

Figure 3.7: Elastic fields during the growth of a pure Ge epilayer. The hydrostatic stress field is reported for different AR values of the Ge layer: (a) 0.1, (b) 0.3, (c) 0.5, (d) 0.7, (e) 1.0.

3.4 Ideal dislocation positioning

In *Sect*. 3.1 we introduced the quasi-3D approach with the assumption on the dislocation position at the center of the structure. In general, the global energy minimization for the dislocation insertion would require a sampling of different position at the interface in order to determine the lowest formation energy. However, we recall that the calculation of each $\bar{h}$ value, as shown for instance in *Fig*. 3.3, required several evaluations of ΔG. For any fixed value of c and B, different h values should be sampled to solve $\Delta G(h \equiv \bar{h}) = 0$, and also with optimized algorithms (as, for instance, with bisection procedures) the addition of another parameter would significantly limit the sampling of the parameter space. So that we fixed the position at the interface in the central position (CP, $x_{\text{dislo}} = 0$). In this section, the minimum-energy position (MP) for the dislocation is discussed, focusing on the interesting case of $B = 75$ nm, analyzed in *Fig*. 3.5(a). In particular for any thickness sampled for the evaluation of $\bar{h}$, MP is searched by moving the dislocation along the interface.

In order to begin our analysis, let us look more in the details at the equilibrium elastic field within the considered VHEs. In *Fig*. 3.7(a) the hydrostatic stress σ_{xyz} is shown for various height-to-base pure-Ge epilayer (AR). Notice that, finding a stress/strain distribution which satisfies the mechanical equilibrium equation is a self-similar problem. The field in the epilayer region strongly depends on the distance from the top free surface. For $\text{AR}_{\text{epi}} \sim 0.3 - 0.7$, a tensile region is also present in the upper portion of the epilayer. This will be key for the following discussion.

In *Fig*. 3.8(a), the MP is shown by filled circles (and a solid guideline) as a function of AR. For very small AR values CP$\sim$MP$\sim$0, i.e. the central position also provides the minimum energy for the dislocation at the interface. This is due to the film-like structure obtained for thin epilayers and every position at the interface, far enough from free surfaces, leads to similar energy values. For $\text{AR}_{\text{epi}} \gtrsim 1$ the correspondence CP$\sim$MP is still obtained but for a different reason. *Fig*. 3.7(e) clearly shows compressive and tensile lobes of σ_{xyz} which are symmetric. The higher stress values are located exactly at the center of the structure so that in order to maximize the relaxation the dislocation is favored in CP. Intermediate AR values show the

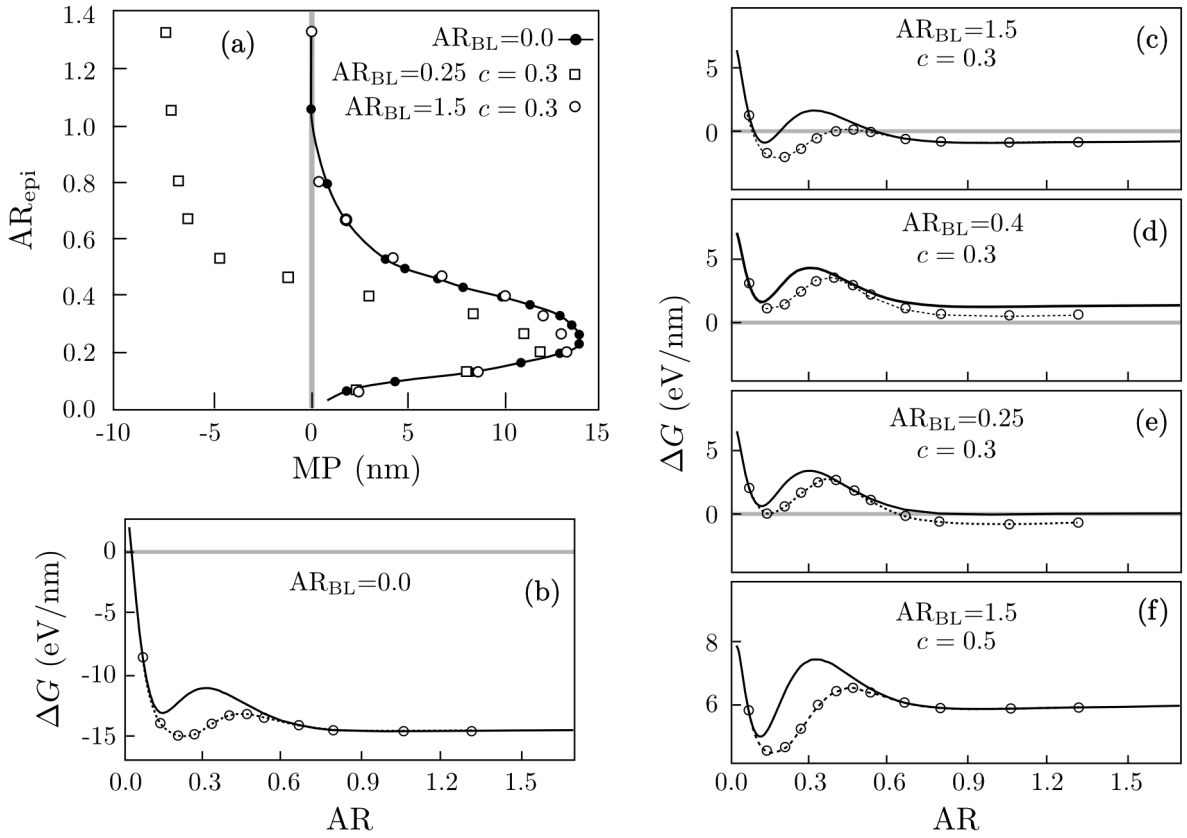

Figure 3.8: Insights on the ideal dislocation positioning. (a) Minimum energy position MP (expressed as relative position with respect to the central position CP), as function of AR. The base value is set to $B = 75$ nm. Filled circles (with a solid guideline) show the single-layer case with a pure Ge epilayer. Open circles show the case of a pure Ge on a BL with $AR_{\mathrm{BL}} = 1.5$ and $c = 0.3$. Open squares show the case of a pure Ge on a BL with $AR_{\mathrm{BL}} = 0.25$ and $c = 0.3$. Comparison between the ΔG values obtained for a dislocation in CP (solid curve) and in MP (open circles with guidelines) are shown for a pure Ge layer with $B = 75$ nm on: (b) pure Si pillar, (c) BL with $\mathrm{AR_{BL}} = 1.5$ and $c = 0.3$, (d) BL with $\mathrm{AR_{BL}} = 0.4$ and $c = 0.3$, (e) BL with $\mathrm{AR_{BL}} = 0.25$ and $c = 0.3$, (f) BL with $\mathrm{AR_{BL}} = 1.5$ and $c = 0.5$.

most intriguing behavior. A shift of the MP with respect to the CP is clearly evidenced towards the right sidewall (the direction of this shift is actually related to the specific choice of the 60° dislocation, considered here as in *Fig.* 3.2(a)). This can be interpreted by using stress maps of *Fig.* 3.4(b) together with dislocation stress shown in *Fig.* 3.2(a). With intermediate AR values, the stress lobes due to the misfit are not symmetric. A central position for the dislocation would lead to an expansion also in the upper part which is mostly relaxed even with a slightly tensile region. A shift to the right side lowers this effect while assuring even a better relaxation of the strong tensile region below the Ge/SiGe interface.

In *Fig.* 3.8(b) the solid line represents ΔG as a function of AR for the central position. The stress distribution and its evolution with the thickness of the epilayer (see *Fig.* 3.7) leads to a non-monotonous behavior with an increase of ΔG when the tensile stress is present for intermediate AR. The curve reporting the formation energy obtained with dislocation in MP is also shown with open circles. When this position coincides to CP (see above) at low and high

AR values, ΔG curves overlap. As expected, a difference is seen for intermediate AR values. Notice that the $\bar{h}$ estimation remains unaltered. Most of the calculation concerning the critical-thickness reported in *Fig.* 3.3 actually corresponds to very low AR values (i.e., $\bar{h}$/B values). Therefore, most of the results reported in the previous sections for the single-layer heterostructure fall in the regime where CP and MP (almost) coincide. The disagreement between CP and MP can be appreciated for a thin region very close (practically coincident) to the critical base (where the thickness rapidly goes to ∞ also exploring the intermediate AR values), thus not affecting the reported results.

Let us now consider a multilayered VHE with a single BL. In this case, the analysis becomes more complex, as we need to check the role of both $\mathrm{AR_{BL}}$ and AR. In *Fig.* 3.8(a), we also reported the MP obtained for a pure Ge epilayer put on a buffer layer. Two different $\mathrm{AR_{BL}}$ values, $\mathrm{AR_{BL}} = 0.25$ (open circles) and $\mathrm{AR_{BL}} = 1.5$ (open squares), are considered as these values leads to qualitatively different stress distributions as shown in *Fig.* 3.4(b)-3.4(d). For the thick BL, results in terms of MP coincide with the single-layer case as the elastic field are still symmetric. Instead, for $\mathrm{AR_{BL}} = 0.25$ (chosen as it was the case showing the most interesting evidence) a more complex behavior appears with two shifts occurring in opposite directions, depending on AR. Moreover, the one observed for large AR is expected to be permanent for larger thicknesses. This behavior can be explained by considering the effect of the buffer layer on the elastic field at different thicknesses of the epilayer. For low AR, with or without the BL, a top film-like configuration is obtained (see *Fig.* 3.7), and MP$\sim$CP as mentioned before. For intermediate AR values, the effects of the elastic relaxation become important, inducing a shift in a positive direction, as previously discussed as well. By increasing AR further, the tensile stress at the upper surface vanishes as shown in *Figs.* 3.7(d) and 3.7(e) but the elastic field at the interface is still affected by the buffer layer contribution, dominated by the superposition of the lobes with opposite sign, as discussed in the main text and qualitatively shown in *Fig.* 3.4(c). Here the symmetry breaking is induced by the stress state within the buffer. Indeed, a dislocation in CP would induce a compressive lobe in a region which is significantly relaxed within the buffer layer (see again *Fig.* 3.4(c)). A shift to the left leads to a reduction of this effect, also yielding a better relaxation of the tensile heteroepitaxial field in the epilayer (with a mirrored situation with respect to the effect for the single layer at intermediate AR).

In *Figs.* 3.8(c)-3.8(f) the deviation in the formation energy due to these shifts is analyzed as in *Fig.*3.8(b). Although the ΔG results different in MP and CP for some AR, we are however interested in the evaluation of $\bar{h}$, i.e. the condition $\Delta G = 0$. The curves with dislocation in CP and MP show a good agreement with such a condition, except for $\mathrm{AR_{BL}} = 0.25$. In this case by considering the $\Delta G(h) = 0$ intercept, we obtain the plasticity onset at $AR \sim 0.6$ for CP and at $AR \sim 0.15$ for MP which means, in terms of explicit critical thickness values for the considered $B = 75$ nm structure, a shift from $\bar{h} \sim 45$ nm (CP) to $\bar{h} \sim 11.25$ nm (MP). This is a significant shift in the absolute values. However, it should be noticed that this difference occurs in the proximity of the critical transition (not-coherent - coherent). Any variation of other parameters, e.g. $\mathrm{AR_{BL}}$, would lead to a shift of both the curves in *Fig.* 3.8(e), delivering again a good agreement between the $\Delta G = 0$ condition with dislocation in CP and MP.

We can actually conclude that the choice of a fixed dislocation in CP, only affects configurations very close to critical transition, which represent a very limited portion of the sampled cases. Moreover, all the conclusions in terms of the delay in plastic relaxation and managing of buffer layer configurations hold as discussed in the previous section.

3.5 Modeling of crack insertion

As discussed in *Sect*. 1.2.2 the crack formation in films can be generally related to the balance of two energy contributions: the surface energy cost in creating free surfaces within the film and the elastic energy release, the latter widely investigated for the evaluation of the plasticity onset in VHEs reported above. Here, exploiting the theoretical tools introduced so far, we provide a simplified investigation of this energy balance delivering some general, useful trends (also used for the discussion about the material quality of merged VHEs in *Sect*. 6.3.4).

Let us consider a regular crack net with spacing L in an infinite film as shown in *Fig.* 3.9(a), as the fractures usually occur with some degree of periodicity across the surface [124]. This is an approximation, as it is observed after a certain thickness above the critical one for cracks insertion. Indeed, the nucleation of cracks is known to be heterogeneous and in close-to-critical conditions an asymmetric distribution can be observed [147]. The single crack is considered as an infinitesimally wide gap occurring from the upper free surface of a (001) film to the Ge/Si interface and we assume that it generates perfect $\{110\}$ planar surfaces, as recognized in a few experiments for similar crystal structures [148, 149]. It corresponds to an ideal through-thickness failure mechanism, without substrate failure or delamination, typical for a crystalline film under tensile strain [124]. For symmetry reasons, we can restrict our investigation to the $L \times L$ region bounded by cracks themselves. The $L \times L \times (h + h_{\mathrm{sub}})$ domain is illustrated in *Fig.* 3.9(b).

According to the presence of free-surface boundary conditions induced by cracks, dedicated 3D FEM simulations are required. The thermal strain (see *Sect*. 2.4) has been considered by imposing an initial eigenstrain $\varepsilon^*_{ij} = -\delta_{ij}\epsilon_{\mathrm{th}}$ in the film and $\varepsilon^*_{ij} = 0$ in the substrate, with ϵ_{th} is the thermal strain from Eq. (2.10). The presence of cracks is modeled by means of the boundary conditions for elasticity equations. Free surface boundary condition, from Eq. (1.14), are imposed at the lateral surfaces of the film, mimicking the free surfaces introduced by cracks. Moreover, such a condition is considered to model the upper free surface of the film. The substrate is modeled as in *Sect*. 3.1. Indeed, the Si domain has been considered five times higher than the L value, obtaining the limit of an infinite thick substrate. Fixed BC, from Eq. (1.15), is imposed at the bottom of the substrate while gliding condition, from Eq. (1.16), is imposed at its lateral surfaces. A finer spatial resolution has been required close to the lateral free surface to careful describe the strongly inhomogeneous elastic field at the ideal tip of the crack. Also in this case, the convergence of the mesh is checked for all the reported simulations.

In *Fig.* 3.9(c) we show the elastic field in terms of $\sigma_{||}/\sigma_0$, where σ_0 is the thermal stress in the film and $\sigma_{||} = 0.5(\sigma_{xx} + \sigma_{yy})$ is the resulting in-plane stress with cracks, in two representative slides of the simulated domain with an epilayer aspect-ratio $\mathrm{AR} = h/L$ of 0.3. These stress maps show the relaxation at the center of the considered domain and close to a fracture,

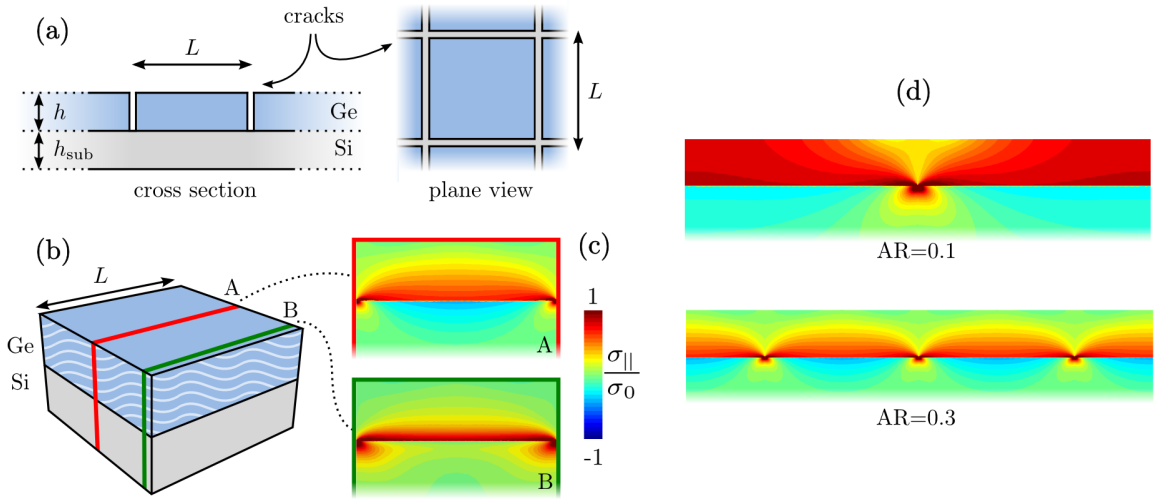

Figure 3.9: Modeling of the crack insertion. (a) Illustrative cross-section and top view of the 3D geometry. (b) FEM-simulation domain, consisting in a $L \times L \times (h + h_{\text{sub}})$ parallelepiped where Ge lateral boundaries (indicated by the wavy pattern) correspond to crack sidewalls. (c) Elastic field in two representative sections (A and B) of the simulation domain in panel (b). They show the elastic field in the central slice and in a close-to-crack slice, respectively. Color maps show the ratio between the resulting in-plane stress $\sigma_{||}$ and the thermal stress of an unrelaxed film σ_0. (d) Elastic relaxation provided by two different crack densities in a film, i.e. with different AR values. The same color map of panel (c) is used.

respectively. At the crack tip, a high tensile strain is recognized in the substrate. On the other hand, a significant relaxation is obtained in the film close to the boundaries, i.e. the crack sidewalls, and it decreases moving toward the central region where a relaxation is still observed but with lower intensity. A slightly compressive stress appears in the substrate at the center of the simulated domain. From the stress map of such a figure, some degrees of similarity appear with the typical heteroepitaxial film obtained for VHEs. Indeed, cracks bound a portion of the film where the relaxation given by free surfaces is present. Here, we focused our attention on cracks which do not propagate into the substrate so that compliance effects are minimized (as can be noticed by comparing *Fig.* 3.9(c) to *Fig.* 3.1(c)). In *Fig.* 3.9(d) we also show a comparison of the thermal strain relaxation in films with the same thickness but different AR values, 0.1 and 0.3 respectively. This corresponds to consider different crack densities. Stress maps are obtained with the procedure discussed above and with a proper shift and repeating of the resulting elastic field. As we can notice the higher is the density the more significant is the relaxation.

By exploiting the calculated elastic field, we can evaluate the energy contributions when a crack net is present. The elastic energy of the considered portion of the film under thermal strain is

$$G_{\text{film}} = \int_V \rho_{\text{film}} d\mathbf{x} = Y \epsilon_{\text{th}}^2 h L^2, \tag{3.7}$$

where Y is the biaxial modulus [86], adopted also in Eq. (2.7). ρ_{film} is the elastic energy density, which is uniform in the film and equal to $Y\epsilon_{\text{th}}^2$ in our case. hL^2 corresponds to the Ge volume. When the strain is relaxed by cracks, the elastic energy is modified by the action of free surfaces,

as shown in *Fig.* 3.9(c). Such a variation can be described by considering a new elastic energy density $\rho_{\rm el}(\mathbf{x}, h, L) = \rho_{\rm film} f(\mathbf{x}, h, L)$, where f is an auxiliary positive-defined function, which assumes values equal to zero where there is no strain. Notice that, when cracks are present, it assumes non-zero values also in the substrate. The resulting elastic energy is then given by

$$G_{\rm el} = \int_V \rho_{\rm film} f(\mathbf{x}, h, L) d\mathbf{x} = Y \epsilon_{\rm th}^2 h L^2 F(\mathrm{AR}). \tag{3.8}$$

$F(\mathrm{AR})$ is the average of the f function on the whole domain normalized by the volume of the stressor, i.e. the Ge volume. Notice that, being the elastic differential equations self-similar, average quantities can be considered depending only on AR. From FEM simulations we can determine a semi-analytic function for such a term as

$$F(\mathrm{AR}) = \frac{1}{hL^2} \int_V f(\mathbf{x}, h, L) d\mathbf{x} = \frac{1}{2} \left[\exp(-p_1 \mathrm{AR}) + \frac{1}{1 + p_2 \mathrm{AR}} \right], \tag{3.9}$$

where a good fit is given by $p_1 = 6.42 \pm 3\%$ and $p_2 = 5.26 \pm 3\%$. With such a result, exploiting the same arguments of *Sect*. 1.2.2, we can define the total energy for the system described in *Fig.* 3.9 as

$$G_{\rm tot} = G_{\rm el} + G_{\rm surf} = Y \epsilon_{\rm th}^2 h L^2 F(\mathrm{AR}) + 4\gamma h L, \tag{3.10}$$

where γ is the surface energy density of the crack sidewalls. For a given film thickness h and within our assumptions, the most favored crack configuration in terms of the spacing L should be the one which minimize Eq. (3.10). In order to consider a feasible crack net we must, however, ensure that the insertion of a crack decreases the total energy with respect to the film without cracks. Following the modeling introduced in *Sect*. 3.1 for the insertion of dislocations, we can define a formation energy of the crack as

$$\Delta G = G_{\rm tot} - G_{\rm el} = G_{\rm tot} - \epsilon^2 Y h L^2, \tag{3.11}$$

and we should check that the $\Delta G < 0$ condition is verified. The minimization of (3.10) is a global evaluation of the system tendency to host a crack net, corresponding to the thermodynamic limit of the system. The crack density estimated by this approach should be the highest possible (under the considered assumptions) and a larger number of cracks per unit area should not be observed.

The balance between the energy cost and gain can also lead to a local condition for the propagation of cracks as discussed in *Sect*. 1.2.2. As far as a fracture occurring from the upper surface to the Ge/Si interface is considered here, we assume the length l of Eq. 1.25 equal to h. In order to compare a meaningful quantity to the critical stress for crack propagation in Eq. (1.25), we evaluate the average of the in-plane stress along the [110] slice at the center of the $L \times L$ region, i.e. slice A in *Fig.* 3.9(b). We define this quantity as $\sigma_{\rm A}$. For a given value of L and h, this is representative of the maxmimum stressed region in the film, corresponding to the position where a further crack may form. As performed in Eq. (3.9), we can provide a fit of FEM simulation for $\sigma_{\rm A}(\mathrm{AR})$ as

$$\sigma_{\rm A}(\mathrm{AR}) = \frac{\sigma_0}{2} \left[\exp(-p_1' \mathrm{AR}) + \frac{1}{1 + p_2' \mathrm{AR}} \right], \tag{3.12}$$

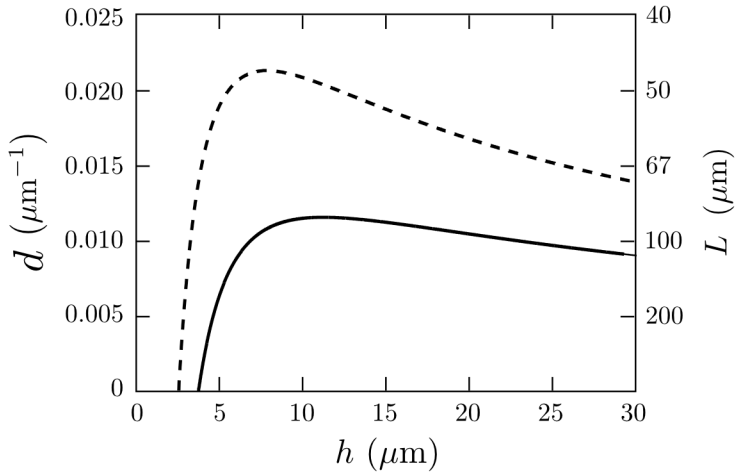

Figure 3.10: Crack densities and spacing predicted by the model as function of the height of the film. Dashed line is obtained by the minimization of Eq. (3.10). Solid line shows the net spacing which satisfies criterion in Eq. (3.13). $\gamma = 7.12$ eV/nm^2 and $\varepsilon_{\mathrm{th}} = 0.15\%$.

with $p_1' = 5.16 \pm 5\%$ and $p_2' = 4.50 \pm 5\%$ and $\sigma_0 = Y\epsilon_{\mathrm{th}}$, representing the stress of the film with no elastic relaxation. If σ_{A} is bigger than $\bar{\sigma}$ from Eq. 1.25, the propagation of an additional crack within the $L \times L$ region along the A plane in *Fig.* 3.9 may occur. The expected spacing L is then given by

$$\sigma_{\mathrm{A}} = \bar{\sigma}, \tag{3.13}$$

that is a condition representative of the critical stress for the addition of a further crack.

3.5.1 Crack density in Ge/Si films

By using the criteria introduced above, we can provide predictions about crack density and/or spacing. In *Fig.* 3.10 we report the spacing L and the relative crack density $d = 1/L$ for a Ge film as a function of the thickness h. With the dashed line, we report the values resulting from the minimization of the total energy (3.10) also checking $\Delta G < 0$ constraint from Eq. (3.11) while the solid curve shows the results obtained from the criterion of Eq. (3.13). We selected for the thermal strain a typical value measured in Ge/Si films of $\varepsilon_{\mathrm{th}} = 0.15\%$ [150] and $\gamma = 7.12$ eV/nm^2 corresponding to the surface energy of $\langle 110 \rangle$ facets [98].

The curve obtained by means of the energy minimization (dashed curve in *Fig.* 3.10) shows a critical thickness for crack insertion of $\sim$2.5 μm, as under such a value, no negative ΔG is obtained for any AR value. Then, by increasing the film thickness above the critical one, we obtain a deep raise of the crack density (and lowering of the crack spacing) until a maximum value at $h \sim 8$ μm. Then, the crack density slightly decreases. This is related to the fact that the energy cost related to the extension of crack sidewalls always increases by increasing the thickness of the film while the elastic strain release saturates for large ARs, as described by Eq. (3.9). So that after a certain thickness we expected to have an increasingly importance of the surface energy term in the energy balance of (3.7), i.e. the relative cost of crack insertion, leading to a consequent lowering of the density. This behavior is related to assumption of the model as other configurations, e.g. cracks shorter than the thickness h or other crack geometries, may be

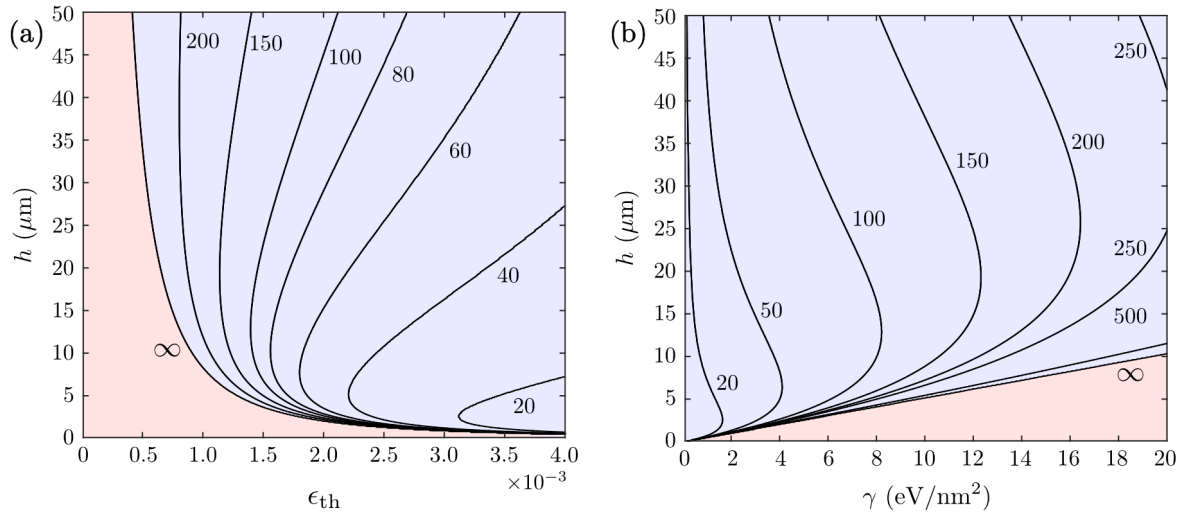

Figure 3.11: Investigation of the onset for crack insertion in a wide parameter space. (a) Crack spacing as function of the $\varepsilon_{\mathrm{th}}$ and h. (b) Crack spacing as function of γ_{th} and h. Isolines show the spacing expressed in μm.

present reducing the cost per unit area.

A similar behavior is obtained for the crack density calculated by means of the stress criterion of Eq. (3.13) (solid curve in *Fig.* 3.10). This approach does not include the information about the global state of the system as described by the minimization of the total energy in Eq. (3.10), but it involves a local stress condition. This produces lower densities as shown in *Fig.* 3.10. However, the qualitative behavior is similar to the one discussed for the curve obtained with the total energy minimization. It shows a critical thickness of ∼4μm corresponding to the thickness which satisfy Eq. (3.13) for $\mathrm{AR} = 0$ ($L \to \infty$). The crack density above the critical thickness rapidly increases until reaching a maximum value and then it slightly decreases as well for larger h values.

Notice that no details are introduced about the nucleation process and about kinetic effects as our analysis is based only on thermodynamic arguments. Despite this, we can consider that the local criterion based on stress values better describes the real crack spacing as it evaluates if locally a crack propagation is favored, once the critical stress condition is reached. Conversely, the energy criterion would deliver the information about the best relaxation of the system by means of an ordered net of cracks, without including any stress condition. However, the results obtained by means of the total energy minimization describe the higher limit in terms of crack density and consists in a theoretical limit which cannot be overcome. In the following the stress criterion is considered in order to show how our predictions vary with changes in γ and ϵ_{th} values. This allows to widen the range of the investigated Ge/Si systems, also by using such parameters as an effective way to account for more complex crack configurations.

3.5.2 Extended results

According to the specific process, ϵ_{th} can be different as the temperature of the growth can vary significantly and also can show different interaction with the compressive residual strain [150]. Moreover, if the film is made of a SiGe alloy, the thermal strain is proportional to the

Ge content c so that $\epsilon_{\rm th}(c) = c\epsilon_{\rm th}$ and the thermal strain should be rescaled. In principle, also the surface energy should account for the different Ge content, but such a dependence is here neglected. In *Fig.* 3.11(a) we show the isolines for spacing L, obtained with the stress criterion of Eq. (3.13), by varying the thickness and also the initial thermal strain values. Under the curve with L $\sim \infty$ we predict a crack-free system. It can be noticed that for small thermal strain no crack is present, as only small elastic energy (zero when $\epsilon_{\rm th} = 0$) should be released, and for a given thickness the crack spacing decrease by increasing the thermal strain. It can be easily seen that for each value of the thermal strain, the variation of the crack spacing as a function of the film thickness h is similar to the discussion reported for *Fig.* 3.10. Once the thermal strain is determined, from calculations or from a specific measurement in an experimental system, one can read an estimation of the expected (thermodynamic) crack net spacing at each thickness up to 50 μm directly from figure 3.11(a).

The surface energy density considered so far is the one of an ideal $[110]$ Ge surface. Different configurations involving several kinds of surfaces can, however, appear with more complex crack geometries. In these cases, γ can be interpreted as a free parameter which can be tuned in an effective way in order to represent the generic cost per unit area related to crack formation (assuming that elastic relaxation is not thereby modified). In *Fig.* 3.11(b) we show a similar analysis to the one shown in *Fig.* 3.11(a), this time by keeping constant the thermal strain and by varying the surface energy density of the crack sidewalls, i.e. the energy cost of creating the free surfaces induced by the fractures. When $\gamma \to 0$ we obtain the theoretical limit of $\sigma_A(\mathrm{AR}) = \bar{\sigma} = 0$, producing AR$\to \infty$ and consequently $L \to 0$. In this regime also $\bar{h}$ tends to zero, but it can be considered as an unphysical condition. By increasing γ, the critical thickness increases as the cost is higher. The same behavior is shown for the spacing values observed at a given γ values and by increasing the film thickness, above the region where no crack are expected (corresponding to the area under the $L \sim \infty$ curve). The qualitative variation of the crack spacing for a fixed value of the surface energy density is similar to *Fig.* 3.10, with different values according to the considered γ.

In order to discuss the results obtained in this section, we can compare the estimation of crack density with well-known experiments present in the literature. In Ref. [149] the investigation of an heterostructure made of ∼5.2 μm thick GaAs/Ge layers grown on Si is reported. Being the thermal expansion coefficients very similar between GaAs and Ge this system closely resembles the one considered here (by neglecting instead the differences in the elastic constants and in the surface energy density). The measured crack density in such a system, after a proper thermal treatment in order to let cracks nucleate as much as possible, is almost 10-15 mm^{-1} (spacing of 66-100 μm) with a measured thermal strain of $\sim 2.0 \times 10^{-3}$. This is in good agreement with the resulting density obtained by our model (see figure 3.11(a)). Similar systems were analyzed in Ref. [148], also showing a good agreement with the analysis reported here.

So that we provided here a model able to give estimations for the onset of mechanical failure and the spacing of the cracks. It has been obtained by directly applying the concept developed for the investigation of plasticity onset in VHEs, and, despite the several approximations, it gives results compatible with the ones present in the literature. As far as a more accurate mod-

eling of this relaxation mechanism would require more sophisticated approaches, this may represent a convenient tool to provide early predictions as a support for the experimental activities.

4

Competitive relaxation mechanisms in real VHEs

The modeling introduced in *Ch.* 3 allowed for a general investigation of the plasticity onset in single-layer and multilayered vertical heterostructures. Despite it was developed by considering simplified geometries with a parallelepipedal shape, it can be easily applied to systems with a more realistic morphology. In particular, this holds true when a representative 2D section of the whole structure can be extracted for the evaluation of the formation energy, in order to apply the quasi-3D procedure described in *Sect*. 3.1.

In this chapter, we report the investigation of realistic VHEs. First, the nanometric structures introduced in *Sect*. 2.5.1 are discussed providing both an assessment of the theoretical modeling and a detailed investigation of specific experimental systems [34, 36, 37]. Then, the validity of the results reported in *Sect*. 3.3, concerning the delay of plastic relaxation when grading the Ge content in VHEs, is demonstrated at the micron scale, delivering an unprecedented result for the growth of high-quality heterostructures [40]. An extension of the study about the thermal strain relaxation, originally provided in Ref. [19], is also shown for what concerns multilayered VHEs [35, 38].

The investigation of the different structures is shown by briefly introducing the main features of the experiments and dedicated sections on the modeling are also reported. Notice that further details and refinements of the method are introduced in order to account for some fine details of the real systems. The work reported in this chapter has been carried out in collaboration with several group that provided the experimental data: Prof. Schröder, Prof. Capellini and their research group at the *Leibniz Institute for Innovative High-Performance Microelectronics* (IHP) for experiments of *Sects*. 4.1 and 4.2; Prof. Sanguinetti, Prof. Isella and their research groups at the *Laboratory of Epitaxial Nanostructures on Silicon and Spintronics* (L-NESS) for experiments of *Sects*. 4.3 and 4.4, respectively; Prof. Von Känel and his research group at *Eidgenössische Technische Hochschule* (ETH) *Zürich* for experiments in *Sects*. 4.4 and 4.5. The missing details concerning the experiments provided by these universities and research centers can be found in the specific references within the sections.

4.1 Coherent Ge on Si with a SiGe buffer layer

The main features of nanoheteroepitaxy have been introduced in *Sect*. 2.5.1. By following this concept, the first attempts to grow fully-coherent structures with sizes exceeding the limit of ~ 40 nm, have been reported in Refs. [130, 138, 151]. However, a clear indication of the presence of dislocations is reported as the extra-relaxation provided by the presence of free surfaces in these systems is not enough to prevent the onset of plastic relaxation. Exploiting the mechanism outlined in *Ch*. 3, the possibility to grow coherent, Ge dot on a 50 nm wide Si nanopillar thanks to the insertion of a SiGe buffer was explored by dedicated experiments, and it is assessed here by dedicated modeling and simulations of strain relaxation [34].

4.1.1 Experiments

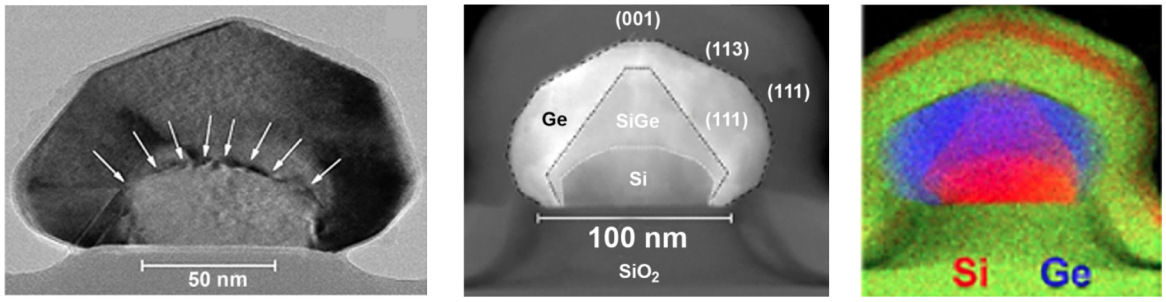

Figure 4.1: Ge on Si nano-islands [34]. (a) Cross-section TEM image of the structure made by pure Ge on ∼50 nm wide Si island. White arrows indicate the presence of misfit dislocation at the Ge/Si interface. (b) Cross-section scanning tunneling electron microscopy (STEM) image of the Ge/SiGe-buffer/Si structure (Covered by SiO_2 for sample preparation). (c) EDX composition of a structure grown as in panel (b) illustrating the abundance of Ge (blue) and Si (red).

The substrate on which the growth of Ge and SiGe alloys have been performed is made of 50 nm wide and 27 nm thick Si islands on top of a ∼100 nm wide and 40 nm thick SiO_2 mesa. They are prepared by a lithographic process, involving structuring via hard mask made by Si_3N_4 layers and subsequent dry etching, from a SOI wafer featuring 29 nm-thick $Si(001)$ top layer on a 145 nm SiO_2 buried oxide layer [34]. Two different samples were grown. The first results by the direct deposition via reduced-pressure chemical vapor deposition (RP-CVD) of pure Ge on the Si island in a two-step process: low temperature ($T = 300$ °C) deposition of a Ge seed followed by standard growth at 550 °C. The same procedure has been adopted for a second sample where a (nominal) $Si_{0.5}Ge_{0.5}$ buffer layer is deposited at 600 °C prior to pure Ge deposition. The results of both the growth processes are shown in *Figs.* 4.1(a) and 4.1(b), respectively.

X-rays analysis of the grown structures has been performed in order to determine the actual composition of the different layers as well as to provide an estimation of the lattice deformation. Details about the fitting procedure of the X-rays measurements leading to the determination of both Ge composition and strain values can be found in Ref. [34] and references therein. From

such an analysis the structure without buffer layers results made by an almost pure Ge ($\sim 95\%$ in the Ge content) and it is unstrained. The absence of strain is a clear indication of the occurrence of plastic relaxation, which was actually confirmed by Transmission electron microscopy (TEM) images of *Fig.* 4.1(a). Indeed, such a figure shows the presence of dislocations with white arrows. For the structure with the buffer layer, a signal compatible with pure Si under a tensile strain of $\sim 1\%$ is obtained. Moreover, a region with a Ge content ranging from 0.4 to 0.6 is recognized with a slightly compressive strain, while an almost pure Ge layer (again with a Ge content of $\sim 95\%$) is observed with a residual compressive strain of $\sim -0.5\%$. According to the measurement technique, such values should be interpreted as in-plane strain, i.e. $\varepsilon_{||} = 0.5(\varepsilon_{xx} + \varepsilon_{yy})$, averaged on the domains with the same Ge content, i.e. the pure Si island, the SiGe buffer and the Ge epilayer, respectively. The composition is also shown by means of the Energy Dispersive X-Ray (EDX) composition mapping reported in *Fig.* 4.1(c). All these measurements strongly suggest that the insertion of the buffer layer allowed compliance effects to be effective in avoiding the formation of dislocations, at variance with pure Ge deposition on Si. In the following section an original theoretical analysis, using the method introduced in *Ch.* 3, is reported in order to assess such an experimental evidence.

4.1.2 Modeling of the realistic geometry and simulations

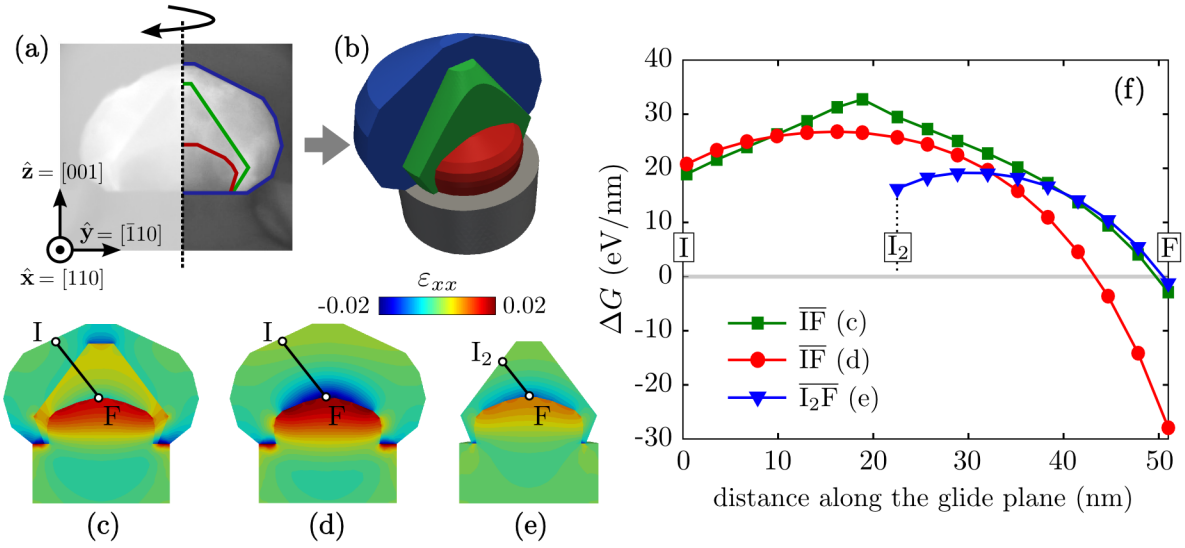

Figure 4.2: Modeling and simulations of the plasticity onset in Ge grown on the Si nano-island. (a) Structure of *Fig.* 4.1(b) with the outline of the different domains highlighted with colored lines: inner Si island (red), SiGe buffer (green), Ge epilayer (blue). (b) 3D geometry obtained by a full rotation of the outlines in panel (a) around the $\hat{\mathbf{z}}$ axis. In plane strain maps as resulting from FEM simulations are shown: (c) structure with the buffer layer, (d) the same structure of (c) with $\sim 95\%$ of Ge content also in the buffer layer domain and (e) same structure in (c) without the Ge epilayer. (f) Formation energies for a 60° dislocation along $\overline{\mathrm{IF}}$ and $\overline{\mathrm{I_2F}}$ segments in panels (c)-(e).

The model introduced in *Sect.* 3.1 has been applied to the investigation of both the Ge/Si and the Ge/SiGe/Si structures reported in *Figs.* 4.1(a) and 4.1(b). In particular, we focus on the structure with the buffer layer, demonstrating that the domain with intermediate Ge content is

key to ensure the coherency of the whole structure. The 2D TEM view of *Fig.* 4.1(b) has been considered and the outlines of the domains with a different Ge content are explicitly tracked as illustrated in *Fig*. 4.2(a). The 3D structure is modeled by considering a full 3D rotation of such profiles along the $\hat{\mathbf{z}} = [001]$ axis as reported in *Fig.* 4.2(b). The ideally infinite substrate under such a 3D geometry was considered as an additional cylinder underlying the structure, five times higher and larger than the actual 100 nm wide oxide pedestal. An initial eigenstrain $\varepsilon_{ij} = -c\varepsilon_{\mathrm{m}}\delta_{ij}$, with c the Ge content as measured by X-Rays, is considered. The mechanical equilibrium equation (1.13) is then numerically solved by FEM, accounting for the proper boundary conditions (BCs): fixed BC, from Eq. (1.15), at the bottom of the substrate, gliding BC, from Eq. (1.16), at its lateral surface and free BC, from Eq. (1.14), at the other surfaces. Elastic constants are assumed isotropic. The SiO_2 substrate is modeled as a continuous medium, with the isotropic elastic constants $E_{\mathrm{SiO_2}} = 70$ GPa and $\nu_{\mathrm{SiO_2}}$=0.17 [152].

The result of the calculation is shown in *Fig.* 4.2(c) in terms of the in-plane strain $\varepsilon_{||}$ in the central cross-section of the whole 3D structure. The Ge layers pull the inner Si island producing a tensile strain of $\sim 1\%$. This effect is present also with minor extent in the SiGe buffer while the external Ge layer is almost relaxed with a slightly compressive region surrounding the SiGe buffer. A stronger compressive lobe is also found in a small region at the top of the structure. So that, a strain state which closely resembles the values obtained by X-rays measurement is observed. The main difference with experiments is found in the comparison of the strain state in the SiGe buffer, which can be explained by accounting for a more detailed modeling of the structure as discussed in *Sect*. 4.1.3.

In order to investigate the difference of this structure with respect to the one without the SiGe buffer, we repeated the simulation by imposing a Ge content of 0.95 also in the SiGe-buffer domain and the resulting map of $\varepsilon_{||}$ is shown in *Fig.* 4.2(d). In such a system, the pulling of the Si is even higher with the appearance of a strongly compressive lobe at the interface ($\sim -1\%$). This does not correspond to the experiments, as an array of misfit dislocation is present in *Fig*. 4.1(a), providing a full (plastic) relaxation of the heteroepitaxial stress.

These elastic calculations provided a qualitative explanation about the higher tendency to host dislocations in the structure without a buffer layer, as regions with a higher local deformation are obtained. However, no quantitative data are provided and dislocation should be explicitly taken into account in order to demonstrate that with a SiGe buffer the plasticity onset is delayed and eventually prevented.

The coherency of the structure including the buffer is assessed by directly applying our quasi-3D model described in *Ch*. 3. The central slice of the full 3D structure is considered to compute the formation energy ΔG for a 60° dislocation in the region where the strain relieved by the dislocation is maximum. In particular we consider the system with and without the buffer layer shown in *Figs.* 4.2(c) and 4.2(d). Moreover, also the structure with the SiGe buffer island prior to pure Ge deposition is considered as shown in *Fig.* 4.2(e), to provide indications about the intermediate structure obtained during the growth of the full system. In this calculation, the geometry of the buffer is assumed to be the same as observed in the final structure. In *Fig*. 4.2(f) ΔG values are shown for the three different cases depicted in *Figs.* 4.2(c)-4.2(e) as

function of the distance from the point I (and I_2 in *Fig.* 4.2(e)) at the free surface. Indeed, these points correspond to the ideal position where dislocations are likely to be nucleated in the form of half loops in order to reach the higher stressed region at the interface with Si (points F) by gliding along their glide plane. Therefore, we are focusing on the dislocation which provides the better strain relaxation i.e. the lower ΔG. The formation energy for the insertion of a dislocation at the interface with $[001]$ orientation between Ge and SiGe was also investigated as stress lobes with opposite signs are found. However, an even larger formation energy with respect to the dislocation placed at the interface considered above is obtained. This holds true also for several other configurations sampled for the insertion of 60° dislocations in the structures shown in *Figs.* 4.2(c)-4.2(e), so that we focus on the central position at the SiGe/Si (or Ge/Si) interface.

As shown in *Fig.* 4.2(f), the formation energy in the system without the SiGe buffer is significantly lower than zero, i.e. the total energy is strongly lowered when inserting a misfit dislocation. Notice that the formation energy is negative not only at the interface but also in a finite region over it. When considering the structure with the SiGe buffer layer, ΔG becomes negative only in a region very close to the interface ($\sim$1 nm) with a significant lowering of the energy gain, from 28 to $3.1\ \mathrm{eV/nm}$. In addition, if the nucleation of the dislocation would occur in the final structure including the SiGe buffer, with the selected orientation to provide the higher relaxation at the SiGe/Si interface, a significant energy barrier should also be accounted for as shown by the green curve in *Fig.* 4.2(f). If the insertion of dislocation is evaluated prior to pure Ge deposition, i.e. in the structure of *Fig.* 4.2(e) (blue curve of *Fig.* 4.2(f)), the tendency towards plastic relaxation is even lowered with $\Delta G = -1.1\ \mathrm{eV/nm}$ at the SiGe/Si interface.

The results discussed above indicate that in the absence of the SiGe buffer, the system is largely overcritical, while when inserting a buffer layer, it is very close to the thermodynamic limit for dislocation insertion. So that we can conclude that the insertion of a dislocation is significantly delayed in the system with the dislocation but the negative formation energy indicates that, in the thermodynamic limit, the plastic relaxation is expected. Being the value of ΔG very small compared to the system without the buffer, it can be possible that dislocations are not observed due to kinetics limitations, which are instead not enough to prevent plasticity with pure Ge on Si deposition. However, further refinements of the model, which better describe the features of the real structure would lead to the conclusion that also the thermodynamic limit is expected to indicate a coherent structure. This analysis, discussed in the next section, provides a more general assessment of the experimental observations.

4.1.3 Deviation from uniform Ge distribution

The results obtained by a direct application of the method in *Sect.* 3.1 implies the presence of a uniform Ge composition within the different domains. While for the growth of Ge on Si an average composition lower than 1 can effectively account for mixing, this assumption is expected to be weaker for the buffer layer. Indeed, a more important intermixing is present as experimental measurements indicate a possible variation of the Ge content within $\sim 0.4 - 0.6$.

According to the elastic-energy minimization, as widely discussed in Ref. [153] for Ge/Si islands during Stranski-Krastanov growth, the SiGe buffer layer is expected to show an accu-

mulation of Ge in the top part with a more Si-rich region at the bottom. Indeed, this would lead to a lattice parameter closer to the one of the epilayer at the Ge/SiGe interface. Moreover, this holds true for the bottom region which would exhibit an average lattice parameter closer to Si. In order to take this effect into account, we repeated the calculations leading to the ΔG curves shown in *Fig.* 4.2(f) by assuming a more realistic Ge content distribution within the buffer-layer. A positive ΔG, i.e. an indication of the absence of plasticity even at the thermodynamic limit is obtained by considering a Ge content distribution with a linear variation along $[001]$ direction from $c = 0.45$ at the SiGe/Si interface to $c = 0.55$ at the Ge/SiGe interface. This indicates that with a small mixing of Si and Ge, the structure results even above the thermodynamic onset for plasticity. In turn, even more extreme conditions in terms of elastic deformation can be exploited as, for instance, by growing larger structures. Notice that the variation in the Ge content considered here leads also to a better comparison to the experimental values concerning the strain in the SiGe layer. Indeed, with higher Ge content at the top, the tensile strain observed in *Fig.* 4.2(c) would vanish, with a resulting slightly negative strain on average in agreement with the experiments. So that, the modeling provided in this section confirm the key feature of the proposed structure, which paves the way to the growth of coherent Ge dot on Si.

According to the results presented here, it was not necessary to consider a more detailed modeling of the intermixing, as for instance in Ref. [153], to assess the coherency of the system [34]. A similar approach to the one discussed here will be adopted also for another heterostructure as discussed in *Sect*. 4.2, where the measured Ge composition will be explicitly considered, thus proving the possibility to account also for more complex Ge distributions.

4.2 Coherent Ge on Si Tip

The realization of an efficient strain partitioning between a mismatched epilayer and a patterned substrate has been achieved by including a buffer layer with intermediate Ge composition, as discussed and demonstrated in *Sect*. 4.1. As a result, a coherent structure with very high Ge content has been obtained with a width larger than the critical size for a single layer heterostructure ($\sim$40 nm). In this section, we investigate the plasticity onset in a Ge island grown on Si(001) tip-patterned substrates embedded in a SiO_2 matrix. This peculiar configuration combined to the local intermixing at the Ge/Si interface, enhanced by the high growth temperature, is demonstrated to provide coherent structures as well.

4.2.1 Experiments

The growth of Ge dots is performed on Si tips buried in SiO_2. This newly developed patterning technique allows for the highly selective deposition of Ge on Si areas with tunable size and periodicity. First, a few hundreds-wide and tall Si domains, ending with a few nanometers wide tip, are fabricated with a prescribed periodicity by advanced lithographic techniques involving reactive ion etching. A SiO_2 layer is then grown by PECVD, burying the tips and filling the space in between. Then, chemical-mechanical polishing (CMP) is performed to expose the Si domain, cutting the tip. The average size of exposed Si area can be tuned by the depth of the CMP. The resulting substrate allows for an extremely selective deposition as the Ge can grow

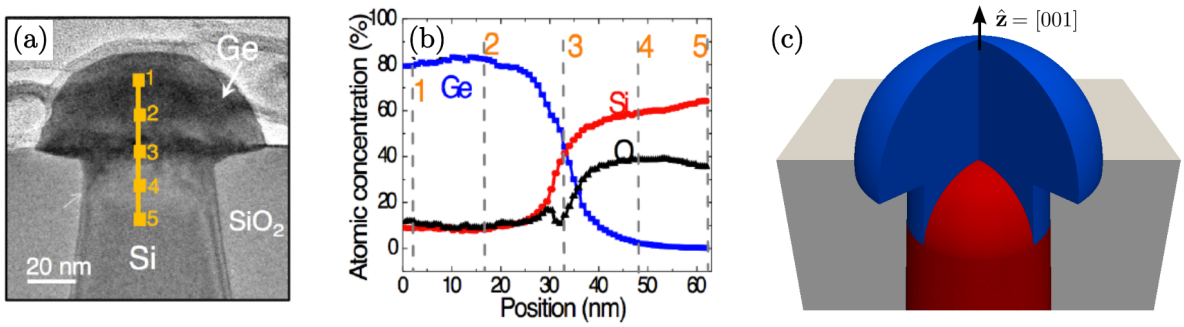

Figure 4.3: Ge on Si tip. (a) HRTEM view of a Ge nano-island grown on a Si tip and (b) composition profile along the yellow line in panel (a) (adapted from Ref. [37]). (c) Geometry modeling for FEM simulation. The same procedure introduced in *Sect.* 4.1, involving the selection of the 2D cross-section and the full rotation along the $\hat{z}$ axis, has been considered.

on the Si window while on the oxide it desorbs quickly at high temperatures. The structure obtained by deposition of Ge at 850 °C is shown in *Fig.* 4.3(a). Composition of Ge (blue) and Si (red) within the grown sample measured by Energy Dispersive X-ray analysis (EDX) along the yellow line in *Fig.* 4.3(a) are reported in *Fig.* 4.3(b). This analysis clearly shows a smooth variation of the Ge content in a region ∼30 nm thick across the nominal interface between Ge and the Si tip. These compositions also account for oxygen (black) as also SiO_2 region behind the analyzed structure is measured. The larger value for the Ge content in *Fig.* 4.3(b) can then be considered ∼0.9 in position 1 of and ∼ 0 in position 5. Notice that such an extended mixing of Si and Ge was not present in the samples discussed in *Sect.* 4.1 due to the lower growth temperature, here set to 850 °C to ensure selective growth. Raman analysis on such a sample showed an almost relaxed Ge dot with a slightly negative residual strain while no clear indication of dislocation is observed from analysis of TEM images [37]. This evidence of coherency is investigated by theoretical calculations in the following section. An important feature of this experiment is that a size distribution is actually obtained for Ge dots on Si tips, as the lateral size of the Si tips ranges from 50 to 75 nm.

4.2.2 Modeling and results

The coherency of the Ge grown on Si tips has been investigated by exploiting the model introduced in *Sect.* 3.1 combined to the approach to real systems described in *Sect.* 4.1. The 3D geometry has been reproduced starting from the experimental (2D) profile of *Fig.* 4.3(a) and considering a full rotation around the [001] direction as shown in *Fig.* 4.3(c). The SiO_2 is modeled as in *Sect.* 4.1. The continuity of this oxide with the Si and Ge domains is assumed by considering that the oxygen diffuses within other materials for a few monolayers, leading to a continuous medium. However, elastic constants of SiO_2 are smaller than Si and Ge as it is softer, and its deformation contributes to the total elastic energy with a lower extent than the other materials. The illustration of the considered geometry is shown in *Fig.* 4.3(c). In such a structure the elastic field is computed as in *Sect.* 4.1 accounting for the mismatch between the high-Ge content epilayer and Si within the tip. In particular, we focus on the larger structure obtained in the experiments, corresponding to a tip lateral size L equal to 75 nm. The resulting

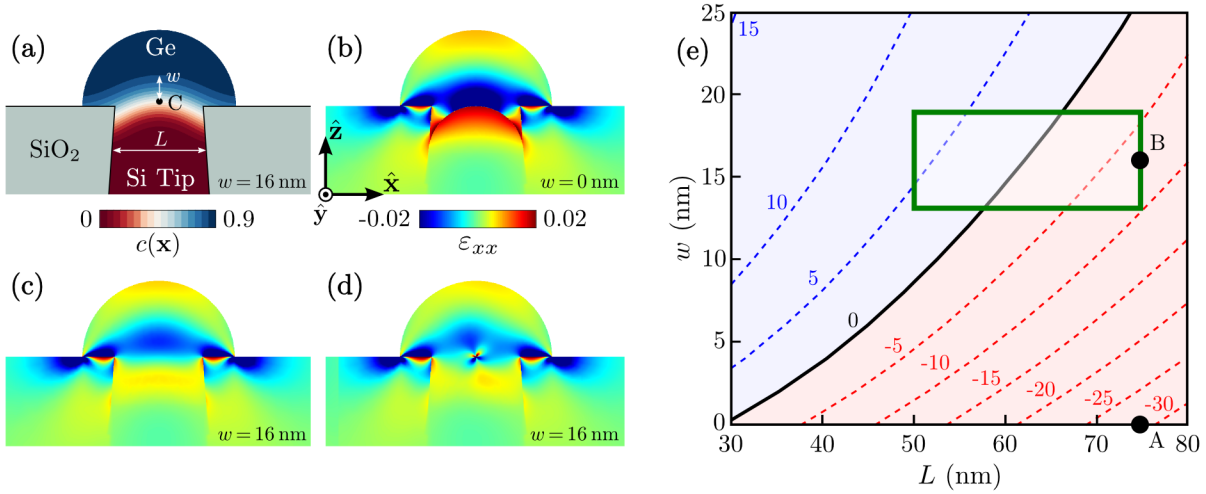

Figure 4.4: Modeling and simulations of the plasticity onset in Ge grown on Si tip. (a) Central section of the Ge on Si tip structure, i.e. the 3D structure sketched in *Fig.* 4.3(c). The color map shows the compositional profile obtained by Eq. (4.1) with $w = 16$ nm, resembling the grading observed in the experiments. (b) Color map of ε_{xx} as obtained by FEM simulation with uniform $x = 0.9$ composition ($w = 0$). (c) Color map of the ε_{xx} as obtained by FEM simulation for the compositional profile reported in (a). (d) same as in (c) with a dislocation segment inserted in the central section of the structure. (e) Phase diagram describing the onset of plasticity in the Ge on Si-tip system. ΔG values are shown by isolines as function of w and L (light-blue region $\Delta G > 0$, red region $\Delta G < 0$). The green box highlights the experimental ranges of L and w. Black circles correspond to the positions in the (L, w) parameters space of the calculations with $\mathrm{A} = (75, 16)$ and $\mathrm{B} = (75, 0)$, respectively.

Ge-island base is 120 nm.

The elastic field computed with an abrupt change in the composition between Si and the Ge rich island, by directly applying the method discussed in the previous section with uniform Ge distributions, is reported by the color map of *Fig.* 4.4(b), showing ε_{xx} values. Lateral free surface of the Ge dot, thanks to its high aspect-ratio, allows for a partial relaxation of the misfit strain. Notice that a tensile strained region is obtained in Si with values around $\varepsilon_{xx} \sim 1\%$ and a compressive strain values at the bottom of the Ge dot with $\varepsilon_{xx} \sim -1\%$. Such a strain partitioning is typical of heterostructures with a sharp interface at the nanoscale as shown in *Sect.* 3.2 and *Sect.* 4.1. Actually, as reported in *Sect.* 4.2.1, the interface at the top of the Si tip is not sharp and a smooth increase of the Ge content is observed. In order to model such a behavior, we introduce a distribution of the Ge content $c(\mathbf{x})$ as follows:

$$c(\mathbf{x}) = \frac{c_{\max}}{2}\left[1 - \tanh\left(\frac{0.5L - d}{w}\right)\right] \cdot \left[1 - \exp\left(-\frac{z}{0.33L}\right)^2\right], \tag{4.1}$$

with $\mathbf{x} = (x, y, z)$, $c_{\max}$ the maximum Ge content value in the system, set to 0.9 as revealed by the experiments of *Sect.* 4.2.1. L and w are the tip opening-area and the half-width of the intermixed region, respectively (see *Fig.* 4.4(a)). $d = \sqrt{x^2 + y^2 + z^2}$ is the distance from the center of the frame of reference $C = (0, 0, 0)$, set as the center of the hemisphere which forms the nominal rounded top of the Si tip (see the 3D geometry in *Fig.* 4.3(c) and the black circle in *Fig.* 4.4(a)). Notice that such a formulation provides a reliable 3D Ge content map correspond-

ing to the observed one in *Fig.* 4.3(b) by setting $w = 16$ nm. Such a Ge distribution is shown as a color map in *Fig.* 4.4(a). Two main factors can be noticed in Eq. (4.1). The first one corresponds to a radial term with respect to C, mimicking the effect of the distance from the nominal top of the Si tip, where the intermixing is assumed to give half of the maximum Ge content. The second one represents a vertical contribution which smoothly lower the Ge content to 0 when approaching the Si tip below the point C, i.e. for $z \leq 0$).

The same calculation performed to obtain the strain map in *Fig.* 4.4(b), are then repeated by explicitly considering the Ge content distribution in Eq. (4.1) with $w = 16$ (see *Fig.* 4.4(a)) mimicking the variation of the Ge content in the real structure (setting $\varepsilon^*_{ij} \propto c(\mathbf{x})$). The resulting ε_{xx} distribution is shown by the color map in *Fig.* 4.4(c). The deformation with a smooth transition between the Si and the Ge-rich dot is lower than the $w = 0$ case in *Fig.* 4.4(b). Then, also higher uniformity is achieved. This strain state is expected to play an important role in the onset of plastic relaxation.

In order to evaluate the tendency to host a dislocation in the Ge dot grown on the Si-tip, the formation energy ΔG for the insertion of a 60° dislocation is calculated. The dislocation is modeled as an ideal misfit segment elongated in the $\hat{\mathbf{y}}$ direction, i.e. perpendicular to the plane of the central cross-section, and the coherent elastic field of the central section. The outline of this 2D domain corresponds to the one in *Figs.* 4.4(a)-4.4(d). Notice that this outline corresponds to all the sections crossing the center thanks to the construction of the 3D geometry so that it can be considered as the plane perpendicular to the $[110]$ direction, i.e. perpendicular to the dislocation line. ΔG is evaluated as described in *Sect.* 3.1, i.e. as the difference in the elastic energy between systems with and without the dislocations. The latter is computed from the elastic field in the 2D section extracted from the 3D geometry (see *Fig.* 4.4(c)) while the former by the superposition of the dislocation elastic field with the heteroepitaxial one in the same 2D section (see *Fig.* 4.4(d)).

The results of ΔG calculations are summarized in *Fig.* 4.4(e). Let us focus first on the two cases discussed above, corresponding with $w = 0$ and $w = 16$, respectively, with $L = 75$ nm as in the experimental structure of *Fig.* 4.3(a). When no intermixing is considered, i.e. $w = 0$, $\Delta G \approx -30\ \mathrm{eV/nm}$ (point A in *Fig.* 4.4(e)), indicating that the system would strongly host a dislocation. By setting $w = 16$ the ΔG is still negative, but its magnitude decreases significantly to -6 eV/nm (point B in *Fig.* 4.4(e)). A lowering of the formation energy is then obtained by taking into account an effective modeling of the intermixing. So that the presence of a smooth variation in the Ge content would generally delay the plasticity onset. It is worth mentioning that, despite ΔG is still negative, the formation energy here calculated corresponds to the larger structure obtained in the system. So that, smaller sizes may lead to a further lowering of the formation energy as the elastic budget would decrease accordingly. Moreover, a fluctuation of the actual transition region, i.e. of the w parameter, is observed. The formation energy obtained by sampling the parameter space given by w and L are shown by the plot in *Fig.* 4.4(e). The island base was scaled proportionally to the lateral size L. The critical parameter curve ($\bar{L}$,$\bar{w}$) corresponds to the solid black line. Isolines show the values of the formation energy which are positive over the critical curve, indicating a coherent structure, and negative under the critical

curve, corresponding to plastically relaxed systems. Notice that when a uniform $Si_{0.1}Ge_{0.9}$ dot is considered the critical L is $\sim$30 nm. When considering intermixing, i.e. $w > 0$, a delay of the onset for plastic relaxation is obtained. The full range of the sizes L obtained in the experiments together with the statistical fluctuation of the Ge content is shown within the green box. The FEM calculations actually predict that this range covers the critical condition for the insertion of dislocations (black line) and structures are predicted to be coherent for the smaller sizes obtained in the experiments. We can further notice that, as mentioned before, our calculations are purely based on the energetics and they are expected to overestimate the tendency towards plastic relaxation. So that we can conclude that the general observation of the absence of dislocation found by the experiments is supported by the theoretical calculations. While for the larger size it may be related to kinetic barriers, calculations show that the smaller size should be coherent also in agreement with the thermodynamic onset. Moreover, this result can be interpreted as resulting from the peculiar geometry of the sample and from the distribution of Ge in the structure. Preliminary experiments performed at IHP, where smaller dots have been grown with a better control of the sizes, with (L, w) parameters lying in the region with $\Delta G > 0$ of *Fig.* 4.4(e), further confirm the coherency of the Ge dots on Si tips, thus further supporting the results obtained in this section.

4.3 Plastic relaxation in InAs dots on GaAs nanowires

As introduced in *Sect.* 2.5.1, nanowires (NWs) represent another heteroepitaxial system where lateral free surfaces play a role in the relaxation of the lattice mismatch. A specific system made by an InAs dot grown on a GaAs nanowire with a sharply defined interface has been investigated by means of our modeling, assessing the observed features of the plastic relaxation.

4.3.1 Experiments

The growth of the InAs island on a GaAs NW is performed by MBE and mainly consists of four different steps. The first step is the growth at 580 °C of the GaAs NWs on Si(111) substrate using the self-assisted mode, i.e. with the growth of the NW resulting by the crystallization of GaAs within a Ga drop on top of the structure. Then, as the second step, a flat $[001]$-top is obtained by the consumption of the Ga droplet, just by closing the supply of Ga in the chamber and decreasing the temperature to 400 °C. In the third step, the deposition of In on the flat top of the NW as a droplet is achieved and the fourth step consists of its arsenization, forming an InAs island. The result of this procedure is shown in *Fig.* 4.5(a). It consists of a $\sim$20 nm tall and $\sim$65 nm wide dome-shaped island formed on top of the GaAs nanowire. Further details of each step including data about pressures in the chamber and growth time as well as other features of the experimental technique are reported in Ref. [36].

Fig. 4.5(b) shows an image of the strain field, obtained by geometrical phase analysis (GPA) [154] of the TEM image, at the interface of the sample reported in *Fig.* 4.5(a). Different strain state is observed for GaAs and InAs as evidenced by different colors with a sharply defined interface between these two materials. This is also assessed by the line scan provided in *Fig.* 4.5(d) which shows a lattice parameter variation of 6.4% when moving from GaAs towards the InAs (consistent with the expected $\sim 6.7\%$, calculated from InAs and GaAs lattice parameter). The

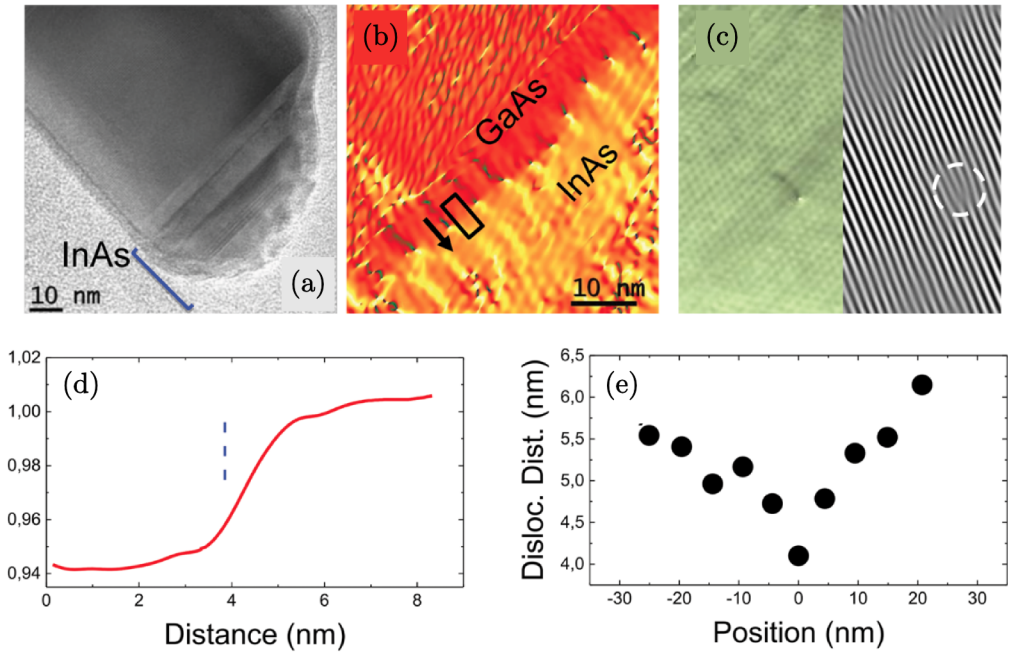

Figure 4.5: InAs dot on a GaAs Nanowire from Ref. [36]. (a) Lateral view TEM image. (b) Strain field as measured at the InAs/GaAs interface. (c) Analysis of dislocation character with GPA strain map superposed to HRTEM image (left) and HRTEM image after Fourier transform highlighting the extra plane typical of an edge dislocation (white circle). (d) Relative variation of the lattice parameter across the interface, i.e. along black arrow in panel (b). (e) Dislocation-dislocation distance as function of the dislocation position as observed in panel (b).

transition between these materials is not found to be abrupt, but a smooth variation is confined within 2-3 nm. Moreover, an array of strain centers is observed at this interface. In *Fig.* 4.5(c) these strain centers are demonstrated to be originated by edge dislocations. Indeed, the strain map over a strain center is overlapped to the HRTEM (left), and it shows almost symmetric lobes, while the typical extra plane present for edge dislocations is obtained after Fourier filtering (right) [36] (see for instance a comparison with *Fig.* 1.1(b)). The dislocations are found to be ordered at the interface. In particular, 11 dislocations are observed, with a spacing which is minimum at the center of the InAs island and increases moving towards the lateral sidewalls as reported in *Fig.* 4.5(e).

4.3.2 Modeling and results

The theoretical modeling developed to investigate elasticity and plasticity in VHEs (see *Sect.* 3.1) is here applied in order to assess the features of the elastic and plastic relaxation observed in the InAs island, grown on the GaAs NW. In *Fig.* 4.6(a) the modeling of the 3D geometry is shown. The elastic field in the structures is computed by considering the eigenstrain as $\varepsilon^*_{ij} = -\varepsilon_{\mathrm{m}}$ with $\varepsilon_{\mathrm{m}} = -6.7\%$ in the InAs island and zero in the GaAs NW. Then the mechanical equilibrium equation is and numerically solved by FEM and it is shown in *Fig.* 4.6(b). For the sake of simplicity, isotropic elastic constants are assumed and set as $E_{\mathrm{InAs}} = 51.4$ GPa, $\nu_{\mathrm{InAs}} = 0.35$, $E_{\mathrm{GaAs}} = 85.9$ GPa, $\nu_{\mathrm{GaAs}} = 0.31$ [155, 156]. An almost relaxed InAs island is found by the calculations, with the typical compressive lobe in the epilayer and the tensile lobe in the substrate

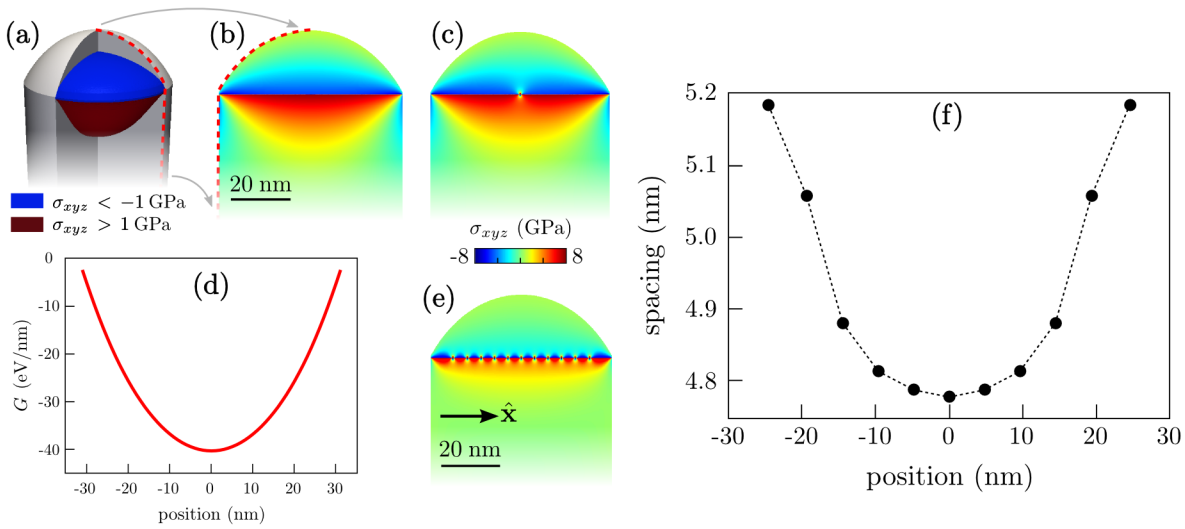

Figure 4.6: Modeling and simulations of plastic relaxation in InAs island grown on GaAs NW. (a) Modeling of the 3D geometry. A dome-like shape is assumed for InAs islands according to *Fig.* 4.5(a). The GaAs NW is set as a simple cylinder. σ_{xyz} isosurfaces at -1 GPa and 1 GPa in the three-dimensional geometry are shown. σ_{xyz} is also reported in the central section by accounting for different relaxation states: (b) pure elastic relaxation, (c) superposition of the elastic field from panel (b) and originating by an edge dislocation at the center of the structure. (d) Formation energy for a single dislocation at the InAs/GaAs interface. (e) System hosting 11 dislocations at the position which minimize the surface energy (computed by a steepest descend algorithm with constrained positions at the interface). (f) Spacing of dislocation in panel (e) as function of the position along the interface (with $x = 0$ the central position).

pedestal observed for VHEs. The plastic relaxation is inspected first by evaluating the formation energy ΔG obtained by applying the quasi-3D approach. Following the experimental indications of *Figs.* 4.5(b) and 4.5(c), we consider dislocations with pure edge character. In the considered FCC system, where (111) interface is present, the dislocation line must be aligned on $\langle 112 \rangle$ directions, as imposed by the $\langle 110 \rangle$ $\{111\}$ slip system (as discussed in *Sect.* 2.3.1). The hydrostatic stress originating from the insertion of this dislocation, superposed to the heteroepitaxial elastic field (reported in *Fig.* 4.6(b)), is shown in *Fig.* 4.6(c). A negative ΔG value is obtained for the insertion of a single dislocation for any position at the interface, as shown in *Fig.* 4.6(d), with a minimum at the center of the structure. This corresponds to the minimum energy for the dislocation as its elastic field is highly symmetric and the heteroepitaxial stress is higher in this region (notice that this is peculiar of the system considered here, as more complex situations are observed for a 60° dislocation at (001) interfaces as discussed in *Sect.* 3.4). The computed formation energy indicates that the system is largely overcritical. Indeed, the critical base determined by evaluating ΔG with a self-similar scaling of the structure is $\sim$15 nm in agreement with the predictions provided in Ref. [18]. This is confirmed by the experiments as dislocations are clearly found at the interface (see *Fig.* 4.5(b)).

In order to investigate the most probable distribution of dislocations in the InAs island on the GaAs NW, we considered $n = 11$ dislocations (as in the experiments) at a constant spacing S of 4 nm with positions along the interface set by $x_i = iS + (n-1)/2$ (with $x = 0$ corresponding to the central position). Then, a steepest descend algorithm is applied to minimize the total energy

allowing only for the motion of dislocations along $\hat{\mathbf{x}}$ direction. In this system, the $[111]$ interface is also a glide plane for the considered dislocations so that the motion at the interface can be observed also in the real system. Forces acting on dislocations are calculated as numerical derivatives of the free energy along the interface by a finite differences approach. In particular, the force acting on the i-th dislocation is

$$f_i = \frac{G(x_i + \Delta x) - G(x_i - \Delta x)}{2\Delta x} \tag{4.2}$$

where $G(x_i \pm \Delta x)$ are calculated via FEM simulations (with the quasi 3D approach) by shifting the position x_i of the i-th dislocation of a quantity $\pm\Delta x$ and keeping all the other dislocations fixed. Δx is here arbitrarily set equal to 0.02 nm. Once forces acting on dislocation are determined, new position x_i^{new} are evaluated as

$$x_i^{\text{new}} = x_i + f_i \Delta s \tag{4.3}$$

where Δs is an arbitrary parameter which set the amount of the shift along the interface for the dislocations. It is scaled to ensure an upper limit for the maximum shift corresponding to Δx.

The procedure described by Eqs.(4.2) and (4.3) is iterated until reaching a minimum of the free energy, i.e. with $f_i \sim 0 \; \forall \; i$. Notice that this procedure has an intrinsic error in the equilibrium positioning of $\sim \Delta x$. The stress distribution with dislocations positioning resulting from this calculation is shown in *Fig.* 4.6(e). In *Fig.* 4.6(f) we report the spacing between dislocations (averaged with respect to the nearest neighbor) as function of the position along $\hat{\mathbf{x}}$. This distribution qualitative reproduces the experimental one in *Fig.* 4.5(e), i.e. the distance is lower at the center of the structure, where the stress is higher while it increases moving towards the boundaries. Therefore, we can state that the model captures the behavior of the real system. This allows us to conclude that in this overcritical system, the dislocation distribution in the InAs island grown on GaAs NW is determined by the strain relaxation, i.e. by the minimization of the free energy. Notice that the elastic energy calculated as described above accounts for the mutual dislocation-dislocation interaction, the effect of the free surfaces parallel to the dislocation and the interaction between dislocation-induced deformation with the heteroepitaxial elastic field. So that, the resulting dislocation distribution results from the simultaneous presence of these effects. In order to provide a detailed quantitative comparison with the experiments, a full 3D modeling would be needed, especially when several dislocations are present. Such further extensions would require a more complex modeling which is far from the scope of the present work.

4.4 Dislocation-free SiGe/Si microstructures

VHEs at the nanoscale are well known to be dislocation free under certain sizes [18]. Structures discussed in *Sects.* 4.1 and 4.2 represent important attempts in the increase of the critical sizes for dislocation insertion but they are still limited to length scales lower than 100 nm. In this section, exploiting the results presented in *Ch.* 3, we describe how these sizes can be significantly increased. The design of a coherent, μm-VHEs is reported with the dedicated experiments performed to prove the general concept. Dedicated simulations are also shown to further assess the main findings about the coherency of the final structures [40].

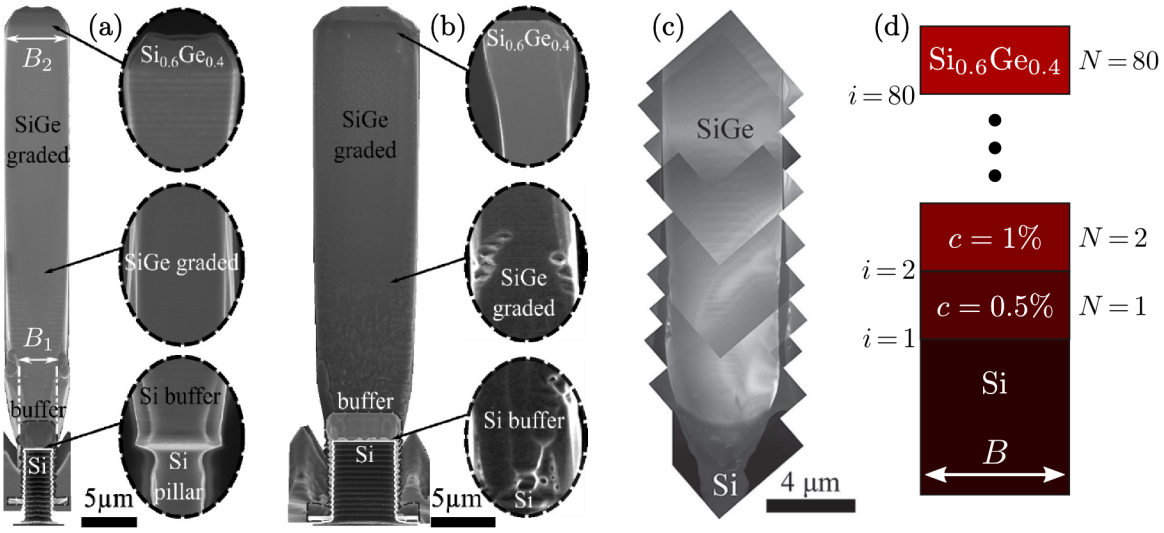

Figure 4.7: SiGe/Si graded heterostructures (adapted from Ref. [40]). (a) Cross-sectional SEM image of the SiGe crystal grown on 2×2 μm^2 wide, 8 μm tall Si pillars spaced by 4 μm wide trenches. Insets show different portion of the crystal after defect etching revealing the absence of dislocations. (b) Cross-sectional SEM image of the SiGe crystal grown on 5×5 μm^2 wide, 8 μm tall Si pillars spaced by 4 μm wide trenches. Insets showing the result of the defect etching, as in panel (a), reveal the presence of dislocations. (c) Cross-section TEM image of the crystal in *Fig.* 4.7(a). (d) Schematic representation of the 2D geometry showing all the parameters used in the simulations discussed in *Sect.* 4.4.2.

4.4.1 Design of the coherent, micrometer-wide VHE

From Eq. (3.6) one can estimate the number of buffer layers required to achieve a coherent VHE. The buffers were assumed to have an height-to-base ratio (~ 1) and the increase in the Ge content of each layer with respect the previous one is given by Eq. (3.5). The typical pattern which allows for vertical growth of Ge by LEPECVD at the micron scale is given by 2×2 μm^2 wide, 8 μm tall Si pillars, separated by trenches of a few microns. Here we inspect the possibility to obtain an intermediate Ge content layer, namely $c = 0.4$, on top of such a structure without the presence of misfit dislocations. This would represent an important proof for the whole method, also direclty usable for optoelectronic applications [40].

When the deposition on deeply patterned substrates by LEPECVD (see *Sect.* 2.5.2) is performed, the vertical growth occurs with an enlargement of crystals up to form a few tens of nanometers wide channel in between. The patterned substrate on which we are focusing here is made of 2×2 μm^2 wide, 8 μm tall Si pillars spaced by 4 μm wide trenches. The vertical growth is expected to almost fill the gap between the Si pillars, i.e. to deliver a width of ~ 6 μm of the Ge crystals.

By considering a top layer with a Ge content c_{epi} for a structure with $B = 6$ μm, the number of buffer layer required to prevent the formation of dislocation is given by the equation

$$n_{\mathrm{BL}}(B) = \frac{c_{\mathrm{epi}}}{\bar{c}(B)} - 1. \tag{4.4}$$

obtained by a change of Eq. (3.5) in order to explicitly account for the Ge content of the epilayer c_{epi} (notice that for $c_{\mathrm{epi}} = 1$ Eq. (3.5) is readily obtained). By evaluating this equation for

$B = 6$ μm we obtain $n_{\mathrm{BL}}(B) \sim 4$. With an aspect ratio of ~ 1 for each buffer, to ensure full relaxation of each layer, a total height of ~ 25 μm is obtained. The averaged grading rate predicted by theory is then 0.016 μm^{-1}.

The experiments following this receipt has been performed by considering the resulting grading rate and performing an almost constant Ge content increase during the growth. In particular, a 0.015 μm^{-1} grading rate is considered, by means of 333 nm thick layers with a Ge content increase of 0.005 for each layer, which is the lower detectable increase in the Ge content of the growth apparatus. The structure obtained by this growth is shown in *Fig.* 4.7(a). Notice that the final crystal is significantly enlarged with respect to the Si pillar, with a final width of 5.5 μm. A Si buffer has been deposited on top of the Si pillar in order to provide an initial enlargement of the structure without strain and limit the spurious growth of Ge on the Si-pillar sidewalls. Our theoretical predictions on coherency, are dependent on the base. In order to proof the validity of the grading recipe, a larger crystal has been grown on 5×5 μm^2 Si pillars with 4 μm trenches (which are expected to be plastically relaxed). The resulting crystal, reaching a lateral size of 8 μm is shown in *Fig.* 4.7(b). The resulting quality of the structures has been evaluated by several experimental techniques. First, an etching procedure, similar to the ones adopted to evaluate dislocation reaching the top surface in *Fig.* 2.5(d), has been adopted. It makes clear the presence of dislocations forming etch-pits at the surface. As shown in the insets of *Fig.* 4.7(a), no indications of etch-pits are found on the lateral sizes of 5.5 μm Ge crystals while they are clearly present on the 8 μm wide crystals (see the insets of *Fig.* 4.7(b)). This is a strong indication of the absence of dislocation in the smaller crystals. Finding etch-pits on larger crystals allows us to be sure about the reliability of the experimental analysis by means of etching and also to confirm that, for larger crystals, the grading rate to be adopted to achieve full coherency should be lower. Second, TEM analysis has been performed. As shown in *Fig.* 4.7(c), no defect are actually found within the smaller structure (found to be present, instead, in the larger crystal [40]). According to these evidences, we can conclude that the receipt provided by the results of *Sect*. 3.3 can be used to design coherent structure by grading the Ge content. Moreover, the validity of the predictions is here verified at the micron scale.

Despite the achievement of this remarkable results, the semi-analytical $\bar{c}(B)$ expression has been directly determined by calculation for $B \leq 300$ nm (see *Sect*. 3.2). Therefore, an extrapolation beyond the simulated sizes has been exploited to provide the estimations discussed in this section. Moreover, an almost constant grading rate is here adopted. Larger sizes cannot be investigated by the quasi-3D approach as the proper meshing of the full 3D structure requires a computational effort beyond our possibilities. However, dedicated simulations, dealing with 2D calculations, can be performed in order to assess the reliability of our predictions.

4.4.2 Assessment by dedicated 2D simulations

In order to verify the theoretical predictions of coherency for micrometer-wide VHEs, and to further consolidate the experimental evidence, we perform 2D calculations based on the linear elasticity theory. In particular, we consider the formation energy of a dislocation as defined in Eq. (3.1). At variance with the modeling adopted before, we evaluate also the pure-elastic field (without the dislocation) in the central 2D section of the structure. This approach allows us

to inspect larger sizes, still providing an elastic field compatible with the complete crystal relaxation achieved for high aspect-ratio vertical structures when 3D calculations are considered [28].

An illustration of the geometry considered here is depicted in *Fig.* 4.7(d). A SiGe crystal made of 333 nm thick buffer layers is considered with a simple parallelepiped shape, by imposing a 0.5% increase of the Ge content per layer up to reach the composition of 40% Ge. The index i labels the interfaces between different layers. A 60° dislocation is considered for the calculation of the ΔG.

According to the experiments in *Fig.* 4.7(a), the lateral size of the Ge crystals grown on 2×2 μm^2 wide Si pillars ranges from $B_1 = 3.5$ μm at the bottom (close to the Si buffer) and $B_2 = 5.5$ μm at the top of the structure. Similarly, for the crystal grown on 5×5 μm^2 wide Si pillars, $B_1 = 6.5$ μm and $B_2 = 8$ μm are considered. For the evaluation of the elastic field, the geometry is modeled with a simple parallelepipedal shape. In particular, the geometries with both the minimum and the maximum width will be investigated as the behavior of the SiGe/Si system with the real crystal shapes is expected to lie in between.

In *Sect.* 3.4 we discussed the positioning of a 60° dislocation when minimizing the elastic energy. As far as it may vary along the interface, in particular when buffer layers with small aspect-ratio are considered, we calculate ΔG by explicitly sampling different dislocation positions. $\Delta G_{\min}$ is the minimum value for the formation energy obtained at a given interface. Let us focus on the first interface ($i = 1$). *Fig.* 4.8(a) shows $\Delta G_{\min}$ with $i = 1$ as function of the number of buffer layer (directly proportional to the total thickness during the Ge deposition). Notice that $N > 40$ has not been considered as the formation energy does not change for further material added on top. The main result of these simulations is that a positive $\Delta G_{\min}$ is observed for L in between 3.5 and 5.5 μm (light-blue area). For SiGe crystals grown on 5×5 μm^2 Si pillars with a size B ranging from 6.5 μm to 8 μm (red area), the $\Delta G_{\min}(N)$ values becomes negative for $N \geq 7$. So that when the deposition reaches a Ge content beyond 3.5%, the system should start to relax plastically. This perfectly agrees with the experimental evidences of *Fig.* 4.7.

So far we limited the calculations to the configuration of a dislocation at the first interface. However, other configurations may be present involving the nucleation of dislocations at interfaces with $i > 1$. In order to account for such possible configurations, the calculations described above are also repeated by considering different interfaces. The resulting $\Delta G_{\min}(i)$ is shown in *Fig.* 4.8(b) for both the structures in *Figs.* 4.7(a) and 4.7(b). Only the maximum sizes B_2 are here considered. It can be noticed that the real minimum is actually shifted to small i larger than 1. However, the variation in the formation energy values is very small. Moreover, we observe a strong increase of the formation energy for large i values pointing out that the favored configuration for the first dislocation is always close to the interface with the pure Si pillars. This behavior has been verified also evaluating $\Delta G_{\min}(i)$ as in *Fig.* 4.8(b) for structures with different N values, i.e. for structures with different thicknesses obtained during the growth. The result is shown by the additional curves in *Fig.* 4.8(c) and are found to have always a larger energy than the N=80 case, i.e. the final structure. This analysis assessed the results of *Fig.* 4.8(a) which can

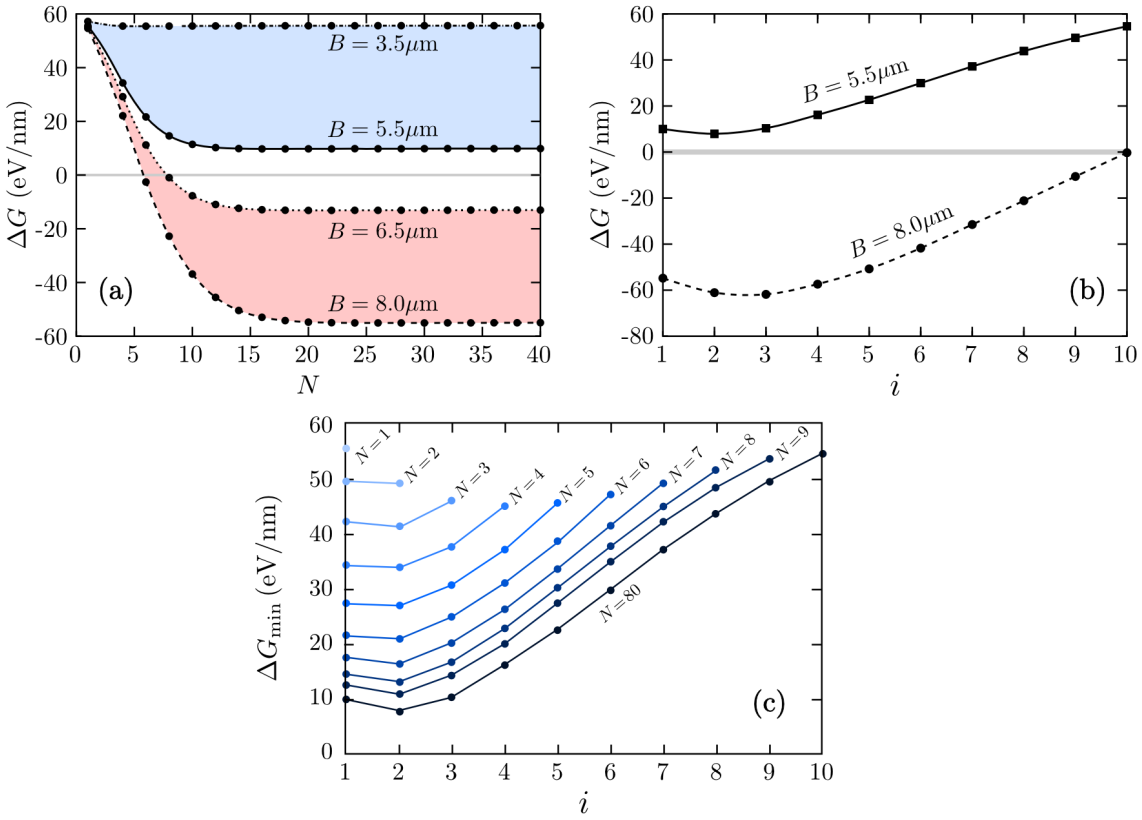

Figure 4.8: Results of 2D simulations. (a) $\Delta G_{\min}(N)$ at the $i = 1$ interface for the SiGe crystal with different values of B, corresponding to the minimum and the maximum size of crystals in *Fig.* 4.9. Light-blue and red regions correspond to the values compatible with the crystal grown on 2×2 μm^2 and 5×5 μm^2 wide Si pillars, respectively. (b) $\Delta G_{\min}(i)$ with $N = 80$ for the maximum lateral sizes for crystals grown on both the substrates. (c) $\Delta G_{\min}(i)$ for different N values.

be then considered as representative of the lower formation energy for a 60° dislocation within the SiGe crystals.

The main evidence of the reported calculation is that the tendency towards the plastic relaxation is significantly hindered when considering the graded SiGe crystal grown on 2×2 μm^2 with respect to the larger crystal. Despite simplified calculation have been performed, the comparison with the experiments, and the connection with the more accurate theory by means of Eq. (4.4), allows us to draw the conclusion that full coherency is here achieved and demonstrated. This is an unprecedented result showing the general possibility to obtain coherent VHEs significantly exceeding the nanometer length scale [40]. The results reported in this section can be considered as the main application of the theoretical concepts introduced in *Ch.* 3.

4.5 Thermal strain relaxation in multilayered VHE

One of the most important property of VHEs grown at the micron scale is the possibility to achieve full relaxation of the thermal stress, as widely discussed in Ref. [19]. However, the proof of this peculiar property has been provided only for what concerns a single-layer VHE. Multilayered VHEs have been also proposed in order to achieve the high-quality integration of GaAs on a small aspect-ratio Ge domain grown on Si pillars. In *Figs.* 4.9(a)-4.9(c) three

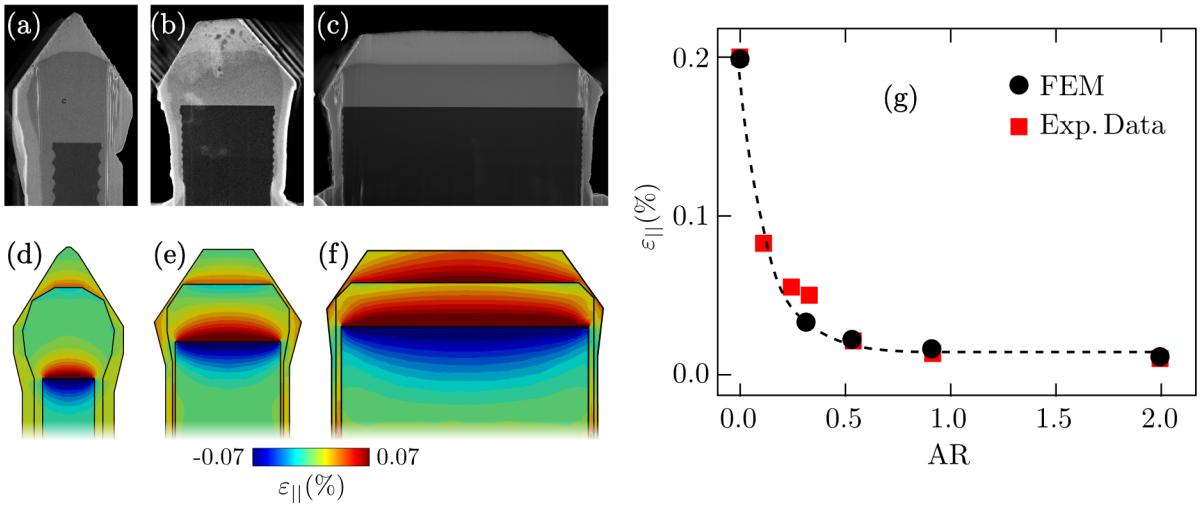

Figure 4.9: Relaxation of thermal strain in GaAs/Ge/Si VHEs [35]. (a)-(c) Cross-section SEM images of the multilayered structures grown on 2×2 μm^2, 5×5 μm^2 and 15×15 μm^2 Si pillars, respectively. (d)-(f) Cross-section of the structures in panels (a)-(c) showing the in plane strain as calculated by FEM simulations. (g) Averaged in-plane strain in GaAs obtained by both FEM simulations and X-rays diffraction experiments.

different GaAs/Ge/Si structures are reported. They were grown on 2×2 μm^2, 5×5 μm^2 and 15×15 μm^2 Si pillars, respectively. The substrates were fabricated with a miscut of 6° with respect to the (001) surface. 2 μm thick Ge layer was grown by LEPECVD at 500 °C while ∼ 3 μm of GaAs was deposited by MOVPE at 780 °C. Details of the growth technique can be found in Ref. [35]. Dislocations are widely present in these structures, as the critical thickness for their insertion in Ge layers consists of a few nanometers. The same applies to the GaAs/Ge interface. So that, during the growth, the structures are fully relaxed by both elastic and plastic relaxation. As described in *Sect.* 2.4, the cooling of the system leads to an accumulation of strain when differences in the thermal expansion coefficient are present. Here the three materials forming the heterostructures of *Figs.* 4.9(a)-4.9(c) exhibit these differences and thermal strain is measured in the structures. Notice that an accurate determination of the thermal strain from theoretical calculations should account for the motion of dislocations due to the rise of thermal stress (during the cooling) and also due to the eventual residual strain. Therefore, it may be a complex task, depending on the specific system.

In order to investigate the thermal strain relaxation in these multilayered structures, we directly consider the measured strain values on the unpatterned area of the sample, consisting of a GaAs/Ge/Si film. Indeed, this region follows the same growth process of the multilayer VHEs, thus accounting for a similar dislocation motion and residual heteroepitaxial strain. The values of the measured thermal strain, with respect to the Si substrate, are $\varepsilon_{||}^{\mathrm{GaAs}} = 0.19\%$ and $\varepsilon_{||}^{\mathrm{Ge}} = 0.14\%$. The mechanical equilibrium equation are solved by imposing an eigen-strain $\varepsilon_{ij}^{*} = -\varepsilon_{||}\delta_{ij}$ for all the materials, with free surfaces boundary conditions at the sidewalls and at top surfaces. In order to provide the best quantitative comparison with experiments, anisotropic elastic constants are selected from Ref. [155, 157]. The elastic fields provided by

3D FEM simulations reproducing the experimental morphologies are reported in the cross-sections of *Figs.* 4.9(d)-4.9(f). A significant relaxation is obtained with respect to the values of the unpatterned regions. Moreover, a compressive strain lobe is present in the Si along with a tensile strain both in Ge and GaAs. The elastic field distributions closely resemble the features of the elastic field in VHEs discussed for the relaxation of the heteroepitaxial strain (with opposite sign in agreement with the misfit considered in the calculation), i.e. the free surfaces significantly contribute to the relaxation and the residual strain is higher at the interfaces. In *Fig.* 4.9(g) the in-plane strain of the GaAs, averaged on its volume, is reported as obtained from FEM simulations and it is compared with the measured values by HRXRD. A good agreement between experiments and simulations is obtained, showing a decrease of the thermal strain by increasing the aspect-ratio of the structure with respect to the planar configuration (whose strain is shown for $AR = 0.0$). This allows us to conclude that the analysis reported in Ref. [19], concerning the thermal strain relaxation, is still valid when considering multilayered structures. From the experimental point of view, this was also confirmed by the presence of cracks in the unpatterned region, which are actually missing in these structures. Notice that this evidence about cracks can be also inferred by looking at the typical crack spacing obtained by the modeling provided in *Sect*. 3.5, with parameters reported in this section, which results larger than the lateral size of the structures.

5

Phase field modeling for the morphological evolution of crystals

When the micrometer-wide VHEs were introduced in Refs. [19, 20], a 2D continuum modeling was proposed to describe the growth mechanism. The peculiar growth conditions were identified as the key factor for the achievement of vertical growth. However, a full 3D modeling of the morphological evolution during the processing was out of the purposes of those works.

In order to go beyond the first preliminary models, a framework able to tackle 3D evolutions and the coupling of different physical phenomena has to be selected. To this purpose, we consider here the *phase-field approach* (PF) [29]. Indeed, it has been proven to easily manage the evolution of three-dimensional systems also when considering complex behavior such as the occurrence of topological changes. It also allows for an efficient coupling of different physical contributions, even when defined on different domains (e.g. bulk and surface properties). Moreover, it has already been applied to the modeling of physical phenomena typical of heterostructures such as surface diffusion [29], elastic strain relaxation [158], dewetting mechanisms [159] and intermixing [160].

In this chapter, we discuss the main developments of the PF modeling carried out to provide the three-dimensional morphological evolution of crystals. In particular, in order to describe the effects induced by high-temperature treatments of VHEs (as will be discussed in *Ch*. 6) we address the modeling of the surface diffusion within the PF framework as discussed in Ref. [29] also introducing a convenient description of surface energy density. This approach, combined with the strong anisotropy management proposed in Ref. [161], is proven to be effective in tackling the evolution by surface diffusion of three-dimensional, faceted morphologies [32]. Some extensions of the PF model dealing with the growth processes are also considered. Indeed, we report a Ray-Tracing Monte Carlo algorithm to compute the incoming material flux on the surface profile, accounting for flux shielding effects. Moreover, the possibility to describe faceted growth is reported [76].

The theoretical model developed with the aid of the PF framework can be considered of general interest as it involves properties common to several crystalline systems. It required a dedicated development of the simulation technique and it is presented here separated from its applications. The modeling reported in this chapter has been carried out in collaboration with Prof. A. Voigt and his research group at the *Technische Universität Dresden* (TU-Dresden).

5.1 Model description

The concept of phase-field (PF) has been mainly introduced in the scientific community within the standard phase-transition theory [162, 163]. A PF model consists of defining a framework where the equations are defined by means of an auxiliary analytic function φ, describing the phases of the system. Moreover, it can be used in the modeling of material properties to describe diffuse interfaces, i.e. the transition between phases within a region of arbitrary thickness ϵ (i.e. *the interface thickness*).

Two different approaches are usually followed in the definition of a PF model. A first approach consists of using φ to conveniently solve equations defined on complex boundaries, where the discretization of the domain is difficult and/or evolves in time, by following a diffuse domain approximation (DDA) [164]. Let us consider, for instance, a computational domain Ω and an equation defined on a domain $\Omega' \subset \Omega$

$$F(u) = g, \tag{5.1}$$

with generic boundary conditions defined on $\Sigma \equiv \partial\Omega'$. The idea of the DDA consists of extending the validity of Eq. (5.1) to Ω by exploiting a characteristic function χ_Ω, which is 1 in Ω' and 0 elsewhere. This is done by considering the weak formulation (see *Sect*. 1.6.1) and then multiplying each term by the characteristic function. The equation is then rewritten as

$$\tilde{F}(u, \chi_\Omega) + \text{BC} = g\chi_\Omega, \tag{5.2}$$

defined in Ω with BC a generic boundary condition (included in the weak form), evaluated thanks to a function δ_Σ defined by $\int_\Omega f\delta_\Sigma d\Omega = \int_\Sigma f d\Sigma$ (with f is a generic function). φ can then be introduced as a continuous definition of χ_Ω, having a smooth transition between $\varphi = 1$ and $\varphi = 0$ within a region of depth ϵ. This allows for the use of numerical approaches to solve the equations in Ω, chosen with a simple shape and boundary conditions, and implicitly describe conditions on Σ. Notice that each feature of the problem can be defined by means of φ. For instance, the δ_Σ can be approximated by $|\nabla\varphi|$. This approach results well-posed if, in the limit for $\epsilon \to 0$, i.e. for $\varphi \to \delta_\Sigma$, the solution of the equations defined on the diffused domain coincides to the original one (i.e. $\tilde{F} \to F$). This correspondence is usually evaluated by the method of Matched Asymptotic Expansions [164]. At variance with this diffused domain approach, the standard definition of the equation is referred to as the *sharp interface* case. For instance, the evolution laws reported in *Sects*. 1.4 and 1.5 represent the sharp interface limit for the evolution laws for φ reported in the following.

A second approach consists of using φ as an order parameter, and to determine the appropriate energy functional for the multiphase system. It includes the energy of bulk phases and the energy of the transition region between phases. Then, evolution laws are derived for φ. Also by following this kind of derivation, the geometrical properties of the phases and in particular of the interface between them can be derived directly from φ. Notice that, within this approach the limit of small interface thickness may be also taken into account, but, according to the specific energy functional, physics behavior can be also described far from this condition.

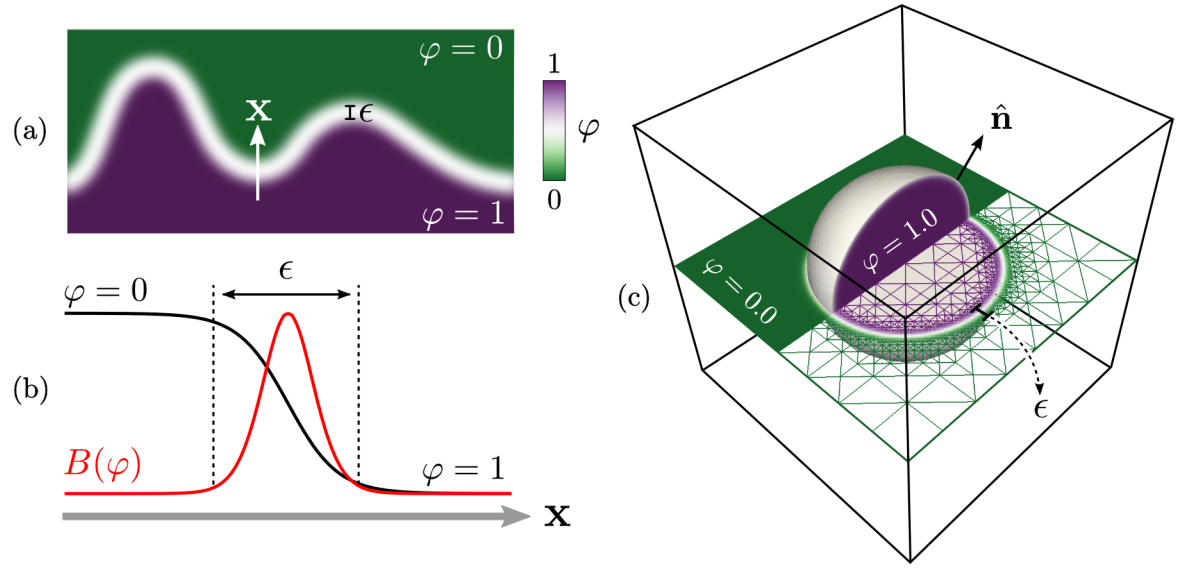

Figure 5.1: Phase-field modeling. (a) Generic 2D surface described by means of φ. (b) Plot of $\varphi(\mathbf{x})$ and $B(\varphi)$ (divided by the $B(0)$ value) along the white arrow in panel (a). (c) Perspective view of a cubic simulation domain embedding a sphere defined by means of φ. A slice of the simulation domain is also shown, revealing the refined mesh grid at the 0.5 isosurface of φ.

Of course, in order to describe a specific phenomenon, both the approaches should give the same results. Indeed, the evolution law for φ obtained as a modification of a sharp-interface equation, or derived from a reasonable guess of the energy functional should coincide.

In this work we consider a definition for φ such to describe the solid phase $\varphi = 1$ and the vacuum (or diluted vapor) phase $\varphi = 0$, with a smooth connection in between. In particular, a convenient choice for φ is [29]:

$$\varphi = \frac{1}{2}\left[1 - \tanh\left(\frac{3d(\mathbf{x})}{\epsilon}\right)\right], \tag{5.3}$$

where ϵ is the interface width and $d(\mathbf{r})$ is the signed distance from the (sharp) interface profile (nominally corresponding to the 0.5 iso-surface of φ), which consists of the surface of the solid phase. The geometrical properties of the surface are described by means of φ as, for instance, the outer-pointing surface normal $\hat{\mathbf{n}} = -\nabla\varphi/|\nabla\varphi|$. In *Fig.* 5.1(a) the definition of a generic 2D surface profile by means of φ is reported. The color map shows the values of φ. The line scan of $\varphi(\mathbf{x})$ along the white arrow is shown in *Fig.* 5.1(b). Notice that Eq. (5.3) allows for the definition of geometries with any dimension, provided that a proper signed distance is adopted. In *Fig.* 5.1(c) we show the definition of a sphere by means of φ, which represent the initial configuration of some of the simulations reported in the following.

The energy of the system described by the order parameter φ can be described by the Ginzburg-Landau functional [29, 162] accounting for the energy of the bulk phases and for the interface cost

$$G_s[\varphi] = \int_\Omega \gamma(\hat{\mathbf{n}})\left(\frac{\epsilon}{2}|\nabla\varphi|^2 + \frac{1}{\epsilon}B(\varphi)\right)dV. \tag{5.4}$$

$B(\varphi) = 18\varphi^2(1-\varphi)^2$ represents the bulk energy term in the form of a double well potential, promoting $\varphi = 0$ and $\varphi = 1$ values. This term tends to shrink the interface as much as possible.

Conversely, the term proportional to $|\nabla\varphi|^2$ quantifies the energy cost of having an interface and the thinner is the thickness the higher is the interface energy. The balance of these two contributions makes the interface with a finite thickness ϵ a stable condition for the system. Eq. (5.4) well represents the surface energy of (1.26) in the PF framework. By comparing this equation to surface energy in Eq. (1.26), the argument of the integral multiplying $\gamma(\hat{\mathbf{n}})$, i.e. $\big(\epsilon/2)|\nabla\varphi|^2 + 1/\epsilon B(\varphi)\big)\, d\mathbf{r}$, can be interpreted as an approximation of the infinitesimal surface element. $\gamma(\hat{\mathbf{n}})$ multiplies both terms to ensure constant interface thickness for any orientation when considering anisotropic surface energy density [161] (at variance with other approaches exhibiting an interface thickness dependent on $\gamma(\hat{\mathbf{n}})$ [165, 166]).

In order to evaluate the dynamics of the surface we have to describe how φ evolves in time. In particular, we focus on the surface diffusion evolution described by Eq. (1.35). The chemical potential μ can be expressed as the variational derivative of Eq. (5.4) with respect to φ [29] (as the phase-field variable can be actually interpreted as the density of the solid phase)

$$\mu = \mu_{\mathrm{s}} = \frac{\delta G_{\mathrm{s}}}{\delta\varphi} \approx -\epsilon\nabla\cdot\left[\gamma(\hat{\mathbf{n}})\nabla\varphi\right] + \frac{1}{\epsilon}\gamma(\hat{\mathbf{n}})B'(\varphi) - \epsilon\nabla\cdot\left[|\nabla\varphi|^2\nabla_{\nabla\varphi}\gamma(\hat{\mathbf{n}})\right], \tag{5.5}$$

where $\nabla_{\nabla\varphi}$ is the gradient along the direction of $\nabla\varphi$. The surface diffusion evolution then reads

$$\frac{\partial\varphi}{\partial t} = \nabla\cdot\left[M(\varphi)\nabla\mu\right], \tag{5.6}$$

with a mobility function set as $M(\varphi) = M_0(2/\epsilon)B(\varphi) = M_0(36/\epsilon)\varphi^2\left(1-\varphi\right)^2$ in order to restrict the diffusion at the surface. Indeed, as shown in *Fig.* 5.1(b), $B(\varphi)$ values are non-vanishing only within the interface region. M_0 sets the timescale of the evolution. It can be shown that the specific choice of φ reported in Eq. (5.3) corresponds to the stationary state (i.e. $\mu = 0$) for an interface between two phases with energy Eq. (5.4) in 1D.

Despite the model discussed so far has been widely used in the literature to describe surface diffusion by a means of a PF approach, it has been shown that it does not recover the correct sharp interface limit, i.e. Eq. (1.35), for $\varepsilon \to 0$, as discussed in Refs. [167–169]. However, a more proper modeling have been introduced by replacing μ with $g(\varphi)\mu$ where $g(\varphi) = 30\varphi^2(1-\varphi)^2$ [158] (see also the implementation in *Sect*. 5.1.1). No asymptotics analysis are shown here, but they can be found in the literature as for instance in Ref. [167]. Notice that the information about the surface profile has been explicitly considered only in the definition of $d(\mathbf{x})$ in Eq. (5.3), which consists of the initial condition for φ. Then, the surface is implicitly described and can be recovered as the 0.5 isosurface of φ. This allows for the description of complex evolutions, as the occurrence of dramatic topological changes, without caring about the explicit description of the geometry during the simulations.

With an isotropic surface energy, or in the weak anisotropy regime, the evolution described by Eqs. (5.5) and (5.6) is well-posed. If $\gamma(\mathbf{n})$ yields to a strong anisotropy condition, a regularization is required as discussed in *Sect*. 1.4. The so-called Willmore regularization [161] is considered in this work, by including in the energy functional a term F_{reg} which approximates the integral of the squared local curvature:

$$G_{\mathrm{reg}} = \frac{\beta}{2\epsilon}\int_\Omega \left(-\epsilon\nabla^2\varphi + \frac{1}{\epsilon}B'(\varphi)\right)^2 dV. \tag{5.7}$$

This regularization term corresponds to the corner rounding described in *Sect*. 1.3. It penalizes regions with high curvatures, thus leading to a local rounding where sharp corners are predicted in the Wulff shape. As in the sharp interface formulation, the extension of the rounded region can be controlled by the parameter β and the radius which quantifies the radius is proportional to $\sim \sqrt{\beta}$ [70]. When including such a regularization in the energy functional, an additional term in the chemical potential appear as $\delta G_{\mathrm{reg}}/\delta\varphi$ leading to

$$\mu = \mu_{\mathrm{s}} + \beta\left(-\nabla^2\kappa + \frac{1}{\epsilon^2}B''(\varphi)\kappa\right), \tag{5.8}$$

where μ_{s} is given by Eq. (5.5) and $\kappa = -\epsilon\nabla^2\varphi + \frac{1}{\epsilon}B'(\varphi)$ is the approximation of the curvature in the PF approach. Notice that, when including this regularization, a 6-th order PDE has to be solved. This can be easily inferred by considering that the κ expression corresponds to a second order term for φ, as $\kappa = \nabla\cdot\hat{\mathbf{n}} = \nabla\cdot(-\nabla\varphi/|\nabla\varphi|)$, and a term proportional to $\nabla^2(\nabla^2\kappa)$ will result in the explicit derivation of $\partial\varphi/\partial t$ (see *Sect*. 5.1.1 for further details on the implementation).

In order to extend the evolution law to the description of a growth dynamics, an additional term can be considered in Eq. (5.6) representing an external material flux which also accounts for the deposition mechanism. Following the discussion of *Sect*. 1.5, and describing the growth within the PF framework, such an additional term in $\partial\varphi/\partial t$ can be defined as

$$\frac{\partial\varphi}{\partial t} = \Phi\chi(\hat{\mathbf{n}})|\nabla\varphi|. \tag{5.9}$$

Φ is the material flux due to deposition, $\chi(\hat{\mathbf{n}})$ is the orientation-dependent incorporation rate, here considered equal to the expression introduced in Eq. (1.46), and $|\nabla\varphi|$ is included in order to restrict such an evolution to the interface also accounting for interface thickness. The full evolution law then results from the coupling between surface diffusion (5.6) and growth (5.9):

$$\frac{\partial\varphi}{\partial t} = \nabla\cdot[M(\varphi)\nabla\mu] + \Phi\chi(\hat{\mathbf{n}})|\nabla\varphi|. \tag{5.10}$$

Some refinements of the model, required to describe realistic systems, will be introduced in *Sects*. 5.2 and 5.4 in order to account for an arbitrary definition of the surface energy density and the modeling of possible flux shielding effects within the PF framework.

5.1.1 Integration scheme and computational details

The PDEs describing the evolution using the PF approach are quite demanding from a numerical point of view and accurate space and time discretization are required. In this work, we adopted the FEM toolbox AMDiS [31, 79], developed and maintained by the Axel Voigt's group (TU-Dresden). It consists of C++ libraries able to solve a broad class of PDEs by means of advanced computational approaches. The efficient implementation of an adaptive mesh is its main feature. Indeed, it allows for highly inhomogeneous spatial discretization in order to ensure enough accuracy where required, and save computational cost with coarse resolution elsewhere (see *Fig.* 5.1(c)). Moreover, other features make this toolbox very useful to achieve an efficient integration of PDEs, as standard or custom adaptive time step (i.e. non-uniform, optimized time discretization), as well as the possibility to use both direct and iterative solvers with optimized preconditioning. AMDiS outputs can be easily exported in different formats,

also compatible with advanced visualization tools such as ParaView [170]. In this work, the output of PF simulations is mostly reported just by exploiting such a software.

In order to integrate the evolution laws, we consider a system of three PDEs for $\partial\varphi/\partial t$, $g(\varphi)\mu$ and κ. In particular, the integration scheme adopted here is semi-implicit. By considering Eqs. (5.6), (5.8) and the expression for κ, at the n-th time step $\tau^{(n)}$, it consists of

$$\begin{bmatrix} \frac{1}{\tau^{(n)}} & \mathrm{A} & 0 \\ \mathrm{B} & g(\varphi^{(n-1)}) & \frac{\beta}{\epsilon}\mathrm{C} \\ \mathrm{C} & 0 & 1 \end{bmatrix} \begin{bmatrix} \varphi^{(n)} \\ \mu^{(n)} \\ \kappa^{(n)} \end{bmatrix} = \begin{bmatrix} \frac{\varphi^{(n-1)}}{\tau^{(n)}} + \mathrm{D} \\ \mathrm{E} \\ \mathrm{F} \end{bmatrix} \tag{5.11}$$

with

$$\begin{aligned}
\mathrm{A} =& -\nabla\cdot\left[M(\varphi^{(n-1)})\nabla\right], \\
\mathrm{B} =& \epsilon\nabla\cdot\left[\gamma(\hat{\mathbf{n}}^{(n-1)})\nabla\right] - \frac{1}{\epsilon}\gamma(\hat{\mathbf{n}}^{(n-1)})B''(\varphi^{(n-1)}), \\
\mathrm{C} =& \left[\epsilon\nabla^2 - \frac{1}{\epsilon}B''(\varphi^{(n-1)})\right], \\
\mathrm{D} =& \Phi\chi(\hat{\mathbf{n}}^{(n-1)})|\nabla\varphi^{(n-1)}| \\
\mathrm{E} =& -\nabla\cdot\left[\epsilon\left|\nabla\varphi^{(n-1)}\right|^2\nabla_{\nabla\varphi}\gamma(\hat{\mathbf{n}}^{(n-1)})\right] + \gamma(\hat{\mathbf{n}}^{(n-1)})\mathrm{F}, \\
\mathrm{F} =& \frac{1}{\epsilon}\left[B'(\varphi^{(n-1)}) - B''(\varphi^{(n-1)})\varphi^{(n-1)}\right].
\end{aligned}$$

Surface normal is defined by

$$\hat{\mathbf{n}}^{(n-1)} = -\frac{\nabla\varphi^{(n-1)}}{|\nabla\varphi^{(n-1)}|}. \tag{5.12}$$

The linearization in time of the double well potential derivative, i.e.

$$B'(\varphi^{(n)}) = B'(\varphi^{(n-1)}) + B''(\varphi^{(n-1)})(\varphi^{(n)} - \varphi^{(n-1)}), \tag{5.13}$$

is adopted as well as the asymptotic limit $\frac{1}{\epsilon}B(\varphi) \to \frac{\epsilon}{2}|\nabla\varphi|^2$ (first term in E).

When anisotropy is weak, the system (5.11) can be reduced to two equations by setting $\beta = 0$ and excluding the third equation for κ. Both sequential and parallel computations (up to 32 cores), with both iterative and direct solvers, were exploited in this work. When strong anisotropy is considered the reported PDE system (5.11) works well with direct solvers. In order to use iterative solvers an exchange of the first and the second rows of the system (i.e. exchange of the equation of $\partial\varphi/\partial t$ and $g(\varphi)\mu$) has been performed, in order to have some of the second order terms on the diagonal. Moreover, further optimizations can be implemented by considering specific stabilizing (from the numerical point of view) terms. For instance, a stabilization can be achieved by adding terms proportional to φ on both the right and the left-hand side of the equation, evaluated at the time $(n-1)$ and (n), respectively. They would lead to a vanishing effect for infinitesimal time-step. For finite time step, they would introduce a controllable error leading, however, to unconditionally stable integration. This would allow for a larger time step, still ensuring reliable simulation results. A more detailed discussion on such stabilizing terms can be found in Ref. [171].

The simulation domain is defined as shown in *Fig.* 5.1(c). A cubic (or parallelepiped) domain is considered with the definition of a surface by means of Eq. (5.3). In particular, *Fig.* 5.1(c) shows the definition of a sphere within a cubic domain, obtained by assuming $d(\mathbf{x}) = \mathbf{x} - R$, with R the radius of the sphere. Zero-flux Neumann BCs are set at all the domain boundaries (faces of the cubic box in *Fig.* 5.1(c)). For the sake of simplicity, the unit of length is dimensionless while the timescale is given in $1/(\gamma_0 D)$ units by setting γ_0 and D equal to 1. Conversely, specific units will be also adopted in *Ch.* 6 to facilitate the comparisons with experiments. This can be formally obtained by setting the proper M_0 coefficient, in order to match the desired time and length scale. The value of the parameters, as ϵ or β, as well as the sizes of the simulation domains are reported within the text along with the simulation results.

5.2 Surface energy density: a convenient form

In *Sect.* 1.3 we introduced the main concepts related to the Wulff shape and to faceted geometries, as resulting from the definition of an anisotropic surface energy density. In this section, we describe a general formulation for $\gamma(\hat{\mathbf{n}})$ function, in order to account for arbitrary faceted morphologies. Notice that the formulation here reported does not rely on the phase-field approach discussed in this chapter, but it provides a general approach that can be exploited within any other framework dealing with continuous surface energy definition. However, it is discussed here as it was developed to provide the description of arbitrary anisotropies within PF.

The main idea under the formulation presented here, is to quantify the difference between the local surface orientation $\hat{\mathbf{n}}$ and the vectors which give minima in the surface energy density ($\hat{\mathbf{m}}_i$) [172]. This is obtained by evaluating the scalar product $\hat{\mathbf{n}} \cdot \hat{\mathbf{m}}_i$ and providing a surface energy density parametrized as

$$\gamma(\hat{\mathbf{n}}) = \gamma_0 \left(1 - \sum_i^N \alpha_i \left(\hat{\mathbf{n}} \cdot \hat{\mathbf{m}}_i \right)^{w_i} \Theta \left(\hat{\mathbf{n}} \cdot \hat{\mathbf{m}}_i \right) \right), \tag{5.14}$$

where N is the total number of energy minima. α_i and w_i are positive coefficients. The former set the depth of the minima. The latter set the width of the minima, i.e. the range of the orientations $\hat{\mathbf{n}}$ around $\hat{\mathbf{m}}_i$ where $\gamma(\hat{\mathbf{n}})$ is lower than γ_0. Differentiability of Eq. (5.14) is ensured by $w_i \geq 2$. In order to control each facet independently, even when orientations are along the same direction (i.e. for $\pm\hat{\mathbf{m}}_i$ facets) the Heaviside step function Θ is introduced, excluding any energy contributions for negative value of $\hat{\mathbf{n}} \cdot \hat{\mathbf{m}}_i$. The behavior of Eq. (5.14) can be easily inferred by focusing on a single minimum along the $\hat{\mathbf{m}}$ direction. $\gamma(\hat{\mathbf{n}})$ results equal to $\gamma_0(1-\alpha)$ if $\hat{\mathbf{n}} \equiv \hat{\mathbf{m}}$, increasing up to γ_0 when the value of $\hat{\mathbf{n}} \cdot \hat{\mathbf{m}}_i$ decreases, i.e. when moving away from $\hat{\mathbf{m}}$. This definition for the surface energy density allows well-known expressions present in the literature to be recovered as special cases. In particular, cubic symmetry resulting from $\gamma(\hat{\mathbf{n}}) = \gamma_0 \left[1 + \tilde{\alpha} \left(n_x^4 + n_y^4 + n_z^4 \right) \right]$ [62, 161] can be obtained directly from Eq. (5.14) by imposing six different minima along the orthogonal axes $\hat{\mathbf{m}}_{1,2}$=[$\pm$100], $\hat{\mathbf{m}}_{3,4} = [0 \pm 10]$, $\hat{\mathbf{m}}_{5,6} = [00 \pm 1]$, with $w_i = 4$ and constant α_i for each minimum.

An illustration of how Eq. (5.14) behaves is shown in *Fig.* 5.2. In particular, *Figs.* 5.2(a)-5.2(c) report bidimensional surface energy density functions $\gamma(\theta)$, where $\theta = -\arctan(n_y/n_x)$ is the angle between the normal vector and the $[10]$ direction. The specific case with minima

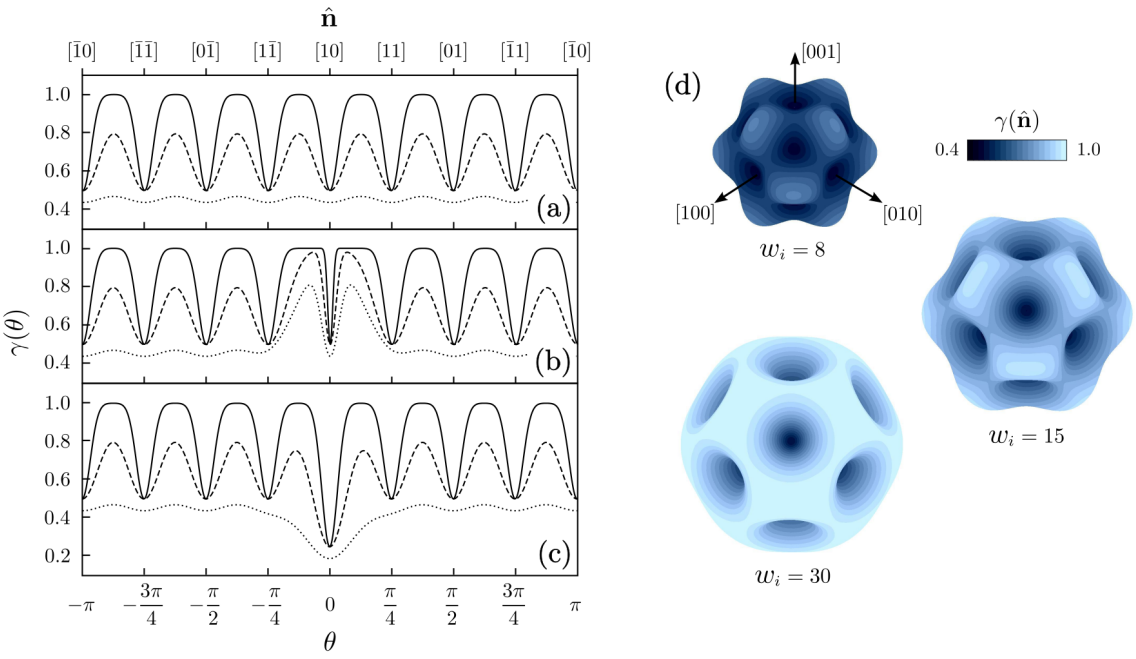

Figure 5.2: Surface energy densities from Eq. (5.14). (a)-(c) 2D $\gamma(\theta)$ function with minima at $\theta_i^* = i\pi/4$, corresponding to $\langle 10\rangle$ and $\langle 11\rangle$ directions, with $\alpha_i = 0.5$ and $\gamma_0 = 1$. (a) $w_i = 8$ (dotted line), $w_i = 20$ (dashed line) and $w_i = 100$ (solid line). (b) $\gamma(\theta)$ with the same parameters of panel (a) and w_0 increased by a factor 10. (c) $\gamma(\theta)$ with the same parameters of panel (a) and $\alpha_0 = 0.75$. (d) 3D $\gamma(\hat{\mathbf{n}})$-plot with minima along $\langle 100\rangle$ and $\langle 111\rangle$ directions, $\alpha_i = 0.5$ and $\gamma_0 = 1$. Three w_i values are selected. $\gamma(\hat{\mathbf{n}})$ values are also plotted as color map.

at $\theta_i^* = i\pi/4$ with $i \in \mathbb{Z}$ (i.e. $\langle 10\rangle$ and $\langle 11\rangle$ directions) is considered. In *Fig.* 5.2(a), three curves with different w_i and same α_i values for each minimum are shown. First, it can be noticed that the real width of minima is inversely proportional to w_i. Moreover, for small values of such a parameter (see $w_i = 8$ curve) the single minima are not well-resolved and significant superposition of the contribution in the summation of Eq. (5.14) is recognized, for all the orientations. This condition leads also to $\gamma(\theta_i^*)$ values lower than $\gamma_0(1-\alpha_i)$ at $\mathbf{m}_i$. By increasing w_i (see the $w_i = 20$ curve), no effective superposition takes place at $\theta = \theta_i^*$ but it is still present for orientations in between. For large enough w_i (see the $w_i = 100$ curve), a full decoupling of the energy minima is achieved and orientations with $\gamma(\theta) = \gamma_0$ appear. This would be the best condition when the full control of minima is required, leading in turn to the full control of the energy of single facets. In order to provide such a control on a specific minimum, other features of Eq. (5.14) can be exploited. This is illustrated in *Fig.* 5.2(b), where the same curves as in *Fig.* 5.2(b) are shown with a value of w_0 (width parameter for the θ_0^* minimum) increased by a factor 10. Furthermore, the energy of a specific minimum can be tuned independently by setting a different α_i value. This is shown in *Fig.* 5.2(c) at $\theta = \theta_0^*$ where lower surface energy is achieved by setting an higher α_i value. Similar arguments can be considered for three-dimensional $\gamma(\hat{\mathbf{n}})$ functions. In this case, the tuning of parameters in order to achieve independent minima definition can be even more complex, but the qualitative discussion reported for the 2D case still holds true. In *Fig.* 5.2(d), the 3D $\gamma(\hat{\mathbf{n}})$-plots are shown for a $\gamma(\hat{\mathbf{n}})$ with

minima along $\langle 100 \rangle$ and $\langle 111 \rangle$ directions. Parameters consists of $w_i = 8$, $w_i = 15$ and $w_i = 30$ for the three different plots, respectively, with $\alpha_i = 0.5$. The color map, showing $\gamma(\hat{\mathbf{n}})$ values, highlights the superposition and the decoupling effects observed by increasing the value of w_i.

5.2.1 Anisotropy regime assessment

The $\gamma(\hat{\mathbf{n}})$ definition of Eq. (5.14) allows for a full customization of the surface energy density. According to its parameters, strong anisotropy condition can be achieved, thus requiring a suitable regularization as reported in Eq. (5.7). Notice that being able to know what is the anisotropy regime before performing simulations, i.e. once surface energy parameters are set, allows one to include the regularization, and the related computationally demanding PDEs, only when strictly necessary. Exploiting the criterion introduced in Ref. [62] and illustrated in *Sect*. 1.3 we can determine a priori the anisotropy regime, provided that derivatives of $\gamma(\hat{\mathbf{n}})$ with respect to $\hat{\mathbf{n}}$ components are known. Such derivatives, calculated for Eq. (5.14) are:

$$
\begin{aligned}
\frac{\partial \gamma}{\partial n_x} &= -\gamma_0 \sum_i^N \alpha_i w_i p_i^{w_i - 1} \left(m_{x,i} - m_{z,i} \frac{n_x}{n_z} \right) \\
\frac{\partial \gamma}{\partial n_y} &= -\gamma_0 \sum_i^N \alpha_i w_i p_i^{w_i - 1} \left(m_{y,i} - m_{z,i} \frac{n_y}{n_z} \right) \\
\frac{\partial^2 \gamma}{\partial n_x^2} &= -\gamma_0 \sum_i^N \alpha_i w_i \left[(w_i - 1) p^{w_i - 2} \left(m_{x,i} - m_{z,i} \frac{n_x}{n_z} \right)^2 - p^{w_i - 1} m_{z,i} \frac{n_x^2 + n_z^2}{n_z^3} \right] \\
\frac{\partial^2 \gamma}{\partial n_y^2} &= -\gamma_0 \sum_i^N \alpha_i w_i \left[(w_i - 1) p^{w_i - 2} \left(m_{y,i} - m_{z,i} \frac{n_y}{n_z} \right)^2 - p^{w_i - 1} m_{z,i} \frac{n_y^2 + n_z^2}{n_z^3} \right] \\
\frac{\partial^2 \gamma}{\partial n_x \partial n_y} &= -\gamma_0 \sum_i^N \alpha_i w_i \left[(w_i - 1) p^{w_i - 2} \left(m_{x,i} - m_{z,i} \frac{n_x}{n_z} \right) \cdot \left(m_{y,i} - m_{z,i} \frac{n_y}{n_z} \right) - p^{w_i - 1} m_{z,i} \frac{n_x n_y}{n_z^3} \right]
\end{aligned}
$$

where $p_i = p\left(\hat{\mathbf{n}}, \hat{\mathbf{m}}_i\right) = \left(\hat{\mathbf{n}} \cdot \hat{\mathbf{m}}_i\right) \Theta\left(\hat{\mathbf{n}} \cdot \hat{\mathbf{m}}_i\right)$. The product $K_1 K_2$ can then be calculated by a numerical evaluation of Eq. (1.28). The critical coefficient $\bar{\alpha}$, as a function of w, has been calculated for a single (arbitrary) minimum direction and it is shown in *Fig*. 5.3. Such a behavior is well reproduced by

$$
\bar{\alpha}(w) = \frac{a_1}{w} + \frac{a_2}{w^2} \tag{5.15}
$$

where $a_1 = 2.26 \pm 0.2\%$ and $a_2 = -2.48 \pm 0.4\%$ deliver the best fit. When the contributions arising from different minima are decoupled, i.e. no significant superposition effects are present for a given set of w_i values, the anisotropy regime can be directly evaluated by comparing the α_i values with the data in *Fig*. 5.3 or with Eq. (5.15). On the other hand, if the superposition of minima is present for some orientations, the explicit numerical evaluation of Eq. (1.28) is required in order to determine the anisotropy regime and the critical parameter $\bar{\alpha}$.

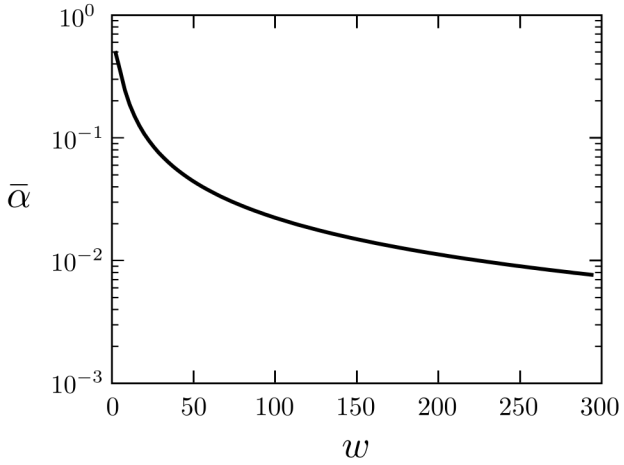

Figure 5.3: $\bar{\alpha}$ values as function of w for the $\gamma(\hat{\mathbf{n}})$ defined by Eq. (5.14) with a single minimum orientation.

5.3 Simulations of surface diffusion

In this section, we simulate surface diffusion evolution as resulting from the phase-field approach described in *Sect*. 5.1. First, the isotropic evolution is shown, crucial for the assessment of the model. Second, weak and strong anisotropy regime are considered exploiting the choice of $\gamma(\hat{\mathbf{n}})$ introduced in *Sect*. 5.2.

5.3.1 Isotropic surface diffusion and model assessment

In order to show the evolution by the PF model of surface diffusion, let us consider a simple 2D domain. In particular, we consider the definition of a surface profile as a cosine function

$$f(x) = h_0 \cos(qx). \tag{5.16}$$

The description of this profile with $h_0 = 0.3$ by means of φ is shown in the first panel ($t = 0.0$) of *Fig*. 5.4(a). Such a profile is obtained by imposing an initial guess for $d(\mathbf{x})$ of *Eq*. (5.3) corresponding to $y - f(x)$ and then calculating the actual signed distance by a numerical routine. The evolution by surface diffusion with isotropic surface energy density is considered by imposing $\gamma(\hat{\mathbf{n}}) = \gamma_0 = 1$ in Eq. (5.4), and it is reported in *Fig*. 5.4(a). Periodic boundary conditions along the $\hat{\mathbf{x}}$ direction are considered. The size of the simulation cells is $1{\times}1$ with $\epsilon = 0.05$. In order to understand the outcome of this simulation, in *Fig*. 5.4(b) the same evolution is reported showing the chemical potential μ within the interface. Notice that only variation of μ within the surface play a role in the surface diffusion as the mobility is restricted to the surface by means of the $M(\varphi)$ function. A constant value is obtained in the normal-to-the-surface direction within the interface, ensured by the choice of φ in Eq. (5.3). Conversely, a distribution of μ is observed along the surface profile, with maxima at the two peaks, and a minimum at the central valley. This produces a material flux from the peaks toward the valley leading to the evolution of *Fig*. 5.4(a), which, in turn, progressively lower differences of μ. The stationary state, i.e. the final stage of the evolution is reached for the flat surface ($t = 10$) showing a homogeneous chemical potential. The volume of the solid phase is conserved, with a numerical error lower than 0.1%. Moreover, the minimization of the surface energy, corresponding here to the surface length, is achieved.

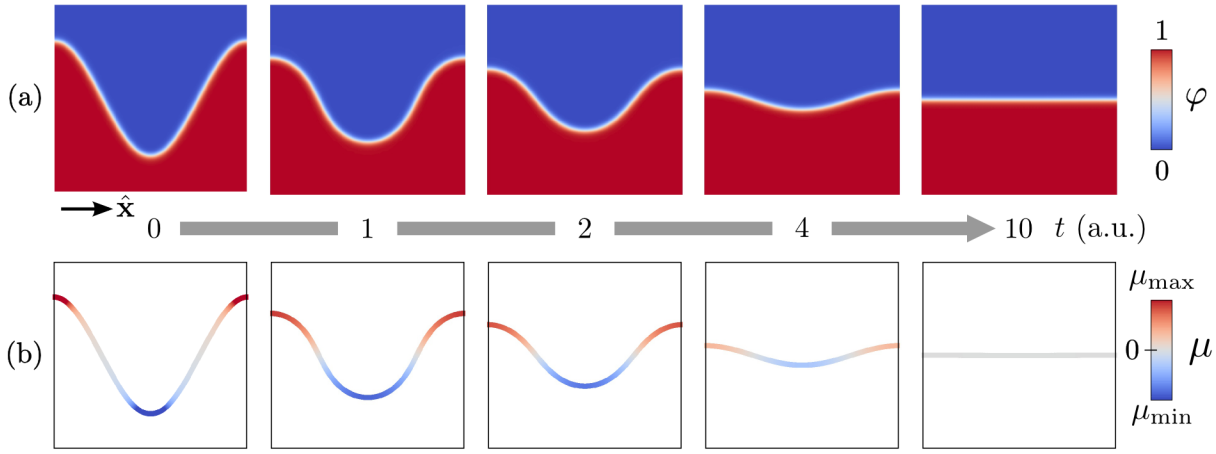

Figure 5.4: Evolution of a cosine profile by PF simulation of surface diffusion. (a) Evolution of the initial profile ($t = 0$) towards the stationary state, i.e. a flat profile ($t = 10$). The color map shows the φ values. (b) Same evolution as in panel (a) showing the chemical potential μ at the surface.

In order to test the reliability of the dynamics described by the PF approach, let us consider a well known analytic solution for the evolution of a cosine perturbation. In the approximation of small amplitudes for Eq. (5.16) the curvature $\kappa \approx f''(x)$ is

$$\kappa = -h_0 q^2 \cos(qx). \tag{5.17}$$

Then, by considering the surface diffusion equation, i.e. Eq. (1.35), in the limit of small amplitudes, we have

$$\frac{\partial f}{\partial t} = \gamma_0 \nabla^2 \kappa \approx \gamma_0 \frac{d^2 \kappa}{dx^2} = -\gamma_0 h_0 q^4 \cos(qx) = -\gamma_0 q^4 f(x). \tag{5.18}$$

So that

$$f(x,t) = h_0 \cos(qx) \exp(-\gamma_0 q^4 t) = f(x) \exp(-\gamma_0 q^4 t). \tag{5.19}$$

Therefore, we obtained an equation that describes the evolution of f, which consists of a decay of the amplitude of the initial cosine profile. A representative quantity to describe the evolution of the perturbation is the length of surface $L = \int_a^b \sqrt{1 + [g'(x)]^2} dx$ with g a generic function. Its explicit expression for the $f(x,t)$ in Eq. (5.19) is

$$L(t) = \int_{x_1}^{x_2} \sqrt{1 + [q h_0 \exp(-\gamma_0 q^4 t) \sin(qx)]^2} dx, \tag{5.20}$$

with x_1 and x_2 the limit of x values. In *Fig.* 5.5, a comparison between Eq. (5.20), PF simulations of surface diffusion as in *Fig.* 5.4(a) with $h_0 = 0.05$ and an explicit integration of Eq. (1.35) (i.e. the sharp interface limit of Eq. (5.6)) by a finite difference approach, are shown. Notice that a good agreement is obtained between the two numerical approaches and the analytic function for $L(t)$. So that, the PF model allows for a reliable description of surface diffusion. Moreover, the values used for ϵ allows to numerically recover the sharp interface limit for such a phenomenon. The comparison to the analytic solution cannot be extended to larger values of h_0 as the small-amplitude approximation adopted in Eq. (5.20) would fail. So that the evolution in time of the profile cannot be described by a simple analytic function. Moreover, the numerical

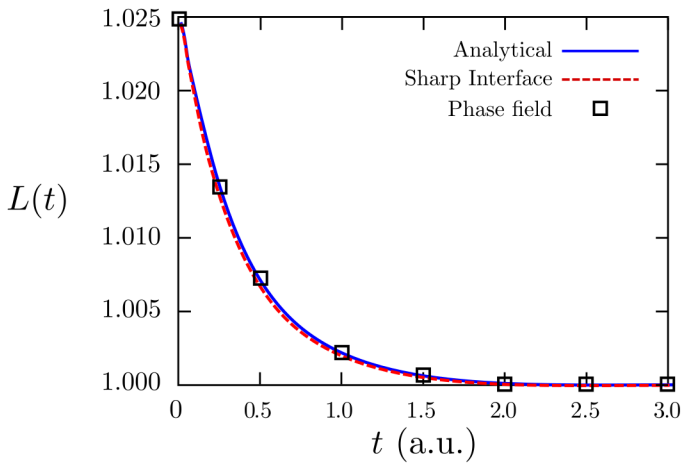

Figure 5.5: Comparison of the surface length decrease during the evolution by surface diffusion of a cosine with a small amplitude, with three different approaches: analytic function from Eq. (5.20) (solid blue line), finite difference simulation for the sharp interface approach (dashed red line), phase-field simulation (black squares).

integration by finite difference approach of the sharp-interface equations can be straightforwardly used for simple evolution in 2D only. PF models, indeed, were considered to overcome the issues of the explicit tracking of the surface in 3D. However, the model considered here is known to converge to the right sharp-interface behavior for small ϵ [167]. Moreover, a numerical check can be always performed by considering smaller and smaller ϵ until reaching convergence of different simulations to the same behavior. For the simulation reported in *Fig.* 5.4 we verified that for $\epsilon < 0.1$ no changes in the evolution are observed. For all the simulations carried out with the PF approach reported here (and also for the ones illustrated in the following and in *Ch.* 6), such a convergence condition with respect to the choice of ϵ has to be checked.

As mentioned in *Sect.* 5.1, the PF approach easily allows for the definition of 3D profiles. In order to provide an example involving a three-dimensional geometry, we consider the evolution by surface diffusion of an ellipsoidal shape with isotropic surface energy. Such an initial profile is shown in *Fig.* 5.6 by means of the 0.5 isosurface of φ, along with the color map showing the chemical potential at the surface (as in the simulations reported in *Fig.* 5.4(b)). Hereafter the reported surface profiles always correspond to the 0.5 iso-surface of $\varphi(\mathbf{x})$. Notice that μ values on the surface correspond to κ when isotropic surface energy is considered with $\gamma(\hat{\mathbf{n}}) = 1$. This initial configuration shows different μ values on the profile so that the evolution by surface diffusion is expected, as obtained by the PF simulation reported in *Fig.* 5.6. In contrast to the evolution reported in *Fig.* 5.4, this profile consists of a closed surface. This would produce a different stationary state that corresponds to a sphere, at variance with the flat profile obtained with an infinitely extended surface perturbation, described by means of periodic boundary conditions for the profile of *Fig.* 5.4.

According to the choice of the initial profile, surface diffusion mechanism can lead to complex evolution, even involving topological changes [29]. This mechanism is observed in experiments as for instance for solid-state dewetting phenomena [173–176] where separation in a

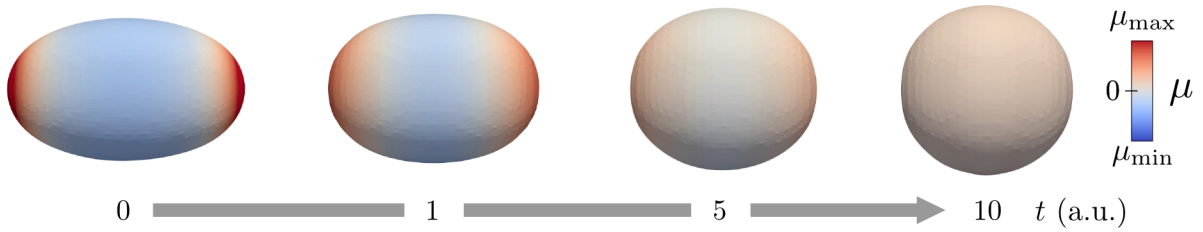

Figure 5.6: Evolution by surface diffusion of an ellipsoidal shape. Color map shows μ values at the surface. It corresponds to κ as isotropic surface energy is adopted with $\gamma(\hat{\mathbf{n}}) = 1$.

few subunits occurs, leading to a local energy minimum. An illustrative evolution by surface diffusion of a parallelepiped with an height-to-base aspect ratio of 10 is reported in *Fig*. 5.7. Two separated subunits are obtained, both showing a spherical shape. Notice that the evolution towards the global equilibrium configuration, corresponding to a single sphere with the same volume of the initial parallelepiped with isotropic surface energy, is here prevented by the kinetic pathway towards the equilibrium.

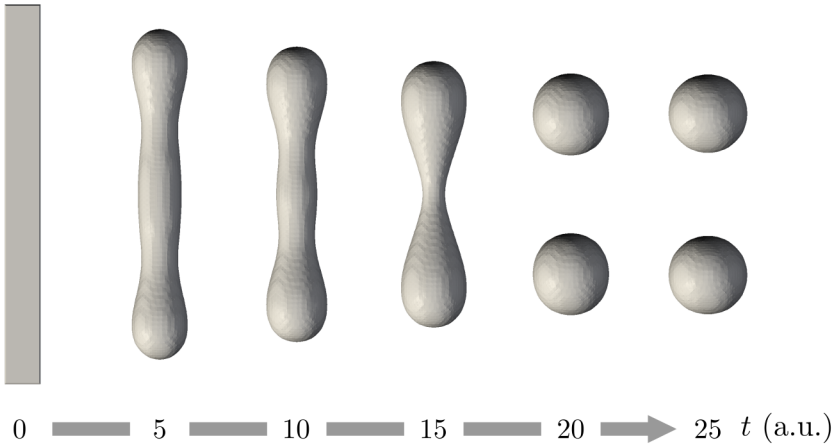

Figure 5.7: Surface diffusion evolution of a parallelepiped shape with isotropic $\gamma(\hat{\mathbf{n}})$ leading to two separated subunits.

5.3.2 Evolution toward faceted equilibrium crystal shapes

So far we considered only an isotropic surface energy. By exploiting the formulation for $\gamma(\hat{\mathbf{n}})$ introduced in *Sect*. 5.2, we can deal with surface diffusion also for faceted geometries, which is key when considering morphologies of real crystals (as will be also shown in *Ch*. 6).

In this section, we investigate morphologies produced by setting different surface-energy definitions and by tuning the parameters of the Eq. (5.14). In particular, we consider the description of the evolution from an initial simple geometry, i.e. a sphere, towards the corresponding ECS. Let us consider a sphere with a diameter of 0.6 as in *Fig*. 5.1(c) and $\epsilon = 0.04$. First, we focus on a $\gamma(\hat{\mathbf{n}})$ function set in order to describe a tetrahedral ECS, i.e. $\hat{\mathbf{m}}_i$ are set to: $[\bar{1}\bar{1}1]$,$[\bar{1}1\bar{1}]$,$[1\bar{1}\bar{1}]$ and $[111]$. The other parameters are $\alpha_i = 1.0$, $w_i = 6$. As far as these parameters lead to strong anisotropy, according to the criterion in *Sect*. 5.2.1, the Willmore regularization is

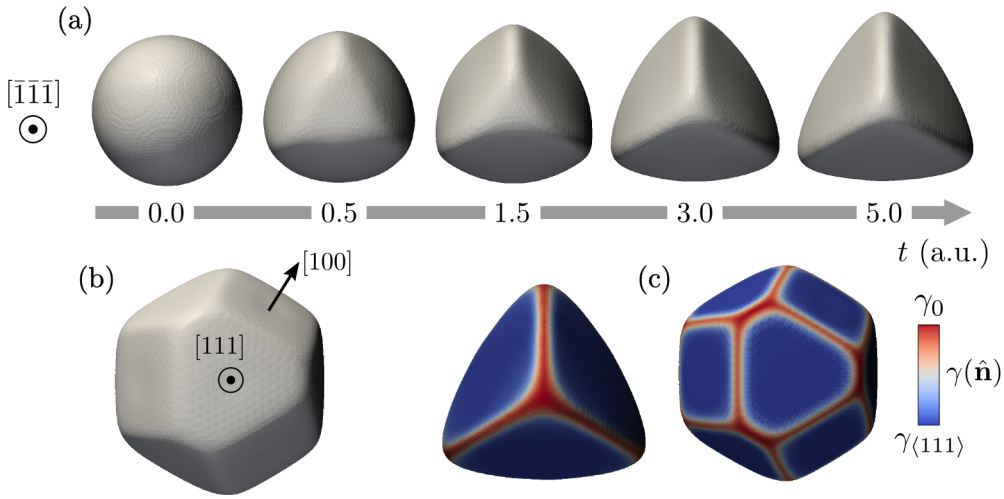

Figure 5.8: PF simulations of surface diffusion evolution toward the ECS. (a) Evolution of a sphere toward a tetrahedron by imposing minima of $\gamma(\hat{\mathbf{n}})$ along $[\bar{1}\bar{1}1]$,$[\bar{1}1\bar{1}]$,$[1\bar{1}\bar{1}]$ and $[111]$ directions with $\alpha_i = 1.0$, $w_i = 6$, $\beta = 0.002$. (b) ECS simulated by considering the evolution of a sphere with minima of $\gamma(\hat{\mathbf{n}})$ along $\langle 100\rangle$ and $\langle 111\rangle$ directions with $\alpha_i = 0.3$, $w_i = 20$ and $\beta = 0.001$. (c) $\gamma(\hat{\mathbf{n}})$ plot as color map at the surfaces of the ECSs shown in panels (a) and (b).

adopted with $\beta = 0.002$. The resulting evolution by surface diffusion is reported in *Fig.* 5.8(a). Notice that facets are gradually formed from the initial spherical profile leading to the expected ECS, as resulting from the dynamics driven by $\nabla\mu$. Another result obtained by considering a different definition of $\gamma(\hat{\mathbf{n}})$ is shown in *Fig.* 5.8(b). Here, two different families of minimum directions are set along $\langle 100\rangle$ and $\langle 111\rangle$. In *Fig.* 5.8(c), we report the surface energy density map at the surface of the ECSs shown in *Figs.* 5.8(a) and 5.8(b). Notice that an almost constant value (blue region) is obtained where the orientation is almost constant, i.e. where facets form. Smooth fittings between facets, showing high $\gamma(\hat{\mathbf{n}})$ values (with red colors), are also present. These correspond to the region where corner regularization of *Eq.* (5.7) is active.

Once the minimum directions are set, it is also possible to inspect the features of the final ECS according to changes of the other parameters in Eq. (5.14). In *Fig.* 5.9(a) different morphologies are obtained with different values for α_i, set to have the same value for each minimum direction. The first two cases show the morphology in the weak anisotropy regime, still exhibiting preferential orientation connected by large rounded regions. By increasing α_i the strength of the anisotropy is higher and higher, thus requiring the corner regularization. For the choice of $\gamma(\hat{\mathbf{n}})$ considered here, the strong anisotropy condition is reached for $\alpha \gtrsim 0.06$. The last two morphologies of *Fig.* 5.9(a) correspond to this condition, obtained with two different values of α_i and $\beta = 0.001$. The morphology of the ECS can be also modified by means of the β coefficient as it controls the extension of the corner rounding. This concept is shown in *Fig.* 5.9(b), where shapes with different values of the β parameter are reported, showing different extensions of the rounded regions at the corners, with $\alpha = 0.3$. In agreement with the work discussed in Refs. [70, 161] such an extension of the rounding results proportional to $\sqrt{\beta}$.

As shown in *Sect.* 1.3, in order to obtain sharp facets, the strong anisotropy regime should be explored. Moreover, the β factor should be lowered as much as possible to do not affect

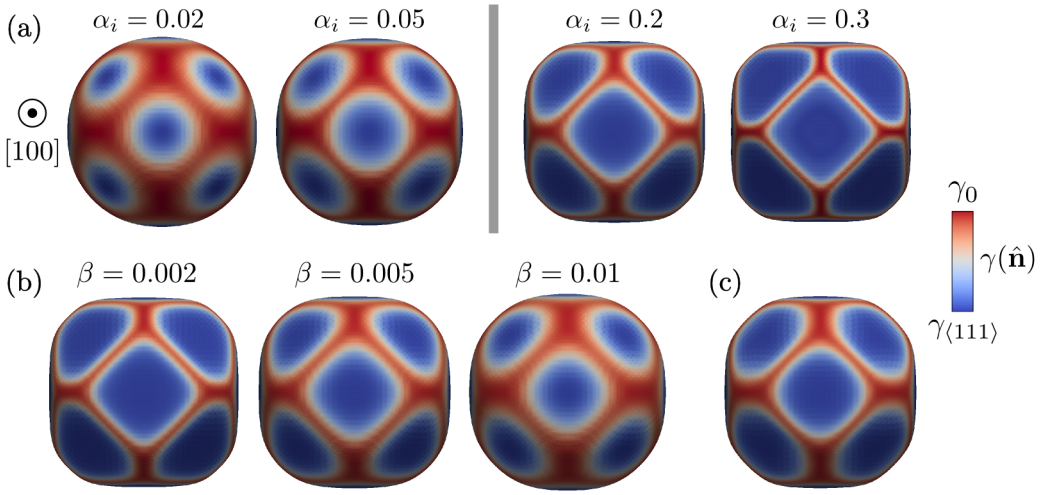

Figure 5.9: Features of the ECS by varying (a) α_i, reproducing the weak (left) and the strong (right) anisotropy regime, (b) β values, (c) the radius of the initial sphere, here considered doubled with respect to the one in panel (b) with $\beta = 0.01$. $\mathbf{m}_i$ directions are set as in *Fig.* 5.8(b).

the global shape with the corner rounding. An inferior limit is inherently present due to the use of a numerical approach. Indeed, the lowest values that can be used for β depends on the resolution adopted in the numerical method, i.e. it is affected by the interface width and by the spatial discretization used in the FEM. A trade-off is then required between the description of sharply faceted geometries and the computational cost. However, notice that at variance with the choice of parameters in $\gamma(\hat{\mathbf{n}})$, whose contributions are self-similar when scaling the crystal volume, the regularization controlled by β is set on an absolute length scale and does not depend on facet extensions [161]. In *Fig.* 5.9(c) we prove this concept showing the ECS obtained with the same parameters of *Fig.* 5.9(b) with $\beta = 0.01$, but with a doubled volume. The extension of the rounded regions at the corners is the same as with the smaller volume, but its relative size compared to the global shape is reduced. As a result, sharper facets are obtained.

The PF approach including our choice of $\gamma(\hat{\mathbf{n}})$ allows for the description of a wide variety of faceted geometries by tuning the different parameters as previously discussed. Moreover, the resulting definition of the surface energy does not include any symmetry, so that it can be exploited to provide arbitrary shapes. Some examples of what can be obtained by playing with parameters and minimum directions are illustrated in *Fig.* 5.10. In particular, in *Fig.* 5.10(a) the effect of setting different α_i values for different minima is reported. Parameters are set as in *Fig.* 5.8(b) but α_i for minima along $\langle 111 \rangle$ directions is lowered by a factor 2. The resulting ECS shows larger $\{100\}$ facets. Asymmetric ECS can also be obtained as in *Figs.* 5.9(b) and 5.9(c). The choices of the $\gamma(\hat{\mathbf{n}})$ reported here have been driven by some experimental shapes recognized in the literature (see e.g. Refs. [177–179]) and similar ECS are actually obtained.

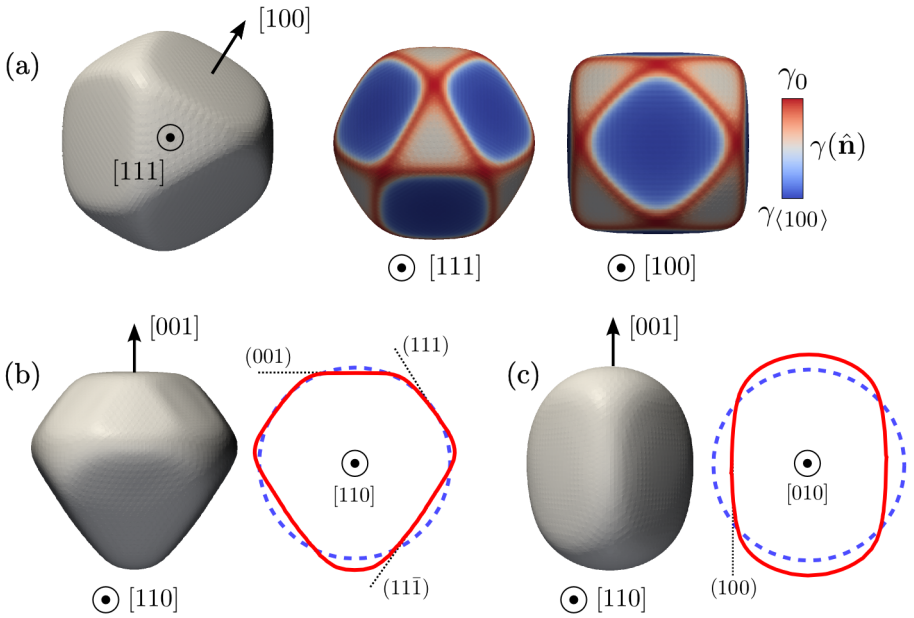

Figure 5.10: Arbitrary shapes by tuning $\gamma(\hat{\mathbf{n}})$. (a) Minima of $\gamma(\hat{\mathbf{n}})$ as in *Fig.* 5.8(b) with α_i halved for $\langle 111\rangle$ directions. A perpective 3D view is shown along with $\gamma(\hat{\mathbf{n}})$ color maps for two shape orientations. Panels (b) and (c) show asymmetric ECSs. Perspective 3D views and the central cross-sections compared to the initial spherical profile are shown. The parameters chosen for such shapes are: (b) $[001]$, $[\pm 1 \pm 11]$, $[\pm 101]$, $[0 \pm 11]$ minima directions with $\alpha_i = 0.2$ and $w_i = 60$, $[\pm 1 \pm 1\bar{1}]$ minima directions with $\alpha_i = 0.4$ and $w_i = 30$, $\beta = 0.002$; (c) minima along $[\pm 100]$ and $[0 \pm 10]$ with $\alpha_i = 0.4$, $w_i = 10$, $\beta = 0.002$.

5.3.3 Reproducing a realistic anisotropy: the case of Ge

When considering anisotropic $\gamma(\hat{\mathbf{n}})$, a discrete set of γ values is typically available in literature (from experiments of atomistic calculations), corresponding to the energies of preferential orientations. The expected ECS can be constructed by means of such values as a convex hull of only the planes corresponding to the preferential orientations, accounting for the $\gamma(\hat{\mathbf{n}})$ values in agreement with the Wulff construction [57]. Let us focus on the surface energy anisotropy of Ge crystals, which will be explicitly used in *Ch.* 6. The shape obtained by considering the main families of facets for Ge, i.e. $\{100\}$, $\{113\}$, $\{111\}$ and $\{110\}$, is reported *Fig.* 5.11(a). This shape is computed by means of Wulffmaker [180] with the surface energy values reported in Ref. [181].

In order to integrate the evolution law for φ as introduced in *Sect.* 5.1, a continuous $\gamma(\hat{\mathbf{n}})$ showing values for each orientation is required. This can be achieved by tuning the parameters of Eq. (5.14). In particular, we select $\hat{\mathbf{m}}_i$ and α_i in order to match the orientations of the minima and the surface energy values for Ge crystals reported in Ref. [181]. As done for the shape in *Fig.* 5.11(a), we consider only the main preferential orientations for Ge, corresponding to $\{100\}$, $\{113\}$, $\{111\}$ and $\{110\}$ facets. We set the energy of the facets with normal along $\langle 100\rangle$ directions as a reference with $\alpha_{\langle 100\rangle} = 0.15$. The α_i coefficients for the other minima are then computed as

$$\alpha_i = 1 - \left(\frac{\gamma_i}{\gamma_{\langle 100\rangle}}\right)\left(1 - a_{\langle 100\rangle}\right), \tag{5.21}$$

where $i = \{113\},\ \{111\},\ \{110\}$ and γ_i are the corresponding surface energy values reported in

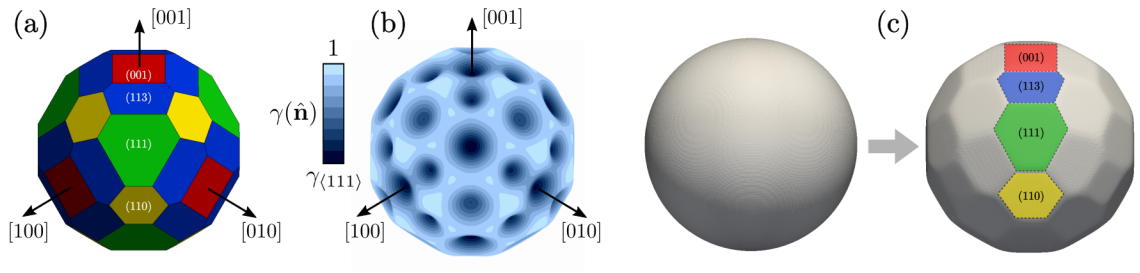

Figure 5.11: Realistic surface energy of Ge crystals. (a) ECS bounded only by the $\{100\}$, $\{113\}$, $\{111\}$ and $\{110\}$ facets, obtained by Wulffmaker [180] with surface energy density values as in Ref. [181]. (b) $\hat{\mathbf{n}}\gamma(\hat{\mathbf{n}})$ plot of surface energy density as obtained by the tuning of the parameters in Eq. (5.14) as described in *Sect.* 5.3.3. The color map shows the values of $\gamma(\hat{\mathbf{n}})$ as in *Fig.* 5.2(d). (c) PF simulation of surface diffusion from a sphere towards the ECS, with the anisotropic $\gamma(\hat{\mathbf{n}})$ of panel (b). The outline of the resulting faceting is highlighted by the colored regions.

Ref. [181]. The parameter γ_0 does not appear in Eq. (5.21). Indeed, it sets the magnitude of the surface energy but does not influence the ratio between different minima. In general, it can be used as a scaling factor to set the proper magnitude of $\gamma(\hat{\mathbf{n}})$. Here, we set $\gamma_0 = 1$. To ensure no superposition of the different contribution in Eq. (5.14) for $\hat{\mathbf{n}} = \hat{\mathbf{m}}_i$, w_i parameters has been selected equal to 100 for minima along $\langle 113\rangle$ directions and to 50 for all the other minimum directions [32].

The $\gamma(\hat{\mathbf{n}})$ function obtained by means of this fitting procedure, is reported in *Fig.* 5.11(b). Notice that by means of such a construction, $\gamma(\hat{\mathbf{n}})$ is a continuous function, i.e. it accounts for each possible orientation of the crystal. This would allow one to tune also the energy for all the orientations between minima with the possibility to tune also maxima of $\gamma(\hat{\mathbf{n}})$ or to describe the energetics of vicinal surfaces. However, these values are generally unknown and difficult to be determined. So that the $\gamma(\hat{\mathbf{n}})$ function set by Eq. (5.14) can be considered as a tool to construct a $\gamma(\hat{\mathbf{n}})$ based on the energy of preferential orientations, with values for any $\hat{\mathbf{n}}$ recovered as continuous fittings.

Following the approach of *Sect.* 5.3.2, we can simulate the evolution by surface diffusion of a sphere towards the faceted ECS, with the $\gamma(\hat{\mathbf{n}})$ function shown in *Fig.* 5.11(b). This evolution is illustrated in *Fig.* 5.11(c), where the initial sphere (left) and the final morphology (right) are reported. To ensure small rounding at corners and edges, the regularization parameter β is arbitrarily set to 0.003. The final shape resembles the morphology reported in *Fig.* 5.11(a), with a surface faceting also involving intermediate orientations with respect to the preferential ones. Notice that due to the presence of the corner rounding, the facets are not sharply defined in the ECS of *Fig.* 5.11(c). Moreover, the more complex $\gamma(\hat{\mathbf{n}})$ including all the possible orientation (see *Fig.* 5.11(b)) leads to a slightly different morphology with respect to the one in *Fig.* 5.11(a). However, the equilibrium configuration keeps all the main features obtained by the Wulff construction, as also shown by the colored areas in *Fig.* 5.11(c).

5.3.4 Morphologies of out-of-equilibrium structures

The results reported so far proved that the phase-field model of surface diffusion is an efficient tool, reproducing the evolution towards the equilibrium crystal shape, with tunable features of

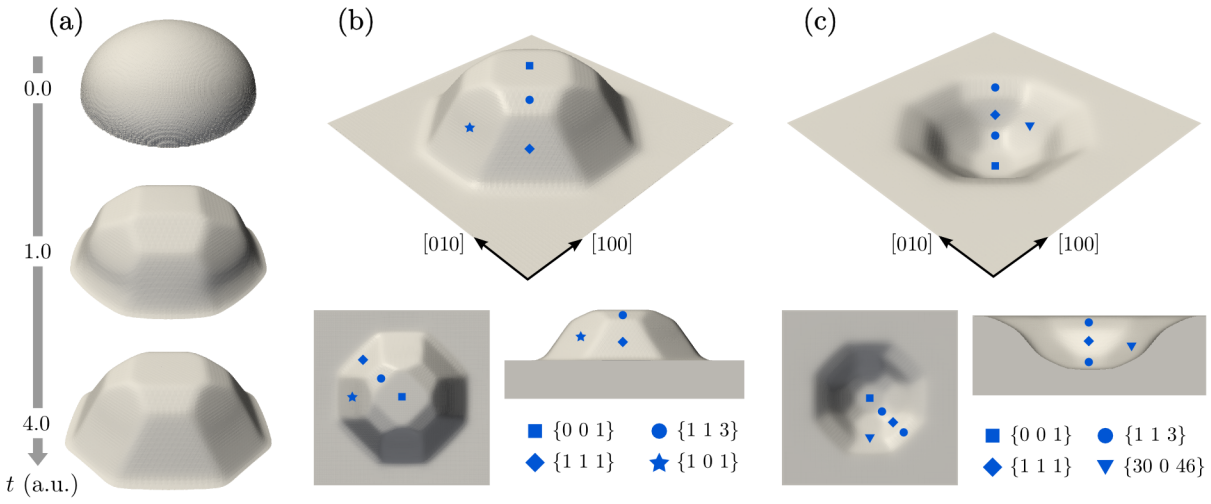

Figure 5.12: Faceted morphologies of structures on surfaces. (a) Evolution by surface diffusion on an half-ellipsoidal shape intersecting a plane by including minima in $\gamma(\hat{\mathbf{n}})$ along $[001]$, $[\pm 1 \pm 11]$, $[\pm 1 \pm 13]$, $[\pm 101]$ and $[0 \pm 11]$ directions [182, 183], $\alpha_i = 0.3$, $\beta = 0.006$. w_i are set as for the $\gamma(\hat{\mathbf{n}})$ definition of *Sect.* 5.3.3. (b) Perspective, top and lateral view of the last stage in panel (a) showing a morphology closely resembling GaAs islands in Ref. [184]. (c) Faceting of a pit-patterned Si substrates as in Ref. [185] obtained by imposing minima in $\gamma(\hat{\mathbf{n}})$ at $[001]$, $[\pm 1 \pm 11]$, $[\pm 1 \pm 13]$, $[\pm 30\ 0\ 46]$ and $[0\ \pm 30\ 46]$ directions,[98] $\alpha_i = 0.3$, $\beta = 0.006$. w_i are set as in as in *Fig.* 5.11(c) and $w_{\{30\ 0\ 46\}} = 100$.

the final morphologies set by means of the model parameters. In real experiments, shapes that are different from the ECS are often observed. Indeed, metastable kinetically frozen or out-of-equilibrium states may appear and they cannot be simply described using the Wulff construction. The same applies to evolving faceted geometries in thermodynamics conditions, where the morphology and the facets extension change despite the definition of $\gamma(\hat{\mathbf{n}})$ is uniquely determined by the materials. In these cases, the actual shape before reaching equilibrium condition is also determined by the dynamics of the evolution. The PF modeling introduced in *Sect.* 5.1, as explicitly shown for the evolution with isotropic $\gamma(\hat{\mathbf{n}})$ in *Fig.* 5.7, can take into account the kinetic pathway towards the equilibrium [32], eventually leading to stationary states that are only local minima of the energy in the phase space. In this section, the faceting and the evolution of some 3D, non-equilibrium geometries are reported. Notice that the evolution here provided, dealing with 3D domain and strong anisotropy, are usually not accessible with standard approaches previously reported in the literature. For instance, the remarkable fully-faceted approach introduced in Ref. [67] can be applied only to 2D domains. For the sake of simplicity, we set here the minimum energy directions in $\gamma(\hat{\mathbf{n}})$ with the same α_i (large enough to obtain sharp facets) and w_i. In all the PF simulations of this section, the interface thickness is set equal to 0.1.

In *Fig.* 5.12(a) we reproduce the morphology of an island starting from a half-ellipsoidal shape intersecting a plane below which $\varphi = 1$. An height-to-base aspect-ratio of 0.35 has been selected. Surace diffusion is considered with an anisotropic $\gamma(\hat{\mathbf{n}})$ with minima along $[001]$,$[\pm 1 \pm 11]$,$[\pm 1 \pm 13]$,$[\pm 101]$ and $[0 \pm 11]$, resembling the surface energy anisotropy of GaAs crystals [182, 183]. It can be noticed that the facets are gradually formed by surface diffusion as

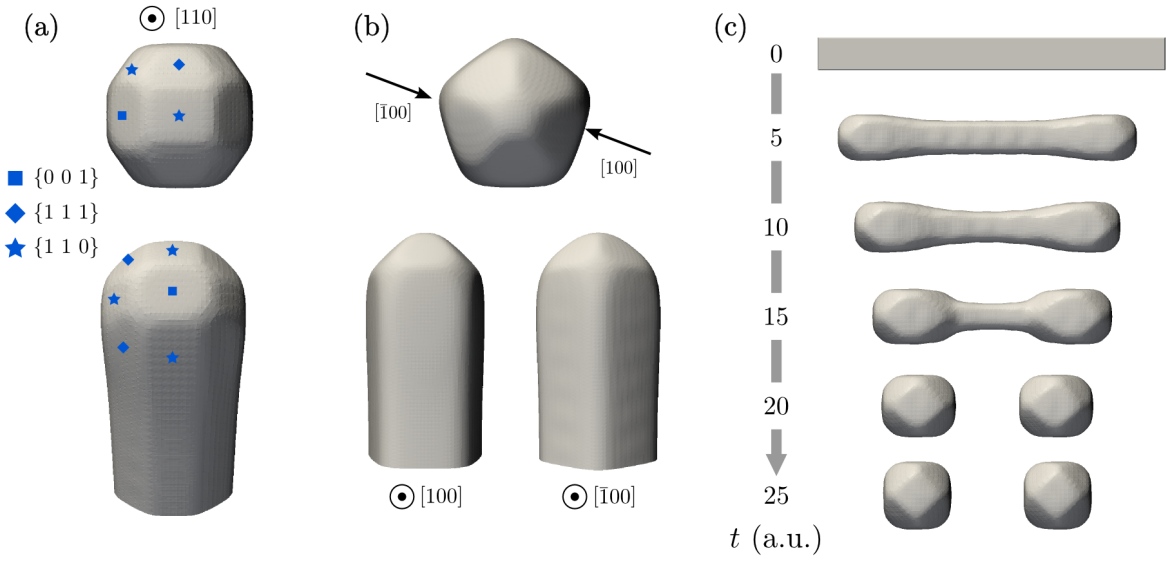

Figure 5.13: Morphology of elongated shapes. (a) Ge nanowire grown along $[110]$ direction, including $\{100\}$, $\{110\}$ and $\{111\}$ facets as in Ref. [186]. It has been obtained by selecting the energy ratio among minima as in *Sect.* 5.3.3. (b) Ag nanowire with pentagonal symmetry [187] obtained by considering $\gamma(\hat{\mathbf{n}})$ with minima along $[\sin(2i\pi/5)\ \cos(2i\pi/5)\ 0]$ and $[\sin(2i\pi/5)\ \cos(2i\pi/5)\ 1]$ directions with $0 \leq i \leq 4$, $\alpha_i = 0.15$, $w_i = 30$, $\beta = 0.002$. (c) Evolution by surface diffusion of an elongated parallelepiped as in *Fig.* 5.7 with the $\gamma(\hat{\mathbf{n}})$ function used in *Fig.* 5.9(a) with $\alpha_i = 0.2$.

in *Fig.* 5.8(a). The last faceted morphology ($t = 4.0$) does not correspond to the equilibrium condition, which is represented by a flat surface. However, similar morphologies are observed in experiments [184] and can be effectively reproduced with the present approach. Such a shape is also shown more in the details in *Fig.* 5.12(b) by means of perspective, lateral and top views. In *Fig.* 5.12(c) the morphology of a pit-patterned substrate is also shown, with the same views as in *Fig.* 5.12(b). The initial profile has been selected as a flat surface with a pit, smoothly connected to the surrounding region. An height-to-base aspect-ratio of 0.3 is selected in order to reproduce typical morphologies by lithographic techniques involving etching [111]. Si-pit morphology is here reproduced by considering the surface diffusion with minimum orientations of $\gamma(\hat{\mathbf{n}})$ set to reproduce the Si surface energy [98]. $\langle 30\ 0\ 46\rangle$ minima directions are considered in order to mimic neighboring $\langle 15\ 3\ 23\rangle$ facets (e.g. $[15\ \pm 3\ 23]$) observed in experiments (see for instance Ref. [111, 185]). Notice that the morphology shown here is affected by both the surface energy definition and the initial profile, as steeper or shallower pits would lead to different morphologies.

Other examples of faceted, out-of-equilibrium structures consist of low-dimensional systems with elongated shapes. Their morphology is clearly far from the minimization of the surface energy. First, such strong elongations cannot be justified by means of non-physical, extremely anisotropic surface energies. Second, if close-to-equilibrium conditions are reached for these systems, the shapes during evolution towards the equilibrium will significantly differ from the ECS.

In *Fig.* 5.13(a) and 5.13(b) realistic nanowires are reproduced by means of surface diffusion.

Initial profile is set as a simplified parallelepiped shape, placed with the base in contact with the domain boundary in order to mimic the continuation of the lateral facets. In particular, *Fig.* 5.13(a) shows the morphology of a Ge nanowire grown along the $[110]$ direction and the faceting of both top and sidewalls is included. The $\gamma(\hat{\mathbf{n}})$ is selected according the procedure of *Sect*. 5.3.3 for the energy minima along $\{100\}$, $\{110\}$ and $\{111\}$ directions. Another nanowire geometry is reproduced in *Fig.* 5.13(b). It deals with pentagonal symmetry recognized for Ag nanowire [187] resulting from twinning of five single crystal subunits exposing only $\{111\}$ facets. This five-fold $\gamma(\hat{\mathbf{n}})$ minima are not meant to reproduce the anisotropy of a single Ag crystal, but to effectively model the rotation around the nanowire axis of each subunit. Notice that the elongation of the morphologies shown in *Figs.* 5.13(a) and 5.13(b) directly result from the definition of the initial profiles and not from a tuning of $\gamma(\hat{\mathbf{n}})$ as done in *Fig.* 5.10(c).

As shown in *Sect*. 5.3.2, surface diffusion evolution may lead to topological changes. The same holds true with an anisotropic surface energy density. An illustrative simulation, starting from the same initial condition of *Fig*. 5.7, is shown in *Fig.* 5.13(c), by setting the same $\gamma(\hat{\mathbf{n}})$ as in *Fig*. 5.9(a) with $\alpha_i = 0.2$. The evolution is characterized by a lowering of the aspect ratio, with an enlargement of the shape at the ends of the structure while the center undergoes a thinning. Eventually, two separated, faceted subunits are formed recovering the evolution shown in *Fig.* 5.7 with facets.

According to the aforementioned results, the PF model considered here allows for the tracking of the evolution towards equilibrium for strongly anisotropic systems, also when accounting for topological changes. Moreover, as discussed in *Sect*. 5.3.3, the description of a realistic surface energy can be addressed. However, notice that the present model does not include the possible energy barriers for the diffusion among different facets. Despite they should not affect the prediction of the ECS, they may play a role in the evolution towards the equilibrium. Indeed, as illustrated in *Figs.* 5.7 and 5.13(c) kinetics may lead to local minima without reaching the predicted ECS. The description of diffusion barrier or anisotropic diffusion coefficient requires a dedicated development of the considered PF framework and was not considered in the present work.

5.4 Flux shielding

The modeling of the deposition included in Eq. (5.10) consists of a function which depends only on the local properties. However, more detailed deposition models should also take into account the self-shielding (or shadowing) effects produced by the surface profile on the incoming material flux from material sources. This effect is known to be important in the growth on patterned substrates and was proven to be crucial in VHEs growth [19, 20]. The more standard approaches, able to describe such effects, deal with Ray-Tracing algorithms. They consist of computing the distribution of the impinging flux by evaluating where rays, originating from the source of the material, hit the surface. However, within diffused interface, the coordinates of the surface are unknown (except for the initial profile), so that dedicated algorithms should be developed. Some attempts were introduced in Refs. [188, 189] for level set approaches, exploiting the so-called fast marching algorithm to identify the surface coordinates. In Ref. [190]

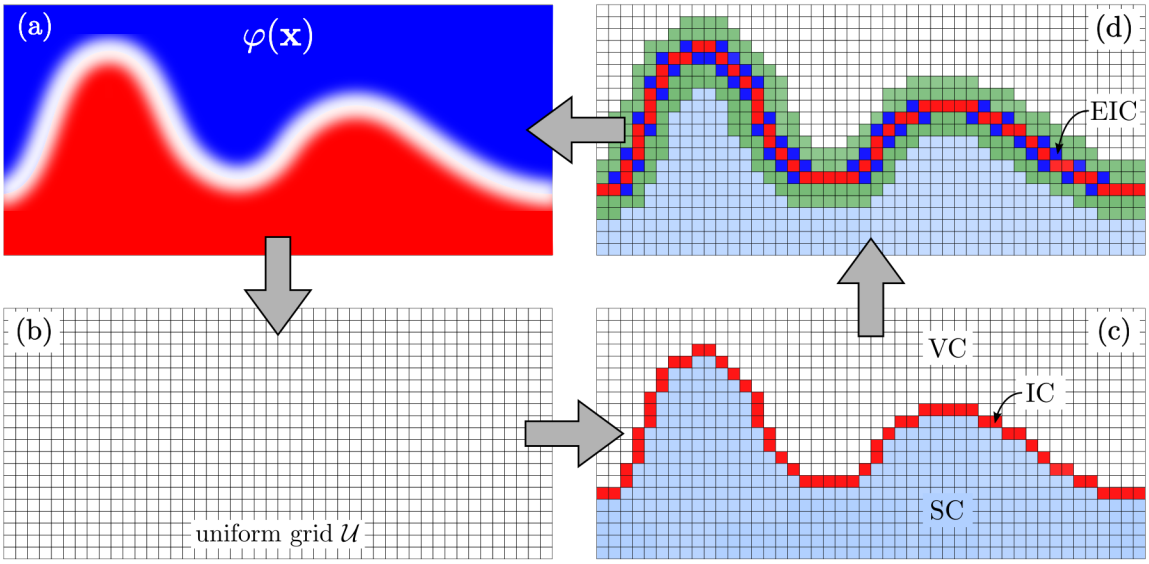

Figure 5.14: Illustration of the algorithm for the flux shielding calculation, reporting the main steps of the procedure described in *Sect.* 5.4. (a) Generic 2D profile defined by $\varphi(\mathbf{x})$ as in *Fig.* 5.1(a). (b) Uniform grid $\mathcal{U}$. (c) Reconstructed profile in $\mathcal{U}$ by means of solid cell SC (light blue), vacuum cells VC (white) and interface cells IC (red). This is the dataset on which the MC procedure is applied. (d) Profile as in panel (c) with the extended interface cells (blue) and the region where $S(\mathbf{x})$ is extended (green) to convert its values to $\mathcal{M}$.

a Monte-Carlo Ray Tracing approach have been used to describe etching processes. In this section, a similar algorithm is introduced in order to provide the material flux distribution within the PF approach. The coordinates of the surface profile are determined and a shielding (or shadowing) function $\mathcal{S}(\mathbf{x})$ is calculated, in order to provide the local impinging flux Φ of Eq. (5.9) as

$$\Phi = \Phi_0 \mathcal{S}(\mathbf{x}). \tag{5.22}$$

Φ_0 represents the amount of material per unit time reaching the surface where no shielding is present (i.e. for $\mathcal{S}(\mathbf{x}) = 1$) and $0 \leq \mathcal{S}(\mathbf{x}) \leq 1$. The procedure is described in the following for a generic 3D profile defined by $\varphi(\mathbf{x})$. It is also illustrated in *Fig.* 5.14 where, for the sake of simplicity, the 2D profile of *Fig.* 5.1(a) is considered.

The first step of the procedure which calculates $\mathcal{S}(\mathbf{x})$, for a surface implicitly defined by φ, consists of defining a uniform grid $\mathcal{U}$ (with coordinates of the points $\mathbf{x}'$), somewhat related to the (refined) mesh used for FEM calculations $\mathcal{M}$ (with coordinates of the points $\mathbf{x}$). This choice is mainly driven by the need to explore a large number of "rays", i.e. to evaluate $\mathcal{S}(\mathbf{x})$ the domain must be crossed many times checking properties of the nodes. A uniform mesh allows for simple and efficient algorithms. Indeed, there is no need to store the coordinates of the nodes, uniquely defined by means of the (uniform) size of the cell and by the domain boundaries. A generic three-dimensional system is here considered. The definition of the regular grid $\mathcal{U}$ is obtained by the following parameters:

- The boundaries of the FEM mesh $\mathcal{M}$ (assumed to be rectangular):

$$\mathbf{x}^{\min} = [\min(x_1), \min(x_2), \min(x_3)], \qquad \mathbf{x}^{\max} = [\max(x_1), \max(x_2), \max(x_3)], \tag{5.23}$$

- Spatial discretization: dx

where x_1,x_2 and x_3 are the three-dimensional coordinates of the system. The uniform mesh is built by means of cubic cells with edge length dx (see *Fig.* 5.14(b)). Every generic quantity A in the uniform mesh is defined as a three dimensional matrix $A_{i,j,k} = A(\mathbf{I})$ with $\mathbf{I} = [i, j, k]$. These indices are defined by

$$i = 1, ..., N_1 \qquad j = 1, ..., N_2 \qquad k = 1, ..., N_3 \tag{5.24}$$

with

$$N_d = \frac{x_d^{\max} - x_d^{\min}}{dx}. \tag{5.25}$$

$\mathbf{x}'(\mathbf{I})$, i.e. the coordinates of the cells in $\mathcal{U}$ are set by

$$x'_d = x_d^{\min} + dx \cdot (I_d - 0.5), \tag{5.26}$$

with $d = 1, ..., 3$. This equation defines $\mathbf{x}'(\mathbf{I})$ as the center points of the cubic cell indexed by $\mathbf{I}$. Notice that for a given point $\mathbf{x}$, the indices of its cell in $\mathcal{U}$ can be determined as

$$I_d = \left\lceil \frac{x_d - x_d^{\min}}{dx} \right\rceil. \tag{5.27}$$

Periodic Boundary Conditions (PBC) can be implemented for $\mathcal{U}$ by acting on indices as: $i = i \mod N_1$, $j = j \mod N_2$, $k = k \mod N_3$. In order to evaluate $\mathcal{S}$, φ and $\nabla\varphi$ should be known in all the discrete points $\mathbf{x}'$ of $\mathcal{U}$, defined by Eq. (5.26). Their values are obtained by the interpolation of such quantities from the values in $\mathcal{M}$ at $\mathbf{x} = \mathbf{x}'$. This results in the definition of $\varphi(\mathbf{x}') = \varphi_{i,j,k}$ and $\nabla\varphi(\mathbf{x}') = \nabla\varphi_{i,j,k}$. Every generic quantity A defined in $\mathcal{U}$ (formed by a set of discrete values indexed by i,j,k) can be considered as a continuous function by exploiting a *trilinear* interpolation on values defined in $\mathbf{x}'$ points. According to this, hereafter every generic $A(\mathbf{x}')$ quantity (as $\varphi(\mathbf{x}')$ or $\nabla\varphi(\mathbf{x}')$) is used as a continuous function.

In the second step the cells which correspond to the solid phase, to the vacuum phase or to the interface in between the two phases are identified. The definition of the cells in $\mathcal{U}$ is given by the following criteria

- Solid cell (SC) if $\varphi(\mathbf{x}') \geq 0.5$
- Vacuum cell (VC) if $\varphi(\mathbf{x}') < 0.5$
- Interface Cell (IC): SCs with at least one of the 6 Nearest Neighbors (NN) given by [$\pm i, j, k$], [$i, \pm j, k$], [$i, j, \pm k$] that is a VC (check over maximum values of indices or PBCs are required)
- Extended Interface Cell (EIC): SCs and VCs with at least one of the 26 Neighbors, including NN and second-NN given by every combination of $\pm i$ or i, $\pm j$ or j, $\pm k$ or k excluding [i,j,k], that is a VC or a SC, respectively (check over maximum values of indices or PBCs are required).

This classification, correponding to the φ distribution of *Fig.* 5.14(a) is illustrated in *Figs.* 5.14(c) and 5.14(d).

Once the cells are identified, the explicit calculation of $\mathcal{S}$ represents the third step. A MC approach is adopted as follows:

1. Random position $\mathbf{x}^0_{\mathrm{MC}}$ are generated (representing the coordinates of incoming particles), according to the features of the incoming flux. For instance, for a uniform flux they should be randomly generated on the entire top boundary. Conversely, they are set to a specific coordinate vector to model a point source.

2. Ballistic regime is here assumed for incoming particles. A velocity direction $\hat{\mathbf{v}}_{\mathrm{MC}}$ is assigned, and its evolution is tracked according to the following iterative scheme

$$\mathbf{x}^t_{\mathrm{MC}} = \hat{\mathbf{v}}_{\mathrm{MC}} \frac{dx}{2} + \mathbf{x}^{t-1}_{\mathrm{MC}}. \tag{5.28}$$

   The factor $dx/2$ is used in order to consider a particle visiting all the cells along the straight line of motion. Also the distribution of $\hat{\mathbf{v}}_{\mathrm{MC}}$ reflects the features of the flux. A random distribution of directions should be adopted for isotropic flux while directional flux can be selected by choosing specific vectors. Other regimes (at variance from the ballistic one) may be considered by changing Eq. (5.28) accordingly. PBC or other conditions at the boundaries are required.

3. When an IC cell is visited, the trajectory is extended to the boundary of the cell $\mathbf{x}'_{\mathrm{b}}$. If $\varphi(\mathbf{x}'_{\mathrm{b}}) < 0.5$ the next iteration of point 2 is considered. If $\varphi(\mathbf{x}'_{\mathrm{b}}) \geq 0.5$ the value of the discrete shielding function $\mathcal{S}_{\bar{i},\bar{j},\bar{k}}$ is increased by one, where $\bar{i}, \bar{j}, \bar{k}$ are the unknown indices of the considered IC obtained by solving Eq. (5.26) with $\mathbf{x}' = \mathbf{x}_{\mathrm{MC}}$ and $\mathbf{I} = [\bar{i}, \bar{j}, \bar{k}]$. If no IC are visited and the particle reaches a SC (as may happen when corners are present in the surface profile in $\mathcal{U}$), the $\mathcal{S}$ function is incremented in the nearest IC along the trajectory $\mathbf{x}^t_{\mathrm{MC}}$.

When $\mathcal{S}$ is incremented in one cell a new position is extracted and this procedure is repeated N_{MC} times. As a result, a map of $S_{i,j,k}$ is obtained, delivering nonzero values only in ICs. In order to use a value of such a function ranging from 0 to 1, the normalization by the expected value of incoming particles on a flat surface should be considered.

The fourth step consists of converting the function $\mathcal{S}$ determined in $\mathcal{U}$ to the PF framework, i.e. to the mesh $\mathcal{M}$. This requires an extension of its values within the entire interface region of φ along the $\hat{\mathbf{n}}$ direction (see *Fig.* 5.14(d)). In this algorithm it is performed in two steps.

1. From IC to EIC. For every EIC, which is not IC, the values of $\mathcal{S}_{i,j,k}$ is evaluated as the average of the values in the NN-IC.

2. From EIC to bulk phases. The values in EIC are extended in the direction of $\nabla\varphi$.

To perform the operation mentioned in the latter point the values of both $\varphi(\mathbf{x}')$ and $\nabla\varphi(\mathbf{x}')$ are used. If a bulk cell has $\mathcal{S} = 0$ and $\mathcal{S} \neq 0$ in one of the NN, then

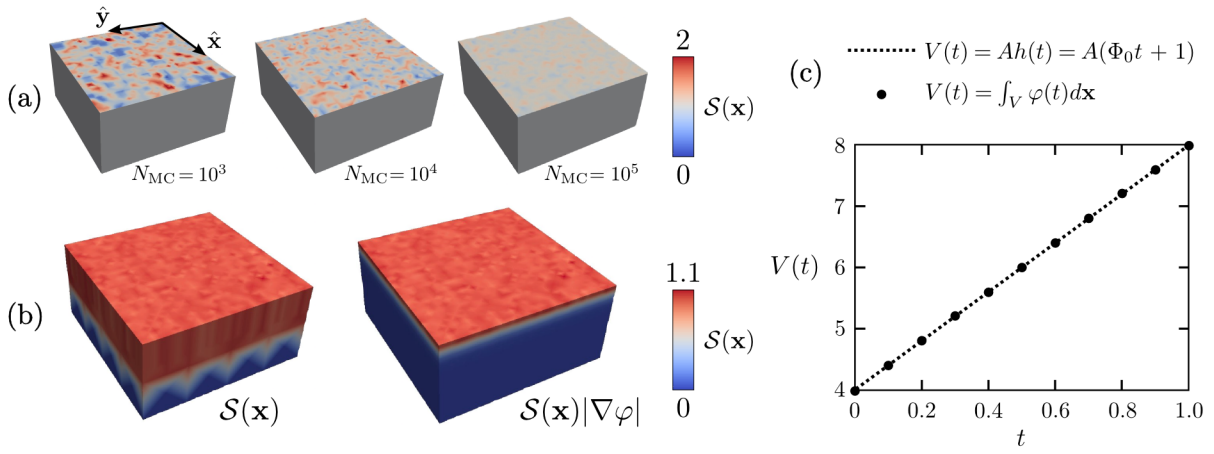

Figure 5.15: Test of the flux-shielding algorithm. (a) $\mathcal{S}(\mathbf{x})$ distribution on a planar surface for different N_{MC} with an isotropic material flux. (b) $\mathcal{S}(\mathbf{x})$ (left) and $\mathcal{S}(\mathbf{x})|\nabla\varphi|$ (right) values at the surface and in the solid phase. (c) Comparison between the volume of the solid phase during the growth of a planar substrate with constant Φ_0 (dashed line) and from isotropic deposition simulated by means of the approach of *Sect.* 5.4 (dots).

- If $\varphi > 0.5$, the first nonzero $\mathcal{S}$ values in direction $\nabla\varphi$ (or $-\hat{\mathbf{n}}$) is assigned.
- if $\varphi < 0.5$, the first nonzero $\mathcal{S}$ values in direction $-\nabla\varphi$ (or $\hat{\mathbf{n}}$) is assigned.

This operation is repeated in order to ensure nonzero $\mathcal{S}$ values in a region ϵ^* larger than the PF interface thickness ϵ. The number of iteration for such an operation (N^{ext}) depends on dx and is given by

$$N^{\mathrm{ext}} = \eta \frac{\epsilon}{dx} \tag{5.29}$$

where η is the factor ϵ^*/ϵ (set to a values larger than 1 to ensure the extension of $\mathcal{S}$ values over a region with a thickness larger than the PF interface ϵ). Values of $\nabla\varphi$ should be usually regularized (with a smooth connection to zero values outside the interface region) to avoid spurious contribution of noisy values when $\varphi < 0.05$ and $\varphi > 0.95$. Finally, $\mathcal{S}(\mathbf{x})$ can be calculated by the trilinear interpolation of the values obtained in $\mathcal{U}$ on the grid point of $\mathcal{M}$, i.e. $\mathcal{S}(\mathbf{x}')$ with $\mathbf{x}' = \mathbf{x}$, and it can be used in Eq. (5.22).

In order to assess this algorithm, the growth of a planar film accounting for an isotropic flux of materials has been considered. The points $\mathbf{x}_{\mathrm{MC}}$ are generated on the top boundary of the simulation domain with random velocity directions. Periodic boundary conditions are set for $\hat{\mathbf{x}}$ and $\hat{\mathbf{y}}$ direction. The $\mathcal{S}(\mathbf{x})$ distribution is reported in *Fig.* 5.15(a) for different values of N_{MC} at the 0.5 isosurface of φ. Notice that the higher is the N_{MC} value the more uniform is the flux distribution on the surface. In *Fig.* 5.15(b), the distribution obtained for $\mathcal{S}(\mathbf{x})$ in the solid volume is reported (left) along with the term $\mathcal{S}(\mathbf{x})|\nabla\varphi|$ (right) which determines the flux at the interface as described by Eq. (5.9) and Eq. (5.22). Notice that the former is extended on a larger area than the interface width (by setting $\eta = 3$ here) and constant values are assumed by $\mathcal{S}(\mathbf{x})$ along the normal-to-the-surface direction. The growth of a planar substrate with an isotropic flux is expected to be uniform, i.e. a translation of the planar surface is expected for a large number of N_{MC}. In *Fig.* 5.15(c) we report the comparison between the volume increase resulting

from a constant flux Φ_0 and the integral over $\varphi(\mathbf{x})$ by considering the procedure described in this section with $N_{\mathrm{MC}} = 10^5$. Notice that the $V(t)$ obtained by computing the flux with the shielding algorithm coincides with the expected variation with a constant flux. So that this comparison assesses the reliability of the reported procedure.

5.5 Illustrative simulations of crystals growth

The PF model described in *Sect*. 5.1 can be used to reproduce the growth kinetic for three-dimensional crystals. In this section, we report some examples of crystal growth simulations by PF. In particular the deposition on patterned substrates by means of the procedure introduced in *Sect*. 5.4 is reported. Then, the possibility to describe faceted growth is shown. Such examples assess the feasibility of the PF modeling considered in this chapter for the description of crystal growth, providing an improvement of the state-of-the-art technique for the modeling of such a phenomenon. Simulations reported here are meant to provide the proof of concept of the method developed and implemented in this thesis to account for material deposition. Further investigations will be devoted in the future to an extensive investigation of the growth process within the PF approach.

5.5.1 Growth on patterned substrates

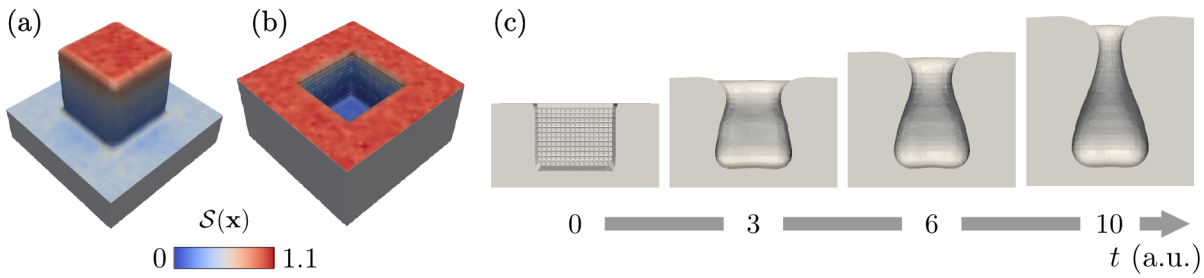

Figure 5.16: Shielding of material flux by patterned substrates. (a) $\mathcal{S}(\mathbf{x})$ at the surface of a pillar-patterned substrate. (b) $\mathcal{S}(\mathbf{x})$ at the surface of a pit-patterned substrate. (c) Time evolution of the profile in panel (b), involving a runtime calculation of $\mathcal{S}(\mathbf{x})$.

Let us consider a surface profile with an external flux as in the simulations of *Fig*. 5.15, i.e. reproducing the deposition by an isotropic material flux with a material source far from the sample. Here, we consider two representative patterned substrates in order to evaluate how their profiles affect the impinging flux distribution at the surface. Moreover, this allows us to apply the flux-shielding algorithm to non-trivial cases. For the sake of simplicity, an isotropic $\chi(\hat{\mathbf{n}})$ is assumed here. Notice that PBCs are adopted at the lateral boundaries, reproducing the condition of infinite patterned substrates. The two geometries are reported in *Figs*. 5.16(a) and 5.16(b) along with the $\mathcal{S}(\mathbf{x})$ distribution at the surface, obtained by the flux-shielding algorithm with $N_{\mathrm{MC}} = 10^5$. They illustrate the flux distribution on pillar- and pit-patterned substrates, respectively. In the former the maximum of the impinging flux is obtained at the top of the pillar where $\mathcal{S}(\mathbf{x}) \sim 1$ with small fluctuations. Then, smaller values are obtained on the sidewalls and the minimum of the impinging flux is present at the bottom. The latter is characterized by

higher values of $\mathcal{S}(\mathbf{x})$ on the flat surface, and a significant flux shielding acting on the region within the pit.

In *Fig.* 5.16(c) the time evolution of the pit-patterned profile is reported by means of the central cross-section of the 3D profile. As described by Eqs. (5.10) and (5.22), the local growth velocity is proportional to the Φ values, here accounting for the flux shielding by means of the $\mathcal{S}(\mathbf{x})$ variable. A small contribution of surface diffusion is also considered, with $M_0 = 10^{-4}$. The resulting dynamics consists of an anisotropic growth velocity at the surface, which is higher on the flat surface than within the pit. Notice that fine details can be accounted for with this description. For instance, the hole at the top surface become smaller and smaller during the growth while no growth is obtained on its sidewalls. This results directly from the flux distribution as the material flux on the top part of the pit is significantly larger than zero while it is negligible at the sidewalls. On the bottom, a small accumulation of material is present due to the opening of the pit, allowing for particles moving along vertical lines to be collected therein.

5.5.2 Faceted growth

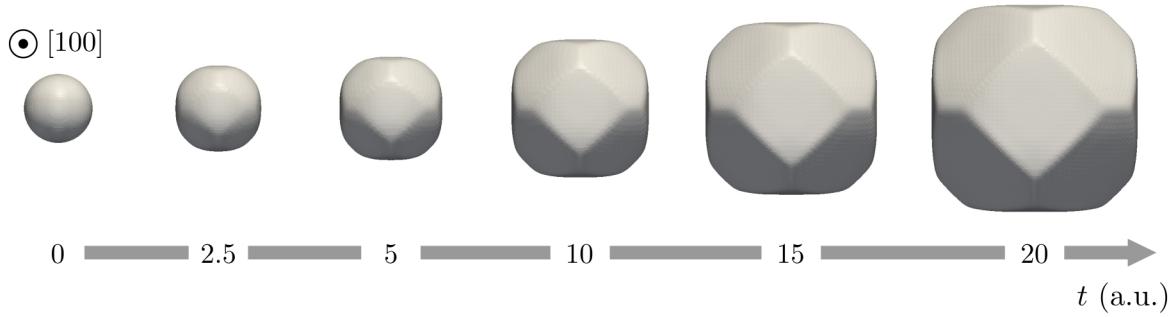

Figure 5.17: Faceted growth by means of PF modeling. The evolution is obtained from an initial spherical profile with anisotropic growth velocity set by Eq. (1.46). A discrete set of velocities corresponding to the normal of $\{100\}$ and $\{111\}$ facets is considered and described by means of a continuous $\chi(\hat{\mathbf{n}})$ distribution using the procedure in *Sect.* 1.5.1.

The description of faceted growth can be achieved within continuum approaches by acting on the growth velocity as described in *Sect.* 1.5.1. Let us consider the spherical profile used in *Fig.* 5.1(c), and adopted as initial condition in *Sect.* 5.3.2. The material flux is here set to a constant value Φ_0 for all the orientations, without flux shielding. In order to describe a faceted growth of an isolated crystal, we set an anisotropic incorporation factor $\chi(\hat{\mathbf{n}})$ introduced in Eq. (5.9). Such an anisotropic function is set equal to the modulus of the normal velocity $|\mathbf{v}(\hat{\mathbf{n}})|$, defined by Eq. (1.46) to account for continuous, anisotropic growth velocity from a set of directions corresponding to the normal vectors of the facets in the growing profile. Here, we focus on velocities oriented along $\langle 100 \rangle$ and $\langle 111 \rangle$ directions, with the same magnitude. In order to avoid the presence of the sharp corners expected between facets (and not compatible with the present continuum description), a contribution of surface diffusion is considered as in *Sect.* 5.5.1. The parameter δ of Eq. 1.47 is set to 10^{-6}. In *Fig.* 5.17(a) the result of such a modeling is presented. Starting from the spherical geometry, a faceted shape is recovered.

After a first transient, where facets are gradually formed, a stationary shape is obtained. This stationary state is in agreement with the outcomes of anisotropic growth velocities depicted by the kinetic Wullf Shape. As stated in Ref. [76] the transient phase is directly determined by the construction of the continuous velocity distribution.

At variance with the evolution by surface diffusion reported in *Sect*. 5.3, the volume increases during the growth. This leads the extension of the surface to become larger and larger. If a fixed domain is used this may lead to computational limitation arising when the solid touch boundaries. A solution may consist in a scaling of the total volume in order to evaluate only morphology changes, but some care is generally needed if the explicit coupling with other physical behavior, e.g. the surface diffusion, are taken into account.

The evolution reported in *Fig.* 5.17 demonstrates that the approach discussed in Ref. [76] leads to faceted growth also when implemented in the considered framework and represents an important step to describe continuum faceted growth models with PF approaches.

6

From VHEs to suspended films

As mentioned in the introduction and reported in *Sect*. 2.5.2, vertical Ge crystals on Si pillars are proven to have high material quality [19, 20] and in *Ch*. 3 we also provided a viable path toward the achievement of dislocation-free VHEs at any lateral size. This was also proved by experiments as discussed in *Sect*. 4.4. So that, vertical crystals represent an interesting system provided that its application may comply with, or even profit of, separated crystals, e.g. for detectors [191]. For many other technological purposes, e.g. for CMOS hetero-integration, continuous layers are highly demanded. A film, showing the material quality obtained with vertical growth at the micron scale, would be a very appealing system. The aim of the investigations reported here is to provide a pathway for the fabrication of suspended layers starting from isolated vertical crystals.

In this chapter, we present the study about the morphological changes induced in VHEs by annealing, which consists of a standard process usually adopted to improve the material quality [19, 20]. In order to describe the effects induced by such a processing on the morphology of VHEs, we focused our attention on the surface diffusion mechanism (see *Sect*. 1.4). The PF model reported in *Ch*. 5 has been selected to provide reliable 3D evolutions, and the generality of the presented approach allowed us to investigate different configurations, exploring the outcomes of ideal experiments. Simulations including both isotropic and anisotropic surface energy are illustrated and allow different details to be considered. From such a theoretical investigation, a pathway towards the realization of suspended layers starting from isolated crystals is identified and then confirmed by dedicated experiments [39] performed at L-NESS, IHP, and ETH-Zürich (as in *Ch*. 4). Moreover, the coalescence process during the growth at high temperature [41] is illustrated and explained with the aid of an extension of the model used in Ref. [19] and preliminary three-dimensional PF simulations. Together with the technology relevant results obtained with the coalescence of vertical crystals, this chapter also delivers some interesting perspectives originating from this thesis.

6.1 Morphological changes by annealing

Vertical Ge crystals are grown by LEPECVD on deeply patterned Si substrates and a faceted shape is usually obtained (as introduced in *Sect*. 2.5.2). A typical as-grown morphology is shown in *Fig*. 6.1(a).

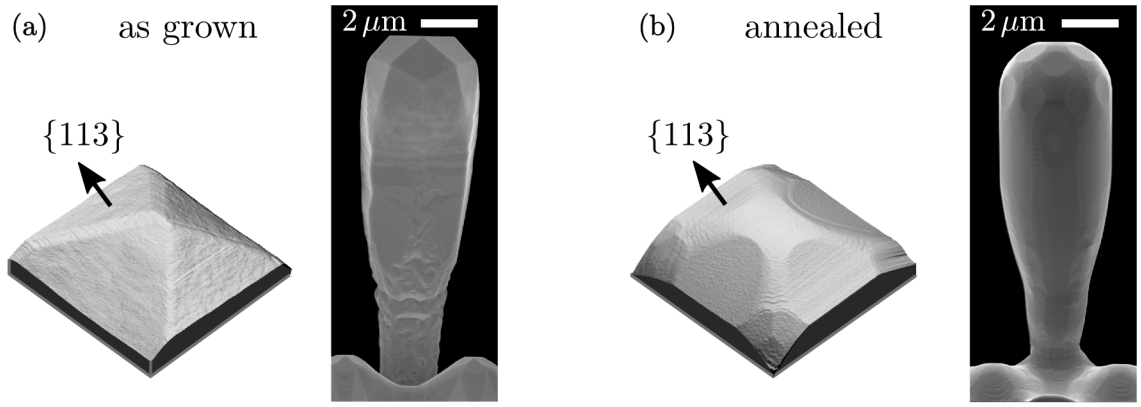

Figure 6.1: Morphological change due to the annealing of an individual crystal. (a) Perspective AFM image and lateral SEM image of a 8 μm tall Ge crystal grown at 500°C on 2×2 μm^2 wide, 8 μm tall Si pillars, separated by 3 μm trenches. (b) as in panel (a) after six annealing cycles from 600°C to 800°C (each one lasting for 6 min).

It consists of 8 μm tall Ge crystal grown at 500°C on a 2×2 μm^2 and 8 μm tall Si pillar, separated from the neighbors by 3 μm trenches. AFM scan of the top morphology and a lateral SEM image are shown. The top of the crystal is made of a pyramid bounded by $\{113\}$ facets with $\{111\}$ lateral facets and $\{110\}$ sidewalls. Notice that this elongated shape is peculiar of the kinetic growth regime as it does not correspond to ECS-like shapes for Ge (see *Fig.* 5.11). Annealing experiments are usually performed on such samples in order to improve the material quality. In *Fig.* 6.1(b) the morphology of vertical crystals after such a processing is shown. In particular, the lateral SEM image and the perspective AFM scan are reported for a sample identical to the one in *Fig.* 6.1(a) after six in-situ thermal cycles between 600-800°C, each one lasting for 6 min. A clear rounding of the edges between facets is obtained and, from the AFM scan it can be noticed that the $[001]$ facet appears at the top. Moreover, the global, vertical shape results slightly enlarged at the half-height of the Ge crystal. Evolution of the surface profile can also be noticed in the area surrounding the Si pillar. Indeed, a wavy profile is present in the as-grown sample due to the material deposited within the gap between pillars. After annealing, even such a surface corrugation results flattened.

6.1.1 2D simulations

In order to investigate the morphological change obtained in *Fig.* 6.1, we selected the surface diffusion model proposed first in Ref. [33]. Indeed, surface evolution may only be ascribed to a material redistribution along the surface as no material deposition is present and the experiment is performed under vacuum (see discussion in *Sect*. 1.4). As reported in Ref. [19], and in agreement with the results provided in *Ch*. 3 and 4, the micrometer-wide VHEs as in *Fig.* 6.1 are strain free, as they are plastically relaxed. Moreover, they allow the thermal stresses to be fully relieved. Therefore, the only contribution to the chemical potential is related to the minimization of the surface energy with all the features introduced in *Sect*. 1.4.

Let us consider first a two-dimensional model, where the surface diffusion as described in Eq. (1.35) is integrated using a finite difference approach, i.e. a discrete set of points is con-

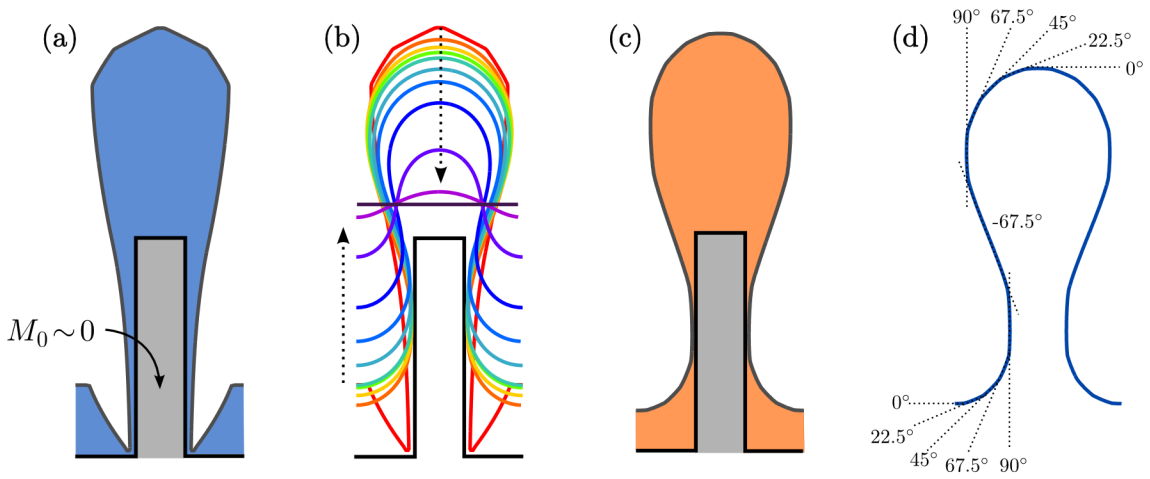

Figure 6.2: 2D simulations of the morphological change due to surface diffusion. (a) Initial profile. (b) Full evolution with isotropic $\gamma(\theta)$ illustrated by representative stages. (c) Representative step obtained with an anisotropic $\gamma(\theta) = 1 - \alpha\cos(16\theta)$ with $\alpha = 0.0039$, resembling the experimental one in *Fig.* 6.1(b). (d) Step of the anisotropic evolution highlighting the preferential orientations at the surface.

sidered to describe the surface of the Ge crystal. We consider an initial profile as in *Fig.* 6.2(a), corresponding to the cross-section of real 3D crystals, directly taken from Ref. [19]. In order to account for the presence of Si, we set vanishing mobility coefficient when surface reaches the Si pillar. Indeed, at the considered annealing temperatures the mobility of Si is significantly lower than the Ge one [192]. Intermixing effects between Ge and Si are here neglected as they affect a region of a few monolayers at the Ge/Si interface, which is negligible compared to the sizes of microcrystals. We consider the evolution with isotropic surface energy density ($\gamma(\theta) = \gamma_0 = 1$), so that $\mu = \kappa$. The local curvature is evaluated as the reciprocal of the radius of curvature, computed by means of the osculating circle of the surface profile. Periodic boundary conditions are adopted, simulating a periodic structure made of vertical Ge crystals on Si. The resulting evolution is reported in *Fig.* 6.2(b). A global rounding is observed and the evolution ends when the chemical potential is homogeneous, i.e. when a flat surface is obtained. The main evidence corresponds to a lowering of the structure, producing at the same time a trench filling. The rounding in the first stages of the simulation leads also to a slightly enlarged crystal, which is then flattened.

The same simulation has been repeated by considering an anisotropic surface energy density, with μ determined by Eq. (1.38). A surface energy density $\gamma(\theta) = 1 - \alpha\cos(16\theta)$ is considered with θ the local orientation of the surface, where minimum-energy orientations are multiples of $22.5°$. This specific function for γ is chosen as it reproduces orientation close to the typical ones for the cross-sections of Ge crystals, as $\{113\}$ facets where $\theta \sim 22°$. α was set to 0.0039 which is the rounded critical value $\bar{\alpha} = 1/(16^2 - 1)$ (see discussion in *Sect.* 1.4) for the considered $\gamma(\theta)$. Notice that no regularization is needed with such a choice as it is slightly lower than the critical anisotropy strength. In *Fig.* 6.2(c) we report a representative stage of the evolution with faceting, closely resembling the morphology in *Fig.* 6.1(b). The resulting facet orientations on the simulated profile are also highlighted in *Fig.* 6.2(d) in a later stages of the

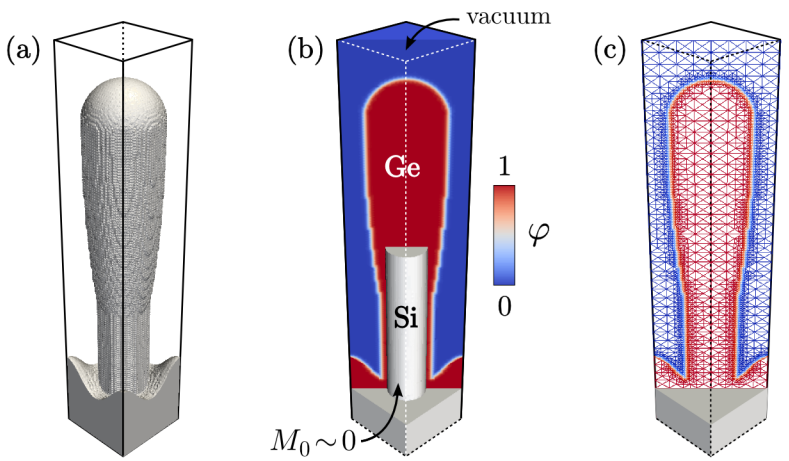

Figure 6.3: Phase-field modeling. (a) Outline of the simulation domain with a pillar-like structure implicitly defined thanks to the PF approach. The surface of the structure is obtained as the 0.5 isosurface of φ. (b) Cross-section of the simulation cell showing φ values. The 3D grey region corresponds to the immobile Si domain ($M_0 \sim 0$). (c) Mesh structure in the central cross-section of the simulation cell, showing local refinement at $\varphi = 0.5$. The color map, shared between panels (b) and (c), reports the values of φ.

evolution with respect to *Fig.* 6.2(c). Notice that the presence of facets does not modify the general behavior as the crystal still results enlarged with a lowering of the aspect ratio. Moreover, even with this simplified 2D simulations, the evolution of the top of the crystal with the appearance of a flat surface is obtained as in the experiments (see *Fig.* 6.1).

6.1.2 3D simulations

In order to extend the modeling to three-dimensional systems we deeply exploited the PF model presented in *Ch.* 5 (where all the details of the method are reported). In *Fig.* 6.3, the modeling of the VHE geometry within the PF framework is shown. In particular, *Fig.* 6.3(a) shows a surface profile of a simplified vertical structure. This profile corresponds to the 0.5 isosurface of the initial condition for φ. In *Fig.* 6.3(b) a cross-section of the simulation cell is reported with a color map showing the φ values. The gray region corresponds to the immobile Si, in agreement with the choice adopted for the simulation in *Sect.* 6.1.1. In *Fig.* 6.3(c) we also report the typical mesh refined at the interface used for the reported FEM calculations. Notice that, within any phase-field approach, distances lower than the interface thickness ϵ cannot be described. For computational reasons, this thickness is always finite and should be set as small as possible to recover the sharp-interface dynamics (see *Ch.* 5). In the simulation reported here, compared to the corresponding experimental systems defined at the micron scale, it can be set in the order of 200-300 nm.

Let us focus our attention on the evolution with isotropic surface energy. It is shown in *Fig.* 6.4(a), where the timescale is provided by using M_0 as a scaling factor to match the timescale of the related experiments (of *Fig.* 6.1, also adopted for other simulations reported in the following sections). This can be done as M_0 only sets the time and length scales but does not affect the qualitative evolution, as can be inferred from Eq. (5.6). In *Fig.* 6.4 we report the

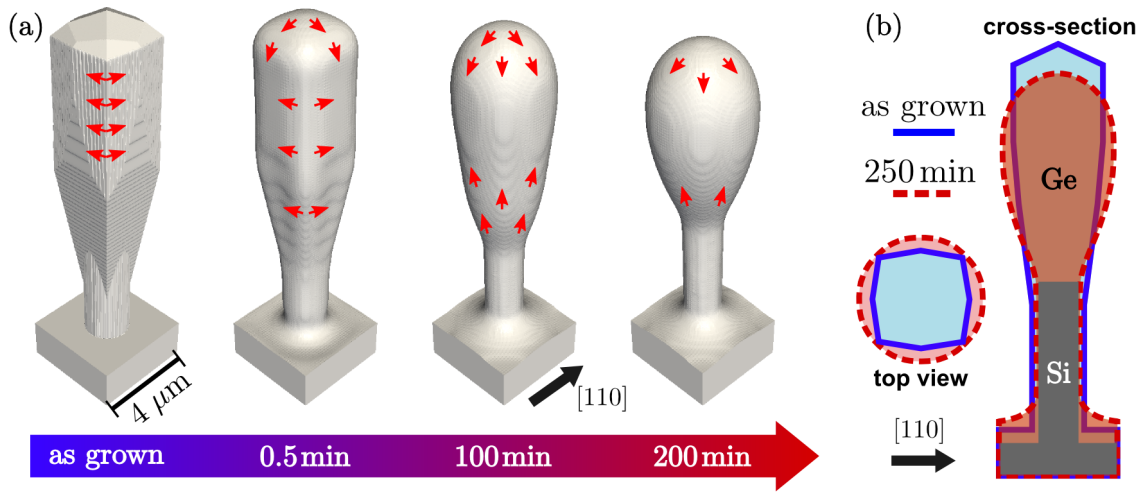

Figure 6.4: Three-dimensional evolution of a single crystal by surface diffusion. (a) PF simulation starting from a geometry reproducing the crystal in *Fig.* 6.1(a). (b) Comparison between the as-grown profile and the morphology after the evolution by surface diffusion, mimicking the annealing experiment.

PF simulation of surface diffusion, starting from an initial profile closely resembling the shape of *Fig.* 6.1(a). A global smoothing of the edges is observed, providing a more realistic 3D evolution including the features already observed with the 2D model. Indeed, the morphology obtained at 0.5 min closely reproduces the shape reported in *Fig.* 6.1(b) and a lateral expansion is observed at later stages (i.e. 100 min and 200 min). A comparison between the as-grown morphology and the profile after the evolution by surface diffusion in cross- and top-view are also shown in *Fig.* 6.4(b) and the lateral expansion can be better appreciated. Notice that the a material transfer at the bottom of the Si pillar is also obtained but with a lower extent than 2D simulations (see *Fig.* 6.2) as the volume to fill within the trenches is significantly higher when considering the 3D geometry. Red arrows on the simulated profiles illustrate the material flux along the surface.

In order to assess the evolution discussed so far and to further refine the simulations results, we also considered the morphological evolution with the $\gamma(\hat{\mathbf{n}})$ definition for Ge crystals discussed in *Sect.* 5.3.3, as shown in the simulation reported in *Fig.* 6.5. Notice that the timescale is here expressed in arbitrary units as it is affected also by the choice of parameters in the $\gamma(\hat{\mathbf{n}})$ definition, and we aim here to a qualitative comparison. They will be adopted also in the following when illustrating general mechanism with simplified initial profiles. In the first stages, the top of the as-grown crystal made of a pyramid bounded by $\{113\}$ facets evolves into a truncated pyramid with the clear appearance of the (001) facet, recovering a shape closer to the equilibrium (see *Fig.* 5.11). The facets which are stable according to the surface energy, and already present in the initial configuration, are preserved. These features correspond to the morphological evolution observed in *Fig.* 6.1 and cannot be reproduced by the evolution with isotropic surface energy. In *Fig.* 6.5(c) a comparison between the top morphologies from AFM scans (EXP) and 3D simulations with anisotropic $\gamma(\hat{\mathbf{n}})$ (SIM) is also reported. By considering the surface energy of the Ge, a good agreement is obtained including the aforementioned appearance of the $[001]$ facet and the nucleation of new facets at the corners. At later stages of the

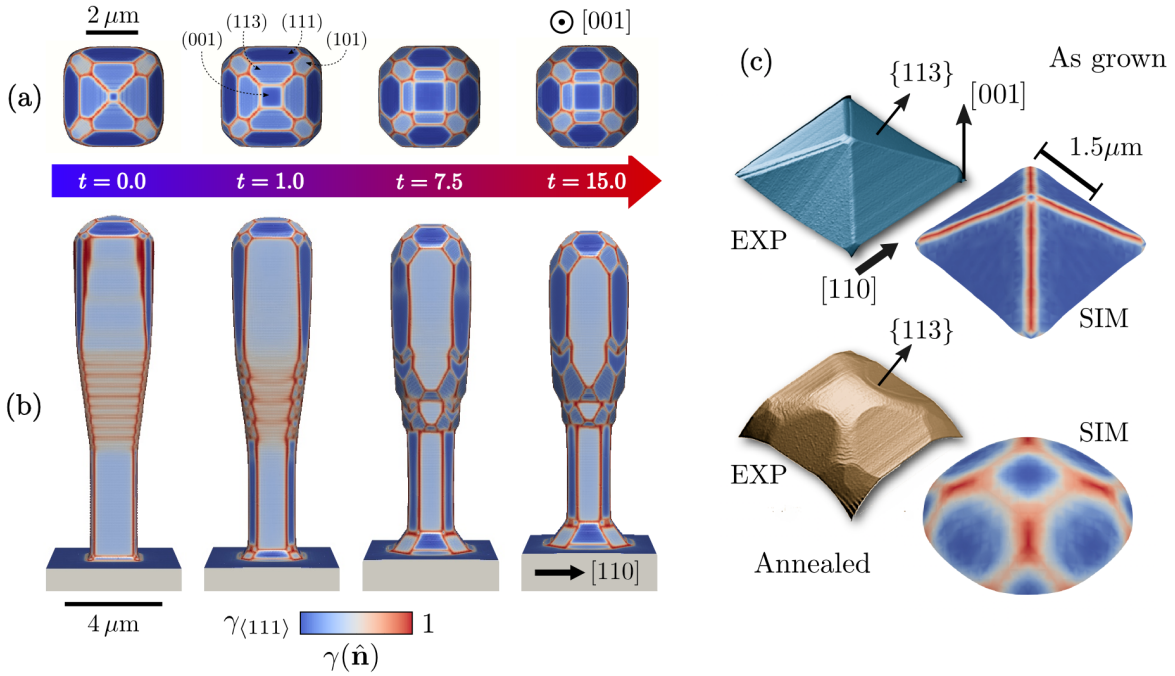

Figure 6.5: Evolution by surface diffusion of an isolated faceted crystal. The initial geometry is set to closely resemble the experimental one obtained at a growth temperature of ∼500°C [19, 20]. (a) Top and (b) lateral view of four representative stages are reported. The color map shows the $\gamma(\hat{\mathbf{n}})$ values. Dashed arrows mark the families of facets. Time is scaled in arbitrary units. (c) Comparison between fine details of the morphology between AFM scans and simulations with the anisotropic $\gamma(\hat{\mathbf{n}})$.

evolution reported in *Fig.* 6.5, faceted sidewalls are recovered with the formation of (± 100) and (0 ± 10) facets at the vertical edges. Close to the Si pillars, a complex faceting is formed at the Ge surface, as the initial profile shows unstable orientations. Material transfer from the region around the Si pedestal towards the substrate is also observed, until exposing the Si. By comparing the initial profile and the last stage at $t = 15$ of the evolution in *Fig.* 6.5, a lowering of the crystal is observed along with a lateral enlargement which is, however, lower than the case with isotropic surface energy. Such an evolution confirms the generality of the overall morphological changes observed so far, also including specific features related to the thermodynamic faceting [193]. In particular, an enlargement of the structure is observed despite the presence of faceted sidewalls. This is in agreement with the evolution reported for strongly anisotropic systems with large height-to-base aspect ratios [32, 67] and also with the evolution of *Fig.* 5.13(c). It is worth pointing out that the experimental profiles after annealing actually show a weaker faceting than the one imposed in this simulation. However, observing the same qualitative behavior for the two limiting cases (isotropic and strongly anisotropic $\gamma(\hat{\mathbf{n}})$) allows us to infer that the intermediate case, corresponding to the experiments, follow the same general trend.

6.2 Self-assembling of suspended layers

The results reported in *Sect.* 6.1.2 allowed for the assessment on the considered modeling and described the long time evolution which mainly leads to a lateral expansion of the Ge crystals. However, vertical heterostructures obtained by LEPECVD in Refs. [19, 20] can be grown on dif-

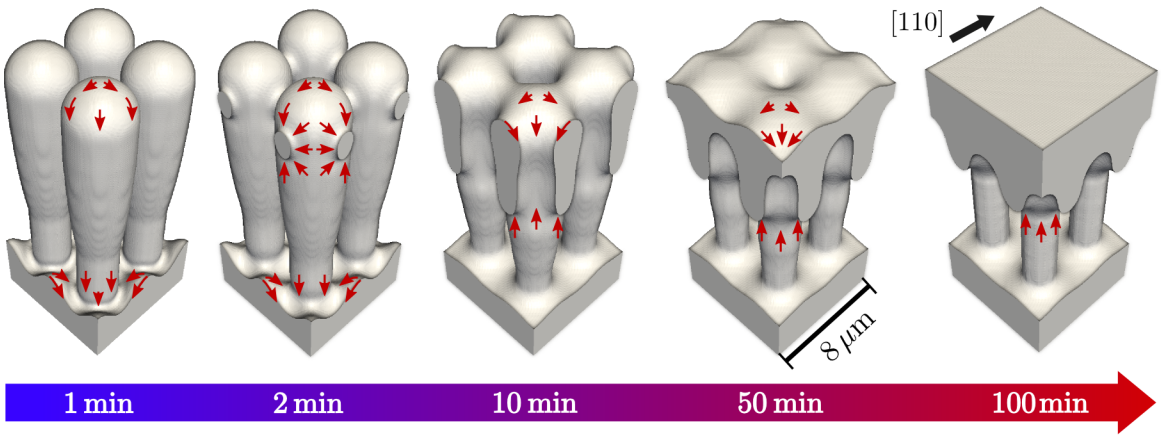

Figure 6.6: PF simulation of the coalescence process. Initial profile (1 min) resembling the experimental shape after the initial smoothing of the edges between facets. Representative stages are reported concerning the onset of the merging process (2 min), the fast zipping of the coalesced region towards the bottom of the Ge (10 min), the filling of the holes at the top (50 min) and the final flattening of the suspended layer (100 min).

ferent patterns characterized by a smaller trenches between Si pillars. In particular, a distance of 2 μm between pillars is often adopted. The resulting structures at the end of the growth on such patterns are separated by only a few tens on nanometers. So that, the enlargement mechanism discussed before, would lead to the coalescence of individual crystals. A dedicated simulation reproducing such a mechanism is shown in *Fig.* 6.6. Isotropic surface energy is considered here with an initial profile that reproduces the height-to-base aspect-ratio of a micrometer-wide VHE. A rounded shape is selected, roughly corresponding to a profile where the smoothing of the edges already occurs. Crystals are arranged in a squared pattern and the distance is set to be slightly larger than the interface thickness (here set to 200 nm, which corresponds to a computational limit for the present approach). Despite this value is larger than the experimental distance between crystals, it is not found to play a crucial role in the simulations, without altering the information delivered therein. Periodic boundary conditions are set along [110] and $[1\bar{1}0]$ directions.

In agreement with the previous discussion, the lateral expansion obtained by the surface diffusion mechanism leads to coalescence. After the onset of the crystal merging, a fast zipping is observed, and holes are present in between the merged regions. Then, for longer annealing times the filling of such holes is achieved and a suspended layer is eventually flattened. Notice that the evolution reported in *Fig.* 6.6 involves dramatic topological changes, which are in general difficult to be treated with an explicit tracking of the surface. The easy managing of such a complex evolution is one of the main advantages of the selected PF approach [29] (see also *Ch.* 5).

The simulation reported in *Fig.* 6.6 stimulated dedicated experiments in order to verify the coalescence mechanism and fabricate the suspended film starting from VHEs. These experiments are reported in *Fig.* 6.7, where the evolution induced by annealing of closely spaced crystals is illustrated by means of four different samples corresponding to different post-growth

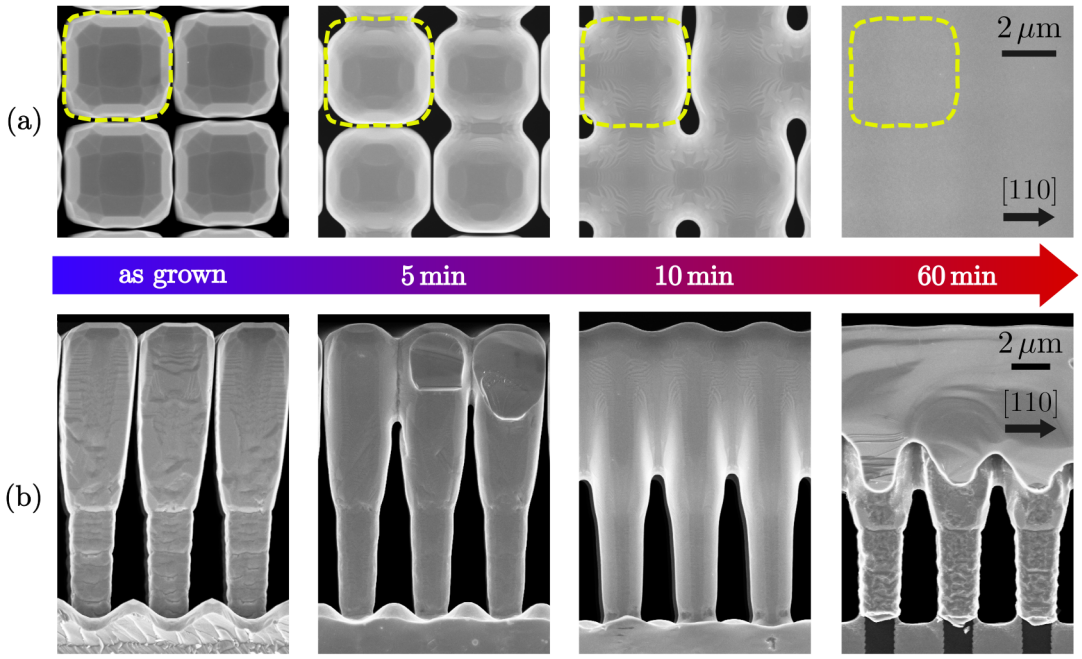

Figure 6.7: Annealing experiments leading to coalescence of individual crystals. (a) Top and (b) lateral SEM images of Ge crystals grown at 450°C on 8 μm tall and 2×2 μm^2 wide Si pillars separated by 2 μm trenches. The four steps are obtained by in-situ annealing experiments with different duration at 800°C.

annealing duration. The as-grown profiles were obtained by Ge deposition at 450°C on 8 μm tall and 2×2 μm^2 wide Si pillars separated by 2 μm trenches (at variance with the 3 μm trenches of *Fig.* 6.1). The coalescence onset in the experiments is observed after annealing for 5 min. Then an extended, fast zipping towards the substrate is obtained after annealing for 10 min. The global flattening with the formation of the suspended layer on top of the structure is achieved by annealing for 60 min. Therefore, the experiments confirm the simulation results proving that the surface diffusion is the main contribution in the considered morphological evolution. Moreover, a viable pathway for the formation of suspended layers starting from isolated crystals is provided.

A deeper understanding of the coalescence process can be achieved by looking at the chemical potential at the surface during the evolution as shown in *Fig.* 6.8. Here, for the sake of simplicity, a cylindrical initial profile is considered with isotropic surface energy. White arrows illustrate the magnitude of the material flux along the surface in representative regions and are set proportional to $-\nabla\mu$. Convex regions, such as the crystal tops, correspond to positive curvatures (red) and hence to maxima of μ. On the contrary, concave regions with negative curvature (blue), correspond to low values of μ. As indicated by the arrows, material flows from the convex regions at higher curvature towards concave regions which behave as collectors. At the beginning of the process, the material is mainly pushed away from the crystal top yielding to a rounded shape. At the same time, at the substrate level, material moves toward the profile valleys. The velocity of the evolution decreases until the onset of the crystal coalescence occur (at around t = 2.0 a.u.). Bridges formed after the contact of crystals significantly attract material because of their small radius (with large negative curvature) as evidenced by the big arrows

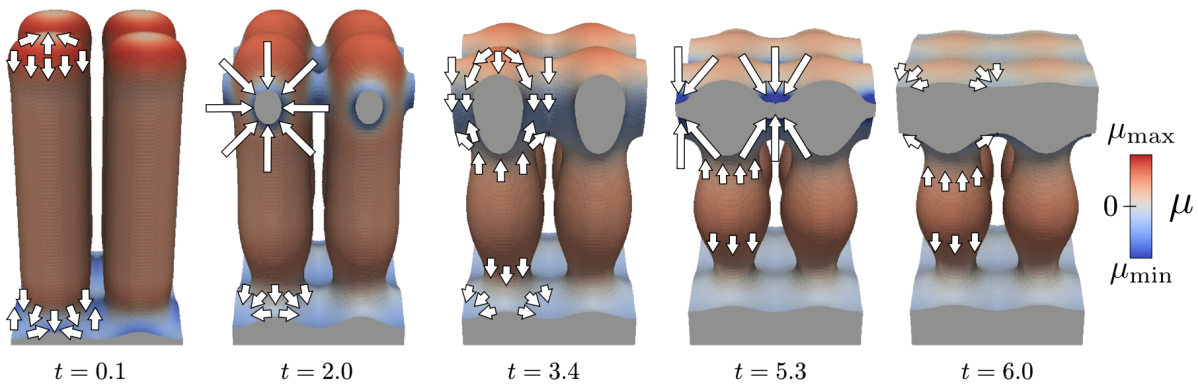

Figure 6.8: Simulation of the coalescence process, for a simplified initial structure, illustrating the chemical potential and the material flux at the surface. The color map shows the chemical potential, here proportional to the local curvature of the profile (red for convex regions and blue for concave regions). Representative arrows indicate the material flow according to the curvature gradients as described by Eq. (1.34).

converging at the junction. Again, the process velocity drops as the curvature at bridges gets smaller (see t = 3.4 a.u.). However, holes are still present in between merged regions. Such concave regions progressively attract material and their radius shrinks with increasing velocity, up to complete closure (t = 5.3 a.u.). The resulting wavy profile at the top of the crystals tends finally to flatten moving materials from the hills to the valleys. Notice also that during the evolution the substrate behaves as a sink attracting material from the pillar sidewalls.

Following a similar discussion to *Sect*. 6.1.2, we also investigated the coalescence process with the anisotropic surface energy density of Ge, in order to verify the occurrence of coalescence also when explicitly accounting for realistic preferential orientation [193]. The initial geometry is set as in *Fig*. 6.5, recovering the as-grown morphology, with an alignment along the $[110]$ and the $[\bar{1}10]$ directions and a periodicity equal to 4 μm. The resulting gap between crystals is ~ 0.4 μm.

The simulation reproducing the coalescence of faceted crystals is reported in *Fig*. 6.9. In the first stages of the evolution, the same morphology as obtained for isolated crystals ($t = 1.0$, as in *Fig*. 6.5) is observed as the vertical structures are not affected by the neighbors. Then, even with anisotropic surface energy, the coalescence of crystals along $[110]$ and $[\bar{1}10]$ directions is obtained, with the formation of bridges (as shown for $t = 2.5$). As discussed in *Fig*. 6.8, these regions collect material and the coalesced region extend (see differences between merging at $t = 2.5$ and $t = 6.0$). This material transfer produces a global lowering of the crystal tops. Moreover, large $\{111\}$ facets disappear while $\{113\}$ facets extend. Also $\{110\}$ facets, which are favored due to the free surface between bridges (see $t = 6.0$), grow larger up to the closure of the holes while (001) facets are formed on top of the coalesced regions. The complete closure of the holes is achieved at later stages, with the formation of a continuous surface still showing a faceted profile as shown at $t = 9.5$. New (001) facets are formed at this stage, and the other flat regions extend when holes are filled. When such a continuous film is obtained, facet extensions are reduced while (001) results larger and larger. Eventually, the suspended film flattens and

a single (001) surface is obtained on top of the structure as the final stage ($t = 15$). This stage is shown at the upper right-hand corner of *Fig.* 6.9. Therefore, we can conclude that the mechanism observed in *Fig.* 6.6 is expected also when accounting for fine details of the anisotropic surface energy.

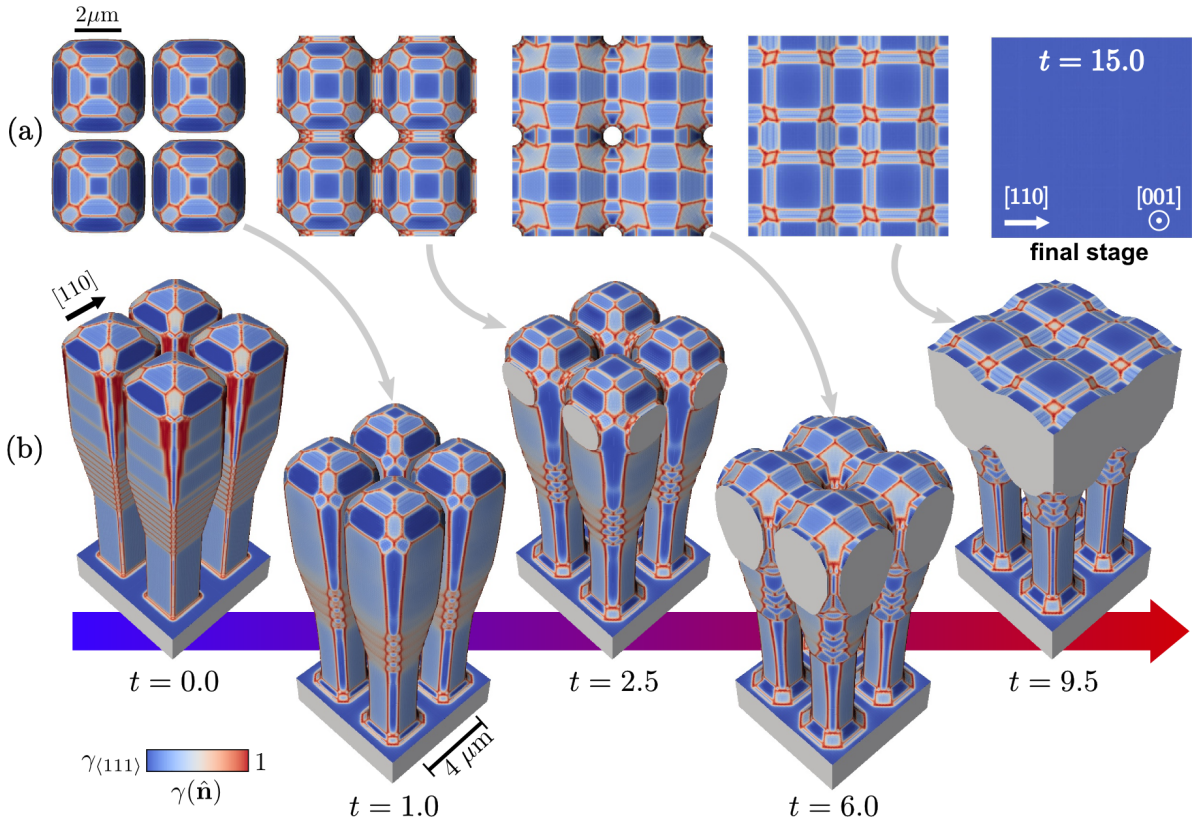

Figure 6.9: PF simulation of the coalescence process including surface energy anisotropy. (a) Top view of the crystals at representative stages of the evolution. The last top view shows the final stage corresponding to the complete flattening of the suspended film. (b) Perspective view of the three-dimensional evolution. Time is expressed in arbitrary units.

A detailed analysis of the coalescence process can be extracted by considering the values of the free energy in time, namely $G(t)$, with G defined by Eq. (5.4) [193]. In *Fig.* 6.10 such a quantity is shown, normalized with respect to the surface energy of the initial configuration (at $t = 0$). Two significant changes of the slope can be easily recognized and correspond to the topological changes of the structure, i.e. the coalescence of the crystals and the filling of the holes. In the other stages, an almost smooth decrease of the energy is observed. The end of the evolution is achieved when $G(t)$ reaches a constant value. Despite this plot is related to the simulation of *Fig.* 6.9, all these features are general as they are observed also with isotropic $\gamma(\hat{\mathbf{n}})$. Furthermore, they are not affected by the specific choice of the surface energy. This plot can be adopted to identify the exact timing of topological changes during the evolution.

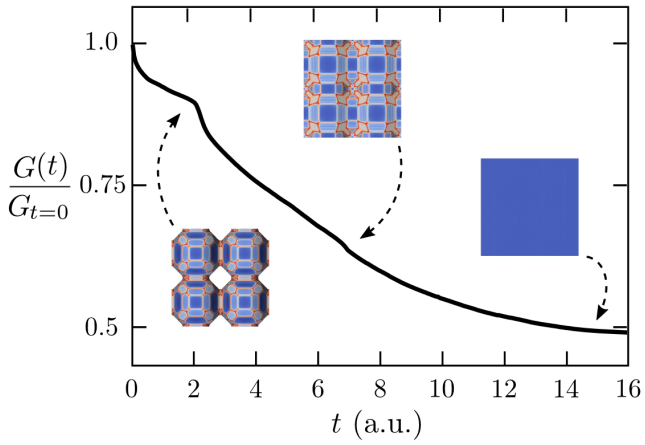

Figure 6.10: Surface energy decrease during the evolution by surface diffusion for the simulation of crystal coalescence reported in *Fig.* 6.9. Insets show the morphology at representative stages.

6.3 Insights on the coalescence process

In *Sect*. 6.2 we presented the general mechanism of coalescence induced by annealing closely spaced crystals. Such a process, originating from the enlargement of individual crystals, is affected by the features of the crystals arrangement and on the shape of the as-grown structures. For instance, a trivial dependence is represented by the distance of the vertical crystals after the growth, as for trenches larger than 2 μm (as in *Fig*. 6.1 with trenches of 3 μm) the lateral expansion required to obtain the coalescence is larger and the merging is expected to occur at later stages with respect to the case of *Fig*. 6.7 deeply analysed in *Sect*. 6.2. Notice that, as shown for instance in the 2D simulation of *Fig*. 6.2, the lateral expansion is not always sufficient to close the gap between crystals, so that a maximum distance exists over which coalescence mechanism is not obtained. In this section, the influences on the coalescence process given by the initial morphology and substrate features are discussed. Here, for the sake of simplicity, we focus our attention on evolution with isotropic surface energy. Indeed, the evolution with an anisotropic $\gamma(\hat{\mathbf{n}})$ has been proven to deliver the same qualitative evolution as discussed in the previous sections. Some details about the material quality assessment of the suspended networks and films originating by the coalescence are also reported in *Sect*. 6.3.4.

6.3.1 Infuence of the as-grown crystal morphology

The coalescence mechanism discussed so far appears as a general behavior. However, we noticed that the role of the chemical potential is crucial, as it determines the dynamics along the surface. Different initial profiles, despite are not expected to affect the occurrence of coalescence, may influence the timescale of the process as the μ distribution at the surface would be different. A proof of concept of this is provided in *Fig*. 6.11 where surface diffusion evolution is considered for the morphologies obtained by the growth at 450°C and 500°C, which are expected to be slightly different [20]. In particular, a pyramidal top is obtained by the growth at 500°C while a large [001] facet is observed at 450°C. Notice that, the section of the morphology at 500°C is closer to a rounded shape, therefore showing smaller curvature gradients than

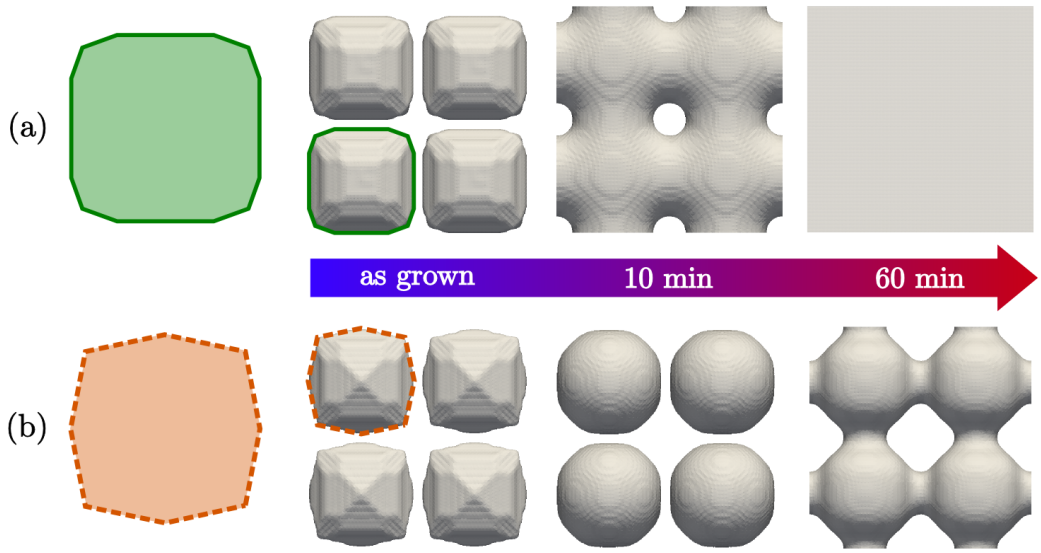

Figure 6.11: Influence of the as-grown crystal morphology on the coalescence process. (a) Top-view morphology of the crystals obtained by Ge deposition on pillar-patterned Si substrate as in *Fig.* 6.7 at 450°C (left, green solid line) and surface diffusion evolution (right). (b) Top-view morphology obtained as in panel (a) with a growth temperature of 500°C (left, orange dashed line) and surface diffusion evolution (right).

the profile obtained at lower temperatures. Indeed, slower evolution is observed for such a morphology, which does not reach the full coalescence achieved for the crystal grown at 450°C after a simulation time which reproduce the annealing for 60 min. Notice that, coalescence of the structures is still observed at later stages, despite it results delayed.

6.3.2 Influence of the substrate pattern

An influence of the size and the arrangement of the Si pattern on the coalescence mechanism is also expected. In *Fig.* 6.12 the coalescence of Ge crystals grown on 8 μm tall, 5×5 μm wide Si pillars separated by 2 μm trenches is shown. In this figure both the experiments and the corresponding PF simulations are reported. The latter is performed as in *Sects.* 6.1.2 and 6.2 by considering initial profile resembling the experimental systems. From *Fig.* 6.12 it can be noticed that, despite the coalescence mechanism ends up with a suspended layer, the contact process is however found to differ from the case with 2×2 μm^2 Si pillars. Indeed, as shown by the experiments in *Fig.* 6.12(a) after annealing for 10 min, the crystals do not touch at the middle of sidewalls, but coalescence starts close to the corners. A dedicated simulation is illustrated in *Fig.* 6.12(b) and *Fig.* 6.12(c) with perspective and top views, respectively. It shows that the experimental evidence is compatible with the surface diffusion evolution which actually forms two bridges close to the edges of the structure. On larger patterns, indeed, the rounding of such edges produces an accumulation of the material in their surroundings. On the crystal grown on 2×2 μm^2 Si pillars this accumulation does not involve enough material to close the gap between crystals while it does when considering large patterns as the one in *Fig.* 6.12(a). In order to observe this peculiar enlargement at the vertical edges, we can look to a similar sample with larger trenches as reported in *Fig.* 6.12(d). Here, both by experiments (EXP) and

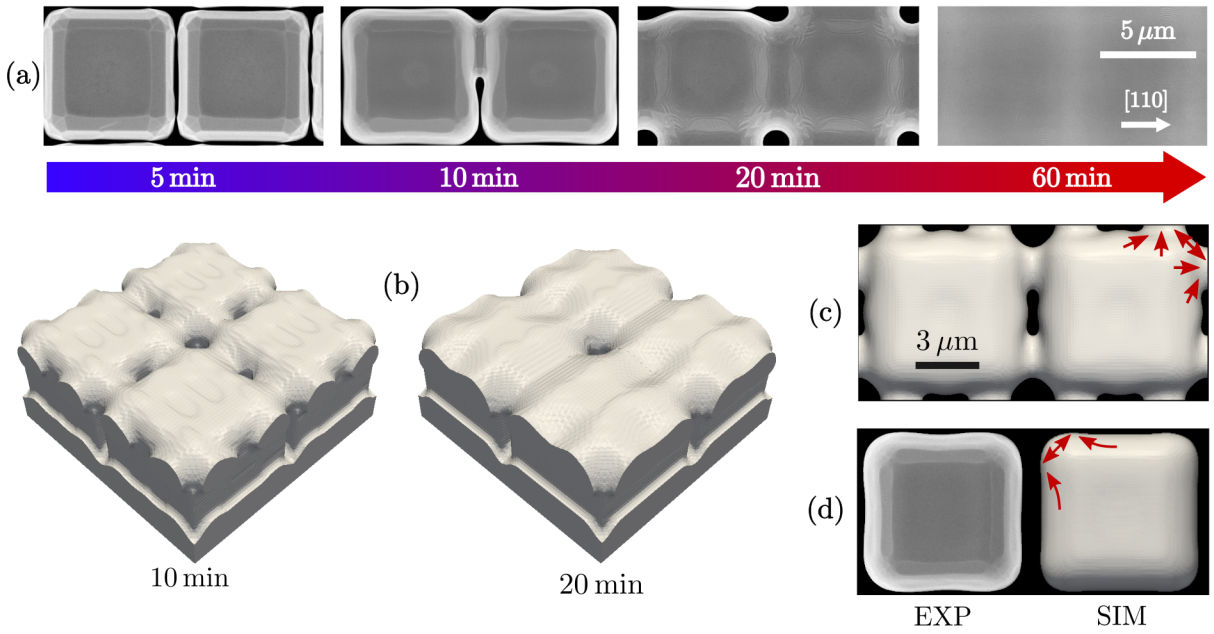

Figure 6.12: Annealing of Ge crystals grown on large Si pillars. (a) Top SEM images of Ge crystals, grown at 450°C on 8 μm tall, 5×5 μm^2 wide Si pillars separated by 2 μm trenches, after annealing experiments. Time indicates the durations of the annealing. (b) Representative steps of the PF simulation of surface diffusion reproducing the features of panel (a). (c) Top view of the PF simulation at $t \sim 10$ min. (d) Outcome of annealing experiment (left) and simulation (right) for crystals grown on Si pillars as in panel (a) with 3 μm trenches. Red arrows illustrate the material flux.

simulations (SIM), it is possible to observe such an accumulation of material close to the edges. This localized enlargement is enough to close the gap between crystal where 2 μm trenches are considered due to the smaller distance between crystals. As shown by the simulations in *Fig.* 6.12(b) corresponding to annealing for 20 min, the holes between the two contact points are filled at later stages, and then the evolution is expected to proceed in a very similar way to the ones discussed in the previous section as actually observed for experiments in *Fig.* 6.12(a).

Differences in patterning can also involve a change in the crystal arrangement. In *Fig.* 6.13 the evolution of two different arrangements of VHEs is shown by PF simulations. Single crystals are modeled with a simplified, cylindrical shape, and arranged in a square and a centered rectangular pattern. Periodic boundary conditions are assumed as in *Sect.* 6.2. Coalescence obtained on such initial structures leads to merged structures with different topology. This behavior is again mainly determined by the differences in the distance between crystals. In the squared-pattern arrangement, each structure has four nearest neighbors and coalescence occurs at the same time (in the idealized simulation) along four directions. Conversely, in the centered rectangular pattern, only two nearest neighbor exist and coalescence due to lateral expansion, i.e. due to the closing of the gaps, starts with these crystals. Notice that an interesting behavior is present for such a pattern. Once the bridges are formed, they attract material from the crystals because of the strong local curvature (see also *Fig.* 6.8), thus preventing the formation of other contact points in the perpendicular direction. This would results in the formation of suspended ridges-like structures as directly shown in *Fig.* 6.13(b). More in general, these sim-

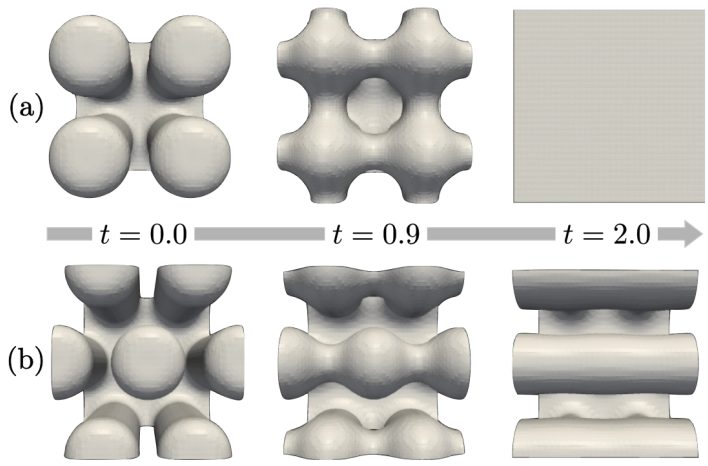

Figure 6.13: Comparison between the evolution by surface diffusion of crystals with (a) squared and (b) centered-rectangular arrangements. Time is expressed in arbitrary units.

ulations indicate that when a contact point is formed, the coalescence along other directions is delayed and may be also prevented. This is useful in the interpretation of experiments where, due to the complexity of the system, asymmetric behavior are always observed. If asymmetries are present in the as-grown sample, e.g. for inherent fluctuation in the deposition flux or imprecisions in the pattern fabrication, and coalescence starts in one specific direction, then all the other ideally equivalent directions for coalescence may be significantly affected. This is for instance observed in the early stages of the coalescence in *Fig.* 6.7.

6.3.3 Coalescence of crystal blocks

The patterns investigated so far have been considered to be periodic in the in-plane directions. Here we inspect what should be the outcome of the experiments when considering coalescence on a finite number of VHEs, i.e. by annealing Ge crystals grown on Si pillars arranged in blocks. In this configuration asymmetries naturally arise also in the idealized conditions of the simulations. In *Fig.* 6.14 an arrangement of 6×6 blocks, modeled as simple cylinders, is considered in a squared pattern. Periodic conditions are assumed but the separation between different blocks is set to be double with respect the separation of single crystals within the block. The evolution with a larger substrate surrounding the blocks leads to a symmetry breaking and coalescence occurs first at the edges between crystals at the boundary ($t = 0.6$). Indeed, slightly larger expansion is observed at the edges of the block. Curvatures in the trenches within the block show larger (negative) values than the region separating different blocks, so that they recall more material thus delaying the enlargement of the structures with respect to borders. At later stages, merging is obtained also within the block and a suspended film with cavities forms ($t = 0.8$). The holes are then filled as observed in the simulation of *Fig.* 6.6 but it occurs in three different stages. First, the hole between the inner crystals are closed ($t = 1.42$), then the process is extended to the cavities close to the edges of the block ($t = 1.46$), and eventually to those at the corners ($t = 2.0$). This can be easily explained by considering the early coalescence at the edges and the material flux at the surface as also discussed for the centered rectangular pattern of *Fig.* 6.13(b). Indeed, the formation of bridges at the edges recalls material, producing

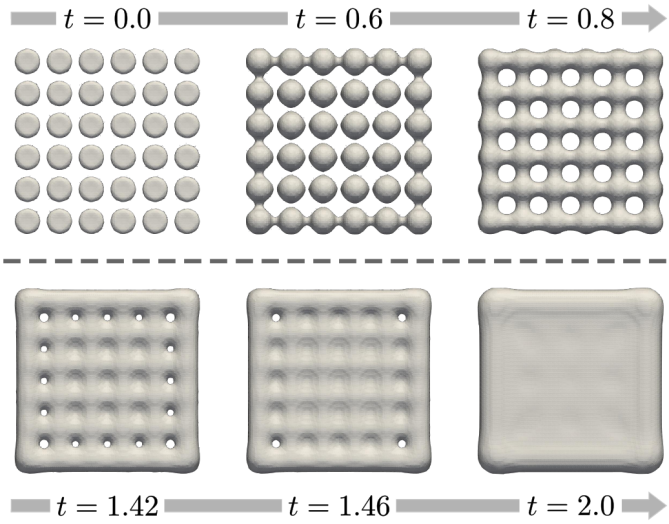

Figure 6.14: PF simulation of the evolution by surface diffusion of a block made of 6×6 crystals. Representative stages are reported, illustrating asymmetries in the coalescence process. Time is expressed in arbitrary units.

an increasing of the distance from the internal rows, and hence leading to larger cavities. The same effect is even magnified at the corners, where curvatures are higher, producing a more important material redistribution that leads to a further delay in the filling of the holes. Due to this transport mechanism, a swelling effect at the edges of the structure is also obtained. Other simulations of ours indicate that the general trend concerning the onset of the coalescence and the hierarchy in the filling of surface cavities is independent on the number of pillars so that it can be considered as a general feature of the system.

6.3.4 Material quality of merged structures

As evidenced by the theoretical analysis reported in previous sections, even supported by experiments, the annealing of vertical Ge/Si structure may be used to fabricate suspended networks and films. These represent interesting systems as they originate from single crystals which are proven to have promising properties in terms of material quality and managing of extended defects [145] (see also *Sect*. 2.5.2). The analysis of defects in the merged structures has been performed by experiments as it is illustrated in Ref. [39] with several techniques. In particular, the merging of crystals grown at 500°C has been investigated as, thanks to the peculiar faceted morphology, it allows to have no dislocations in the top region of the crystal [21]. So that no defects are present in the region where coalescence occurs. When bridges are formed between crystals, also the resulting suspended network appears to be dislocation free, delivering a new solution for the formation of high-quality connected domains of Ge integrated in Si [39]. This paves the way for all the applications or the integrations of semiconductors which require dislocation-free surfaces and interfaces.

The analysis of the continuous suspended film, i.e. the final stages of the coalescence process discussed so far, was not possible as the experimental apparatus was limited to annealing of 60 min. This was not sufficient to provide the full coalescence of crystals with the pyramidal top, as illustrated and explained with simulations of *Fig.* 6.11. Conversely, the crystals with a

(001) facet at the top are expected to have dislocation reaching the upper portion of the crystals [21, 22] so that the suspended film originating from such structures shows high defectivity. Preliminary tests of ours, however, indicate that also when considering other crystals with a dislocation-free top and the full coalescence is reached, linear defects are formed at the filling of the holes, despite the suspended networks with holes in between are always found to be dislocation-free. Further optimization of the process and theoretical investigations are then required in order to solve this issue. A first attempt which directly originates from this thesis will consist of annealing the defect-free vertical structures reported in *Sect*. 4.4, to evaluate what is the outcome of the merging process where dislocation are not present also in the lower part of the crystals.

Notice that, when coalescence of vertical crystals occurs, the elastic relaxation provided by the lateral free surfaces is significantly affected. So that in VHEs where the compliance of buffer layers is exploited in order to have dislocation-free structures, the coalescence must be realized after growing a thick epilayer to ensure full relaxation in the merged regions. For VHEs as in *Fig*. 6.7 this issue is not present as plastic relaxation at the Ge/Si interface fully relieves the strain within the structure. Conversely, the formation of connected networks or layers reintroduces the presence of thermal strain as the cooling to room temperature of the samples is performed after the merging. This would lead to the presence of crack for thick layers. However, exploiting the model of *Sect*. 3.5, we can estimate a critical thickness in the order of 3-4 μm. Therefore, for a thickness of the merged region under such a size, a crack-free system is still expected. This feature is actually confirmed by experiments.

6.4 Coalescence during growth

In *Sects*. 6.1 and 6.2 we focused on Ge crystals grown on 2 μm and 3 μm trenches. Actually, vertical Ge structures can be grown also on pillar-patterned substrates with thinner trenches. The morphology of Ge crystals grown at 490°C on 8 μm tall and 2×2 μm^2 wide Si pillars with 1 μm trenches are shown in *Fig.* 6.15(a). Separated crystals are obtained with a morphology close to the one of *Fig.* 6.1(a), exhibiting, in turn, smaller gaps between crystals than the as-grown sample in *Fig.* 6.7. A sample obtained with a higher deposition temperature of 550°C is shown in *Fig.* 6.15(b). This growth condition actually yields to a suspended layer where crystals are directly merged during the Ge deposition, at variance with the self-aligned growth. Despite the process involves also the growth kinetics, the final structure shows strong similarities to the ones obtained just by post-growth annealing.

Other growth results, leading to the coalescence directly during the Ge deposition are shown in *Figs.* 6.15(c)-6.15(h). Also in these experiments the similarity with the annealing-driven coalescence is compelling. In particular, *Fig.* 6.15(c) and *Fig.* 6.15(d) shows the result of Ge deposition at 550°C on 2×2 μm^2 Si pillars spaced by 1 μm wide trenches with squared and centered-rectangular arrangement, respectively. The merged structure is actually well represented by simulation results of *Fig.* 6.13, where the evolution by surface diffusion of simplified pillars have been considered. *Figs.* 6.15(e) and 6.15(f) show SEM top-view and cross-section of a suspended Ge film obtained by 8 μm Ge deposition at 600°C on 2×2 μm^2 wide Si pillars,

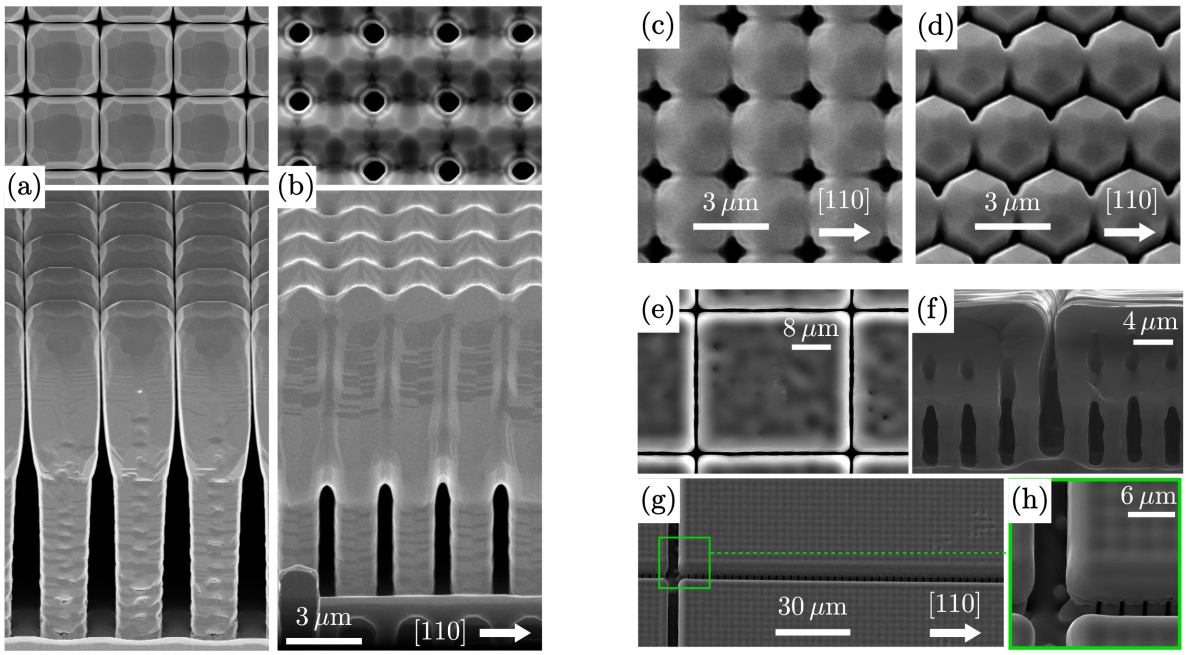

Figure 6.15: Coalescence of Ge crystals during growth. Top and lateral SEM images of 8 μm Ge deposition by LEPECVD at (a) 490°C and (b) 550°C on 8 μm tall, 2×2 μm^2 large Si pillars, spaced by 1 μm wide trenches. Top SEM image of the structure resulting after 5 μm Ge deposition at 550°C on the same Si pillars as in panel (b) with (c) squared and (d) centered-rectangular arrangement. (e) Top and (f) cross-section SEM images of the suspended Ge film obtained by 8 μm Ge deposition at 600°C on blocks of 10×10 Si pillars. Blocks are separated by 4 μm wide trenches. (g) Top SEM image of 8 μm Ge deposition at 600°C on 300 μm wide blocks formed by 2×2 μm^2 large Si pillars spaced by 1 μm trenches. Blocks are separated by 8 μm wide trenches. (h) Magnified view of the corner region in panel (g) highlighting a swelling effect at the sidewalls. After the growth, samples were annealed by six thermal cycles ranging from 600°C to 800°C.

arranged in 10×10 blocks with a spacing of 2 μm. Blocks are separated by 4 μm. Notice that the same trenches as in *Fig.* 6.7 are present here, but the temperature is higher (of ∼100°C). Suspended structures originating by the deposition of Ge are also shown in *Figs.* 6.15(g)-6.15(h), where an arrangement of 300×300 pillars has been considered with the same growth condition of *Figs.* 6.15(e) and 6.15(f).

It is worth mentioning that all the morphologies reported in *Fig.* 6.15 closely resemble the results of the previous sections. This strong similarity suggests the general mechanism is related to similar driving forces. Moreover, by looking at the result of *Figs.* 6.15(a) and 6.15(b) or in *Fig.* 6.15(f) compared to *Fig.* 6.7, the key enabling factor to induce coalescence during the growth can be identified as the increase of the growth temperature.

6.4.1 Analysis and simulations

The coalescence process occurring during the growth has been investigated by a dedicated experiment and it is here assessed by dedicated simulations. In *Fig.* 6.16(a) we show the cross-section SEM image of the structure obtained by the Ge deposition on a Si pattern as in *Fig.* 6.15(a). Thin layers (with a thickness of a few nm) of a SiGe alloy with 10% of Si content

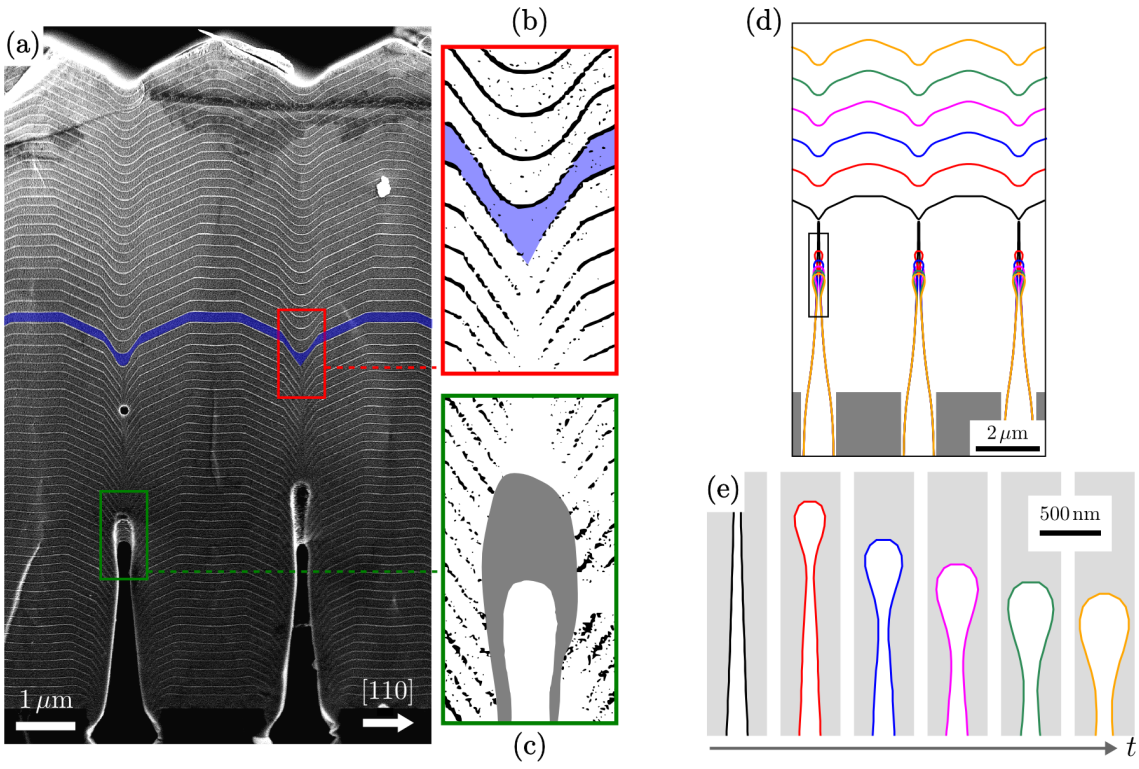

Figure 6.16: Analysis of the coalescence process during growth. (a) Lateral SEM image of crystals fusion with marker layers made of ∼10 nm $Si_{0.1}Ge_{0.9}$. The deposition is performed at 675°C and the final thickness of the Ge crystals is ∼10 µm. The substrate is made of 8 µm tall, 2×2 µm^2 large Si pillars, spaced by 1 µm wide trenches. The blue region shows the profile when coalescence occurred. (b) Magnified region showing the onset of the coalescence with enhanced contrast. (c) Detail of the morphology at the bottom of the coalesced region with enhanced contrast. (d) Simulation of deposition including surface diffusion. The initial profile is set to match the blue profile in panel (a). The growth rate is set to 4 nm/s and the profiles are shown every 1 µm. Incorporation factors χ for (001), {113} and {111} facets are set to 0.91, 0.87 and 0.99 respectively. The diffusion rate is set to $7.5{\cdot}10^{-7}$ cm^2/s, selected to match the experimental results in *Fig.* 6.15(b). (e) Detail of the simulation in panel (d) at the bottom of the coalesced region.

has been deposited at regular intervals during the growth of pure Ge. These layers allow the growing profile to be tracked as they offer a different contrast in the SEM image, without significantly affecting the growth dynamics. In order to compensate the lower mobility of the Si [192], the temperature of the deposition is increased with respect to previous experiments, up to 675°C. The facets evolution highlighted by markers in the growing profile is the typical one usually observed for this process (for a detailed discussion see Ref. [20]).

A deeper analysis of the marker lines permits to identify the transition from individual crystals to a continuous profile. In particular, this is made evident in *Fig.* 6.16(b), where the markers at the coalesced region are highlighted by black-and-white contrast. The transition between separated markers and a continuous line is highlighted by the blue region both in *Figs.* 6.16(a) and 6.16(b). When coalescence occurs, a single growth front is formed with a faceted outline. Under the merging point, a zipping is recognized producing a smeared region where the markers are not defined, as shown in *Fig.* 6.16(c). This is a strong indication of a

diffusion mechanism and a similarity with the zipping stage discussed in Sect. 6.2 is evident.

In order to investigate this mechanism, we consider the 2D model reported in [19], which is able to track the evolution of crystals during the deposition by LEPECVD. It consists of an explicit description of the surface profile during growth as introduced in Sect 1.5. An effective calculation of the flux shielding by the growing profile exploiting a ray-tracing algorithm (similar to the one mentioned in *Sect*. 5.4) is also included. The incorporation factors $\chi(\hat{\mathbf{n}})$ are estimated from the marker sequence to provide the best fit of the experimental evolution, consistently with the values in Ref. [20]. In order to include the description of surface diffusion, it has been coupled with the calculus of the surface curvature as performed in *Sect*. 6.1.1 with a realistic diffusion rate, incorporated in the mobility M of $\sim 10^{-7}$. The results starting from the coalesced profile (blue region in *Fig*. 6.16(a)) are reported in *Fig*. 6.16(d). The correspondence between the simulated profiles and the marker lines allows the profile evolution to be identified as the superposition of growth and surface diffusion. At the top of the structure, the crystal growth is dominating the dynamics with the formation of $\{113\}$ facets in agreement with both *Figs*. 6.15(b), 6.15(c) and 6.16(a). Due to the formation of such $\{113\}$ pyramids, which offer a low height-to-base aspect ratio, the shielding effects are not affecting too much the evolution. Indeed, despite the flux shielding from the lateral facets, the rounding is suppressed also above the bridges and the profile grow almost conformally. Below the coalesced region, no external material flux is present due to the shielding of the merged layer. Indeed, the surface diffusion mechanism dominates. An enlarged view of the zipping under the bridge is shown in *Fig*. 6.16(e). A rounded region forms immediately and a fast zipping is observed at the first stage due to the high local curvature occurring at the merging. Then, its velocity drops as the curvature becomes smaller. Notice that the competition between surface diffusion and growth kinetics can be generally modified by the growth conditions [41], i.e. temperature and deposition flux. Therefore, the morphology of the structure can be tuned by such parameters.

According to the 2D simulation of *Fig*. 6.16(d), the evolution during growth can be effectively described as the superposition of material deposition and surface diffusion. The latter is thermally activated as it is related to the presence of adatoms at the surface, whose density increases with temperature [33]. This can be modeled by considering a mobility coefficient for material fluxes at the surface (see *Sect*. 1.4) which scales according to the considered temperature. In *Fig*. 6.17 the growth on a patterned substrate is reproduced by means of illustrative PF simulations to cope with three-dimensionality and possible merging of the structure. A simplified vertical flux is considered while two different values of the mobility coefficient are set. As can be readily observed in *Fig*. 6.17(a), with a small mobility the surface diffusion mechanism is negligible and vertical growth is obtained. Conversely, by increasing the mobility factor, surface diffusion become more important as reported in *Fig*. 6.17(b). So that a more pronounced enlargement of the structure is obtained during the deposition. This results in the coalescence of crystals and it is qualitatively in agreement with the experimental observation. It is worth recalling that the annealing at a very high temperatures was necessary to induce coalescence without deposition flux. Here just a small, but not negligible, contribution of surface diffusion is enough as the gap closure is also facilitated by deposition on a crystal which is

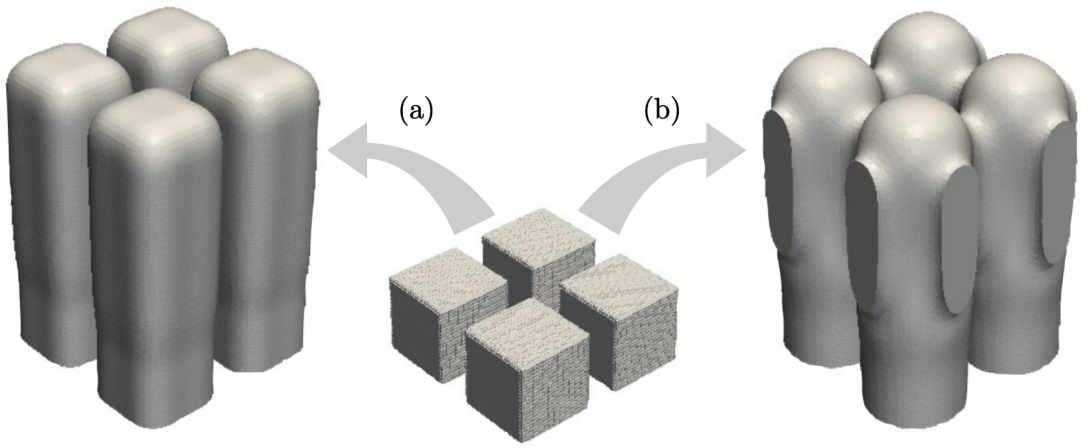

Figure 6.17: 3D PF simulations involving both surface diffusion and growth kinetics from vertical deposition with $\Phi = 1$. (a) $M_0 = 10^{-4}$ and (b) $M_0 = 5 \cdot 10^{-4}$.

undergoing to a rounded shape. Notice that a careful modeling of the real experiments should be considered, involving the shadowing algorithm introduced in *Sect*. 5.4. This would result in a better description of the timescale for the coalescence as confirmed by preliminary tests of ours. However, this cannot be considered without taking into account the presence of facets (see *Sect*. 5.5.2), achievable with a reliable 3D distribution of $\chi(\hat{\mathbf{n}})$ (with a similar approach to the one reported in *Sect*. 5.3.3 to determine the $\gamma(\hat{\mathbf{n}})$ values for Ge). Such an accurate modeling is still lacking and may consist of an interesting research topic for the future. Therefore, we refrained from adding complexity to the PF simulations, including only the main physical contribution to qualitatively describe the competing mechanisms. In conclusion, as experimental evidence of *Figs.* 6.15(a) and 6.15(b) is here reproduced, the role of the temperature in the merging of crystals during growth is assessed.

Conclusions

The elastic properties and the evolution of vertical heterostructures were modeled by continuum approaches, in order to provide a deep understanding of the physical mechanisms and suitable tools for their investigations. The study was focused on the technology relevant Ge/Si system, looking for new solutions in limiting the plastic relaxation or, at least, allowing for the confinement of defects at the interface between different materials. Several numerical simulations have been performed to assess the reliability of the models, to explain the outcomes of targeted experiments and to suggest the design of structures with novel properties. Nanostructures with large aspect ratios were proven to be coherent under certain sizes in agreement with the well-known properties observed for nanowires [18]. Moreover, the increasing of the sizes of coherent structures was shown to be possible, providing a lowering of the effective misfit across interfaces [28, 34, 37]. According to the reported results, when this is achieved by a proper configuration of buffer layers, the size can be significantly increased. Indeed, the fine tuning of buffer-layer sizes and Ge contents was demonstrated to allow for coherent structures up to the micron scale [40]. This result delivers Ge/Si micrometer-wide heterostructures with unprecedented material quality. Unfortunately, separated crystals, even for sizes of a few microns, are not suited for all the applications developed for planar films. Therefore, we inspected under what conditions it is possible to transfer the good properties of VHEs to planar configurations. The post-growth annealing of vertical crystals revealed to be effective in inducing coalescence with the formation of suspended networks and, eventually, layers [39]. Despite the experimental proof was given on pure Ge pillars, where misfit dislocations are present at the Ge/Si interface, the merged structures revealed to be dislocation-free at the top when formed by bridges [39]. Experimental studies are still needed for the assessment of the quality for fully-merged layers.

The investigation of VHEs coherency was carried out using the linear elasticity theory equations, solved by Finite Element Method (FEM) simulations as proposed in Ref. [146]. In particular, an original quasi-3D approach was developed as reported in *Ch*. 3. It allowed for the calculation of the formation energy for dislocations, delivering the estimation of critical parameters according to thermodynamics [28]. Such critical parameters were determined for a single-layer structure, made of a SiGe layer on a Si pillar, and then generalized to multilayer configurations. Moreover, the possibility to grow coherent structures at any size, when considering a proper grading of the Ge content, was reported. A convenient semi-analytical expression delivering the parameters for the achievement of such dislocation-free VHEs was also introduced. In addition, we reported the simplified evaluation of the onset for crack insertion in heteroepitaxial

films. As illustrated in *Ch*. 4, the modeling of the plasticity onset was applied to the investigation of competitive relaxation mechanisms in real heterostructures. Proper extensions were implemented to account for a more accurate description of the experimental systems. It is worth pointing out that the growth of dislocation-free microstructures of *Sect*. 4.4 were directly stimulated by the theoretical predictions about coherency when grading the Ge content during the growth.

The evolution in time of vertical micro-crystals during annealing was modeled with the aid of the phase-field method and FEM simulations. The developed approach is based on a standard PF model [29], that was extended in order to account for the morphological evolution of realistic structures. In particular, we addressed the modeling of the surface diffusion mechanism with a general description of anisotropic surface energies as reported in *Ch*. 5 [32]. Other extensions are also proposed for the modeling of crystal growth, dealing with the description of material flux shielding by patterned substrates during deposition, and with the tracking of faceted crystal growth. As discussed in *Ch*. 6, PF simulations allowed the evolution driven by annealing of single structures to be described. Then, the coalescence mechanism for crystal arrays, resulting in the formation of a suspended film, has been predicted. Such an evolution was confirmed by dedicated experiments and leads to the fabrication of a promising system for the high-quality heterogeneous integration of semiconductors [39]. Moreover, the evidence delivered by this investigation has been exploited to assess the coalescence occurring for closely spaced crystals during growth at high temperature [41].

Notice that, despite the approaches reported in this thesis have been mostly used to describe Ge/Si systems, they are defined in a rather general way and can be readily applied and extended to other similar systems. For the modeling of the plasticity onset, this can be done by including the proper elastic constants, dislocation types, and geometry of the system. For the morphological evolution by the PF model, when surface diffusion is the mechanism responsible for the evolution, the extension to other systems can be achieved by accounting for the proper definition of the surface energy. Within such a modeling, a fine tuning of parameters would also allow for a careful investigation of competition between surface diffusion and growth kinetics.

It is worth mentioning that the aforementioned results open interesting perspectives for future studies. Indeed, the extensions of the model for the evaluation of plasticity onset reported in *Ch*. 4, as for instance the description of realistic Ge content distributions, can be the subject of dedicated theoretical analysis. Moreover, we proved that PF modeling dealing with three-dimensional geometries can be used for the investigation of realistic systems. So that future investigations can directly apply the developed methodology including further physical phenomena such as elasticity [158] or intermixing [160] for a thorough study of the evolution of nanostructured systems. Further investigations can be also focused on the application of the PF technique to the optimization of the growth process of VHEs. From the technological point of view, the assessment and the optimization of the material quality for the suspended films discussed in *Ch*. 6 will be the crucial task for the achievement of defect-free planar systems exploiting the material properties of isolated, vertical crystals.

List of Publications

- G. M. Vanacore, M. Chaigneau, N. Barrett, M. Bollani, F. Boioli, **M. Salvalaglio**, F. Montalenti, N. Manini, L. Caramella, P. Biagioni, D. Chrastina, G. Isella, O. Renault, M. Zani, R. Sordan, G. Onida, R. Ossikovski, H.J. Drouhin and A. Tagliaferri.
  Hydrostatic strain enhancement in laterally confined SiGe stripes.
  Phys. Rev. B **88**, 115309 (2013).

- A. Marzegalli, M. Brunetto, **M. Salvalaglio**, F. Montalenti, G. Nicotra, M. Scuderi, C. Spinella, M. De Seta and G. Capellini.
  Onset of plastic relaxation in low-temperature Ge growth on Si(001): atomic-scale microscopy and dislocation modeling.
  Phys. Rev. B **88**, 165418 (2013).

- F. Montalenti, **M. Salvalaglio**, A. Marzegalli, P. Zaumseil, G. Capellini, T. U. Schlli, M. A. Schubert, Y. Yamamoto, B. Tillack and T. Schroeder.
  Fully coherent growth of Ge on free-standing Si(001) nanomesas.
  Phys. Rev. B **89**, 014101 (2014).

- A. G. Taboada, T. Kreiliger, C. V. Falub, F. Isa, **M. Salvalaglio**, L. Wewior, D. Fuster, M. Richter, E. Uccelli, P. Niedermann, A. Neels, F. Mancarella, J. Fompeyrine, B. Aln, L. Miglio, A. Dommann, G. Isella and H. von Känel.
  Strain relaxation on GaAs/Ge crystals on patterned Si substrates.
  Appl. Phys. Lett. **104**, 022112 (2014).

- F. Pezzoli, F. Isa, G. Isella, C.V. Falub, T. Kreiliger, **M. Salvalaglio**,R. Bergamaschini, E. Grilli, M. Guzzi, H. von Kanel, and Leo Miglio.
  Ge crystals on Si show their light.
  Phys. Rev. Applied **1**, 044005 (2014).

- **M. Salvalaglio** and F. Montalenti.
  Fine control of plastic and elastic relaxation in three-dimensional Ge/Si vertical heterostructures.
  J. Appl. Phys. **116**, 104306 (2014).

- **M. Salvalaglio**, R. Backofen, R. Bergamaschini, F. Montalenti and A. Voigt.
  Faceting of equilibrium and metastable nanostructures: a Phase-Field model of surface diffusion tackling realistic shapes.
  Cryst. Growth Des. **15**, 2787 (2015).

- D. Scarpellini, C. Somaschini, A. Fedorov, S. Bietti, C. Frigeri, V. Grillo, L. Esposito, **M. Salvalaglio**, A. Marzegalli, F. Montalenti, E. Bonera, P. G. Medaglia and S. Sanguinetti.
  InAs/GaAs sharply-defined axial heterostructures in self-assisted nanowires.
  Nano Letters, **15**, 3677 (2015).

- **M. Salvalaglio**, R. Bergamaschini, F. Isa, A. Scaccabarozzi, G. Isella, R. Backofen, A. Voigt, F. Montalenti, G. Capellini, T. Schroeder, H. von Knel and L. Miglio.
  Engineered coalescence by annealing 3D Ge microstructures into high-quality suspended layers on Si.
  ACS Appl. Mater. Interfaces, **7**, 19219 (2015).

- N. Gang, G. Capellini, T. Niermann, G. Lupina, **M. Salvalaglio**, A. Marzegalli, M. A. Schubert, P. Zaumseil, M. Lehmann, F. Montalenti, Y. Xie and T. Schroeder.
  Photodetection in hybrid single layer graphene/fully coherent Ge island nanostructures selectively grown on Si nano-tip patterns.
  ACS Appl. Mater Interfaces. In press.

- F. Isa, **M. Salvalaglio**, Y. A. Rojas Dasilva, M. Medua, M. Barget, A. Jung, T. Kreiliger, G. Isella, R. Erni, F. Pezzoli, E. Bonera, P. Niedermann, P. Groning, F. Montalenti and H. von Knel.
  Highly mismatched, dislocation-free SiGe/Si(001) heterostructures.
  Advanced Materials. In press.

- A. G. Taboada, M. Meduna, **M. Salvalaglio**, F. Isa, T. Kreiliger, C. V. Falub, E. Barthazy Meier, E. Müller, L. Miglio, G. Isella, and H. von Känel.
  GaAs/Ge crystals grown on Si substrates patterned down to the micron scale.
  Journal of Applied Physics. In press.

- R. Bergamaschini, **M. Salvalaglio**, A. Scaccabarozzi, F. Isa, C. V. Falub, G. Isella, H. von Känel, F. Montalenti, L. Miglio.
  Temperature-controlled coalescence during the growth of Ge crystals on deeply patterned Si substrates.
  Submitted.

- R. Bergamaschini, **M. Salvalaglio**, R.Backofen, A. Voigt, F. Montalenti.
  Continuum Modeling of Heteroepitaxy.
  Submitted.

- **M. Salvalaglio**, R. Bergamaschini, R.Backofen, A. Voigt, F. Montalenti, L. Miglio.
  Phase-field simulations of faceted Ge/Si-crystal arrays, merging into a suspended film.
  Submitted.

Acknowledgements

First and foremost, I would like to acknowledge my supervisor, Prof. Leo Miglio, who gave me the opportunity to carry on the Ph.D. research activity in his group. I thank him for his support and all the valuable advice.

Special thanks are due to Prof. Francesco Montalenti, for the support since the very beginning of my Master thesis and the work done together during these years.

I am deeply grateful to Prof. Axel Voigt who hosted me in his research group at TU-Dresden, teaching me about phase field modeling and actively supporting my work. I sincerely thank Rainer Backofen and all the people of the Institute of Scientific Computing for their invaluable help in working on the AMDiS code and for sharing with me a wonderful period in Dresden.

I would like to show my gratitude to the people who contributed to the experimental activities at L-NESS, ETH-Zürich and Leibnitz-Institute IHP. Their work has been extremely precious for having interesting hints during these years and for testing our daily work. In particular, I would like to thank Fabio Isa, Andrea Scaccabarozzi, Prof. Stefano Sanguinetti, Prof. Giovanni Isella, and Prof. Hans von Känel. Moreover, I am indebted to Prof. Thomas Schroeder e Prof. Giovanni Capellini, for their warm hospitality during my visits at IHP, the trust and the support.

This thesis, along with these nice years, would not have been possible without the people I met in the group of Prof. Miglio. In particular, I owe my deepest gratitude to Roberto Bergamaschini, for his constant support, help and friendship. Moreover, I would like to thank Francesca Boioli, who first introduced me in materials science research, and Anna Marzegalli for her advice. I also thank all the other people that have been part of the group - Matteo, Daniele, Riccardo, Andrea, Jacopo, Iacopo, Gabriele, Gaia, up to the newcomers Marco e Fabrizio - together with the many people of the materials science department met outside the office. Sharing coffee breaks, nights, seminars and much more has made these years amazing.

At the end of this, let's say, journey, I have to thank the people who more than anyone made it possible. My parents, Tina and Silvano, for the tireless support in every moment and for being always a great example to follow. My brother, Matteo, along with Chicca e Giacomo, for being there every time, and for showing me that there are things that will never change. A thought naturally goes to my best friends, for the wonderful experiences lived together and for all the time shared.

Last lines are for Marta, who painted these years with wonderful colors, in a way I would have never imagined before. Thanks.

Marco

Bibliography

[1] J. Bardeen and W. H. Brattain, *Physical Review* **74**, 230 (1948).

[2] D. J. Paul, *Semiconductor Science Technology* **19**, R75 (2004).

[3] D. J. Paul, *Advanced Materials* **11**, 191 (1999).

[4] T.-C. Chang, F.-Y. Jian, S.-C. Chen, and Y.-T. Tsai, *Materials Today* **14**, 608 (2011).

[5] M. Dresselhaus *et al.*, *Advanced Materials* **19**, 1043 (2007).

[6] E. C. Garnett, M. L. Brongersma, Y. Cui, and M. D. McGehee, *Annual Review of Materials Research* **41**, 269 (2011).

[7] I. Prieto *et al.*, *Applied Physics Letters* **94**, 191102 (2009).

[8] J. Michel, J. Liu, and L. C. Kimerling, *Nature Photonics* **4**, 527 (2010).

[9] R. Pillarisetty, *Nature* **479**, 324 (2011).

[10] D. Dunstan, *Journal of Material Science - Materials in Electronics* **8**, 337 (1997).

[11] J. E. Ayers, *Heteroepitaxy of Semiconductors: Theory, Group and Characterization* (CRC Press - Taylor & Francis Group, 2007).

[12] International technology roadmap for semiconductors: http://www.itrs.net.

[13] A. D. Franklin *et al.*, *Nano Letters* **12**, 758 (2012).

[14] L. A. Ponomarenko *et al.*, *Science* **320**, 356 (2008).

[15] M. Fuechsle *et al.*, *Nature Nanotechnology* **7**, 242 (2012).

[16] S. Yip, *Nature Materials* **2**, 3 (2003).

[17] G. Medeiros-Ribeiro, A. M. Bratkovski, T. I. Kamins, D. A. A. Ohlberg, and R. S. Williams, *Science* **279**, 353 (1998).

[18] F. Glas, *Physical Review B* **74**, 121302 (2006).

[19] C. V. Falub *et al.*, *Science* **335**, 1330 (2012).

[20] R. Bergamaschini *et al.*, *Surface Science Reports* **68**, 390 (2013).

[21] A. Marzegalli *et al.*, *Advanced Materials* **25**, 4408 (2013).

[22] F. Isa *et al.*, *APL Materials* **1**, 052109 (2013).

[23] G. Crabtree and J. Sarrao, *MRS Bulletin* **37**, 1079 (2012).

[24] S. Yip and M. P. Short, *Nature Materials* **12**, 774 (2013).

[25] L. Landau and E. Lifshitz, *Theory of elasticity*, 3rd ed. (Butterworth Heinemann, Oxford, 1986).

[26] J. P. Hirth and J. Lothe, *Theory of Dislocations* (Krieger Publishing Company, 1992).

[27] D. Hull and D. J. Bacon, *Introduction to dislocations* (Pergamon Press, 1984).

[28] M. Salvalaglio and F. Montalenti, *Journal of Applied Physics* **116**, 104306 (2014).

[29] Bo Li, J. Lowengrub, A. Rätz, and A. Voigt, *Communications in Computational Physics* **6**, 433 (2009).

[30] N. Provatas and K. Elder, *Phase-field Methods in Materials Science and Engineering* (Wiley-VCH, 2010).

[31] S. Vey and A. Voigt, *Computing and Visualization in Science* **10**, 57 (2007).

[32] M. Salvalaglio, R. Backofen, R. Bergamaschini, F. Montalenti, and A. Voigt, *Crystal Growth & Design* **15**, 2787 (2015).

[33] W. W. Mullins, *Journal of Applied Physics* **28**, 333 (1957).

[34] F. Montalenti *et al.*, *Physical Review B* **89**, 014101 (2014).

[35] A. G. Taboada *et al.*, *Applied Physics Letters* **104**, 022112 (2014).

[36] D. Scarpellini *et al.*, *Nano Letters* **15**, 3677 (2015).

[37] G. Niu *et al.*, Photodetection in hybrid single layer graphene/fully coherent Ge island nanostructures selectively grown on Si nano-tip patterns. *ACS Applied Materials & Interfaces*. In press.

[38] A. Taboada *et al.*, GaAs/Ge crystals grown on Si substrates patterned down to the micron scale. *Journal of Applied Physics*. In press.

[39] M. Salvalaglio *et al.*, *ACS Applied Materials & Interfaces* **7**, 19219 (2015).

[40] F. Isa *et al.*, Highly mismatched, dislocation-free SiGe/Si(001) heterostructures. *Advanced Materials*. In press.

[41] R. Bergamaschini *et al.*, Temperature-controlled coalescence during the growth of Ge crystals on deeply patterned Si substrates. *Submitted*.

[42] J. D. Eshelby, *Proceedings of the Royal Society of London A* **241**, 376 (1957).

[43] A. K. Head, *Proceedings of the Physical Society. Section B* **66**, 793 (1953).

[44] A. Marzegalli *et al.*, *Physical Review B* **88**, 165418 (2013).

[45] V. M. Kaganer, R. Köhler, M. Schmidbauer, R. Opitz, and B. Jenichen, *Physical Review B* **55**, 1793 (1997).

[46] R. Gatti, F. Uhlk, and F. Montalenti, *New Journal of Physics* **10**, 083039 (2008).

[47] E. Bonera *et al.*, *Applied Physics Letters* **103**, 053104 (2013).

[48] W. Cai, A. Arsenlis, C. R. Weinberger, and V. V. Bulatov, *Journal of the Mechanics and Physics of Solids* **54**, 561 (2006).

[49] A. A. Griffith, *Philosophical Transactions of the Royal Society of London A: Mathematical, Physical and Engineering Sciences* **221**, 163 (1921).

[50] A. Pimpinelli and J. Villain, *Physics of Crystal Growth* (Cambridge University Press, 1998).

[51] C. Herring, *Physical Review* **82**, 87 (1951).

[52] R. C. Cammarata, *Progress in Surface Science* **46**, 1 (1994).

[53] M. E. Gurtin, J. Weissmüller, and F. Larché, *Philosophical Magazine A* **78**, 1093 (1998).

[54] A. A. Stekolnikov, J. Furthmüller, and F. Bechstedt, *Physical Review B* **65**, 115318 (2002).

[55] M. J. Beck, A. van de Walle, and M. Asta, *Physical Review B* **70**, 205337 (2004).

[56] P. Müller and J. Metois, *Thin Solid Films* **517**, 65 (2008).

[57] G. Wulff, *Zeitschrift fur Krystallographie und Mineralogie* **34**, 449 (1901).

[58] J. W. Cahn and W. C. Carter, *Metallurgical and Materials Transactions A* **27**, 1431 (1996).

[59] D. W. Hoffman and J. W. Cahn, *Surface Science* **31**, 368 (1972).

[60] J. W. Cahn and D. W. Hoffman, *Acta Metallurgica* **22**, 1205 (1974).

[61] A. Wheeler, *Journal of Statistical Physics* **95**, 1245 (1999).

[62] R. F. Sekerka, *Journal of Crystal Growth* **275**, 77 (2005).

[63] D. Chandler, *Introduction to modern statistical mechanics* (Oxford University Press, 1987).

[64] L. Onsager, *Physical Review* **37**, 405 (1931).

[65] L. Onsager, *Physical Review* **38**, 2265 (1931).

[66] P. Politi, G. Grenet, A. Marty, A. Ponchet, and J. Villain, *Physics Reports* **324**, 271 (2000).

[67] W. Carter, A. Roosen, J. Cahn, and J. Taylor, *Acta Metallurgica et Materialia* **43**, 4309 (1995).

[68] J. J. Eggleston, G. B. McFadden, and P. W. Voorhees, *Physica D: Nonlinear Phenomena* **150**, 91 (2001).

[69] M. E. Gurtin, *Thermomechanics of evolving phase boundaries in the plane.* (Oxford University Press, New York, 1993).

[70] B. J. Spencer, *Physical Review E* **69**, 011603 (2004).

[71] A. Di Carlo, M. Gurtin, and P. Podio-Guidugli, *SIAM Journal on Applied Mathematics* **52**, 1111 (1992).

[72] M. E. Gurtin and M. E. Jabbour, *Archive for Rational Mechanics and Analysis* **163**, 171 (2002).

[73] A. A. Chernov, *Soviet Physics Crystallography* **7**, 728 (1963).

[74] F. C. Frank, On the Kinematic Theory of Crystal Growth and Dissolution Processes, in *Growth and Perfection in Crystals*, edited by T. D. Doremus R. H., Roberts B. W., John Wiley & Sons, New York, 1958.

[75] D. W. Shaw, *Journal of Crystal Growth* **47**, 509 (1979).

[76] G. Russo and P. Smereka, *SIAM Journal of Scientific Computing* **21**, 2073 (2000).

[77] S. Jones, L. Seidel, K. Lau, and M. Harold, *Journal of Crystal Growth* **108**, 73 (1991).

[78] C. Grossmann, H.-G. Roos, and M. Stynes, *Numerical Treatment of Partial Differential Equations* (Springer-Verlag Berlin Heidelberg, 2007).

[79] T. Witkowski, S. Ling, S. Praetorius, and A. Voigt, *Advances in Computational Mathematics* **41**, 1145 (2015).

[80] R. Asaro and W. Tiller, *Metallurgical Transactions* **3**, 1789 (1972).

[81] M. Grinfeld, *Journal of Nonlinear Science* **3**, 35 (1993).

[82] D. J. Srolovitz, *Acta Metallurgica* **37**, 621 (1989).

[83] J. Tersoff, A. W. Denier van der Gon, and R. M. Tromp, *Physical Review Letters* **72**, 266 (1994).

[84] R. Gatti, F. Pezzoli, F. Boioli, F. Montalenti, and L. Miglio, *Journal of Physics: Condensed Matter* **24**, 104018 (2012).

[85] F. Montalenti *et al.*, *Physical Review Letters* **93**, 216102 (2004).

[86] E. A. Fitzgerald, *Materials Science Reports* **7**, 87 (1991).

[87] Y.-W. Mo, D. E. Savage, B. S. Swartzentruber, and M. G. Lagally, *Physical Review Letters* **65**, 1020 (1990).

[88] D. J. Eaglesham and M. Cerullo, *Physical Review Letters* **64**, 1943 (1990).

[89] V. A. Shchukin and D. Bimberg, *Review of Modern Physics* **71**, 1125 (1999).

[90] J. Stangl, V. Holý, and G. Bauer, *Review of Modern Physics* **76**, 725 (2004).

[91] L. Miglio and F. Montalenti, Modeling the evolution of germanium islands on silicon(001) thin films, in *Silicon-germanium (SiGe) nanostructures: production, properties, and applications in electronics*, edited by Y. Shiraki and N. Usami, Woodhead Publishing - UK, 2011.

[92] G.-H. Lu, M. Cuma, and F. Liu, *Physical Review B* **72**, 125415 (2005).

[93] D. Migas, S. Cereda, F. Montalenti, and L. Miglio, *Surface Science* **556**, 121 (2004).

[94] G.-H. Lu, M. Cuma, and F. Liu, *Physical Review B* **72**, 125415 (2005).

[95] M. Brehm, H. Lichtenberger, T. Fromherz, and G. Springholz, *Nanoscale Research Letters* **6**, 70 (2011).

[96] J. T. Robinson, A. Rastelli, O. Schmidt, and O. D. Dubon, *Nanotechnology* **20**, 085708 (2009).

[97] P. Kratzer *et al.*, *Physical Review B* **73**, 205347 (2006).

[98] A. A. Stekolnikov and F. Bechstedt, *Physical Review B* **72**, 125326 (2005).

[99] J. Tersoff, *Applied Physics Letters* **83**, 353 (2003).

[100] B. J. Spencer, P. W. Voorhees, and J. Tersoff, *Physical Review Letters* **84**, 2449 (2000).

[101] B. J. Spencer, P. W. Voorhees, and J. Tersoff, *Physical Review B* **64**, 235318 (2001).

[102] F. Zipoli *et al.*, *Applied Physics Letters* **92**, 191908 (2008).

[103] M. Brehm *et al.*, *Applied Physics Letters* **93**, 121901 (2008).

[104] G. Katsaros *et al.*, *Physical Review B* **72**, 195320 (2005).

[105] G. Capellini *et al.*, *Journal of Applied Physics* **107**, 063504 (2010).

[106] M. A. Migliorato, A. G. Cullis, M. Fearn, and J. H. Jefferson, *Physical Review B* **65**, 115316 (2002).

[107] G. Hadjisavvas and P. C. Kelires, *Physical Review B* **72**, 075334 (2005).

[108] C. Lang, D. J. H. Cockayne, and D. Nguyen-Manh, *Physical Review B* **72**, 155328 (2005).

[109] B. J. Spencer, P. W. Voorhees, and J. Tersoff, *Physical Review B* **64**, 235318 (2001).

[110] Y. Tu and J. Tersoff, *Physical Review Letters* **98**, 096103 (2007).

[111] R. Bergamaschini *et al.*, *Physical Review Letters* **109**, 156101 (2012).

[112] M. Rondanini, S. Cereda, F. Montalenti, L. Miglio, and C. Cavallotti, *Surface and Coatings Technology* **201**, 8863 (2007).

[113] M. Rondanini *et al.*, *Journal of Applied Physics* **104**, 013304 (2008).

[114] A. Marzegalli *et al.*, *Physical Review Letters* **99**, 235505 (2007).

[115] J. W. Matthews and A. E. Blakeslee, *Journal of Crystal Growth* **27**, 118 (1974).

[116] Y. Zhu *et al.*, *Acta Materialia* **59**, 812 (2011).

[117] F. Boioli, *Dislocation modelling in realistic Si-Ge nanostructures*, PhD thesis, Universitá degli Studi di Milano-Bicocca, 2012.

[118] J. H. Van Der Merwe, *Journal of Applied Physics* **34**, 117 (1963).

[119] J. H. Van Der Merwe, *Journal of Applied Physics* **34**, 123 (1963).

[120] E. Kasper and H.-J. Herzog, *Thin Solid Films* **44**, 357 (1977).

[121] E. Kasper, *Surface Science* **174**, 630 (1986).

[122] J. W. Matthews, *Journal of Vacuum Science & Technology* **12**, 126 (1975).

[123] R. People and J. C. Bean, *Applied Physics Letters* **47**, 322 (1985).

[124] E. Strawbrigde and H. E. Evans, *Engineering Failure Analysis* **2**, 85 (1995).

[125] H. P. Singh, *Acta Crystallographica Section A* **24**, 469 (1968).

[126] Y. Okada and Y. Tokumaru, *Journal of Applied Physics* **56**, 314 (1984).

[127] C. Teichert, *Physics Reports* **365**, 335 (2002).

[128] K. Brunner, *Reports on Progress in Physics* **65**, 27 (2002).

[129] D. Zubia and S. D. Hersee, *Journal of Applied Physics* **85**, 6492 (1999).

[130] G. Kozlowski *et al.*, *Nanotechnology* **23**, 115704 (2012).

[131] T. I. Kamins, X. Li, R. S. Williams, and X. Liu, *Nano Letters* **4**, 503 (2004).

[132] H.-Y. Chang *et al.*, *Applied Physics Letters* **95**, 133120 (2009).

[133] S. Luryi and E. Suhir, *Applied Physics Letters* **49**, 140 (1986).

[134] F. Y. Huang, *Physical Review Letters* **85**, 784 (2000).

[135] D. Zubia, S. D. Hersee, and T. Khraishi, *Applied Physics Letters* **80**, 740 (2002).

[136] Z. Zhong *et al.*, *Physical Review Letters* **98**, 176102 (2007).

[137] F. Boioli *et al.*, *Applied Physics Letters* **99**, 033106 (2011).

[138] P. Zaumseil *et al.*, *Journal of Applied Physics* **112**, 043506 (2012).

[139] P. Zaumseil, G. Kozlowski, Y. Yamamoto, M. A. Schubert, and T. Schroeder, *Journal of Applied Crystallography* **46**, 868 (2013).

[140] J. Xiang *et al.*, *Nature* **441**, 489 (2006).

[141] E. Ertekin, P. A. Greaney, D. C. Chrzan, and T. D. Sands, *Journal of Applied Physics* **97**, 114325 (2005).

[142] H. Ye *et al.*, *Nano Letters* **9**, 1921 (2009).

[143] F. Laermer and A. Schilp, *Method of anisotropically etching silicon*, US Patent US6531068 B2, 1996.

[144] F. Pezzoli *et al.*, *Physical Review Applied* **1**, 044005 (2014).

[145] C. V. Falub *et al.*, *Scientific Reports* **3**, 2276 (2013).

[146] R. Gatti, A. Marzegalli, V. A. Zinovyev, F. Montalenti, and L. Miglio, *Physical Review B* **78**, 184104 (2008).

[147] R. T. Murray, C. J. Kiely, and M. Hopkinson, *Semiconductor Science and Technology* **15**, 325 (2000).

[148] V. K. Yang *et al.*, *Journal of Applied Physics* **93**, 3859 (2003).

[149] D. Colombo *et al.*, *Journal of Applied Physics* **101**, 103519 (2007).

[150] G. Capellini, M. De Seta, P. Zaumseil, G. Kozlowski, and T. Schroeder, *Journal of Applied Physics* **111**, 073518 (2012).

[151] G. Kozlowski *et al.*, *Journal of Applied Physics* **110**, 053509 (2011).

[152] M. T. Kim, *Thin Solid Films* **283**, 12 (1996).

[153] D. Digiuni, R. Gatti, and F. Montalenti, *Physical Review B* **80**, 155436 (2009).

[154] V. Grillo and F. Rossi, *Ultramicroscopy* **125**, 112 (2013).

[155] Y. A. Burenkov, Y. M. Burdukov, S. Y. Davidov, and S. P. Nikanorov, *Soviet Physics. Solid state* **15**, 1175 (1973).

[156] Y. A. Burenkov, S. Y. Davidov, and S. P. Nikanorov, *Soviet Physics. Solid state* **17**, 1446 (1973).

[157] J. J. Wortman and R. A. Evans, *Journal of Applied Physics* **36**, 153 (1965).

[158] A. Rätz, A. Ribalta, and A. Voigt, *Journal of Computational Physics* **214**, 187 (2006).

[159] W. Jiang, W. Bao, C. V. Thompson, and D. J. Srolovitz, *Acta Materialia* **60**, 5578 (2012).

[160] R. Backofen, R. Bergamaschini, and A. Voigt, *Philosophical Magazine* **94**, 2162 (2014).

[161] S. Torabi, J. Lowengrub, A. Voigt, and S. Wise, *Proceedings of the Royal Society A* **465**, 1337 (2009).

[162] J. E. Cahn and J. W. Hilliard, *The Journal of Chemical Physics* **28**, 258 (1958).

[163] B. I. Halperin, P. C. Hohenberg, and S. K. Ma, *Physical Review B* **10**, 139 (1974).

[164] X. Li, J. Lowengrub, A. Rätz, and A. Voigt, *Communications in Mathematical Sciences* **7**, 81 (2009).

[165] R. Kobayashi, *Physica D: Nonlinear Phenomena* **63**, 410 (1993).

[166] A. A. Wheeler, G. B. McFadden, and W. J. Boettinger, *Proceedings of the Royal Society of London A* **452**, 495 (1996).

[167] C. Gugenberger, R. Spatschek, and K. Kassner, *Physical Review E* **78**, 016703 (2008).

[168] S. Dai and Q. Du, *Multiscale Modeling and Simulations* **12**, 1870 (2014).

[169] A. A. Lee, A. Münch, and E. Süli, *Applied Physics Letters* **107**, 081603 (2015).

[170] Paraview website: http://www.paraview.org.

[171] F. Chen and J. Shen, *Communications in Computational Physics* **13**, 1189 (2013).

[172] E. J. Siem and W. C. Carter, *Journal of Materials Science* **40**, 3107 (2005).

[173] M. K. Santala and A. M. Glaeser, *Acta Materialia* **56**, 1967 (2008).

[174] G. Capellini *et al.*, *Journal of Applied Physics* **105**, 093525 (2009).

[175] J. Ye and C. V. Thompson, *Advanced Materials* **23**, 1567 (2011).

[176] R. W. Day *et al.*, *Nature Nanotechnology* **10**, 345 (2015).

[177] Y. Sun and Y. Xia, *Science* **298**, 2176 (2002).

[178] A. R. Tao, S. Habas, and P. Yang, *Small* **4**, 310 (2008).

[179] A. S. Barnard, N. P. Young, A. I. Kirkland, M. A. van Huis, and H. Xu, *ACS Nano* **3**, 1431 (2009).

[180] R. V. Zucker, D. Chatain, U. Dahmen, S. Hagge, and W. C. Carter, *Journal of Materials Science* **47**, 8290 (2012).

[181] Z. Gai, W. S. Yang, R. G. Zhao, and T. Sakurai, *Physical Review B* **59**, 15230 (1999).

[182] N. Moll, A. Kley, E. Pehlke, and M. Scheffler, *Physical Review B* **54**, 8844 (1996).

[183] J. Platen *et al.*, *Journal of Applied Physics* **85**, 3597 (1999).

[184] P. S. Wong, B. Liang, R. Molecke, J. Tatebayashi, and D. L. Huffaker, *Crystal Growth and Design* **10**, 2509 (2010).

[185] J. J. Zhang *et al.*, *Applied Physics Letters* **91**, 173115 (2007).

[186] T. Hanrath and B. A. Korgel, *Small* **1**, 717 (2005).

[187] B. Wiley, Y. Sun, B. Mayers, and Y. Xia, *Chemistry - A European Journal* **11**, 454 (2005).

[188] D. Adalsteinsson and J. A. Sethian, *Journal of Computational Physics* **120**, 128 (1995).

[189] D. Adalsteinsson and J. A. Sethian, *Journal of Computational Physics* **122**, 348 (1995).

[190] O. Ertl and S. Selberherr, *Microelectronic Engineering* **87**, 20 (2010).

[191] T. Kreiliger *et al.*, *Journal of Instrumentation* **9**, C03019 (2014).

[192] L. Huang, F. Liu, G.-H. Lu, and X. G. Gong, *Physical Review Letters* **96**, 016103 (2006).

[193] M. Salvalaglio *et al.*, Phase-field simulations of faceted Ge/Si-crystal arrays, merging into a suspended film. *Submitted*.